Fast Estimation of the Dynamic Start-Up Behavior of Line-Start Synchronous Reluctance Machines with Modern Rotor Designs

A thesis approved for the academic degree of

Doktor der Ingenieurwissenschaften (Dr.-Ing.)

at the

Faculty of Electrical Engineering and Information Technology

TU Dortmund University

by

Jannik Rituper, M.Sc.

Supervisor:	Prof. Dr.-Ing. Martin Pfost, TU Dortmund University
Co-Advisor:	Prof. Dr.-Ing. Raimund Gottkehaskamp, University of Applied Sciences Düsseldorf

Date of Oral Examination: 22.01.2025

Author:	Jannik Rituper
Date of Submission:	08.04.2024
Date of Oral Examination:	22.01.2025
Date of Publication:	May 2025
Faculty:	Electrical Engineering and Information Technology, Dortmund

Abstract

Line-Start Synchronous Reluctance Machines are considered a more efficient and sustainable alternative to the widely used Induction Machines. However, the research has been impeded by the lack of appropriate simulation models, as most of the studies only use the time-consuming transient two-dimensional Finite Element Method. This thesis aims to fill this gap by presenting an improved numerical parameter model that can support the development process of Line-Start Synchronous Reluctance Machines in a fast and accurate way. The focus is on machine designs, in which the conductors are placed within the flux barriers.

First, a circuit-coupled two-dimensional Finite Element model is derived. In this context, a 3D Finite Element-based method is introduced with which the end ring parameters can be calculated accurately. It is demonstrated that it is also important to take the skin effect into account for the end ring. This has a major influence on the rotor cage, as the bars are usually much deeper than in classic Induction Machines. In this model, the effect is considered by applying the multi-layer method, which divides the rotor cage into multiple separate cages to account for the changing resistance and inductance.

Secondly, a Finite Element-based parameter model is adapted to be applied to non-standard rotor cage geometries of Line-Start Synchronous Reluctance Machines. Especially the consideration of skin effect and saturation are improved. For the skin effect, the multi-layer method is adopted from the Finite Element model. For the saturation, on the other hand, the existing global saturation factor method is extended to a dq-saturation factor method, which takes the different saturation behavior of the machine's d- and q-axis into account. The validation with measurements and the Finite Element model prove that both methods can significantly improve the accuracy of the model with regard to the studied effects.

The research results represent a further step towards developing fast and accurate simulation models that can enhance the design process and therefore the development of Line-Start Synchronous Reluctance Machines. In particular, the numerical parameter model turns out to be faster from the first start-up simulation on, as it takes minutes instead of hours for one single start-up as soon as the parameters for the model have been determined.

Acknowledgements

First and foremost, I would like to thank Prof. Dr.-Ing. Raimund Gottkehaskamp, who taught me a lot about the world of electric machines from my bachelor's thesis to the completion of my dissertation. It was only thanks to his encouragement, his many valuable tips, and his willingness to engage in detailed and passionate discussions that this work could be successfully completed.

I also want to express my gratitude to Prof. Dr.-Ing. Martin Pfost for his interest in my work and the opportunity to do my doctorate at his chair.

Moreover, I am very grateful to Prof. Loïc Quéval for hosting me for half a year at the GeePs laboratory, CentraleSupélec, Université Paris-Saclay, where I was able to learn a lot, not only for my thesis.

My sincere thanks go to André Au, who always took the time to help and support me by sharing his extensive knowledge in theory and practice and being a constant source of reassurance and optimism, which in many ways contributed significantly to the success of the work.

Thanks also to the staff of the Faculty of Electrical Engineering & Information Technology at University of Applied Sciences Düsseldorf. A very special thank you goes out to the staff of the Laboratory for Electromagnetic Field Theory and Electric Machines, particularly David Orth, Christian Alteheld and Jan Güdelhöfer.

I would also like to thank my colleagues at GeePs for the pleasant working atmosphere, with special thanks to the HVDC group.

Of course, heartfelt thanks go to my parents, who have paved the way for me to this point, to my older brother, who has always had my back, and to Pete for always being supportive.

Finally, I must express my sincere appreciation to all my friends for their constant and continued support and patience throughout the thesis.

Table of Contents

1 Introduction **1**
1.1 Motivation . . . 1
1.2 Aims of this work . . . 8

2 Theoretical Background **11**
2.1 System overview . . . 11
2.2 The start-up process . . . 12
2.2.1 Steady-state behavior . . . 12
2.2.2 Transient behavior . . . 14
2.3 Requirements for a start-up simulation model . . . 16
2.4 Relation between the different coordinate systems . . . 17

3 Finite Element Model **19**
3.1 Introduction . . . 19
3.2 Investigated motors . . . 20
3.3 Two-dimensional Finite Element model . . . 23
3.3.1 Equations . . . 23
3.3.2 Boundary conditions and symmetries . . . 24
3.3.3 Materials . . . 24
3.3.4 Mesh generation . . . 25
3.4 Stator winding . . . 28
3.5 Rotor cage . . . 29
3.5.1 Analytical method . . . 29
3.5.2 Improved 3D FEM-assisted method . . . 32
3.5.3 Influence of ring resistances on the motor behavior . . . 35
3.5.4 Consideration of skin effect . . . 37
3.6 Torque and equation of motion . . . 40
3.7 Skewing . . . 40
3.8 Solution . . . 41
3.8.1 Number of time steps per electrical period . . . 41
3.8.2 Segregated solution of mechanical equations . . . 41
3.9 Experimental validation . . . 42
3.9.1 Synchronous torque measurement . . . 42
3.9.2 No-load measurement . . . 48
3.9.3 Locked rotor measurement . . . 53
3.9.4 Start-up measurement . . . 59
3.10 Conclusion . . . 69

4 Finite Element-Based Parameter Model **71**
4.1 Introduction . . . 71
4.2 Electromagnetic machine model . . . 72
4.2.1 Stator voltage equations . . . 72
4.2.2 Rotor voltage equations . . . 73
4.2.3 Full system of equations for linear materials without skin effect . . 74
4.2.4 Consideration of the skin effect . . . 76
4.2.5 Consideration of saturation . . . 80
4.2.6 Final system of equations (electromagnetic) . . . 96
4.2.7 Parameter calculation . . . 97
4.3 Mechanical machine model . . . 105
4.4 Solution . . . 106
4.5 Validation with FEM . . . 109
4.5.1 Validation of the skin effect model . . . 109
4.5.2 Validation of the saturation model . . . 114
4.5.3 Steady-state torque versus speed simulation . . . 125
4.5.4 Start-up simulation . . . 134
4.6 Validation with measurements . . . 142
4.7 Comparison of the computing time . . . 147
4.8 Conclusion . . . 148

5 Conclusion **149**

Appendices **165**

A Geometries of the Tested Motors **167**
A.1 Stator geometry . . . 167
A.2 Rotor geometries . . . 168

B Lumped Parameter Model of a Single Coil **169**
B.1 Derivation of the equation . . . 169

Chapter 1

Introduction

1.1 Motivation

To mitigate the impact of climate change, not only the worldwide energy production should be transferred to sustainable technologies, but also the consumption in total must be reduced. This includes, of course, electrically supplied applications whose overall efficiency should be optimized as much as possible. In addition, we should aim to use our resources as sustainable as possible.

When it comes to electrical energy consumption, the share of electric motors in the European Union, for example, is estimated at 50%, caused by about 8 billion electric motors [1]. The vast majority of these motors are Induction Machines (IM), a well-known technology with major advantages like mechanical robustness, simple construction, and reliability. Furthermore, in contrast to Synchronous Machines (SM), the IM comes with the big advantage that due to its rotor being equipped with a rotor cage (so-called squirrel cage), it has the ability to start directly connected to the grid without any need for an additional electronic device.

The main drawback, however, is that it usually has a low efficiency rating due to its inherent rotor Joule losses. This is beginning to cause problems for manufacturers, as the efficiency requirements for motors on the market have been and will continue to be increased in order to achieve the above-mentioned targets. For example, the European Commission has increased the ecodesign requirements (in accordance with the IEC 60034-30-1 standard) and extended their scope to a wider range of output power [2].

Recent years have therefore witnessed a growing academic and industrial interest in alternative technologies that can meet the increasing requirements in the future. Thus far, three different approaches have emerged for this purpose.

The first one aims to optimize the machine design for a better performance. This could be done by optimizing the geometry of the laminations and the winding configuration of both stator and rotor. In addition, the use of higher-quality materials such as lower-loss electrical steel or a copper rotor cage can further reduce overall losses and thus increase efficiency. Reducing the additional losses is also possible [3]. However, detailed examination of the potential of optimization strategies for induction machines by Villani et al. [4] showed that the impact on the efficiency could only be classified as low to medium, whereas the manufacturing and material costs could rise unreasonably.

The second option is to equip the induction machine with an inverter. This way, the machine can be controlled and the efficiency at each operating point can be maximized,

which is not possible if the machine is connected to the grid with a fixed voltage and frequency. There are, however, disadvantages to this approach: An additional inverter is expensive, uses more environmentally critical material, has a reduced life cycle, and less robustness to harsh environments.

Hence, the option that has been identified as the most promising approach to reach the efficiency improvement goals sustainably is to replace induction machines by Line-Start Synchronous Machines [4]–[6]. This type of machine is basically a combination of Induction and Synchronous Machine technology, providing a rotor cage for the asynchronous start-up and synchronous torque for the operation at synchronous speed. Their big advantage is that as soon as the rotor cage has accelerated the rotor to synchronous speed, the rotor fundamental current is zero and only harmonic currents remain. This means that, unlike the induction machine, a Line-Start Synchronous Machine has relatively small rotor Joule losses during operation. Therefore, it can achieve a higher efficiency just by replacing the motor without any need for an inverter.

There are two types of Line-Start Synchronous Machines which are considered to be the most promising alternatives. These are Line-Start Permanent Magnet Synchronous Machines (LSPMSM) and Line-Start Synchronous Reluctance Machines (LSSynRM). The former integrates permanent magnets into the rotor structure to produce synchronous torque (Figure 1.1 left). The latter achieves this through magnetic anisotropy, that is, the inductance difference of its synchronous axes, which is obtained by adding so-called flux barriers to the rotor (Figure 1.1 right).

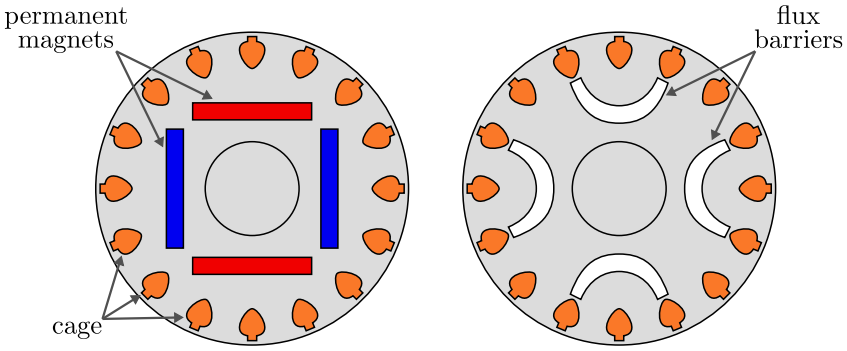

Figure 1.1: Examples of the rotor of a Line-Start Synchronous Permanent Magnet Machine (left) and a Line-Start Synchronous Reluctance Machine (right).

The vast majority of studies in the technical literature concern Line-Start Permanent Magnet Machines (Figure 1.2). Due to the simple adaption from Induction Machines and the high torque density which can even rule out IMs, they are believed to be a good option [6]. However, a major disadvantage can be identified here as well: The utilized rare earth permanent magnets have a negative environmental impact during mining and manufacturing [7]. Furthermore, the availability of those magnets is limited, which leads to high variations in price. During overload operation or in harsh environments, the magnets could also demagnetize due to high temperature. Lastly, the generation of a back-EMF when the stator is currentless can cause problems.

Line-Start Synchronous Reluctance Machines, on the other hand, do not use magnets and thus consist of the same materials as Induction Machines, which is why they are receiving increasing attention. The manufacturing process is very similar as well, so the costs to adapt the manufacturing site remain within reasonable limits [4].

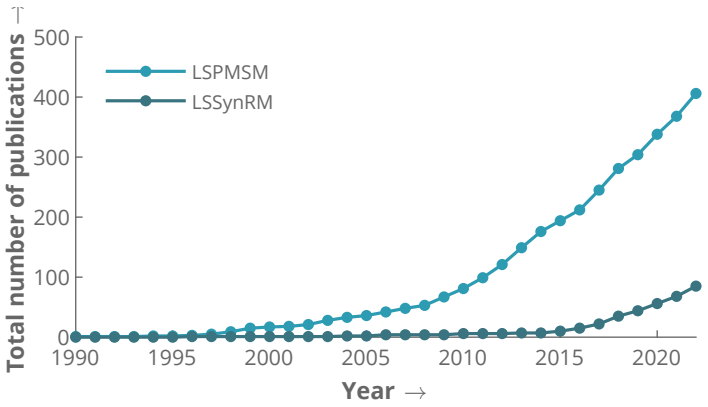

Figure 1.2: Comparison of the total number of online publications on Line-Start Permanent Magnet Machines (LSPMSM) and Line-Start Synchronous Reluctance Machines (LSSynRM) from 1990 to 2022 (for LSSynRM, also the term "Direct-on-line" instead of "Line-Start" has been included). Data obtained on 24/10/2023 from Digital Science's Dimensions platform [8]. Comparison does not claim to be exhaustive.

However, although the technology already has a long history, it is not yet mature and sufficiently understood to be able to offer market-ready products that allow a large-scale replacement of induction machines. This will be explained in more detail below after a brief historical overview of the machine's development.

In fact, research into Line-Start Synchronous Reluctance Machine technology started over 100 years ago. Kostko even claimed in 1923 [9] that it was older than induction motor technology. Yet, this cannot be fully proven and is also a question of definition. Nonetheless, the invention of three-phase synchronous machines with salient poles (also without excitation) dates back to the same era in the 19th century [10], [11].

In the next century, numerous inventions and improvements were followed by the first models for the theoretical calculation of such machines. In 1913, for instance, Jasse [12] carried out what is believed to be the first comprehensive model on synchronous machines without excitation, which were called "Synchronous Reaction Motors" at that time (and still nowadays) due to the reluctance torque also being called "reaction torque". The lack of electronics back then led to the fact that these motors usually had to start by themselves, for example by eddy currents in solid rotors. The advantage of fixed speed, simple design and hence manufacturing already made the motor quite popular for many applications where only a small output torque had to be achieved.

Due to the technology being adapted from Synchronous Machines with salient poles, the first topologies equipped with a rotor cage (adapted from damper cages providing asynchronous torque for salient-pole SMs as well) relied on external flux barriers (Figure 1.3a) [13]–[15]. These are areas that have been cut out of the highly permeable iron and which reduce the magnetic flux due to the much lower permeability of air. This reduces the inductance of the axis that has more air in it (q-axis) in comparison to the axis which still mainly consists of iron (d-axis) except for the air gap. However, in such designs also the d-axis inductance was decreased due to the higher carter factor caused by the varying air gap width. Consequently, these motors required higher magnetization currents and thus had poor efficiency ratings.

Over time, the introduction of rotors with (additional) flux barriers underneath the rotor cage followed, which could be as simple as circular or rectangular cut-outs or more adapted forms such as radial or more complex flux barriers, sometimes in segmented

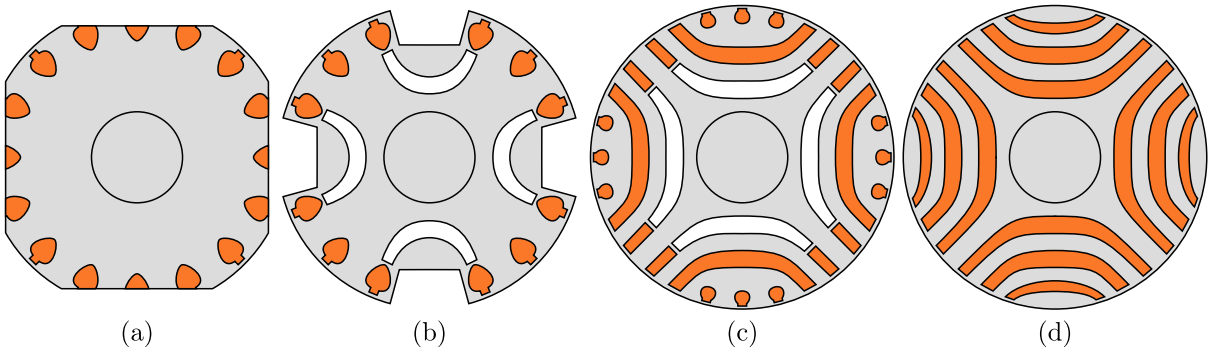

Figure 1.3: Examples for different types of rotor topologies of a four-pole Line-Start Synchronous Reluctance Machines: (a) cut-offs on the rotor outer diameter as flux barriers, (b) flux barriers underneath a standard rotor cage in addition to cut-offs, (c) hybrid induction machine and SynRM rotor structure, (d) rotor cage exclusively placed in flux barriers of SynRM.

rotors [16]–[18] (e.g., Figure 1.3b). Yet, during the second half of the 20th century, the improvements in LSSynRM technology were very little. The design challenges were high due to the absence of enough computational power. Apart from hardly any studies except for example from Honsinger in 1972 [19], which already showed a trend to new rotor designs being hybrid topologies of SynRM and IM elements (cf. Figure 1.3c), mainly LSPMSM have been studied due to the introduction of and improvements in rare-earth permanent magnet materials [20].

The improvements in design of classic Synchronous Reluctance Machines which accelerated in the 1990s [21], [22], and the potential of further optimizing their efficiency with increasing computational power, then led to new rotor topologies being introduced in the literature of LSSynRM. The main design aspect to be mentioned is that flux barriers, which follow the "natural" path of the magnetic flux in the d-axis, are completely or partially filled with conductive material (Figure 1.3d). This comes with the advantage that the d-axis inductance is nearly maintained, while only that of the q-axis is reduced as much as possible. In addition, the rotor cage does not initially affect the steady-state performance (even though the flux barriers can also be adjusted to improve the start-up behavior, which is associated with a reduction in the steady-state behavior). Perhaps the best-known study using this approach was carried out by Gamba et al. in 2013 [23] (and also the follow-up work [24]).

There is now a broad consensus that LSSynRMs are a viable option as an alternative to IMs [5], owing to the major improvements in the designs in terms of steady-state efficiency. In previous work, it could also be proven that even replacing the rotor of an induction machine with a non-optimized LSSynRM rotor can already lead to much higher efficiency [A1]. This can be beneficial especially for small motors, in which the cage resistance of the IM and thus the losses in rated operation are typically high due to the small volume. However, the question of the extent to which this can happen and with what restrictions remains unanswered due to the gaps in our knowledge.

One major theoretical issue that still has dominated the field for many years now concerns the challenge of ensuring a reliable start-up (cf. [23]–[31]). After accelerating to almost synchronous speed, the rotor must be pulled into step, which means it has to synchronize to the rotating stator field. However, this synchronization process is not ensured for every load torque below the pull-out torque. Instead, there is a maximum

load torque that can be synchronized, which in addition depends on the total moment of inertia of the rotating parts. If this limit is exceeded, the motor will stay in unstable and therefore undesired asynchronous operation.

The reason for this problem is that the asynchronous and synchronous torque each place different, sometimes conflicting, demands on the rotor design. In order to achieve good asynchronous start-up behavior, the conductive material must be placed as close as possible to the air gap. This is the case for all standard Induction Machines with rotor cages. On the contrary, the synchronous operating behavior is improved by maximizing the difference between the inductances of the d- and q-axis L_d and L_q. Especially in new designs focusing on maximum steady-state efficiency to meet the efficiency requirements, and therefore maximum $L_\mathrm{d}/L_\mathrm{q}$ ratio (as in Figure 1.3c and d), the flux barrier design leaves less space to place conductive material near the air gap. Furthermore, the start-up behavior deteriorates even more if the rotor cage becomes unsymmetrical due to the rotor design, as in Figure 1.3d [32]–[35].

In contrast, the start-up of an Induction Machine is only limited by thermal constraints. As long as the load torque is lower than the pull-up torque of the machine at the given voltage, the steady state is reached with a certain slip remaining. Since the LSSynRM must in addition overcome this slip and synchronize to the stator field, its start-up is far more critical and therefore of particular interest for the design process, especially if the motor is to be a one-to-one replacement for IMs. Nonetheless, the prospect of higher efficiency in an application using the same materials as induction machines and maintaining manufacturing costs makes it interesting to investigate the technology and its challenges.

Yet, it appears that this research has been impeded by the lack of appropriate simulation models for the transient start-up process. For each design and set of parameters, many simulations have to be carried out, leading to hundreds or thousands of simulations during the design process [36]. This makes the task very time-consuming. As mentioned before, especially new conductor designs of flux barriers filled with aluminum pose a major challenge. Hence, models should be adapted to provide fast results while still maintaining sufficient accuracy for any kind of geometry.

Most of the design studies to date have been carried out employing the Finite Element Method (FEM) [27], [28], [31], [36]–[46]. Its versatility regarding the wide variety of geometries while providing accurate results and profound insight in local physical effects is the reason for it to be considered state of the art. Nonetheless, the research to date has tended to rely on available computational power. In practice, the method still leads to time-consuming simulations for each single start-up which deteriorates the result of optimization studies because only few geometries could be studied in a small number of iterations, for example in [41].

A different type of model can be grouped under the term of numerical parameter models, including for example dq-models [23], [29], [47]–[52] that reduce stator and rotor windings to two equations each. However, this comes at a cost, namely the neglection of harmonics, which can lead to less accurate results. Furthermore, as already stated in [23], [53], the parameter estimation for these models is complex and error-prone, often leading to effects being neglected or oversimplified (mostly saturation and skin effect). As already pointed out in [47], however, the saturation effects of anisotropic motors are more complex than in isotropic machines and important to consider.

In contrast, Güdelhöfer presented a semi-analytical parameter model, which can be considered an important step towards a fast and accurate calculation procedure of

LSSynRM [54], [55]. By deriving a phase-domain model that accounts for saturation in a simplified way and even considers geometry-induced space harmonics and inter-bar currents, he has been able to estimate the start-up behavior of LSSynRM with standard IM cages much faster with a good accuracy.

However, this model still has weaknesses that need to be overcome. Firstly, the method of considering saturation with a single saturation factor is incomplete as it ignores the aforementioned particular saturation characteristics of an LSSynRM. Due to the rotor's anisotropy, the saturation of d- and q-axes is different, which cannot be accurately modelled by using a single factor. Secondly, as the model is applied to LSSynRM with standard Induction Machine cages, it uses skin effect factors that manipulate the resistance and inductance of the rotor bars. However, these are not applicable to modern LSSynRM geometries in which the conductors are placed inside the flux barriers. Thirdly, the existing model does not clarify how the iron bridges at the air gap and inside the rotor can be considered for modern rotor designs. The previous motor designs only had internal bridges, if any, which were set to air in the model and thus neglected regarding the magnetizing current. Lastly, the derivation of the system of the equation itself can be simplified to obtain a more comprehensive model.

Apart from these parameter models, there is a third type, that is usually preferred from an engineer's perspective. Fully analytical models are much faster due to their simple solution, and also provide insight on the machine's working principle and interrelationships, which is crucial for understanding and improving the technology. However, studies from the past [19], [56] as well as more recent ones [57] showed that it is quite difficult to derive accurate models. This is caused by the complex rotor topology which can consist of rotor bars of many different shapes and sizes (cf. Figure 1.3) as well as flux barriers embedded in the rotor that cannot be represented easily and therefore cause oversimplified approaches to fail [57]. To the author's best knowledge, there is no work introducing a sufficiently accurate analytical model for the start-up of LSSynRM so far.

In addition, all of these presented studies in the literature share the problem of mostly poor experimental validation, as discussed in the following.

Firstly, there are numerous studies which do not provide any experimental validation at all [28], [36], [37], [41], [42], [45], [57], [58]. This may still be useful for qualitative studies on the general behavior of the motors. However, since it is known that the dynamic start-up is an extremely challenging discipline, the results of these studies are often only of limited significance.

Secondly, there are studies in which measurement results are presented but not directly compared with those of the simulation [40], [49], [52].

Lastly, there are indeed studies that compare the results of measurements with simulations. However, even when the dynamic behavior is discussed in the paper, some studies are restricted to steady-state measurements for validation [30], [38], [39], [44].

The studies in [30], [51], on the other hand, are limited in that the experiments do not reflect the real conditions of the designated applications and are hence of limited significance as well. Here, the synchronization tests are carried out by gradually decreasing the load torque until the motor eventually synchronizes. Apart from the obvious difference to the real start-up procedure, also the temperature and therefore the stator and rotor resistances are unknown.

In some studies where the dynamic start-up is compared, the significance is sometimes limited, as only one or a few cases are shown [59]. Moreover, in [43], for example, only the current versus time but no other quantity is compared for the dynamic start-up. In

[29], the synchronization behavior depending on load torque and moment of inertia have been compared, but not in the same plot and with visible differences. The comparison of the dynamic start-up is missing.

Other studies, by contrast, provide good approaches for reliable experimental validation of the models, but also report problems that occur. Often it appears that there are too many unknowns in the experiment, which is briefly discussed in the following.

On the one hand, recording the winding temperatures poses a major problem. The cage temperature is often estimated, which can result in a large difference between simulation and measurement. In [23], it has already been reported that for the dynamic start-up the temperature is critical. This is because the motor has to cool down if the start-up should be measured for the cold motor. Therefore, doubts about the experiments are stated.

Likewise, in [50], the measurement is carried out for "cold and hot motor", whereas the simulation has a fixed temperature, which causes the results to differ. Furthermore, the test setup in this study is unknown and only one single dynamic start-up measurement is shown.

The same problems are reported in [31], where steady-state measurements are followed by a dynamic start-up. It is assumed that temperature is the key factor causing deviations, as the model and the measurement have different resistance values. Furthermore, a comparison of speed or torque over time is not made in the paper.

In [27], on the other hand, the moment of inertia of the rotating system is reported as an uncertainty factor. In particular, the load moment of inertia is considered to be incorrect, which is why its value is adjusted until the simulations match the measurement. Furthermore, the experimental setup contains claw couplings and a torque sensor as non-rigid elements on the rotating shaft, which can further influence the dynamic behavior.

Güdelhöfer [54], [55], in addition, failed to compare the speed versus time curves during start-up, which hence lacks information about the accuracy of the model in the dynamic case.

Prior studies have also not been able to account for the end-ring portion of the rotor cage in a physically reasonable way. Instead, much of the literature on the start-up behavior focuses on the rotor bar design using 2D FEM, therefore ignoring the end-rings in their calculations and assuming ideally short-circuited rotor bars [28], [30], [31], [36], [37], [40], [43], [51]. This might be valid for optimization studies, where different (rotor) geometries are compared to each other. The assumption that the end-ring's influence on the asynchronous behavior is the same for every geometry seems reasonable regarding the possible savings in the already critical computing times.

As soon as the real start-up behavior is to be simulated and the results are compared to measurements, however, it loses validity. The end-ring will always increase the total rotor resistance and therefore decrease asynchronous torque near synchronous speed. This means that not taking the rings into account will overestimate the synchronization capability.

Apart from the above-mentioned design studies, there are a few studies that introduce dq models which include the total rotor resistance of each axis [29], [48], [49], [51]. However, there is no comment on how to obtain the total resistance that includes the end-ring.

The only known study on modern LSSynRM that couples a rotor circuit to the 2D FE model and provides insight on the end-ring resistance calculation is presented in [39]. Here, an analytical approach known from induction machines is used to compute the

resistance for one slot pitch, which is assumed to be the same for each pair of rotor bars. Yet, as the geometry of each bar differs, this will lead to inaccurate results for more complex cage geometries.

Furthermore, a value for the ring resistance is specified in [59]. However, this is calculated analytically and set to the same value for each rotor loop. As this does not reflect the real end ring, which is unsymmetrical, the simulation results may not be reliable as well.

Overall, the lack of appropriate models in all aforementioned studies highlights the need for a versatile model that can be adapted to any rotor cage geometry.

From all the studies reviewed, it is evident that there is still need for improvement in the existing models to be able to simulate the start-up of Line-Start Synchronous Reluctance Machines in a reliable and fast manner. Finite Element models are incomplete because they ignore the complexity of the full rotor cage, including its end rings. Furthermore, the computing time is still too high for the application in the design process. Güdelhöfer [54], [55] has created a good basis for parameter models, but there is still need for improvement for LSSynRM in general and modern geometries in particular.

1.2 Aims of this work

As a result, this work aims to eliminate the mentioned weaknesses in existing Finite Element models and numerical parameter models in order to drive the further development of highly efficient Line-Start Synchronous Reluctance Machines. This is intended to have reliable tools at hand for different stages in the design process that deliver reliable results while taking into account the given requirements. Both the simulation of the start-up of standard designs and new types of LSSynRM should be able to be simulated either precisely or particularly fast using these methods. The thesis takes the form of five chapters.

Firstly, a closer look is taken at the start-up process in Chapter 2. An introduction to the system to be modeled and an insight into the challenges to be faced form the basis for a more detailed discussion in the following chapters.

In Chapter 3, a Finite Element model is developed to provide a reference related to the real behavior of LSSynRM. The weaknesses in current models regarding their comparability with measurements are worked out so that, in theory, this model can serve as a reference without the need for measurements in large parts of a motor design process or to validate other models. Special attention will also be paid to the calculation and the importance of accurate end-ring parameters, which tend to be neglected in most of the studies. Furthermore, the validation with measurements is carried out carefully with all suitable types of tests to be sure that it is successful and that potential weaknesses of the model are known.

In Chapter 4, a fast numerical parameter model will be derived based on the one presented by Güdelhöfer [54], [55]. This way, time-consuming FE studies are replaced by a model in which an analytical system of equations is derived. The parameters required in the model are calculated using 2D magnetostatic FEM. In practice, this is significantly more time-efficient than solving a transient FE model. In contrast to dq models, the approach of a phase domain model will also include geometry-induced space harmonics and therefore lead to more accurate results. Particular attention is paid to the consideration of saturation and the skin effect for non-standard rotor cage geometries. Both effects are

the most critical for achieving sufficient accuracy for start-up simulations, and have not been correctly considered so far. The model will then be validated with FEM as well as with measurements. Even though previous publications of the author could already prove the validity of the single methods [A2]–[A4], a comprehensive validation including measurements is still pending and will be carried out in this chapter.

In conclusion, this thesis aims to contribute to the growing area of research into Line-Start Synchronous Reluctance Machines by providing two different models focusing on the critical start-up process. Depending on the engineer's aim, either a slow but precise FE model or a fast and slightly less accurate numerical parameter model can be chosen. Focusing on key effects in each model and clarifying their benefits and limitations will help to improve the design process and its many challenges.

It is, however, not the task of this thesis to study LSSynRM technology itself. Based on numerous promising studies as presented above, the author is convinced that LSSynRM can be a sustainable and efficient replacement for induction machines under certain conditions. The presented models and methods may help to work out these conditions and widen the area of applications that the LSSynRM will be suited for in the future. Nonetheless, a full discussion of how to optimize the start-up lies beyond the scope of this dissertation.

Chapter 2

Theoretical Background

The purpose of this chapter is to introduce the start-up process, its challenges and the requirements for a simulation model. Firstly, an overview of the system to be modelled will be given to clarify the important global parameters. Secondly, the three different phases of a start-up process as well as the characterization of the start-up performance of a Line-Start Synchronous Reluctance Machine are explained. Thirdly, the requirements for a suited simulation model are discussed. Finally, the relation between the coordinate systems used in this work is illustrated.

2.1 System overview

To develop an accurate and well-suited simulation model, first the system that has to be modelled needs to be defined. A simplified overview is shown in Figure 2.1.

The Line-Start Synchronous Reluctance Machine is directly connected to the grid, which provides a three-phase AC system, usually with a voltage of 400 V at a frequency of 50 Hz. However, any other AC voltage supply is possible to model.

By converting the electric energy provided by the grid into mechanical energy (that is, producing electromagnetic torque T_{el}), different types of loads with different characteristics can be driven. For fans and pumps, which are the most frequently discussed applications for LSSynRM, the load torque T_{load} typically increases with increasing speed n. Here, T_{load} mainly consists of the ventilation torque as well as the friction torque due to bearings. The total moment of inertia J_{tot} of the drive is fixed. Depending on the application, however, further load torques even with time- or speed-dependent profiles could be applied and should also be considered when investigating the machine's start-up behavior.

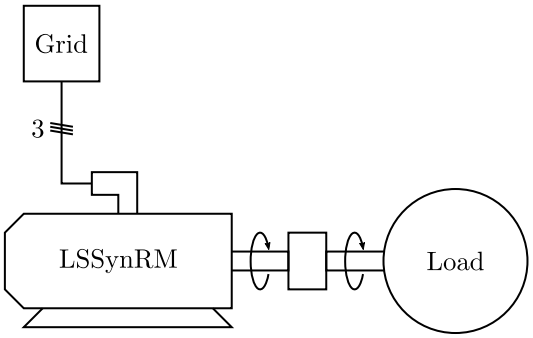

Figure 2.1: Overview of the system that has to be modelled. The LSSynRM is fed by a three-phase grid at a fixed frequency and drives a load.

2.2 The start-up process

2.2.1 Steady-state behavior

Before proceeding to examine the transient start-up process, it would be useful at this stage to consider the steady-state representation of a Line-Start Synchronous Reluctance Machine to understand its behavior. By pointing out its similarities and differences compared to an Induction Machine, it will then be more clear which challenges have to be faced.

Figure 2.2 shows the idealized steady-state fundamental torque versus speed curve (solid red line) as presented in [60]. In general, the curve resembles that of an Induction Machine over a large area. The theory is briefly introduced in the following [61], [62].

If the motor is at a standstill and the voltage at the terminals is switched on, currents flow in the stator winding. As the coils of the individual phases are distributed around the stator according to the phase shift of the voltages, a rotating magnetic field of frequency f_s is created, whereby the index s stands for stator. This field induces electromotive forces (EMFs) in the stator phases themselves because it rotates relative to the stator coils, and the individual flux linkages of the coils therefore vary over time.

In addition, as the stator field rotates around the rotor, it also induces EMFs in the electrically conductive rotor cage. This causes so-called eddy currents to flow that always form closed loops, which themselves create a magnetic field. According to Lenz's Law, the eddy currents flow in such a way that their generated magnetic field counteracts their cause (the magnetic field of the stator).

Regarding the rotational speed of both magnetic fields, it is to mention that the fundamental of the rotating stator field always causes the fundamental of the rotor field to rotate with the same speed. If this speed is defined as synchronous speed n_0, then the following expression for the slip is obtained:

$$s = 1 - \frac{n}{n_0}. \tag{2.1}$$

Hence, at standstill the slip equals 1, which means that the rotor frequency is equal to the stator frequency:

$$f_\mathrm{r} = s f_\mathrm{s}. \tag{2.2}$$

Furthermore, it would follow from Lenz's law that, ideally, the induced rotor field is phase-shifted by 180° in relation to the generating stator field. However, as the rotor cage has a finite electrical resistance, the phase shift is decreased. This means that the magnetic

poles of both fields are also shifted against each other, which produces an electromagnetic torque that causes the rotor to start to rotate. The greater the rotor resistance, the greater the phase shift and therefore the greater the torque, which is called *locked rotor torque* at $s = 1$.

With increasing speed, the rotor frequency will now adapt according to the decreasing slip (2.2). The fundamentals of the stator and rotor magnetic fields continue to have the same speed. Hence, their interaction still produces asynchronous torque. This fundamental torque usually increases with increasing speed until it reaches the *breakdown torque*, of which the value and the corresponding slip differ for each motor. Subsequently, the cage torque will successively decrease until it finally reaches zero at $s = 0$ because the rotor speed is then synchronized to the stator magnetic field ($f_\mathrm{r} = 0$) and no more EMFs are induced into the rotor cage (dotted red line).

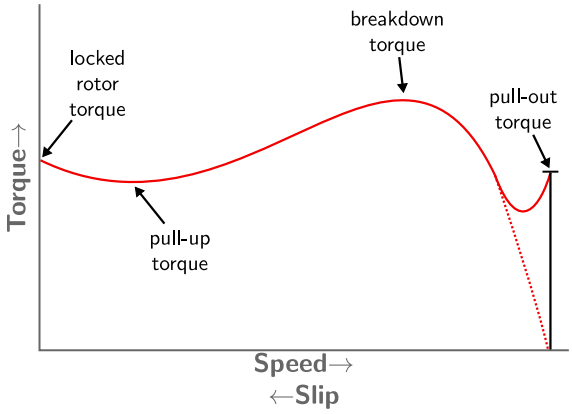

Figure 2.2: Idealized steady-state torque versus speed curve of a Line-Start Synchronous Reluctance Machine [60].

While an Induction Machine would operate at a remaining slip where it can provide the required load torque, the Line-Start Synchronous Reluctance Machine now enters the synchronization area. More precisely, because of its anisotropy, the rotor constantly tries to align with the stator magnetic field and therefore produces a further torque component, the so-called *reluctance torque* (or *reaction torque*). It is obvious that the anisotropy is coupled to the rotor speed, which means that the reluctance torque is a pulsating torque component of which the mean value is zero for $s > 0$. The frequency of the torque oscillation results from the relative speed of the stator field to the rotor to $2f_\mathrm{r}$. The factor 2 is because both the d and q axes are aligned with the stator field twice for each full revolution.

However, when the slip now gets close to zero, the kinetic energy needed to overcome the remaining speed difference $n_0 - n = n_\mathrm{s}$ may be provided by the electromagnetic torque of the motor. This means that $T_\mathrm{el} - T_\mathrm{load}$ must be positive and J_tot small enough so that the rotor can overcome the speed difference in half a torque cycle [56]. This is a dynamic process which starts from the point where the solid red line and the dotted red line separate in Figure 2.2.

As mentioned before, the rotor cage is inactive once the synchronous speed n_0 is reached, which means that the motor only provides synchronous torque (solid black line) that for LSSynRM exclusively consists of reluctance torque. The motor will hence stay in synchronous operation as long as the total load torque is lower than the *pull-out torque*, which is the maximum value of the reluctance torque at $s = 0$. However, it is also possible that the motor cannot synchronize because the reluctance torque is too small

to provide enough energy to accelerate the rotor to overcome the speed difference. The motor will then remain in asynchronous operation, oscillating around a mean speed due to the pulsating reluctance torque component.

In addition to the fundamental torque components, a Line-Start Synchronous Reluctance Machine also has parasitic torque components that have to be considered. They can again be classified into rotor cage and reluctance torque components. Generally, most of the parasitic torque components coming from the interaction of the stator field with the rotor cage are the same as known from standard Induction Machines [63], [64].

A further difference to standard Induction Machines can be observed due to unsymmetrical rotor cages, which are typical for modern LSSynRM designs (cf. Figure 1.3 c and d). The effect is already known from large salient-pole Synchronous Machines, of which the start-up is ensured by a rotor cage as well. If the resistances of the rotor's d- and q-axes differs, an alternating magnetic field is generated relative to the rotor winding [34]. This alternating field can be split into two rotating fields in opposite directions.

One of these components has the same frequency as the stator field and therefore interacts with the stator fundamental field. The other component has a resulting frequency $(1 - 2s)f_s$. For this, the stator winding behaves similarly to a cage, as the phases are short-circuited via the grid due to its much lower impedance. Since the synchronous speed of this component is at $s = 0.5$ [34], [35], it creates an accelerating torque for $s > 0.5$ and a braking torque for $s < 0.5$. For the torque-speed-curve, this typically results in an observable torque dip at $s = 0.5$ [33], [40], which is known as *Goerges' phenomenon* [32]. It can be more or less pronounced, depending on the rotor cage geometry.

Moreover, as pointed out in [35], both the unsymmetrical rotor cage and the anisotropy of the rotor itself can create these harmonic air gap field components. Therefore, it has to be considered that the real torque-speed-curve will differ from the idealized description in literature.

2.2.2 Transient behavior

Having described the steady-state start-up behavior, the following section will explain the dynamic start-up process. Figure 2.3 displays the torque versus speed function of a transient start-up simulation from FEM. Here, a successful (left) and an unsuccessful start-up (right) were compared. Higher torque harmonics have been filtered to improve visualization.

What is immediately noticeable is that the torque curve now shows pronounced oscillations around the average asynchronous torque. This comes from both, the rotor cage torque and the reluctance torque, as has been described in the previous section. While both simulations look similar for a wide range, there are significant differences near the synchronous speed n_0. In the first case (Figure 2.3 left), the synchronization is observable as a circulating function converging to the point of synchronous speed and approximately zero torque (dashed gray line). In the case of an unsuccessful synchronization (right), the torque remains in a state that circulates with the same radius and never converges. The speed is always smaller than the synchronous speed.

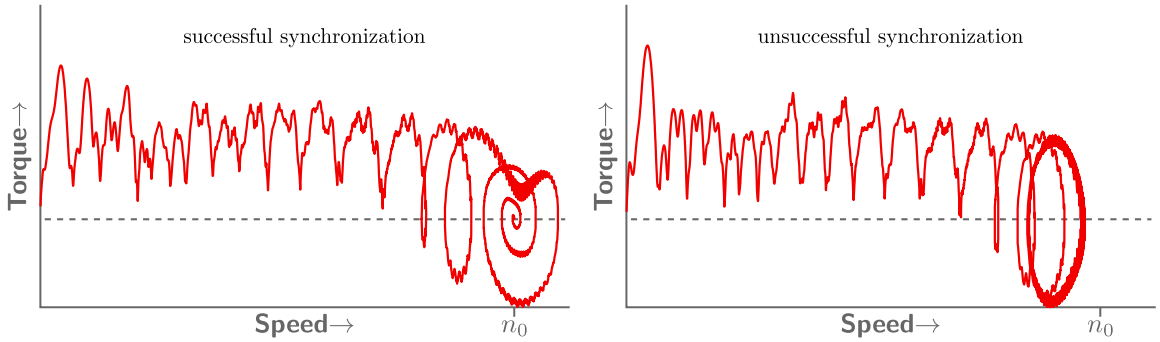

Figure 2.3: Comparison of transient torque versus speed curves of a 2-pole Line-Start Synchronous Reluctance Machine from time-stepping Finite Element Analyses that result in a successful (left) and an unsuccessful synchronization (right). The dashed gray line indicates zero torque. In both cases, the highest torque harmonics are filtered for better illustration.

To develop a more profound understanding of the synchronization process, the speed versus time curves of both start-ups are now discussed (Figure 2.4). At first, when the voltage is switched on, the rotor accelerates from standstill to synchronous speed (phase **A**). This acceleration is provided by the asynchronous torque, as described for the steady-state case. This means that the problems to solve for modelling this phase will remain quite similar to modelling Induction Machines. However, the geometry of Line-Start Synchronous Reluctance Machines is often far more complex than the one from an Induction Machine (cf. Figure 1.3). There is, on the one hand, the additional anisotropy in the rotor and on the other hand, the varying conductor design of modern Line-Start Synchronous Reluctance Machines that can greatly differ from symmetrically distributed Induction Machine rotor bars. These reasons further complicate the modelling process.

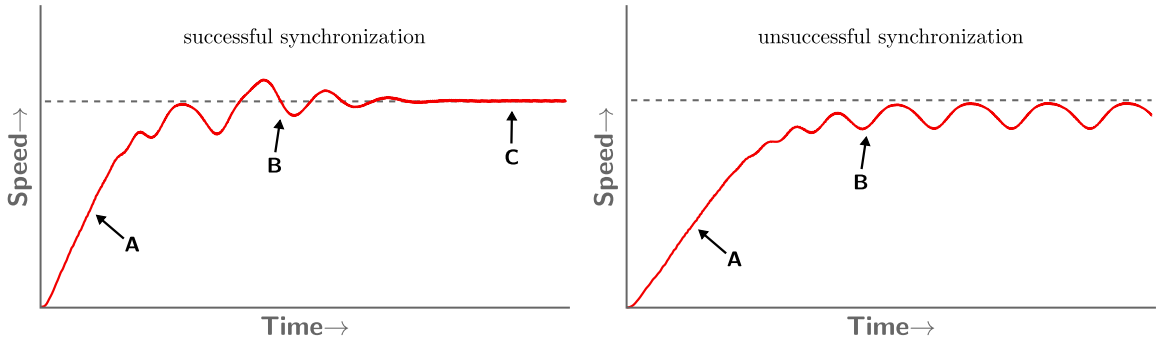

Figure 2.4: Speed versus time curves from measurements of a successful (left) and unsuccessful (right) start-up of a Line-Start Synchronous Reluctance Machine (corresponds to Figure 2.3). Phase **A** is the acceleration phase, phase **B** is the synchronization phase and phase **C** is the steady-state operation.

After accelerating to almost synchronous speed, the frequency of the pulsating reluctance torque component is very low because s is small. Now, the rotor has to synchronize or *pull into step* (phase **B**), which means that the reluctance torque has to accelerate the rotor to overcome the speed difference of the stator field and the rotor during one half of a torque cycle. This synchronization is a dynamic process as well.

Once the motor reached synchronous speed and all transients have disappeared, the rotor is in *steady state* (phase **C**). Here, the rotor cage only acts as a damper winding.

The synchronous torque is only provided by the anisotropy, that is, the reluctance torque.

If the motor cannot synchronize, phase **B** is never left and the motor reaches a quasi-steady state (Figure 2.4 right). Here, it is clearly observable that the speed oscillates around a mean value, which is defined by the steady-state torque versus speed behavior. The frequency of the oscillation equals twice the slip frequency for the given average torque.

The quantity describing whether the motor can pull into step or not is the *critical load torque* T_{crit}. This is not fixed but depends on the total moment of inertia J_{tot} of the rotating shaft. The result is therefore a characteristic curve for $T_{\mathrm{crit}} = f(J_{\mathrm{tot}})$, as presented in Figure 2.5.

The function itself has to be estimated by evaluating the start-up process for different combinations of load torque and inertia. The limit is then found in the interval between a successful (○) and an unsuccessful (×) start-up. If this characteristic curve for a given voltage is known, the engineer can decide if the motor is suitable for a specified application.

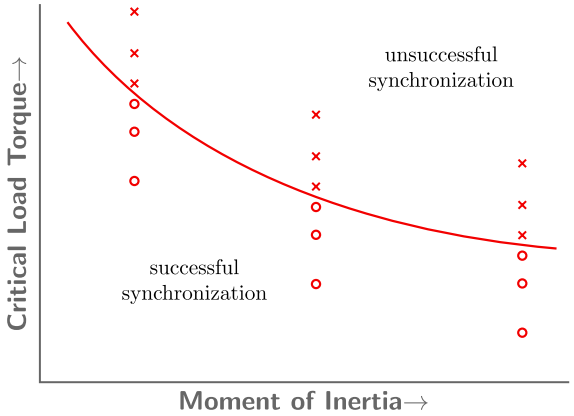

Figure 2.5: Critical load torque versus total moment of inertia for a Line-Start Synchronous Reluctance Machine. All load torque-inertia combinations below the curve can be synchronized by the studied motor. ○ marks a successful and × an unsuccessful start-up observed in simulations/measurements, which are needed to approximate the limit curve.

In conclusion, numerous evaluations have to be carried out to approximate this characteristic curve for a single motor. A suited model for this evaluation therefore has to be fast but also precise concerning the resulting values. Otherwise, the task of selecting a suited motor for an application cannot be done reliably. Hence, the next section will briefly describe the requirements for a simulation model.

2.3 Requirements for a start-up simulation model

The aim of a machine model is to simulate the machine behavior for the specified input parameters, that is, phase voltage, frequency, load torque and moment of inertia. Depending on the type and the complexity of the model, the outputs (current, torque, speed, etc.) will be more or less close to the real machine behavior which can be studied with measurements.

For the simulation of the start-up of a Line-Start Synchronous Reluctance Machine, a model has to consist of two subsystems: electromagnetic (voltage equations) and mechanical (equation of motion). The former provides the outputs of the electromagnetic quantities such as current, flux linkage, torque, etc. The latter describes the mechanical

behavior of the system, that is, the rotor position and speed. It is obvious that these two systems are coupled because the electromagnetic system depends on the outputs of the mechanical system and vice versa. The main quantity that couples both systems is the electromagnetic torque produced by the rotor. It is the resulting quantity of the conversion of electrical energy provided by the grid into mechanical energy which drives the load of the application. Therefore, a particular interest of a suited model for the aim of this work lies in the accurate modelling of the torque.

2.4 Relation between the different coordinate systems

As already mentioned in the introduction, the dq coordinate system is often used for the calculation or description of synchronous motors. It transforms the three-phase, static stator coordinate system (abc) into a two-phase, rotating rotor coordinate system (dq). Even though the abc coordinate system is the basis for deriving the models in this thesis, the dq coordinate system will be used for explanations and derivations as well.

Hence, Figure 2.6 displays the relation between both coordinate systems. The axes of the coils a, b and c are marked with dashed arrows. Here, the axis of coil a lies in the center of the first coil group of the first phase. The rotor angle ϑ_r is defined as zero if the d-axis is aligned with axis a.

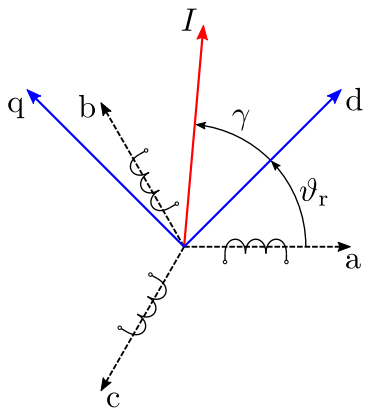

Figure 2.6: Definition and relation between the used abc and dq0 coordinate systems in this work. A current space vector of magnitude I and angle γ is shown as an example.

Moreover, a stator current space vector has been drawn in the diagram as an example. This always refers to the dq0 coordinate system. It is described by its magnitude I and the angle to the d-axis γ. The latter is referred to as current angle in the following. Other space vectors, such as flux linkage, will also be described in this way.

In Line-Start Synchronous Reluctance Machines, the d-axis is always defined as the axis with the highest permeance, that is, the iron axis between two poles with flux barriers. In contrast, the q-axis defines the axis orthogonal to the center of the flux barriers. It is hence at an angle of $90°_\mathrm{el}$ or $90°_\mathrm{mech}/p$ to the d-axis.

Chapter 3

Finite Element Model

3.1 Introduction

The Finite Element Method (FEM) is the most used method when it comes to precise modelling of physical problems since it can provide very accurate results no matter the complexity of the problem. The main principle is based on partial differential equations (PDEs) which are solved for a finite number of elements which represent the model geometry. The domain's boundaries have additional boundary conditions which define the properties of the element boundaries not connected to other elements. For the study of electric machines, mostly two-dimensional (2D) but also three-dimensional (3D) FEM is applied.

A well-derived and validated Finite Element model can accurately predict a motor's performance, while also being able to provide insights on the electromagnetic circuit. In practice, this means that important steps in the development process can be replaced by simulations before another prototype has to be built and measured. Reliable simulation results can be obtained, especially for designs that are similar to the validated prototype. To achieve this aim for the simulation of Line-Start Synchronous Reluctance Machine start-ups, this chapter proposes an accurate two-dimensional model. It then also serves as a reference for the numerical parameter model.

The chapter starts by introducing three different prototypes that have been designed and manufactured to serve as test objects for the introduced models. Section 3.3 then derives the two-dimensional model, whereby the materials and the mesh generation receive special attention. To represent the windings, Sections 3.4 and 3.5 introduce electric circuits that account for the three-phase stator winding and the rotor cage, respectively. As stated in Section 1.2, this also includes a new 3D Finite Element-based model for non-standard rotor cage geometries. After presenting the used methods for torque calculation in the equation of motion (Section 3.6) and consideration of skewing (Section 3.7), the chapter gives advice on a fast and reliable solution of the time-dependent study (Section 3.8). It then moves on to an extensive experimental validation of the proposed model in Section 3.9, including different modes of operation. Lastly, it closes with a conclusion on the presented results.

Note: All Finite Element models in this work are implemented with COMSOL Multiphysics® (version 5.6) [65].

3.2 Investigated motors

Before proceeding to introduce the Finite Element model, it is important to choose multiple motors for it to be tested and to be studied in detail. The most suitable motors for this purpose are those that are not optimized in terms of their operating behavior. This means that fairly pronounced parasitic effects and poor start-up behavior are intentional. This is the only way to ensure that the models can reliably represent all aspects of operating behavior, no matter the geometry. In addition, certain effects should become visible through the choice of motors.

Hence, three motors that serve this purpose are presented in this section. They are used throughout the whole thesis. All three motors are based on a specially designed Induction Machine (IM) which is optimized for spindle applications at speeds around 9000 1/min. The higher frequency is provided by an inverter feeding multiple machines, meaning they all have to be able to start by themselves. Furthermore, the machine is embedded in a totally enclosed non-ventilated (TENV) housing because it is externally cooled by its designated application.

The first motor to be introduced is Motor I. It has the same stator and rotor core as the Induction Machine. Two additional flux barriers per pole in the rotor core, which were introduced into the completely manufactured rotor below the cage by wire erosion, create an anisotropy. Its geometry, as well as the important data, is shown in Figure 3.1. The full geometries of all three motors and their dimensions are given in the Appendix A. Even though this work focuses on new designs of LSSynRM with conductive material filled in the flux barriers, this basic design with a standard squirrel cage will provide a good example for explaining different aspects of the model. It makes it also possible to compare the results and the accuracy when moving from this standard geometry to newer ones.

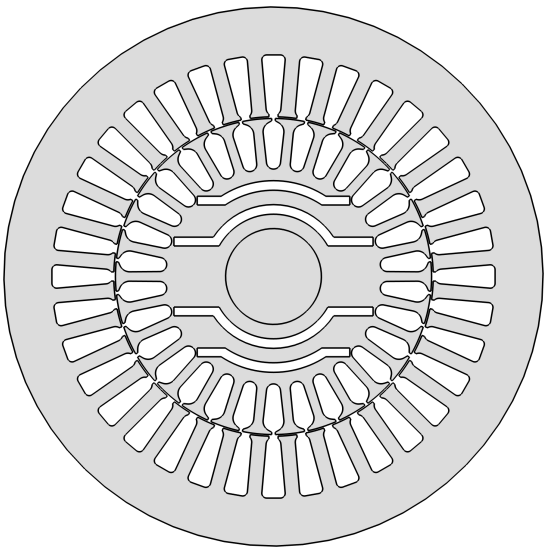

Parameter		**Value**
Outer stator diameter	D_o	135 mm
Inner stator diameter	D_i	80 mm
Core length	l_e	40 mm
Air-Gap width	δ_g	0.42 mm
Number of stator slots	Z_1	36
Number of phases	m	3
Number of poles	$2p$	2
Number of turns of a coil	N	45
Stator phase resistance at 20°C	R_ph	4.14 Ω
Electrical steel		M250-35A
Rotor cage material		Aluminum

Figure 3.1: Geometry and important data of Motor I.

Apart from the flux barriers, it is worth mentioning that this motor and all others to be presented have a rotor cage made of aluminum, which is obtained by die-casting. Furthermore, it can be highlighted that the stator geometry, which is a IEC90 standard

lamination (originally for a 4-pole motor), has been used for all other motors as well. Due to its designated application at high frequencies (e.g., 150 Hz fixed), the used material is M250-35A to reduce iron losses.

The second motor is also a 2-pole LSSynRM but with a completely redesigned laser-cut rotor core (Motor II, Figure 3.2). As stated in the Introduction, the best operating behavior regarding high efficiency at steady state can be achieved by designing a SynRM rotor and then filling the flux barriers with conductive material and adding end rings to obtain a rotor cage that provides asynchronous torque for line start. However, as stated at the beginning of the section, the motor should not be optimized, which is why the design is poor in terms of $L_\mathrm{d}/L_\mathrm{q}$ ratio and torque ripple.

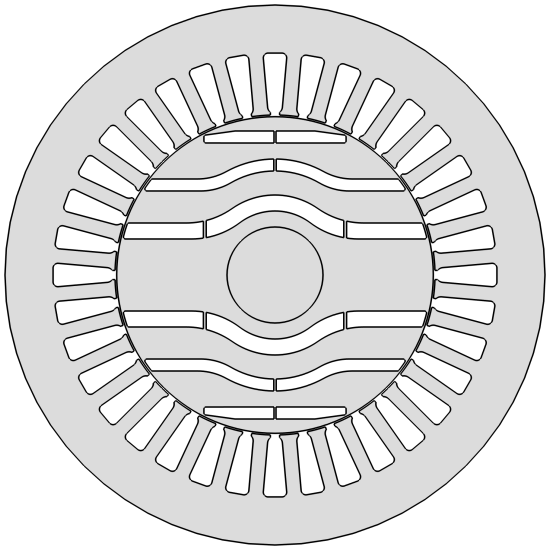

Parameter		**Value**
Outer stator diameter	D_o	135 mm
Inner stator diameter	D_i	80 mm
Core length	l_e	40 mm
Air-Gap width	δ_g	0.42 mm
Number of stator slots	Z_1	36
Number of phases	m	3
Number of poles	$2p$	2
Number of turns of a coil	N	45
Stator phase resistance at 20°C	R_ph	4.14 Ω
Electrical steel	stator	M250-35A
	rotor	M800-50A
Rotor cage material		Aluminum

Figure 3.2: Geometry and important data of Motor II.

The three barriers per pole are all divided by iron bridges in the middle, whereby the innermost one has two separated bridges that are placed so that the aluminum filled area ends at the inner radius of the ring (leaving air in between both bridges). Both other flux barriers (the two outermost) are completely filled with aluminum. The ring geometry differs from Motor I because a different casting mold had to be used. The areas filled with aluminum and the area covered by the end ring are illustrated in Figure 3.4 for all motors at the end of this section. Furthermore, as is known for SynRMs, the rotor surface is smooth due to the placement of the mandatory iron bridges providing mechanical stability for the rotor core at its outer diameter.

Figure 3.3 shows Motor III, which is a 4-pole version. This means that it also has a different stator winding compared to the 2-pole designs that is, however, placed in a stator core of the same geometry. Its rotor has four barriers per pole, where the innermost also has two separated iron bridges in the middle with air in between. The three other barriers only have bridges at the rotor outer radius.

All parameters given in the tables in Figures 3.1 to 3.3 are mainly fixed geometry parameters except for the stator resistance, which has been measured. All other necessary parameters are initially unknown and therefore will be calculated in the course of this chapter. Whenever any parameter of the motor is varied, it will be mentioned in the text.

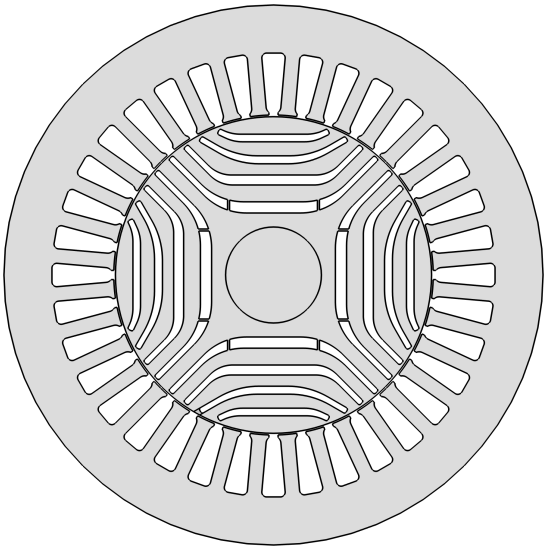

Parameter		Value
Outer stator diameter	D_o	135 mm
Inner stator diameter	D_i	80 mm
Core length	l_e	40 mm
Air-Gap width	δ_g	0.42 mm
Number of stator slots	Z_1	36
Number of phases	m	3
Number of poles	$2p$	4
Number of turns of a coil	N	42
Stator phase resistance at 20°C	R_{ph}	2.23 Ω
Electrical steel	stator	M250-35A
	rotor	M800-50A
Rotor cage material		Aluminum

Figure 3.3: Geometry and important data of Motor III.

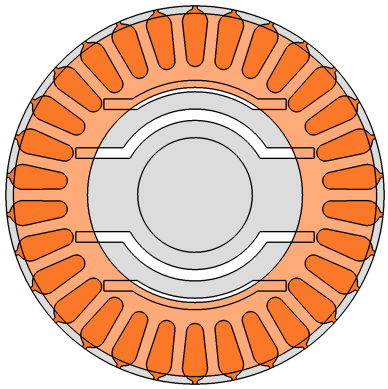

(a) Motor I

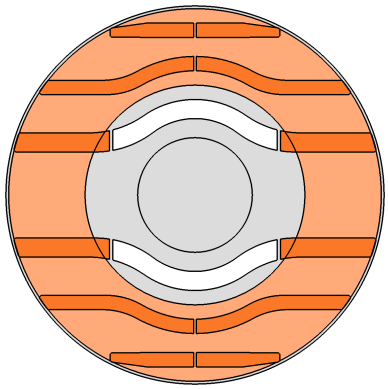

(b) Motor II

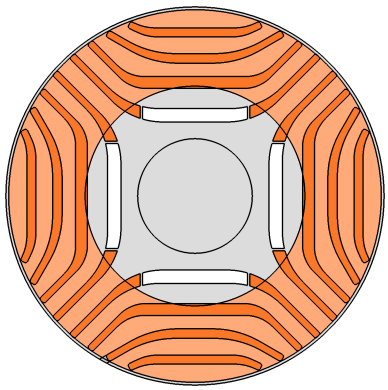

(c) Motor III

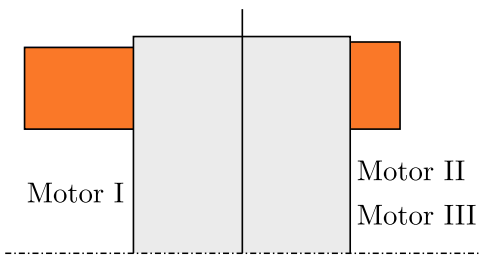

(d) simplified axial cross-section of the rotor geometry

Figure 3.4: Geometry of the rotor cages for Motor I, Motor II, and Motor III. The rotor bars are colored orange, while the area covered by the end ring is depicted in a lighter orange. The cross-sectional area of the respective end rings is indicated in (d).

3.3 Two-dimensional Finite Element model

In this section, the two-dimensional Finite Element model will be derived successively. Starting from the underlying equations, the boundary conditions, the rules for meshing, and the material modelling will be briefly explained.

3.3.1 Equations

Starting from Maxwell's first equation in the differential form

$$\vec{\nabla} \times \vec{H} = \vec{J} + \frac{\partial \vec{D}}{\partial t}, \tag{3.1}$$

the frequencies in the motor are assumed to be low enough so that the last term can be neglected. In

$$\vec{\nabla} \times \vec{H} = \vec{J} \tag{3.2}$$

the magnetic field strength $\vec{H}$ can also be replaced by transforming

$$\vec{B} = \boldsymbol{\mu} \vec{H}. \tag{3.3}$$

Since the magnetic flux density $\vec{B}$ can be represented by a magnetic vector potential $\vec{A}$ with

$$\vec{\nabla} \times \vec{A} = \vec{B} \tag{3.4}$$

Equation (3.1) yields:

$$\vec{\nabla} \times \left(\boldsymbol{\mu}^{-1} \left(\vec{\nabla} \times \vec{A} \right) \right) = \vec{J}. \tag{3.5}$$

All magnetic materials used in the machine are considered fully isotropic (in the xy-plane), so the magnetic permeability $\boldsymbol{\mu}$ can be expressed as a scalar μ. Furthermore, the current density vector $\vec{J}$ is a sum of all possible current sources:

$$\vec{J} = -\kappa \vec{\nabla} \varphi - \kappa \frac{\partial \vec{A}}{\partial t} + \kappa \vec{E}_\mathrm{e} + \vec{J}_\mathrm{e}. \tag{3.6}$$

Here, the first term represents current flow due to an electric field $\vec{E}$ which is replaced with the electric scalar potential

$$\vec{E} = -\vec{\nabla} \varphi. \tag{3.7}$$

The time derivative of $\vec{A}$ in the second term represents the electromagnetic induction. In addition, the last two terms can account for any electric fields or currents that are impressed externally.

By substituting the current components in Equation (3.5) and sorting all terms with unknowns, that is, $\vec{A}$ and φ, on the left-hand side the final equation to be solved is obtained:

$$\vec{\nabla} \times \left(\frac{1}{\mu} \left(\vec{\nabla} \times \vec{A} \right) \right) + \kappa \frac{\partial \vec{A}}{\partial t} + \kappa \vec{\nabla} \varphi = \kappa \vec{E}_\mathrm{e} + \vec{J}_\mathrm{e}. \tag{3.8}$$

3.3.2 Boundary conditions and symmetries

To solve the model, boundary conditions have to be set that only allow for a single solution. The first one is the Dirichlet boundary condition at the outer boundaries of the domain. This specifies that no flux can leave the model domain by forcing the normal vector of the flux density to zero:

$$\vec{n} \cdot \vec{B} = \vec{0}, \tag{3.9}$$

which means that the magnetic vector potential $\vec{A}$ on this boundary is constant according to Equation (3.4).

To accelerate the model, the size of the equation system can then be reduced drastically by applying antiperiodic boundary conditions to the pole-symmetric motor. This means that by knowing that the vector potential on one boundary is the negative vector potential of the corresponding boundary with

$$\vec{A}_{\text{left}} = -\vec{A}_{\text{right}}, \tag{3.10}$$

only one pole of the motor has to be modelled. This results in a so-called sector model. The boundary conditions for the four-pole motor are illustrated in Figure 3.5.

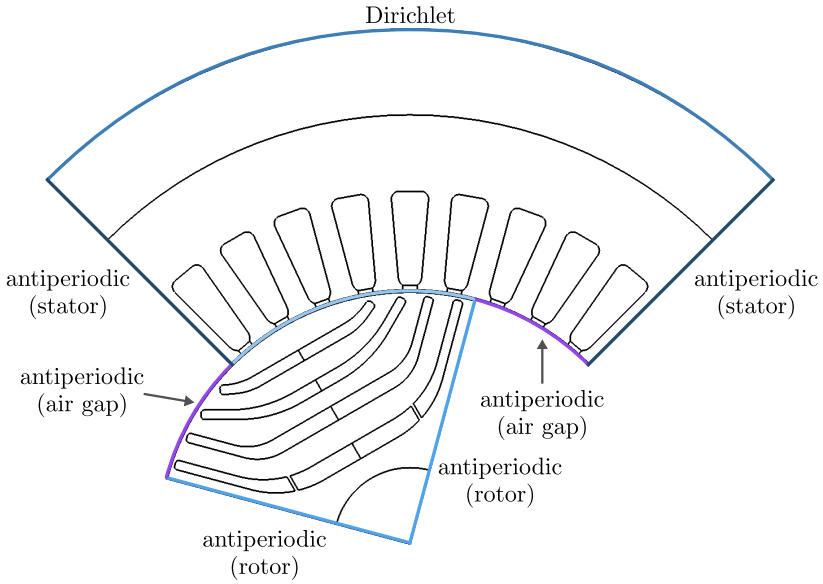

Figure 3.5: Definition of Dirichlet boundaries and antiperiodic boundaries for the sector model.

Here, it is shown in addition that the antiperiodic boundary condition is also applied to the air gap boundary that divides stator and rotor at half the air-gap width. It is a combination of the sliding surface method to account for rotation of the rotor with the boundary condition to account for symmetry. This method is usually available per default in commonly used FEM software.

3.3.3 Materials

Apart from linear materials, like air and aluminum, of which the properties are constants, also the non-linear magnetic behavior of the stator and rotor laminations has to be considered. This is done by defining the $B(H)$-curve for the respective steel type, which is provided by the manufacturer.

It is known, however, that this data usually does not fit the real behavior of electric machine cores because the cutting process as well as other steps during the manufacturing procedure deteriorate the magnetic properties [66]–[68]. Especially for machines of small frame sizes, simulations of saturated states tend to differ from comparative measurements. Therefore, it is recommended to adjust the material data beforehand.

All the machines discussed in this work have been developed starting from the same Induction Machine (IM). Since for this machine plenty of measurements have been carried out in the past, its magnetic behavior is well-known. Because the stator core of each LSSynRM is identical to the Induction Machine, it is fair to assume that using a material curve adapted to the Induction Machine will provide good results. The original $B(H)$-curve for M250–35A provided by the manufacturer and the modified curve are shown in Figure 3.6.

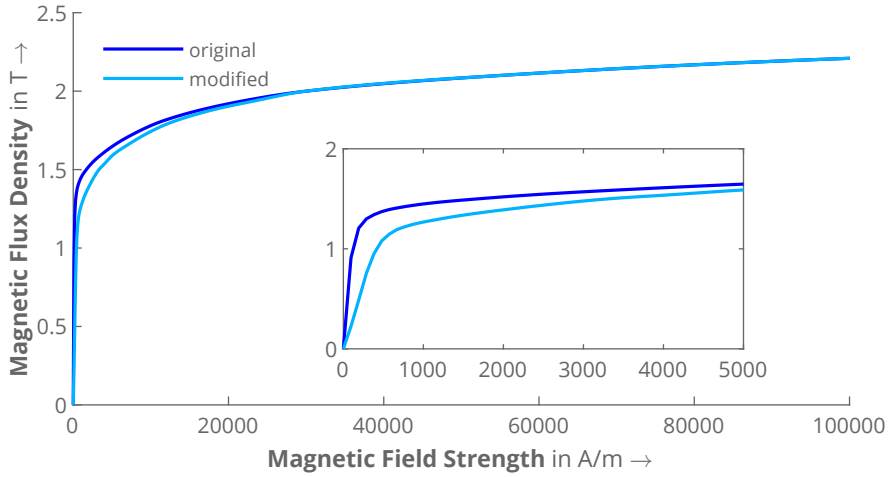

Figure 3.6: Interpolated non-linear $B(H)$-curve for M250-35A from manufacturer and modified curve.

It can be observed that there is a difference, especially for the area below a flux density of 1.8 T. This will result in a reduced permeability μ compared to the original material data. However, when the material is saturated, both the original and the modified data converge to the same curve, which eventually has the slope μ_0.

For the rotors of both other motors, Motor II and Motor III, a different steel grade has been used (M800–50A). Hence, there are no measurements for the IM with this material. Furthermore, the rotor geometry of both motors is more complex than those of Induction Machine rotors, which means that there are more edges that are influenced by the manufacturing process. Nevertheless, it is recommended to use any material data that has been adapted to motors of a similar size. In this way, the influence on the magnetic properties can still be taken into account up to a certain point. It is assumed that the result will therefore be closer to reality than with the original material data.

From this point, no further adjustments of the motors' material data have been made in this work.

3.3.4 Mesh generation

One of the most important steps for an accurate and fast calculation is the generation of the mesh. On the one hand, the size of the finite elements defines the accuracy of the field solution in the corresponding areas. A fine mesh consisting of many small elements

can therefore approximate the exact field solution better than a coarse mesh consisting of fewer large elements. On the other hand, the number of elements also determines the number of unknowns to be solved and therefore the calculation time. A finer mesh results in a larger system of equations that has to be solved. Thus, a compromise must be found between both aspects.

This objective implies the following recommendations that should be taken into account when generating the mesh: Firstly, the mesh should only be finely discretized where this will actually lead to a better accuracy of the solution. Secondly, the order of the finite elements should be as small as possible (preferably linear elements). Finally, adaptive mesh refinement is to be avoided because it takes more time and does not lead to satisfactory results for rotating electrical machines in many generalist FEM software tools. The application of these guidelines to the 2D modeling of Line-Start Synchronous Reluctance Machines is explained below.

In the case of transient electromagnetic ("magnetodynamic") problems, areas with high magnetic energy (density) are of particular interest. Hence, in domains where this energy W_m changes the most, the mesh should be discretized more finely in order to approximate the field quantities correctly. Since

$$W_\mathrm{m} \propto \frac{1}{\mu} B^2$$

applies, the magnetic energy in iron, where $\mu_\mathrm{r} \gg 1$, is usually lower than in air, copper and aluminum regions, where $\mu_\mathrm{r} = 1$. These are therefore the most important areas.

Another important parameter is the element order, that is, the order of the polynomial functions, which approximate the potential and hence the resulting electromagnetic quantities in each finite element [69]. Due to the variable adaptation to complex geometries, triangular finite elements are usually defined in 2D problems. If the potential to be solved is approximated with linear functions, each element has three nodes. The resulting field quantities, such as the magnetic flux density (see Equation (3.4)), are therefore constant for the entire element. In contrast, a finite element of quadratic order would require six nodes, whereby the field quantities change linearly within the element.

Therefore, for a simple geometry, either a finer mesh of linear elements or a coarser mesh of quadratic (or higher order) elements could achieve a similar accuracy. Since the number of unknowns is similar in both cases, the choice of order would be irrelevant for the calculation time in this case if the mesh is adapted accordingly.

In complex geometries such as the LSSynRM, however, a very fine mesh is enforced in many areas by default. The gain in accuracy for higher-order elements in this case is often negligible, while the computing time increases considerably. It is therefore recommended to generate a mesh exclusively from linear finite elements, which is only finer in areas with $\mu_\mathrm{r} = 1$.

Starting with the air gap, it is divided at half its radius into a stator air gap and a rotor air gap to be able to account for rotation of the rotor. Each air gap layer is now discretized so that there are two elements per layer in radial direction. This means that four elements are counted from the stator inner diameter to the rotor outer diameter. The accuracy of this mesh is comparable to one with two quadratic finite elements in the radial direction.

Furthermore, to account for skin effect, the mesh in conductive areas has to be fine as well. Because the resulting air gap mesh is already fine, the conductive areas near it will usually be discretized fine enough as well. A good indicator for the quality of the

generated mesh in the conductors can be the skin depth as described for a Finite Difference model in [70], where two to three elements per skin depth are considered accurate.

For machines with electrically insulated laminations, the iron domains are not conductive and therefore do not require a fine mesh at the surface. If the iron losses are to be calculated in these areas, there are numerous models in the literature [71], [72], of which one has already been applied to LSSynRMs in [S1]. However, iron losses are neglected in this thesis.

To account for flux that leaves the stator core of the machine when its yoke is highly saturated, an air domain is added. Since the flux density is usually very low, this area does not need to be discretized as finely. The final mesh for Motor III is shown in Figure 3.7 as an example.

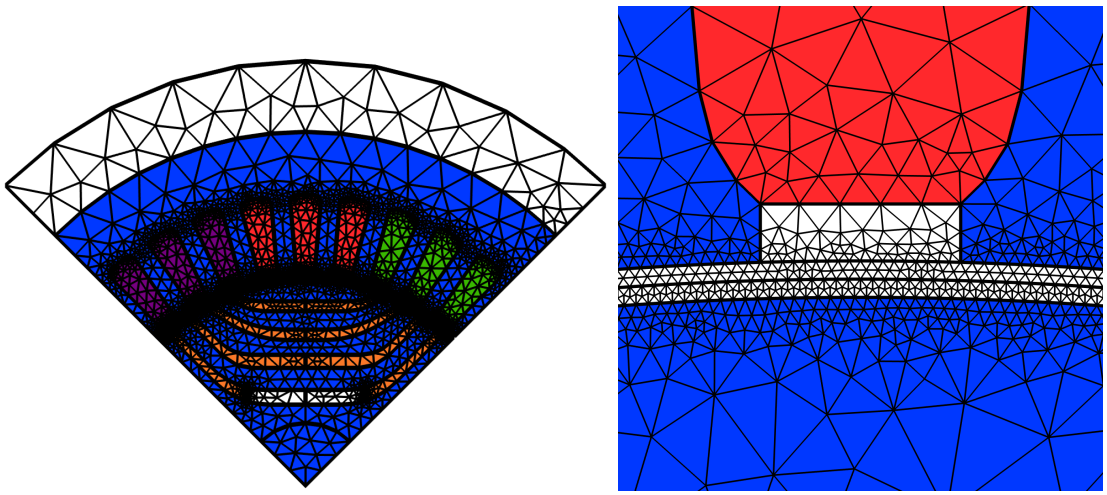

(a) full model with mesh **(b)** air gap mesh

Figure 3.7: Finite Element mesh for Motor III considering the instructions given in this section. The full mesh is shown on the left, a close up on the air gap on the right.

By experience, a well-defined mesh like this can provide satisfactory results with linear finite elements and without adaptive mesh refinement. The remaining difference that can occur compared to quadratic elements and a refined mesh is usually much smaller than the error between both results and the real measurement.

After deriving the system of equations, setting the boundary conditions, defining the materials, and creating a mesh, the 2D model is now complete. The next step is to take both the stator and rotor windings into account.

3.4 Stator winding

As shown in the schematic in Figure 2.1, the machine is always connected to the grid, which means the line-to-line voltage is the known parameter for the simulation. However, the 2D FE-model requires currents to be inserted into the equations. Therefore, the electrical circuit of the stator windings has to be taken into account. To this end, many Finite Element software tools provide the opportunity to couple external electrical circuits consisting of lumped elements to the respective model. The derivation and implementation of the circuit as done in this work is presented in the following.

In general, the full voltage equation of the k-th phase with $k = 1, 2, 3$ can be written as:

$$u_{\mathrm{k}}(t) = R_{\mathrm{ph,k}} i_{\mathrm{k}} + \frac{\mathrm{d}}{\mathrm{d}t}\psi_{\mathrm{k}}. \tag{3.11}$$

Here, u_{k} is the phase voltage, i_{k} the phase current and $R_{\mathrm{ph,k}}$ the total resistance of the k-th phase. The flux linkage ψ_{k} consists of various main flux and leakage flux components, most of which are contained in the 2D model.

However, this does not apply to the flux in both end regions of the machine. On the one hand, there is an air gap flux component that does not lie exactly under the stator and rotor, but flows over the end region outside the iron core. However, this is usually negligible if, as in this case, the air-gap width δ_{g} is much smaller than the iron length l_{e} of the machine [35]. On the other hand, the end winding produces leakage flux $\psi_{\mathrm{\sigma e,k}}$ in the end regions. This can be considered in the 2D model by introducing end winding leakage inductances $L_{\mathrm{\sigma e,k}}$ estimated from leakage factors [73].

Hence, separating the flux linkage in Equation (3.11) into the FEM-included component $\psi_{\mathrm{FEM,k}}$ and the one represented by the end winding leakage inductance $L_{\mathrm{\sigma e,k}}$ yields:

$$u_{\mathrm{k}}(t) = R_{\mathrm{ph,k}} i_{\mathrm{k}} + L_{\mathrm{\sigma e,k}} \frac{\mathrm{d}}{\mathrm{d}t} i_{\mathrm{k}} + \frac{\mathrm{d}}{\mathrm{d}t}\psi_{\mathrm{FEM,k}}. \tag{3.12}$$

From this, the equivalent circuit for all three stator phases can now be constructed. Because all motors in this work are equipped with star-connected stator windings, the circuit is built as shown in Figure 3.8.

Here, it is to mention that the term for the time-derivative of the flux linkage $\psi_{\mathrm{FEM,k}}$ has been replaced with the EMF

$$e_{\mathrm{k}} = -\frac{\mathrm{d}}{\mathrm{d}t}\psi_{\mathrm{FEM,k}}, \tag{3.13}$$

as defined in Appendix B. Furthermore, instead of the phase voltages u_1, u_2, u_3, the line-to-line voltages u_{12} and u_{23} are known. These voltages fed by the grid are considered as ideally sinusoidal. If the measured voltages differ too much, however, it is also possible to provide approximated functions, that consider voltage harmonics. Moreover, the impedance of the grid is neglected, as it is usually much smaller than the winding impedances of motors of the same output power and frame size as in this thesis.

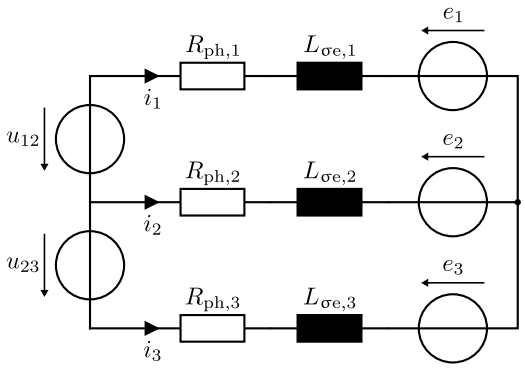

Figure 3.8: Equivalent electrical circuit for the three-phase stator winding in star connection.

3.5 Rotor cage

For every kind of line-start motor, the rotor cage is a crucial part. Due to the stator magnetic field rotating around the rotor with a slip frequency of sf_s, an electromotive force is induced into each rotor bar, causing currents to flow that are short-circuited by end-rings on both sides of the rotor. These currents create a magnetic field as well, which, together with the stator magnetic field, produces asynchronous torque that accelerates the rotor from standstill to synchronous speed.

The electromagnetic induction that causes currents to flow in the rotor bars is already considered for in the 2D model presented in Section 3.3 (Equation (3.8)). Due to the model being two-dimensional, however, the end-rings do not appear in the model yet. Therefore, a method has to be found, which takes the effects into account that are caused by the end-rings.

The model presented in this section has already been published in [A5]. Starting from a well-known analytical method for Induction Machines, a 3D FE-assisted approach is derived to be able to handle every possible cage geometry. To clarify the method and for better illustration, the procedure for a standard squirrel cage (as for Motor I) is described and validated as well.

3.5.1 Analytical method

Figure 3.9 shows a simplified rotor cage with the geometric end ring parameters. While the geometry of the rotor bars is arbitrary, usually the end-ring is shaped as a short hollow cylinder. For manufacturing reasons, the end-ring of die-cast squirrel cages is slightly conical, meaning that the radial width w_R at the contact surface of bars and ring is greater than at its end.

The general approach for modelling the end-rings of such squirrel cages in transient 2D FE models is adapted from [74], where resistors for the bar ends R_be protruding from the iron core on both sides are connected to the bars. Each of these resistors is then connected to its neighbor by one resistor R_R and inductance L_R in series.

Following [70], it is further assumed that the inductance of the bar ends is included in the ring elements. The inductance of the ring elements L_R themselves are estimated by empirical formulas as known for Induction Machines [73], [75]. Due to the complexity of the rotor cage and the need for a full 3D model of the motor's end region to calculate the inductances [76], the effort is not worth the result. This means that both end winding

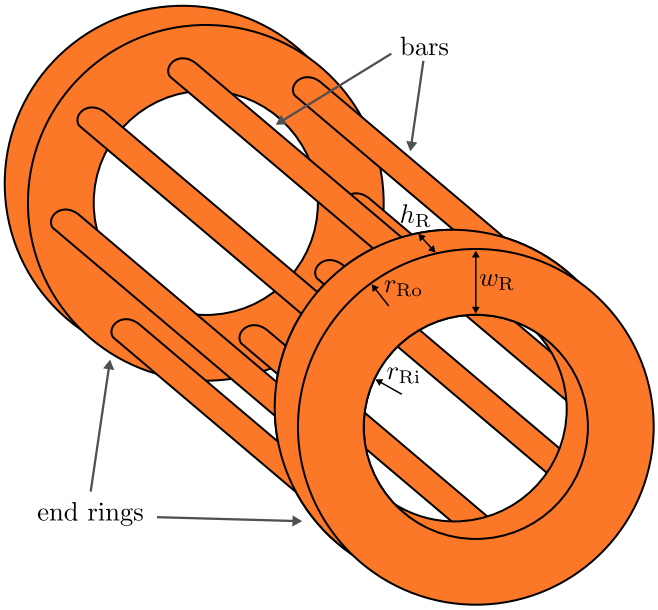

Figure 3.9: Simplified geometry of a squirrel cage with illustration of the parameters of the end rings.

leakage inductances of stator and rotor will remain the only uncertainty parameter of the model. The rest is either modelled as precisely as possible or reasonably simplified.

The ring equivalent circuit and its coupling to the 2D FE model is illustrated in Figure 3.10. Because the aim is a general model for non-standard cage geometries where each element can be different, an index i for each loop of the cage is added.

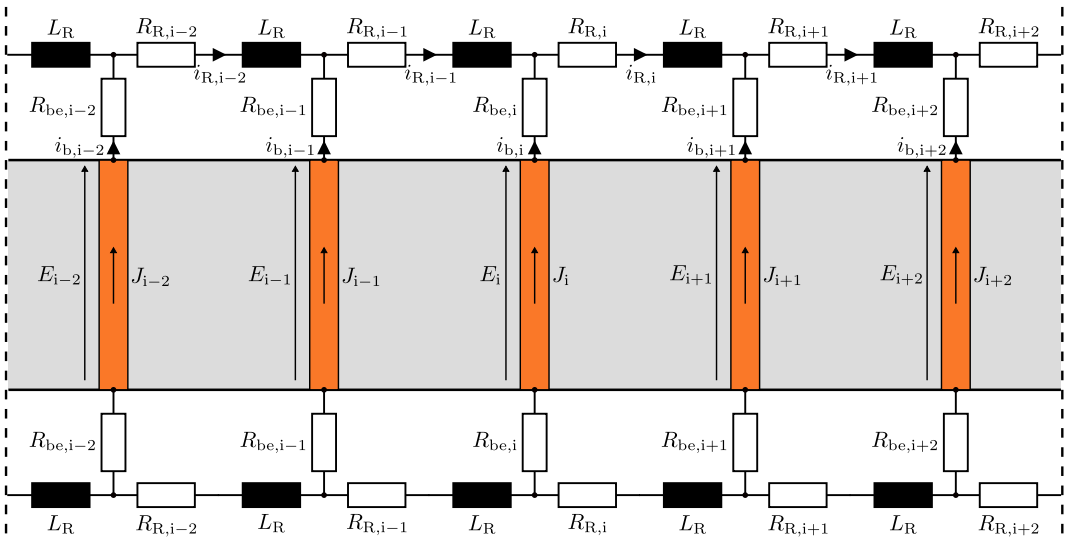

Figure 3.10: Circuit coupled to the rotor bars (orange) in the rotor core (gray) in a 2D Finite Element model to account for the end-rings of the squirrel cage.

From all possible manufacturing and assembling procedures, the die-cast squirrel cage is a special case. Instead of having protruding rotor bars, the end-rings sit directly on the rotor core. However, it has proved useful to retain the division into bar and ring elements from Figure 3.10 to account for the current path inside the end-ring.

To be more precise, the current is assumed to flow exclusively in the axial direction

up to half the ring's axial height $h_{\mathrm{R,i}}$ in a virtually extended bar [70], [77], as illustrated in Figure 3.11. This share is attributed to $R_{\mathrm{be,i}}$. The resistor $R_{\mathrm{R,i}}$ connecting $R_{\mathrm{be,i}}$ and

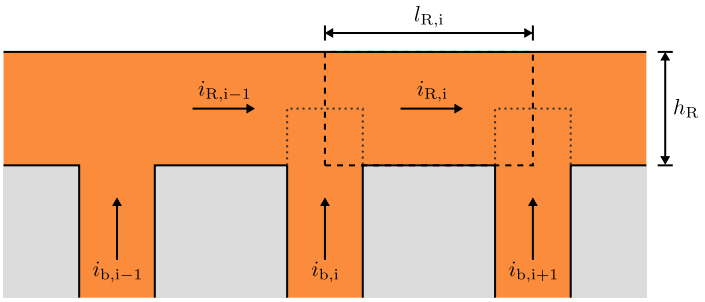

Figure 3.11: Illustration of the virtually extended rotor bars (dotted lines) into the corresponding end ring element (dashed line).

$R_{\mathrm{be,i+1}}$ therefore only represents the current path in azimuthal direction. With

$$R_{\mathrm{be,i}} = \frac{1}{2}\frac{h_{\mathrm{R}}}{\kappa S_{\mathrm{b,i}}} \tag{3.14}$$

where $S_{\mathrm{b,i}}$ is the surface area of the rotor bar, the resistance of one side of the virtual bar end is obtained. For the ring, it is assumed:

$$R_{\mathrm{R,i}} = \frac{l_{\mathrm{R,i}}}{\kappa S_{\mathrm{R,i}}}. \tag{3.15}$$

For Induction Machines, $l_{\mathrm{R,i}}$ is usually the rotor slot pitch at the average diameter of the ring [78]:

$$l_{\mathrm{R,i}} = l_{\mathrm{R}} = \frac{2\pi}{Z_2}\frac{r_{\mathrm{Ro}} + r_{\mathrm{Ri}}}{2}, \tag{3.16}$$

with the number of rotor slots Z_2.

This method, however, has several limitations. As for the Induction Machine (IM) and Motor I for example, the end-rings have a huge cross-sectional area S_{R} that is mainly caused by the large axial height of h_{R}=20 mm (on a 40 mm long rotor core). As demonstrated in [S2], increasing the ring height will simultaneously reduce R_{R} and increase R_{be}. This means that from a certain ring height on, the total resistance for this method will increase due to increasing R_{be}, even though in reality it would be expected that the resistance will tend to decrease for larger ring heights.

Additionally, regarding non-standard cage geometries in Line-Start Synchronous Reluctance Machines, a second problem arises. This is illustrated using the example of Motor II, whose ring cross-section is shown in Figure 3.12. The bars indexed with b,i and the ring elements R,i all differ from their neighbors in shape, size, position, and orientation. Hence, the formula (3.15) including the length $l_{\mathrm{R,i}}$ cannot be defined as simple anymore. On top of this, the bars are not necessarily oriented radially anymore, therefore making it unclear how to define the area $S_{\mathrm{R,i}}$.

Because all the above-mentioned problems would require further assumptions and simplifications to the already simplified model, a more precise method to estimate the equivalent end-ring parameters should be found. Nonetheless, the underlying model should be retained in the process, since it has proven to be accurate in many Induction Machine studies. The aim is therefore to tackle the complexity of the geometry with a suitable calculation method to feed the well-proven equivalent ring circuit model.

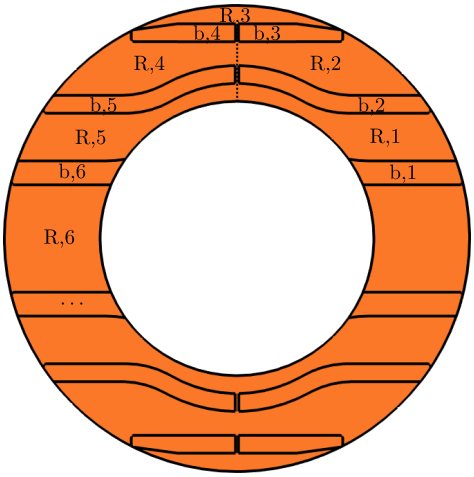

Figure 3.12: Cross-section of the end-ring of Motor II with indicated outlines of the rotor bars. The bars b,i and ring elements R,i are labeled for the first pole. The dotted line in the numbered pole indicates the division of the ring elements on the left and right side.

3.5.2 Improved 3D FEM-assisted method

The best option for this is the 3D Finite Element Method, which can compute the resistance of arbitrary conductor geometries with high precision. For the ring resistance between two adjacent bars, each ring segment can be defined as 3D geometry, which consists of the space above the contact surfaces of the bar and ring as well as the space between two bars. In an electrostatic study, a voltage of 1 V is applied between two bars by setting the contact surfaces to different electric potentials φ (1 V and 0 V, Figure 3.13).

By evaluating the total Joule losses

$$P_{\text{loss}} = \iiint_{\text{segment}} \frac{1}{\kappa} \left|\vec{J}\right|^2 \mathrm{d}V, \tag{3.17}$$

the resistance can be calculated with:

$$R_{\text{3D,i}} = \frac{(1\,\text{V})^2}{P_{\text{loss}}}. \tag{3.18}$$

Usually, the flux barriers of one pole are symmetrical, which means that the resistances of either side are the same (R,1 and R,5, for example). For Motor II, only four different segments have to be calculated (Figure 3.14). Consequently, the calculation time is very low, especially compared to the transient study for which these parameters are required.

Coming back to the equivalent circuit model for the end-ring, there are still more steps needed. Since 3D FEM yields only one resistance $R_{\text{3D,i}}$ for the whole current path between two bars, it would combine the previously defined bar end and ring elements $R_{\text{be,i}}$, $R_{\text{be,i+1}}$ and $R_{\text{R,i}}$. Thus, two neighboring ring elements, $R_{\text{R,i}}$ and $R_{\text{R,i+1}}$, would both contain the portion of the extended bar $R_{\text{be,i+1}}$. An equivalent circuit, in which two resistors are defined for the same current path, yields incorrect total losses and therefore loses its validity.

The equivalent circuit introduced in Figure 3.10, in contrast, defined that different currents flow in each of these elements: $i_{\text{b,i}}$ in $R_{\text{be,i}}$, $i_{\text{R,i}}$ in $R_{\text{R,i}}$, and $i_{\text{b,i+1}}$ in $R_{\text{be,i+1}}$. Thus,

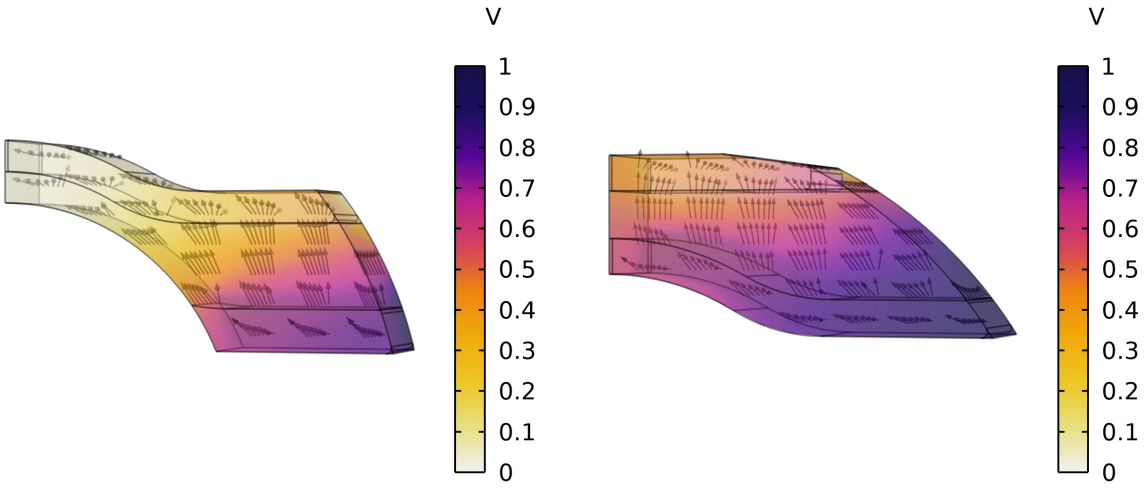

(a) ring element R,1 with bars b,1 and b,2 **(b)** ring element R,2 with bars b,2 and b,3

Figure 3.13: Electric potential calculated for the first two ring elements of Motor II with 3D electrostatic FEM. The contact surfaces of the rotor bars to the ring element (backside) are set to 1 V and 0 V, respectively. Arrows indicate the direction of the current density, whereby the length of the arrows is normalized for better visualization.

the resistance $R_{3D,i}$ has to be split up as well, so that it can be used in the equivalent circuit. To separate $R_{3D,i}$ into two virtual bar ends $R_{be,i}$, $R_{be,i+1}$, and one ring element $R_{R,i}$, the latter must be calculated.

For simple cage geometries, as for IM and Motor I for example, Equation (3.15) can be applied because it is the fastest possible and yet quite accurate method. As stated in [78], however, for large radial ring widths w_R compared to the slot height, the average diameter will lead to a false resistance for one slot pitch.

Thus, if a simple analytical calculation is too inaccurate, as for Motor II for example, 3D FEM can be used as an alternative to calculate $R_{R,i}$. To this end, the potentials are defined on a surface that results from extruding an additional center line of the bar through the whole ring axial height h_R. The center lines for one selected element are marked in red and blue in Figure 3.14.

If a voltage is now defined between both resulting boundary faces, the resistance $R_{R,i}$ can be calculated. The resulting potential distribution and current density vectors are shown in Figure 3.15. It is obvious that the current density now no longer has an axial component (into the bar), which is why in practice a 2D FE model is sufficient for this step.

For two bars of the same geometry (as in IM and Motor I) the bar end resistance is then defined as half of the remaining resistance:

$$R_{be,i} = \frac{1}{2}\left(R_{3D,i} - R_{R,i}\right). \tag{3.19}$$

In non-standard cages as for Motor II, however, two adjacent rotor bars differ from each other (for example b,1 and b,2 in Figure 3.14). Splitting the resulting resistance $R_{3D,i} - R_{R,i}$ into the two bar end resistances $R_{be,i}$ and $R_{be,i+1}$ is more difficult because the contributions to the total resistance cannot be separated for both bars.

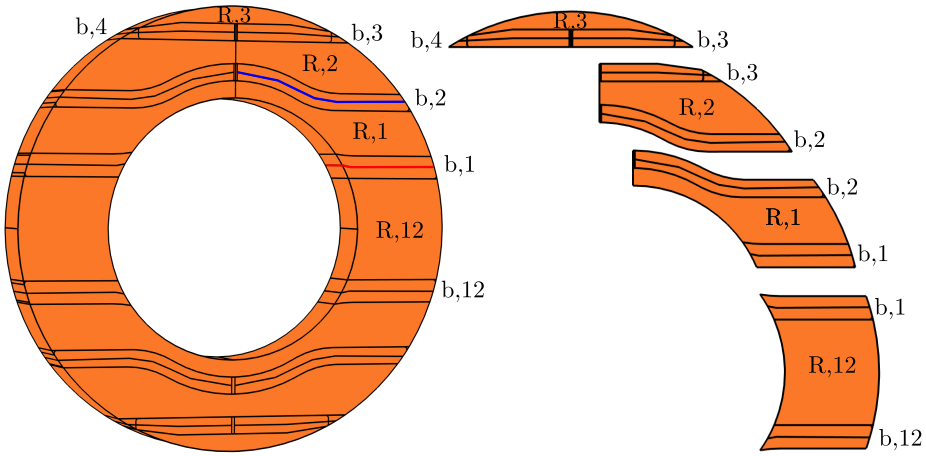

Figure 3.14: Full 3D FEM end-ring geometry of Motor II (left) with indicated center lines of the rotor bars. The elements are split up into single segments (right) for calculating the resistance $R_{\mathrm{R,i}}$ by defining a voltage between each boundary resulting from extruding the center lines. The potentials are indicated with red and blue lines for bars b,1 and b,2 as an example.

In addition, two adjacent ring segments that do not have the same geometry will also yield different results for the bar ends. In Figure 3.14, the bar b,2, for example, is part of two differently shaped end ring segments, for which both calculations will yield a different value for $R_{\mathrm{be,2}}$. Hence, the calculation is simplified by still applying Equation (3.19) to all segments and then evaluating the mean value of both results.

In practice, this will lead to the smallest possible error for the least possible effort for such complex geometries. Only in the most extreme cases in which the ring's axial height h_{R} is large in relation to the distance between both rotor bars, $R_{\mathrm{be,i}}$ and $R_{\mathrm{be,i+1}}$ are dominant for the total ring resistance of one segment. If two adjacent ring elements are extremely different, the error would be higher as well.

However, the simplification of taking the mean value of both calculations to determine $R_{\mathrm{be,i}}$ is still assumed to be valid. In the vast majority of cases, the resistance of the bar end only represents a small portion of the total resistance of a rotor loop.

In summary, with the aid of the 3D Finite Element Method, the known and proven equivalent circuit for the end ring can still be used. The approach is therefore a viable alternative to complex approaches as in [79], where a 3D model of the motor is used to investigate the current distribution in the whole cage, but empirical correction factors still have to be used.

To prove that the accurate representation of the end rings is mandatory for achieving valid results, this section now moves on to investigate the influence on the motor behavior in a simplified case.

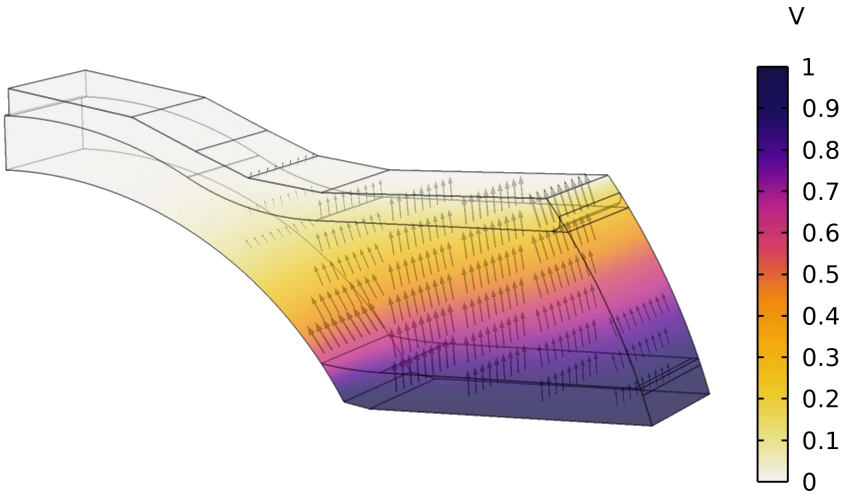

Figure 3.15: Electric potential calculated for ring element R,1 of Motor II with 3D electrostatic FEM. The surfaces resulting from extruding the center lines of the rotor bars (top and bottom faces in this figure) are set to 0 V and 1 V, respectively. Arrows indicate the direction of the current density.

3.5.3 Influence of ring resistances on the motor behavior

For demonstration purposes and to study the influence of the ring resistance on the motor behavior, the single-phase equivalent circuit is used as an example. Since the standard formulas assume that each bar and each ring segment are the same, the following analysis is carried out for Motor I. Since the classical analytical formulas for evaluating the equivalent ring parameters [73] apply as well in this case, both methods will be compared. Due to the identical equivalent circuit elements, the index i is not used in this section.

The rotor resistance R_2 contains twice the ring resistance R_R and the total bar resistance R_b. As the equivalent circuit from Figure 3.10 contains both bar and ring currents i_b and i_R, one of the two variables must be transformed to the other in order to obtain only one current per rotor loop. In this case, ring currents are used, which yields the following formula for the rotor resistance:

$$R_2 = 2R_\mathrm{R} + R_\mathrm{b}\left(2\sin\left(p\frac{\pi}{Z_2}\right)\right)^2. \tag{3.20}$$

R_b contains the bar embedded in the rotor core as well as both bar ends:

$$R_\mathrm{b} = R_\mathrm{bc} + 2R_\mathrm{be}. \tag{3.21}$$

The method using bar currents and the corresponding transformation rules can also be found in the standard literature [61], [73], [80].

Then, the rotor resistance can be transformed into the stator current system with

$$R_2' = R_2\frac{Z_2}{m}n_\mathrm{T}^2, \tag{3.22}$$

where n_T is the effective turns ratio [61], [73]. If the skin effect, saturation, and iron losses

are neglected, the current at $s = 1$ (locked rotor) can be approximated with

$$I_\mathrm{k} = \frac{U}{\sqrt{(R_1 + R_2')^2 + (X_{1\sigma} + X_{2\sigma}')^2}}. \tag{3.23}$$

This allows for a qualitative comparison of the presented methods.

The results for a voltage of $U = 50\,\mathrm{V}$ with $f_\mathrm{s} = 50\,\mathrm{Hz}$ are given in Table 3.1. Here, "analytical" refers to the analytical formulas (3.14) and (3.15) and "numerical" to the 3D FEM-assisted approach presented in Section 3.5.2. The values of the remaining variables for this calculation were:

$$R_1 = 4.12\,\Omega,\ X_{1\sigma} = 4.02\,\Omega,\ X_{2\sigma}' = 2.53\,\Omega,\ R_\mathrm{bc} = 24.537\,\mu\Omega, \text{ and } n_\mathrm{T} = 246.97.$$

	analytical	**numerical**
R_R	0.684 µΩ	0.684 µΩ
R_be	6.134 µΩ	1.335 µΩ
R_2'	1.816 Ω	1.560 Ω
I_k	5.66 A	5.77A

Table 3.1: Ring and bar end resistances, resulting rotor resistance and current at locked rotor for the analytical and 3D-FEM assisted (numerical) method using Motor I as an example.

As can be seen from the table, the results from the analytical method and the numerical method look quite similar. Even though the resistance of the bar end changes quite a lot when evaluated for the numerical method, the current only changes by about 2%. This can be explained by the fact that the total bar resistance is reduced by a factor of approximately 0.022 when transformed to ring currents.

If the rotor cage losses are evaluated, however, the analytical method predicts 12% more losses than the proposed 3D FEM-assisted method (174.5 W instead of 155.8 W). Hence, the upcoming validation with measurements must prove that the new method is accurate.

This example also shows that neglecting the ring resistances, as has been common in the literature on modern Line-Start Synchronous Reluctance Machines, leads to incorrect results. If R_be and R_R were neglected, the current would result to 6.17 A. If the starting torque

$$T_\mathrm{el} = \frac{p}{s\omega_\mathrm{s}} m R_2' I_2'^2, \tag{3.24}$$

with

$$\omega_\mathrm{s} = 2\pi f_\mathrm{s} \tag{3.25}$$

is evaluated for the case of neglected ring resistances, only 0.43 times the value is obtained compared to the case of analytically determined ring parameters (or 0.48 times the value from the numerical method).

3.5.4 Consideration of skin effect

Line-Start Synchronous Reluctance Machines with conductors embedded in the flux barriers usually have very deep bars. Previously, it was assumed that for small radial bar heights and ring widths, the current will flow in the whole end ring. However, it must now be clarified that if the skin effect causes the rotor bar currents to flow predominantly near the air gap, this can also influence the ring current distribution [81]. While in cages with protruding bars a uniform current density distribution could be assumed for the contact surface of the bar and the ring [82], this is not true for die-cast rotor cages in which the ring sits directly on the rotor iron core.

Figure 3.16 displays the magnitude of the current density obtained from a locked rotor simulation from time-harmonic 2D FEM of Motor I and Motor II to demonstrate the difference between standard and non-standard cages. Comparing the two results, it can be seen that the current density is almost homogeneously distributed in the rotor bars of Motor I in Figure 3.16a. If the radial ring width is not much higher than the bars, the previous assumption is therefore valid for this case.

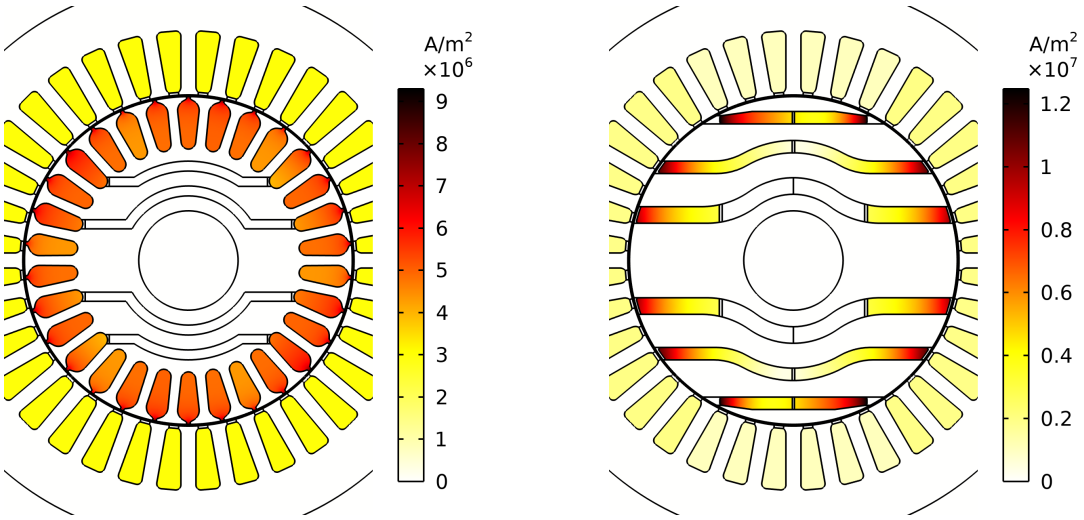

(a) Motor I (b) Motor II

Figure 3.16: Magnitude of the current density from locked rotor simulation with 2D FEM in the frequency domain for $U = 80\,\mathrm{V}$ at $f = 50\,\mathrm{Hz}$. The iron of the stator and rotor core is set to a constant relative permeability of $\mu_\mathrm{r} = 1000$. The iron bridges are set to air to avoid magnetic short-circuits due to the constant permeability.

In contrast, the distribution in the rotor bars of Motor II in Figure 3.16b shows a massive influence of the skin effect, as the current density decreases significantly from the rotor surface to the center. Because the end ring covers the whole surface of every bar (see Figure 3.4), the current in it will probably not be homogeneously distributed. This means that although the ring is surrounded by air on all sides except for the rotor core, the skin effect will be indirectly effective for it due to the current distribution in the bars.

Yet, connecting the bar end and end ring resistances to the bars embedded in the rotor core would assume that the current will flow through the whole cross-sectional area of the end ring. This influences the ring losses and thus the asynchronous torque of the motor. In addition, investigations have indicated that the skin effect in the rotor cage is not only pronounced at high slip, but also influences the synchronization behavior. This is why the presented end ring model has to be adapted to account for this effect.

A suitable approach is to divide the rotor cage into multiple electrically insulated layers. Usually, this method is used when the skin effect in a solid conductor is to be modelled analytically [75], [83], [84]. However, the method can also be used to counter the problem of uneven current distribution in the ring. Specifically, this means that for Motor I, for example, the ring is divided radially into two or more layers. The current therefore only flows from the uppermost layer of the bar into the uppermost layer of the ring. The same applies accordingly to the layers below.

The distribution of the layers in this case should be logarithmic, which follows the approximately exponential current density distribution [A2], [85]. Hence, the layers near the air gap are smaller, while layers near the center of the rotor are larger.

Figure 3.17 shows the same results from Figure 3.16, but the division of the rotor bars into three layers is indicated. Looking at the current density in each layer, it is apparent that the outermost rotor cage layer will carry the most current, while the innermost layer has significantly less current. With this approach, it is therefore expected that the results for Motor I will not change by a lot. But for Motor II, an observable change is expected.

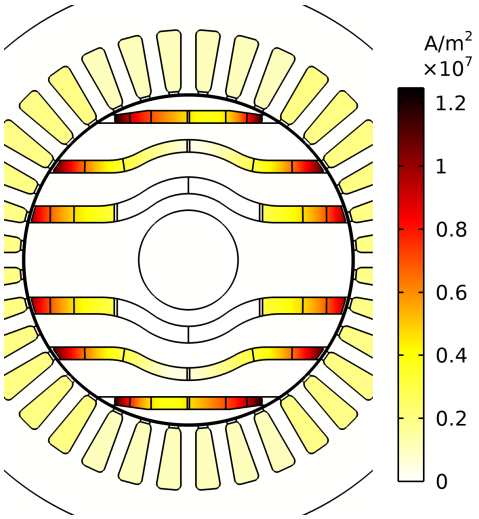

Figure 3.17: Magnitude of the current density from locked rotor simulation of Motor II in the frequency domain for $U = 80\,\mathrm{V}$ at $f = 50\,\mathrm{Hz}$. The iron of the stator and rotor core is set to a constant relative permeability of $\mu_\mathrm{r} = 1000$. The iron bridges are set to air to avoid magnetic short-circuits due to the linear rotor core. Each rotor bar is graphically divided into three layers to illustrate the current density distribution in individual layers.

The calculation of the end-ring resistances has to be adapted accordingly. In Figure 3.18, the division of the ring segments of Motor I and Motor II into three layers is shown as an example.

What can clearly be seen in this figure is the difference in the discretization of layers. For the standard cage of Motor I (left), the layers for each rotor bar are the same, therefore leading to azimuthal current flow in each ring layer. For the non-standard geometry of Motor II (right), however, each layer differs in width from one bar to the next due to the bars having different shapes and sizes.

For the calculation of the equivalent resistances, the approach from Section 3.5.2 is now applied to each layer. For example, this leads to a potential distribution and current flow as illustrated in Figure 3.19 for the first layer.

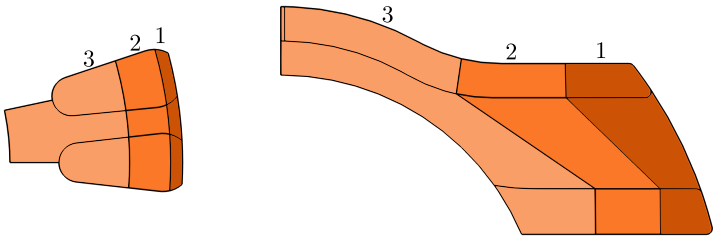

Figure 3.18: One element of the end ring divided into three layers for Motor I (left, one slot pitch) and Motor II (right). Each layer is numbered and colored in a different shade.

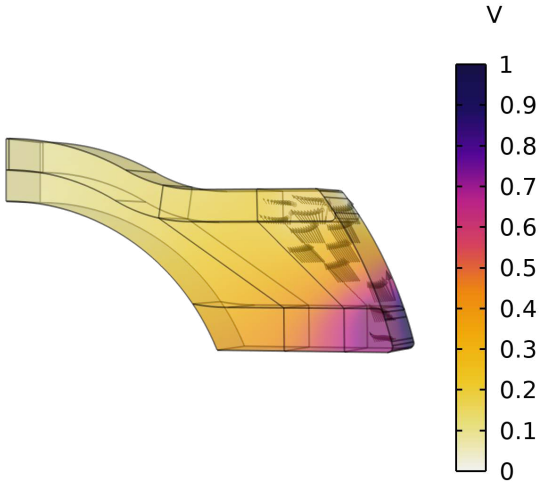

Figure 3.19: Electric potential calculated for the first of three layers of ring element R,1 of Motor II with 3D electrostatic FEM. The contact surfaces of the rotor bars to the ring element (backside) are set to 1 V and 0 V, respectively. The conductivity of the other two layers is set to zero. Arrows indicate the direction of the current density, whereby the length of the arrows is normalized for better visualization.

In addition to the calculation of the parameters, there are also two important changes for the 2D circuit-coupled Finite Element model itself if the ring is calculated with more than one layer. On the one hand, a separate rotor circuit is now required for each layer. Hence, there are now multiple sets of rotor equations, one for each layer.

On the other hand, the fact that the cage is modeled in separate layers means that the skin effect in the rotor bars may not be solved with the field equations of the FEM (3.8) anymore. This would be physically incorrect because the current distribution in the cage is already forced by the multi-layer cage model, where each layer of a rotor bar is coupled to a separate end ring. This means that a homogeneous current density is now assumed for each layer of each bar. This is possible either by defining separate rotor equations as described in [77] or by using a built-in function for homogenized current densities in coils.

This multi-layer method is also used for the parameter model in Chapter 4. Therefore, please refer to Section 4.2.4 for further explanations and a more detailed examination of the skin effect and the required number of layers. For the Finite Element model in this chapter, the focus is on the consideration of the non-standard ring, which is hereby considered complete.

3.6 Torque and equation of motion

The most important quantity for investigating the transient start-up behavior is the electromagnetic torque. In many Finite Element models, the so-called Arkkio's method is used [74]. This method is a modification of Maxwell's stress tensor applied to cylindrical rotor geometries of electrical machines. Hence, the formula for the cylindrical coordinate system yields:

$$T_{\mathrm{el}} = \frac{l_{\mathrm{e}}}{\mu_0 \delta_{\mathrm{g}}} \int_{S_{\mathrm{ag}}} B_{\rho} B_{\alpha} \mathrm{d}S. \tag{3.26}$$

Here, S_{ag} is the cross-sectional area of the air gap in the $\rho\alpha$-plane, whereby ρ is the radial distance and α is the azimuth. Accordingly, B_{ρ} and B_{α} are the radial and azimuthal components of the air gap flux density.

Together with the sum of all load torques T_{load}, which is subtracted from the electromagnetic torque, the equation of motion for a rigid rotor with a rigid shaft finally results in:

$$\frac{\mathrm{d}\omega_{\mathrm{m}}}{\mathrm{d}t} = \frac{T_{\mathrm{el}} - T_{\mathrm{load}}}{J_{\mathrm{tot}}}. \tag{3.27}$$

Here, J_{tot} is the sum of all moments of inertia on the rotating axis. The load torque T_{load}, on the other hand, consists of all torques that oppose the electromagnetic torque T_{el}. As mentioned in Chapter 2, these can be different types of constant and speed-dependent loads.

Since the rotor angle ϑ_{m} is needed for the FE model, a second differential equation is introduced:

$$\frac{\mathrm{d}\vartheta_{\mathrm{m}}}{\mathrm{d}t} = \omega_{\mathrm{m}}. \tag{3.28}$$

3.7 Skewing

To reduce torque ripple during synchronous operation as well as parasitic harmonic torques during asynchronous start-up, the rotor of LSSynRM can be skewed as known for Induction Machines. Since a simple 2D model cannot represent a skewed motor, the multi-slice method should be applied [86]–[88]. This connects multiple 2D models while adapting the rotor angle for each slice according to the skewing angle. However, none of the presented motors in this thesis is skewed, which is why the method will not be used.

3.8 Solution

For the solution, the following aspects have to be considered to provide a fast solution while also maintaining a good convergence.

3.8.1 Number of time steps per electrical period

For transient problems, a time step solver is used. It has proven useful to define the time step as fixed to ensure convergence for each type of problem. For this, it is recommended to define the number of time steps per electrical period N_{steps} rather than the time step t_{step} itself. In this way, the time step

$$t_{\text{step}} = \frac{1}{N_{\text{steps}}} \cdot \frac{1}{f_{\text{s}}} \tag{3.29}$$

is automatically adapted to the frequency f_{s} of the applied voltage.

With a well-defined model, as for the reference model introduced in this chapter, 500 steps per period (time step $t_{\text{step}} = 40\ \mu\text{s}$ for $f_{\text{s}} = 50\ \text{Hz}$) provide satisfactory results, no matter the study (start-up, locked rotor, fixed speed, etc.). Depending on the required accuracy of harmonic torque, for example, N_{steps} could also be adapted (but not less than 300 steps per period).

3.8.2 Segregated solution of mechanical equations

Since in electrical machines the mechanical time constants are usually much higher than the electrical ones, the mechanical subsystem will change very slowly compared to the electromagnetic quantities. For this reason, the mechanical equations from Section 3.6 can be solved separately. By avoiding the iteration of the rotor angle in every iteration step of the non-linear electromagnetic system of equations, the computing time can be reduced.

3.9 Experimental validation

For validating the Finite Element model, several tests can be carried out that allow for an accurate and in-depth validation of different aspects. The measurements are carried out step by step in an order that increases the complexity of the measurement and the corresponding simulation.

3.9.1 Synchronous torque measurement

The most simple method to start with is the measurement of the synchronous torque T_{syn} as a function of the rotor mechanical angle ϑ_{m}. By this, the modelling of the magnetic circuit as well as the implemented method for the torque evaluation can be validated.

The test motor is supplied by a DC power supply which is connected as indicated in Figure 3.20. The direct current I_{DC} flowing through phase one and half its negative value flowing back through phases 2 and 3 lead to the same state as a three-phase AC supply at $t = 0$ for cosine currents. This is often referred to as locked MMF because the magnetomotive force does not rotate but is locked in place. When the rotor is turned, the torque will change with the rotor angle ϑ_{m}. This angle can then be transformed to the current angle γ, which is defined as the angle between the rotor's d-axis (which rotates) and the angle of the stator current space vector (which is locked in place). In contrast to previous work [54], [89], the rotor in this experiment is coupled to a servo motor as load, which allows for much more precision than rotating it manually. A fixed speed of 1 rpm yields a quasi-steady state for each measured point. A torque sensor coupled between both motors can then measure the torque as a function of the rotor angle. The experimental setup is shown in Figure 3.21.

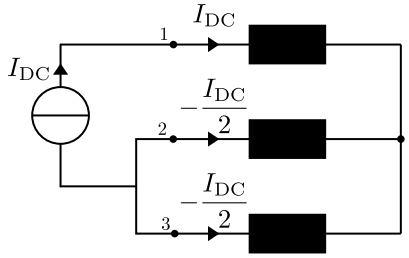

Figure 3.20: Connection of the DC power supply to the windings of the test motor to provide a locked MMF for the synchronous torque measurement.

The used torque sensor has a high resolution of 8192 pulses per revolution. A measurement range of 0 to 4 N·m allows for an accurate torque measurement for the studied motors (rated torque 1 N·m). Because the load motor as well as the rest of the test setup applies friction torque to the test motor, the measurement must be carried out for rotation in both directions. The friction torque can then be eliminated by evaluating the mean value of both tests.

For the simulation, it is sufficient to carry out magnetostatic FE studies for different rotor angles with the same current I_{DC} as applied in the measurement. The reason for that is the low rotational speed of the motor that justifies the assumption of a quasi-steady state at every rotor position because the electromagnetic time constants are much lower than the mechanical ones. This allows for a fast computation with accurate results.

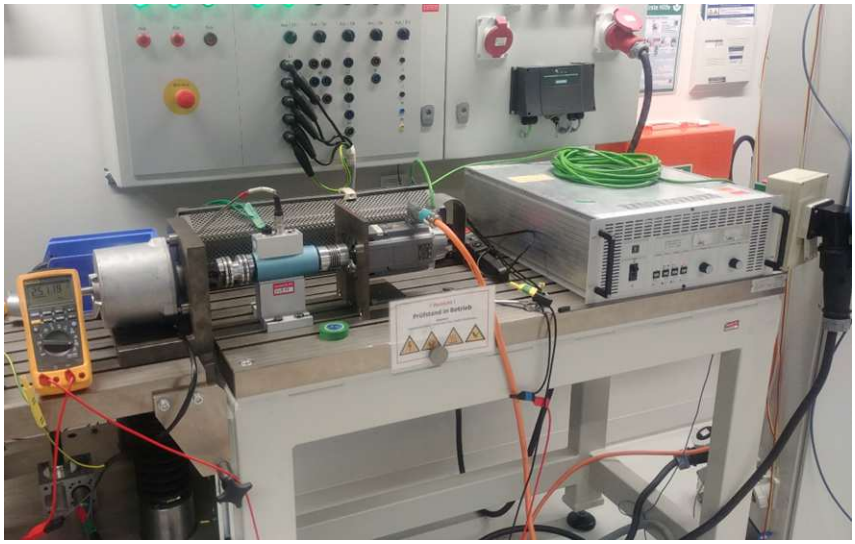

(a) photo

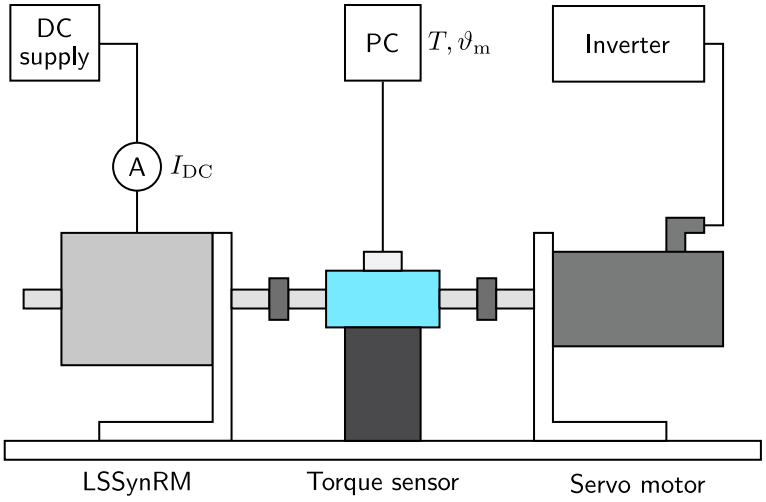

(b) drawing

Figure 3.21: Experimental setup for synchronous torque measurements.

3.9.1.1 Motor I

The first comparison will be evaluated for Motor I, which has an Induction Machine rotor cage with open slots at the air gap that will cause slot harmonics of high frequencies. Because the motor has already been studied in [55], the comparison with the existing results can provide a further statement about the validity of the presented FE model. Furthermore, the improvement in the accuracy of the measurement can be evaluated.

Figure 3.22 shows the synchronous torque for a current of $I_\mathrm{DC} = 2$ A that causes moderate saturation in the iron parts. For improved visualization, only the range from 0 to 180 electrical degrees is shown in this and all following plots. Foremost, it can be observed that the shape of the curve fits the FEM results presented in [55]. Comparing the measurement, it appears that there is also an improvement due to the fact that the servo motor provides a constant speed of rotation and also allows for multiple similar revolutions to evaluate the reproducibility of the results. This was not possible with the original experimental setup because the motor had to be turned manually with a bar attached to the shaft.

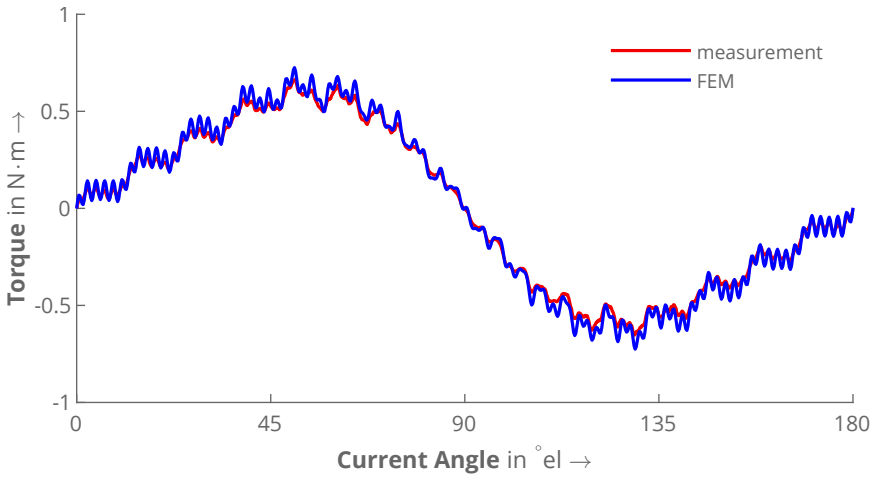

Figure 3.22: Torque versus current angle from the synchronous torque measurement of Motor I for $I_{\mathrm{DC}} = 2\,\mathrm{A}$ compared with FEM.

As for simulation, it can be stated that the results are overall accurate and in good agreement with the measured torque. However, a small difference in the amplitude of the harmonics can be seen, which, on the one hand, may be due to the measurement accuracy. On the other hand, it is known that the material properties of the stator and rotor laminations near the air gap area at the tooth tips deteriorate during the manufacturing process and during the cutting procedure [66]–[68].

Concerning the shape itself, the effect of the shifted torque maximum to around 55°el due to saturation can be clearly seen here. What also stands out is that around a current angle of 90°el, the harmonics are significantly less pronounced. The reason for this is the already large magnetic resistance of the q-axis, in which the rather small influence of the slotting (that is, the relative position of stator and rotor teeth) is hardly perceptible [55].

Figure 3.23 shows the comparison for a current of 3 A leading to a maximum fundamental torque of around 1 N·m, which is the rated torque of the machine. The results at this state of higher saturation also fit well with the same slight deviations as discussed for the first comparison.

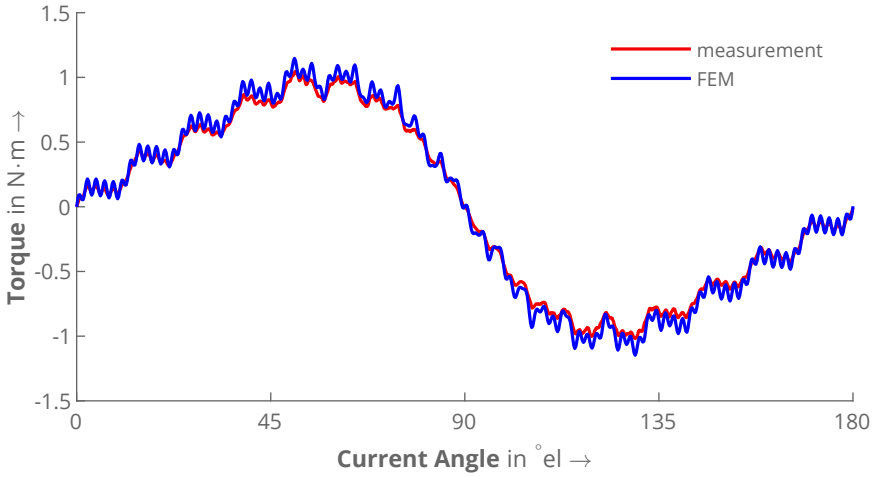

Figure 3.23: Torque versus current angle from the synchronous torque measurement of Motor I for $I_{\mathrm{DC}} = 3\,\mathrm{A}$ compared with FEM.

3.9.1.2 Motor II

The second motor for validation is Motor II, which has no standard Induction Machine slots in the rotor, but a cage embedded in its flux barriers. However, due to the low number of only three non-optimized flux barriers per pole, strongly pronounced torque harmonics should also be observable and therefore still allow for a good validation of the magnetic circuit.

Especially the saturation of the iron bridges at the rotor outer diameter, but also the ones placed in the middle of the flux barriers, can make a difference because of the unknown magnetic properties due to manufacturing. The small widths of the bridges of less than 1 mm basically mean that the whole area of the bridges is affected and can cause deviations in the results.

Because the torque is measured over a whole revolution, the influence of the bridges on the magnetic circuit behavior will change as well. While for a d-axis flux only the outer bridges will slightly saturate because they "collect" the air gap flux, a q-axis flux will lead to a high saturation of all iron bridges since they are the only material in the flux paths that have a high permeance when unsaturated. This is illustrated in Figure 3.24.

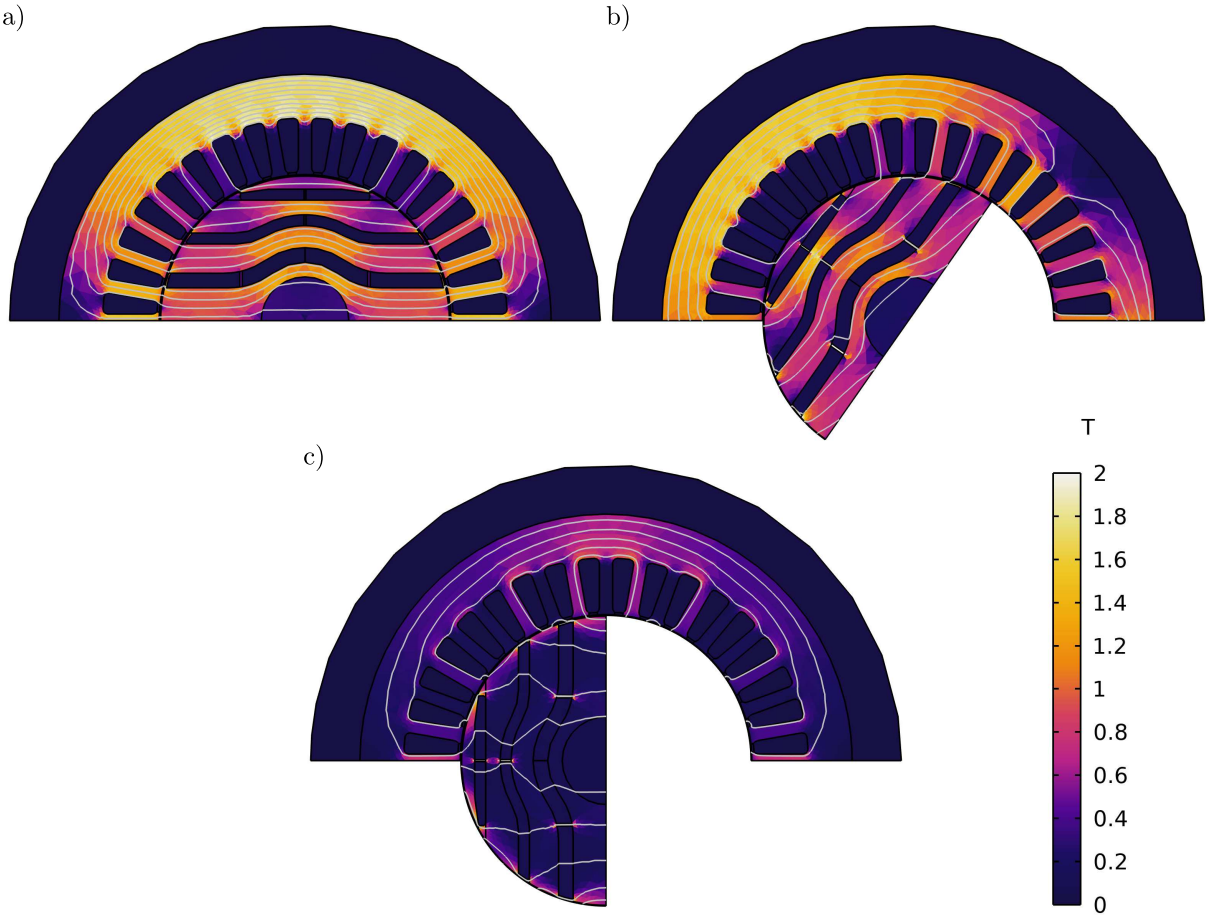

Figure 3.24: Flux density plots with indicated flux lines from the synchronous torque simulation of Motor II for 3 A at current angles of a) 0°, b) 55°, and c) 90°.

With increasing current angles, the saturation of the iron bridges increases, as has been explained above. As shown in Figure 3.6, there is an area in the $B(H)$-curve of the motor that deviates from the original material characteristic curve. Since this behavior can only be estimated, it is to be expected that deviations will occur in this area (i.e.,

for medium saturation in the bridges). At the same time, the saturation of the stator yoke decreases with increasing current angles, which means the influence of the narrow flux paths becomes higher. The following measurements should provide information on whether this influences the results.

Figures 3.25 and 3.26 therefore show the comparison of measured and simulated synchronous torque for two different currents, of which the lower one causes a medium saturation and the higher one a high saturation. In both cases, a good agreement is observable. The fundamental torque as well as its harmonics are accurately simulated by FEM. As the rotor surface is smooth, only the flux barriers in combination with the stator teeth are responsible for harmonics. Hence, the frequencies of those harmonics are lower than for Motor I.

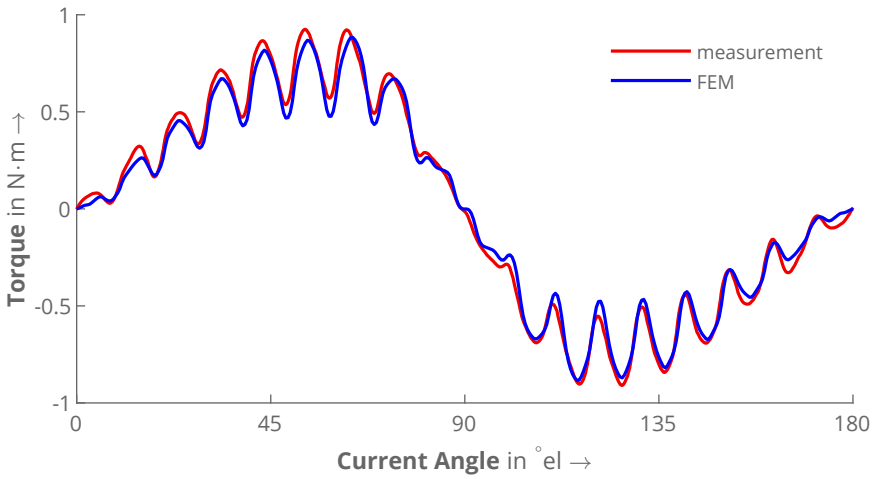

Figure 3.25: Torque versus current angle from the synchronous torque measurement of Motor II for $I_{\mathrm{DC}} = 2\,\mathrm{A}$ compared with FEM.

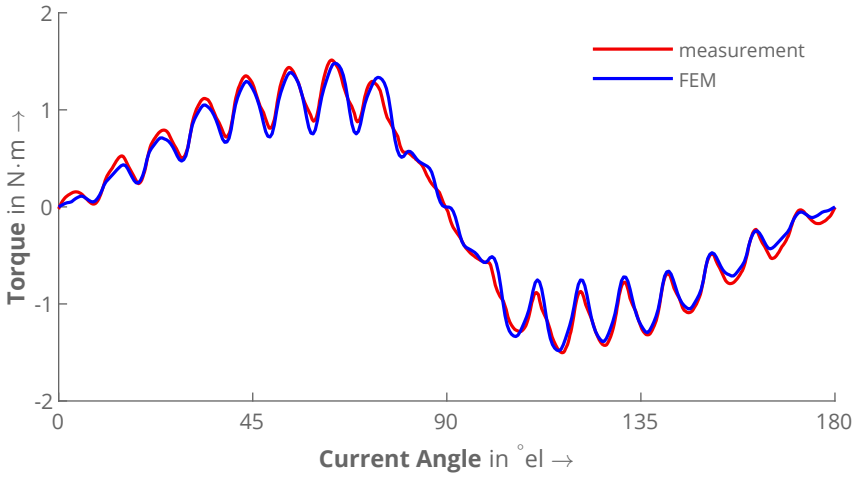

Figure 3.26: Torque versus current angle from the synchronous torque measurement of Motor II for $I_{\mathrm{DC}} = 3\,\mathrm{A}$ compared with FEM.

As far as the material properties of the iron bridges are concerned, it should be mentioned that their influence is not apparent from the results in this case. As shown in the results from FEM in Figure 3.24, however, their saturation is high, especially for larger current angles. It can therefore be assumed that the flux densities are already in

the range where the material curve corresponds to the original curve again, even for areas with manufacturing influence. Indeed, both converge again from around 2 T, as shown in Figure 3.6.

3.9.1.3 Motor III

Lastly, Motor III is to be studied. Due to its 4 flux barriers per pole, it is to be expected that the torque harmonics will be less pronounced. In contrast to the two-pole rotor of Motor II, there are significantly more iron bridges distributed around the rotor circumference. This can change the result of the FEM simulation more visibly compared to the measurement.

Figures 3.27 and 3.28 prove that both assumptions were right. The shape of the curve is much smoother as for both other rotors because of the lack of rotor slot openings and the high number of flux barriers that are known to reduce torque ripple. The FEM simulation predicts slightly more pronounced harmonics than the measurement. The overall agreement is once again satisfactory.

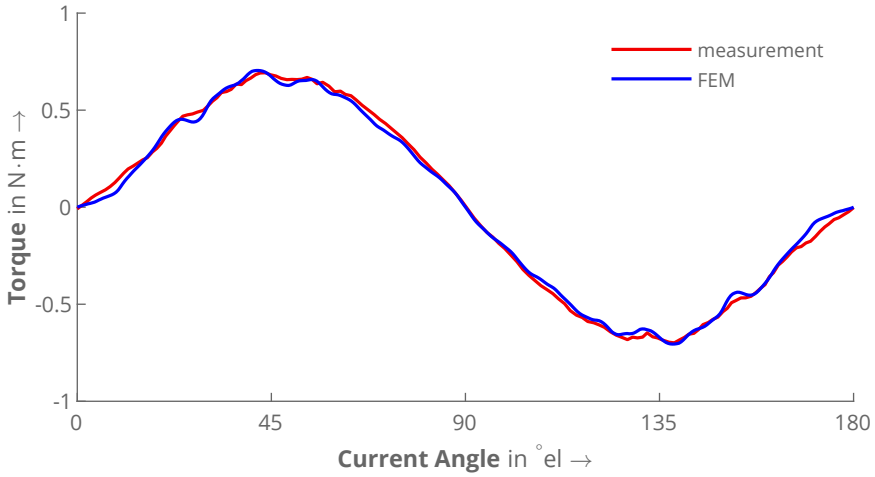

Figure 3.27: Torque versus current angle from the synchronous torque measurement of Motor III for $I_{\mathrm{DC}} = 2.5$ A compared with FEM.

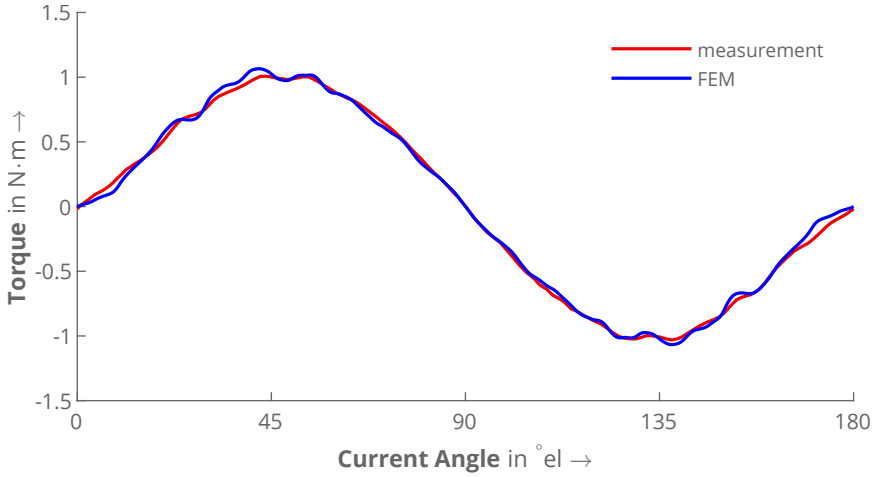

Figure 3.28: Torque versus current angle from the synchronous torque measurement of Motor III for $I_{\mathrm{DC}} = 3$ A compared with FEM.

3.9.2 No-load measurement

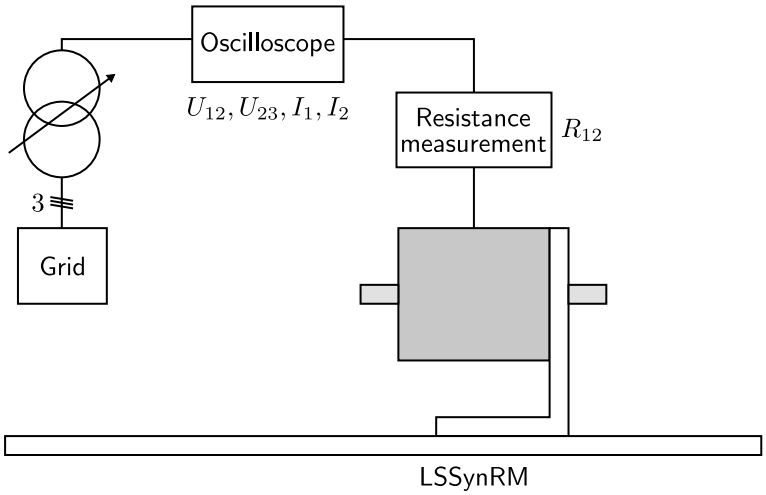

Figure 3.29: Experimental setup for no-load measurements.

To further study the magnetic circuit in general and the accuracy of the non-linear material data in particular, no-load measurements provide helpful insights. To this end, the motor is connected to a three-phase transformer and the shaft is completely uncoupled (Figure 3.29).

The methodology is similar to the no-load test from IEC 60034-30-1 standard. The motor is warmed up to a steady-state temperature at its rated current to avoid rapid changes in phase temperature between different points. Then the voltage can be set to the desired values using the transformer. In this case, the values of voltages and current over time are recorded with an oscilloscope (for two of the three phases). This allows for a good comparison of simulated and measured values.

For the resistance measurement, an online resistance measurement device is used. This means that the motor does not have to be switched off between measurement of different points, which will cause the resistance to be measured accurately and the temperature to decrease slowly.

The simulation requires a transient study, taking the equation of motion into account. This is necessary because the load angle, that is, the angle between the voltage phasor and the d-axis of the rotor, is difficult to estimate in a simulation with fixed rotational velocity. Furthermore, the incorporation of friction, which is relatively high for the test motors, provides more accuracy compared to measurements.

In contrast to synchronous torque measurements, the measured phase voltages are applied to the stator circuit, and the phase resistances are set to the measured values. Because only the resistance R_{12} between phase 1 and 2 is measured, the remaining resistances are adapted with respect to the relation of the values measured at room temperature.

For the no-load simulation, the start-up process is ignored, as it would lead to unsuccessful synchronization due to the low voltage anyway (in both simulation and measurement). This is why the starting condition for the equation of motion is $\omega_\mathrm{r} = \omega_0$, that is, synchronous speed. Then the voltage is switched on, and the simulation is carried on until the rotor has synchronized to the stator magnetic field and all transients have disappeared. To avoid numerical problems at the initial steps, the voltage amplitude is slowly increased with a smooth step function over one period, as shown in Figure 3.30.

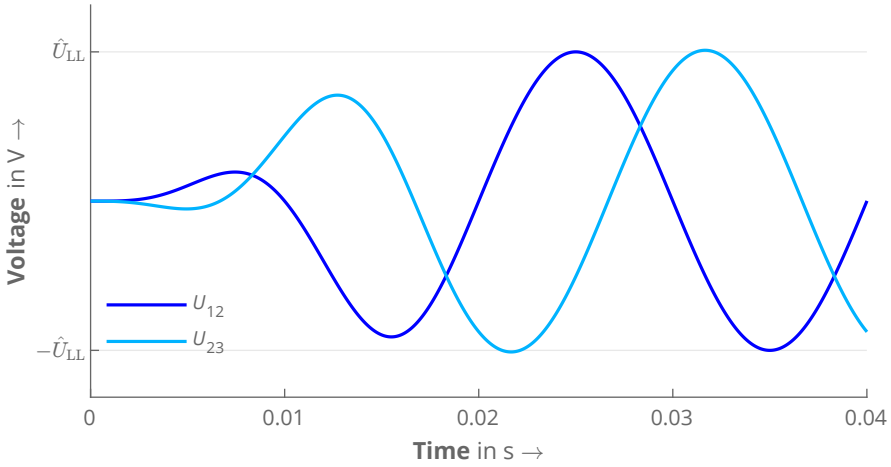

Figure 3.30: The amplitude of the line-to-line voltage $\hat{U}_{LL}$ is ramped up over one cycle in the Finite Element model.

3.9.2.1 Motor I

The LSSynRM with the original Induction Machine rotor cage is once again compared at first. The results for the typical no-load characteristic curve in Figure 3.31 show a good agreement with the measurements. Only the values of the two highest voltages, that is, at high saturation, deviate slightly. Several factors could explain this observation.

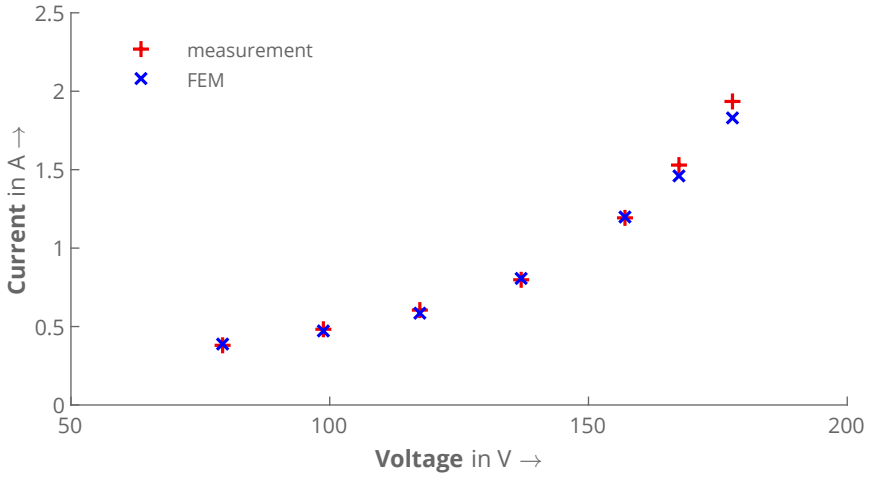

Figure 3.31: RMS current versus voltage from no-load measurements for Motor I compared to FEM. Each current value is the average of all three phases.

Firstly, the used material curve is likely to differ from the real behavior of the motor. This fits the findings from the synchronous torque validation in Section 3.9.1. The torque of the FE simulation for high currents was already slightly higher, meaning that the magnetic circuit was less saturated.

Secondly, as the iron losses are neglected in the Finite Element model, the current can differ especially at high voltages. As the flux is determined by the voltage level, a certain magnetizing current is required. The phase currents must be correspondingly higher if they also have to compensate for eddy current losses in the motor's iron cores. The measurement data shows that the power factor increases for these points, which supports the thesis.

Nevertheless, the results are within a satisfactory range of accuracy. The comparison of all three phase currents versus time at 160 V in Figure 3.32 further shows that the form of the functions, including most harmonics, fits good. While the slotting harmonics are accurately modelled, the measurement shows a more pronounced fifth harmonic due to saturation, which in this case causes the current to be more conical at its maximum.

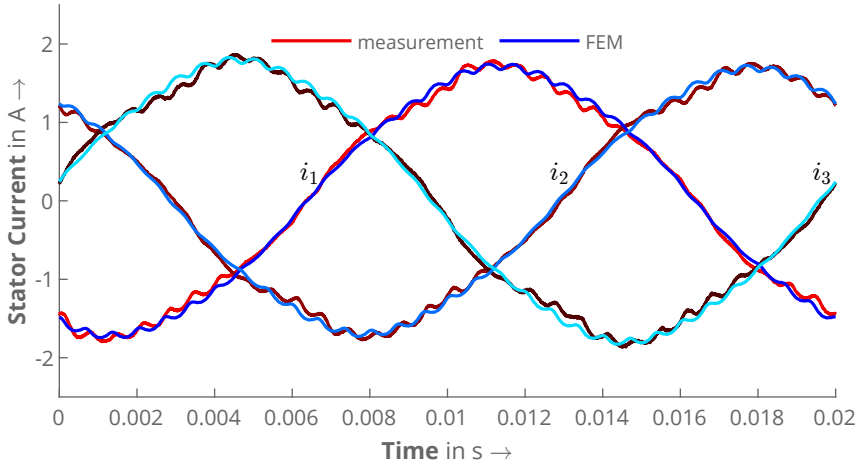

Figure 3.32: Current versus time from no-load measurement at $U = 160$ V for Motor I compared to FEM. The three currents of the measurement are shown in different shades of red, and those of the FEM in shades of blue.

Despite the slight deviations, the overall agreement is good enough to proceed with the validation. Should measurements be performed at correspondingly high voltages, a deviation in the current must then be expected.

3.9.2.2 Motor II

The new 2-pole version, Motor II, again has the rotor placed in the same stator. Here, the results for the no-load test fit good over the whole voltage range, as shown in Figure 3.33.

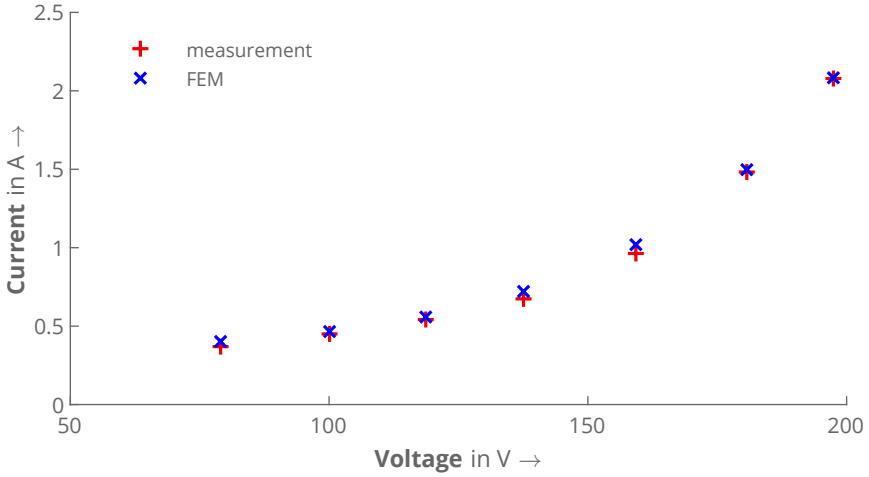

Figure 3.33: RMS current versus voltage from no-load measurements for Motor II compared to FEM. Each current value is the average of all three phases.

The curve is somewhat flatter, which means that saturation sets in later than with Motor I. This is due to much more iron in the flux paths of the rotor because of the lack

of a separate rotor cage. Furthermore, the area of medium saturation, that is, 140 V and 160 V, shows slight deviations.

What is striking, however, is the higher current at low voltages. This is explained as follows: Because in the simulation the machine has to find its steady state after the voltage being switched on to the currentless motor rotating at synchronous speed, the poor damping of the non-optimized rotor cage is not sufficient for the oscillations to disappear after 2 s of simulation time.

Therefore, the best practice is to evaluate the mean value of the RMS current over a few of the last cycles. In this case, 15 cycles (= 0.3 s) were sufficient to have a good approximation of the resulting value for the steady state.

The current versus time behavior is also compared, which proves the good accuracy of the FE model (Figure 3.34). There is much more harmonic content than for Motor I, which was expected due to the poor design. Since the Finite Element Method can model these harmonics accurately, it can be considered valid.

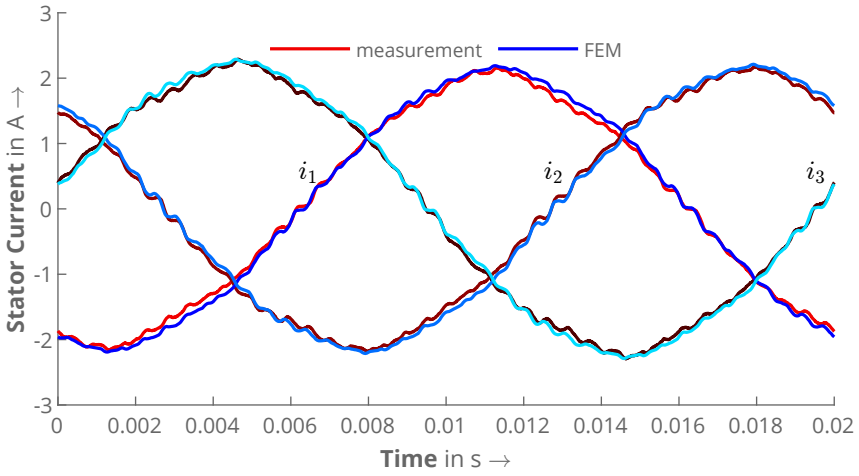

Figure 3.34: Current versus time from no-load measurement at $U = 180$ V for Motor II compared to FEM. The three currents of the measurement are shown in different shades of red, and those of the FEM in shades of blue.

3.9.2.3 Motor III

As can be observed in Figure 3.35, the measurement of Motor III shows a similar behavior as for Motor I. Up to a voltage of 140 V with a current of around 3 A, the results look fine. This fits the findings from the synchronous torque compared in Section 3.9.1. When the voltage is further increased, however, the measured motor shows more saturation than in the simulation. This leads to a deviation of up to 9% for the current at the highest measured voltage.

These deviations could be partly explained by the already mentioned material properties. The iron bridges at the air gap will saturate at high d-axis currents, as shown in a magnetostatic simulation with for 6 A in Figure 3.36. Since the flux densities in the iron near the air gap vary greatly, especially around the bridges, it can be assumed that the influence of manufacturing is noticeable. This means that the real permeability is not known for these areas, which would change the Carter factor and thus explain a part of the deviations.

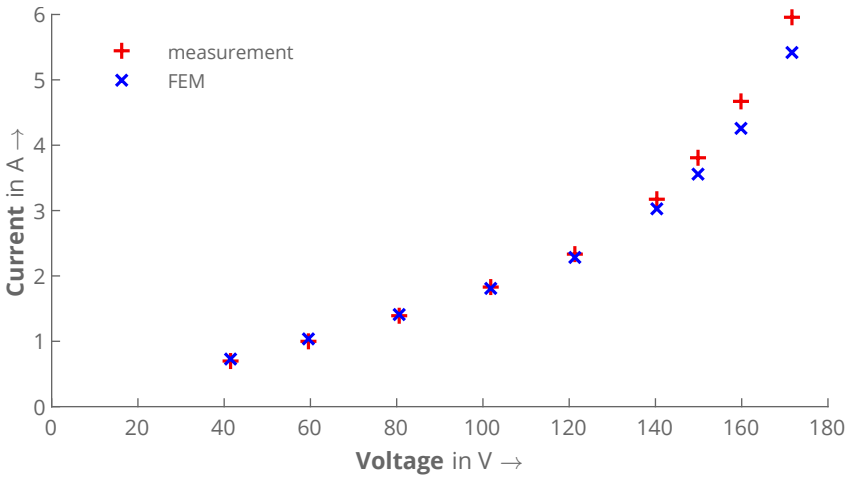

Figure 3.35: RMS current versus voltage from no-load measurements for Motor III compared to FEM. Each current value is the average of all three phases.

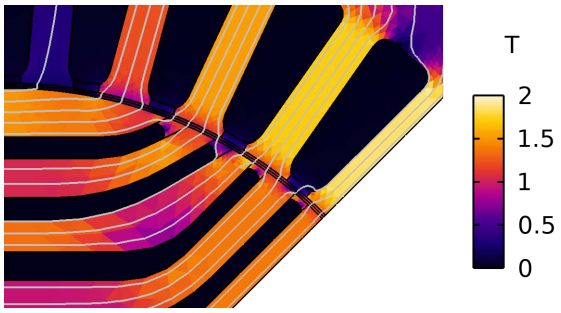

Figure 3.36: Flux density distribution from a magnetostatic simulation of Motor III with a d-axis current of 6 A.

However, other reasons for the deviations were identified as well. The evaluation of the measurement data again shows that the power factor increases at high voltages. This suggests that the discrepancy occurs also due to losses that have not been taken into account in the FE model. The most important components here are iron losses and additional losses.

Nonetheless, in all further measurements the voltage will be lower than or equal to 140V anyway, which means that the deviation for highly saturated states will not affect the accuracy of the results. Furthermore, the saturation is the highest for no-load operation ($\gamma = 0°$). As soon as a mechanical load is applied, the current angle increases and therefore the flux consists of both d- and q-axis flux, which causes saturation to decrease. Since medium and low saturation fit well, the results are expected to be accurate enough. However, if the motor is to be optimized, it should be considered that the material data used is not correct over the whole range and therefore would underestimate the saturation.

In contrast to both other motors, the stator currents of Motor III show hardly any geometry-induced harmonics (Figure 3.37). Due to the rotor surface having no slot openings and the number of flux barriers being high enough, the main inductance does not change too much during rotation, which is why the measured and simulated currents are nearly sinusoidal.

Since this comparison also shows an overall good agreement between measurements and simulations, both the magnetic circuit modelling and the torque evaluation (as proved in Section 3.9.1) can be considered validated.

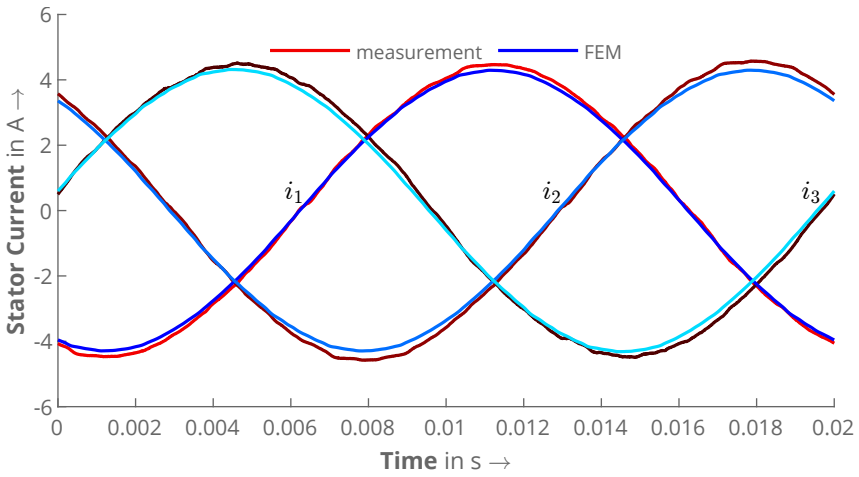

Figure 3.37: Current versus time from no-load measurement at $U = 140$ V for Motor III compared to FEM. The three currents of the measurement are shown in different shades of red, and those of the FEM in shades of blue.

3.9.3 Locked rotor measurement

The next step is therefore to validate the rotor circuit model. The best method for this is to perform locked rotor tests. Here, the rotor cage is fully active because the stator magnetic field rotates with its fundamental frequency around the rotor, hence inducing EMFs into the rotor cage which cause currents to flow. The skin effect is also most distinct in this case. Regarding the general single-phase equivalent circuit of Induction Machines, it is known that the winding parameters such as resistances and leakage inductances will influence the result the most at this operating point (see Section 3.5.3).

For the measurement, the d-axis of the rotor is aligned with the center of the first coil group of the first phase by applying a locked MMF as described for the synchronous torque measurement in Section 3.9.1. It is then locked mechanically to a fixed shaft. To ensure that the temperature rise for varying voltages during the measurement is kept small, the motor is warmed up to a steady-state temperature.

For each measured point, the voltage is set to the desired level with a three-phase transformer. The line-to-line voltages u_{12} and u_{23} as well as the phase currents i_1 and i_2 are recorded over two cycles with an oscilloscope. To measure the temperature of the stator winding, an online resistance measurement device has been used (Figures 3.38 and 3.39). The rotor temperature is measured with a thermocouple placed in the end ring. For the simulation, it is assumed that the whole rotor cage has the same temperature. Furthermore, the same stator is used for both 2-pole rotors to ensure as much comparability as possible.

For the simulation, the rotor is set to the same position as in the measurement. The equation of motion is neglected because the rotor does not rotate. Then the voltage is switched on, and the simulation is carried on until all transients have disappeared, which is after about 1 s in this case. A good indicator is the evaluated torque, which has to be periodical without transients. This validation has been partly presented in [A5] but it will be explained more detailed and has also been expanded for this work.

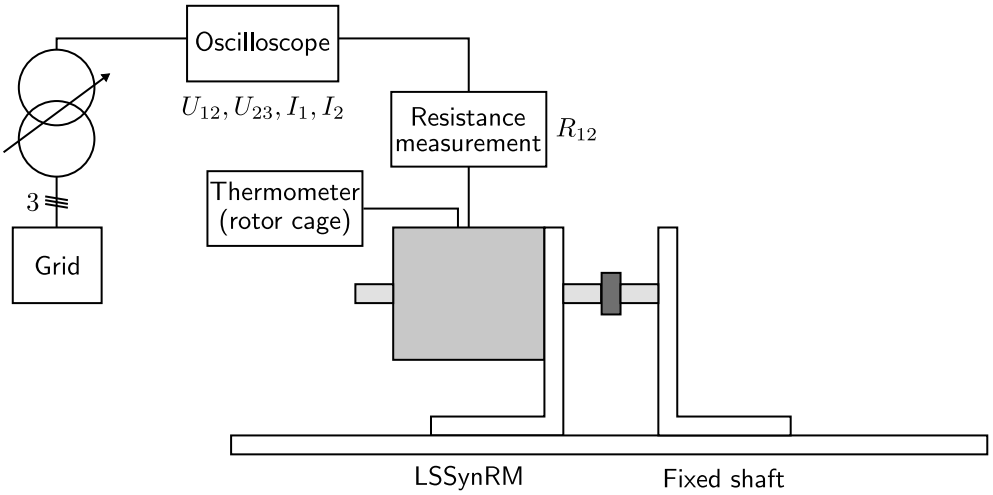

Figure 3.38: Experimental setup for locked rotor measurements.

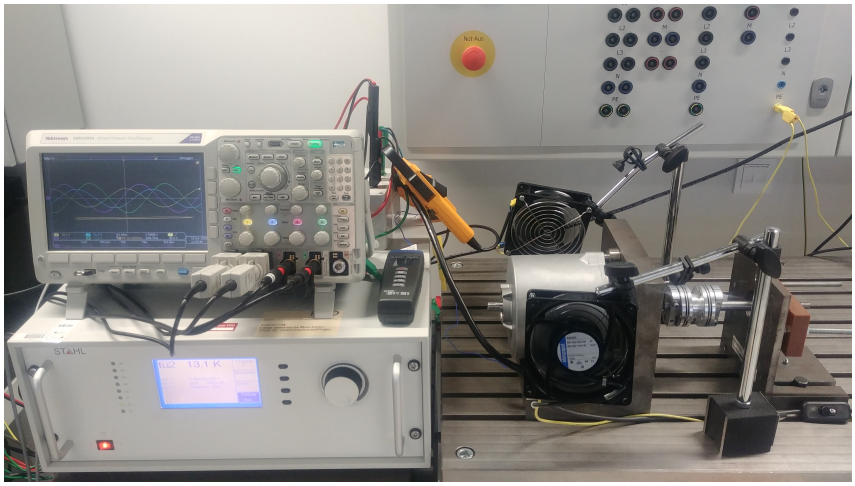

Figure 3.39: Photo of the experimental setup for locked rotor measurements.

3.9.3.1 Motor I

The validation starts with Motor I because the stator and rotor windings are the same as in the original Induction Machine. In particular, for the rotor cage model presented in Section 3.5, this provides a simple cage geometry to start with before moving on to the more complex geometries of the other two motors. The motor's rotor slot height of 12.7 mm is approximately equal to the skin depth of aluminum at 50 Hz and at the rotor temperature measured during the experiment. This means that the skin effect will not have a big impact, and therefore the results for a model with one or three layers for the rotor cage should provide the same results.

Figure 3.40 provides the comparison of the measured stator currents at different voltages with FEM, which has been simulated with one and three rotor cage layers. It is obvious that the previous assumption was correct because all simulated currents for the respective voltage are approximately the same.

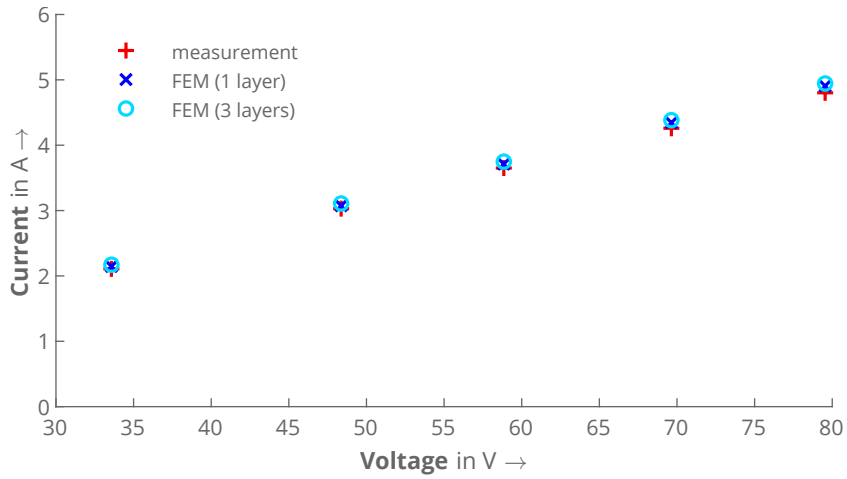

Figure 3.40: RMS current versus voltage from locked rotor measurements for Motor I compared with FEM. Each current value is the average of all three phases (currents are nearly symmetrical). The rotor cage is divided into 1 and 3 layers.

Looking at the current versus time plot in Figure 3.41 for the highest voltage of 80 V, the accuracy is once more proven. It can be observed that all phase currents are sinusoidal and have the same amplitude. This is also in accordance with FEM.

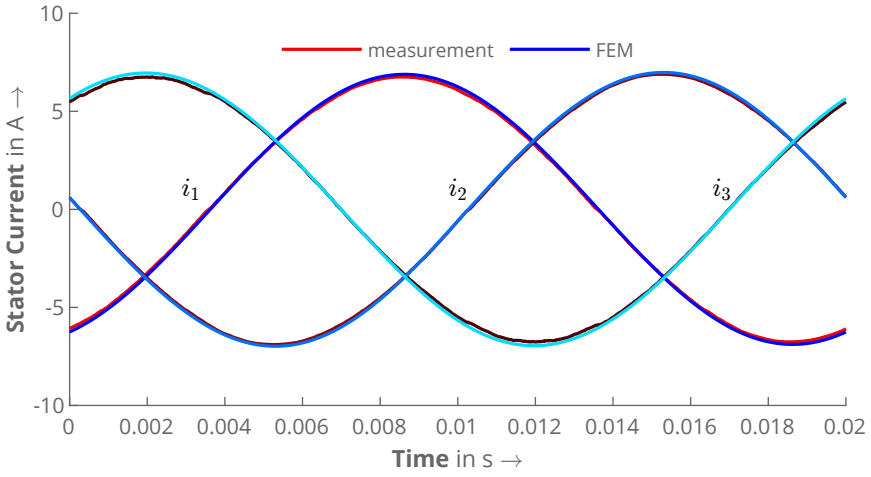

Figure 3.41: Current versus time from locked rotor measurements at $U = 80\,\mathrm{V}$ for Motor I compared with FEM (1 layer). The three currents of the measurement are shown in different shades of red, and those of the FEM in shades of blue.

The proposed 3D-FEM assisted method to calculate the end ring resistances could be validated for Motor I with a symmetrical rotor cage. Thus, the next step is to apply the method to both Line-Start Synchronous Reluctance Machines with conductors in the flux barriers.

3.9.3.2 Motor II

For the two-pole version (Motor II), the same stator has been used as for Motor I to provide good comparability. The end winding leakage inductances of stator and rotor, which represent the only remaining uncertainty factor, are therefore not changed. Only the rotor was replaced.

Figure 3.42 shows the results for the measurements as well as for the simulations with one and three layers for the rotor cage. To prove that the end ring resistances have to be considered, the simulation is also carried out for the case if they are neglected.

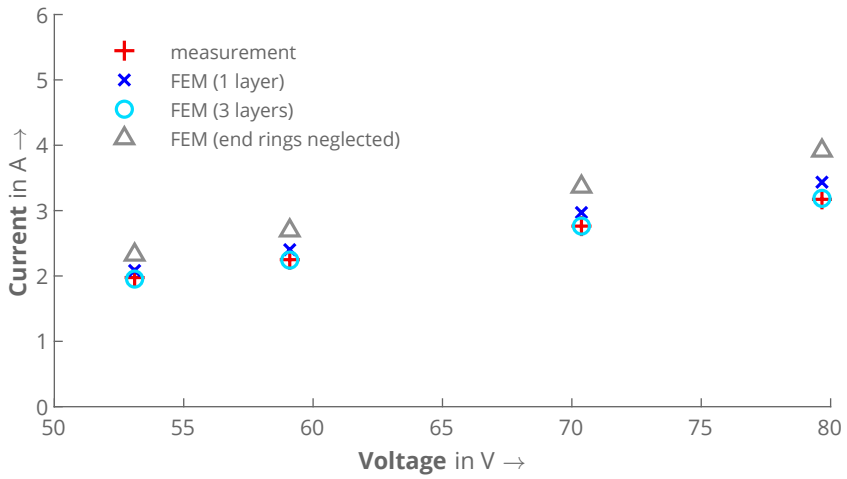

Figure 3.42: RMS current versus voltage from locked rotor measurements for Motor II compared with FEM. The cases of a rotor cage model with one and three layers as well with neglected end rings are shown. Each current value is the average of all three phases.

Despite all results of the FE model still having sufficient accuracy, the difference between one and three layers is more distinct. In this case, due to the very deep rotor bars, the skin effect is more pronounced, which is why the results for three layers better fit the measurement. Neglecting the end rings leads to higher currents due to the underestimation of the rotor resistance.

Figure 3.43 in addition shows the current versus time plots for both cases at a voltage of 70 V. Here, the difference between the FE models with one or three layers gets clear, as well as the fact that the shape of the current changes and is not sinusoidal anymore. The latter differs from the behavior observed for Motor I and can be explained as follows.

Since the symmetrical rotor cage in Motor I shields the anisotropy of the rotor, it does not affect the stator current. The symmetrical cage itself also does not generate any visible harmonics that do not correspond to the fundamental frequency. In the case of Motor II, however, the cage is asymmetrical and inserted into the anisotropy. On the one hand, the anisotropy cannot be shielded and causes the stator windings to have different inductances that depend on their relative position to the rotor. On the other hand, the cage itself generates harmonics that do not match the fundamental frequency.

When looking closely at the current form, there is also a slight difference in the harmonic content of both models with 1 and 3 rotor cage layers. Nonetheless, the difference would be small enough to reduce the rotor cage model to one layer and therefore from 18 to six rotor equations (because only half of the motor is modelled). It remains to be investigated during the validation, however, what influence the number of layers has on the overall start-up behavior.

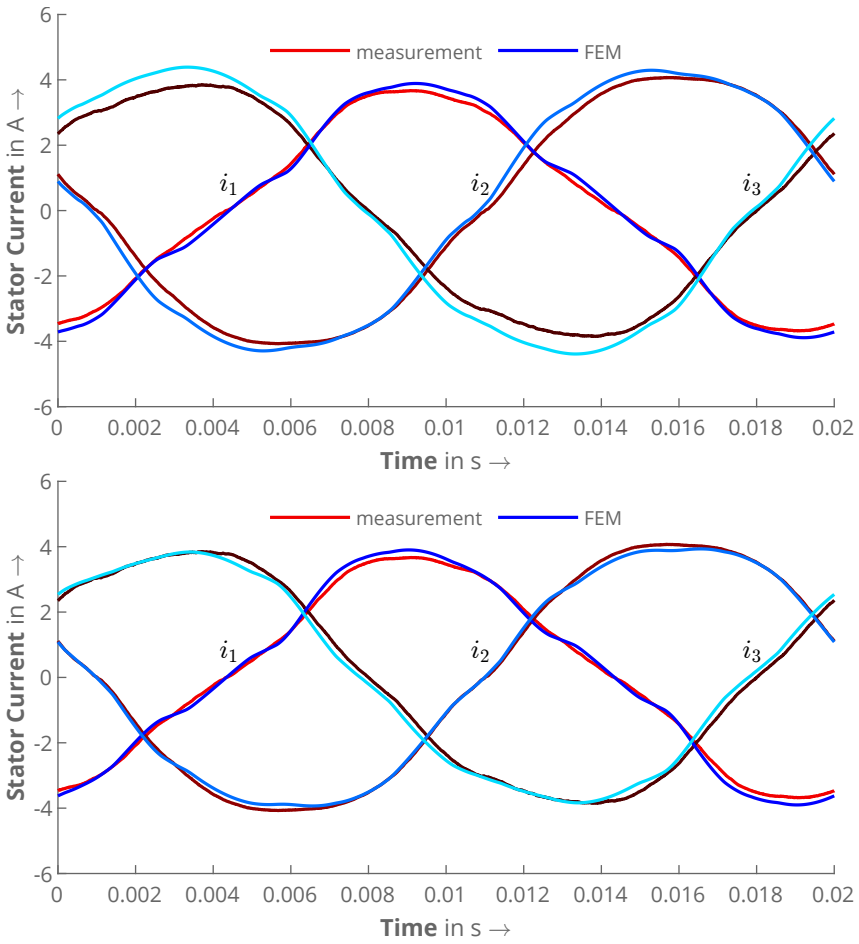

Figure 3.43: Current versus time from locked rotor measurements at $U = 70\,\mathrm{V}$ for Motor II compared with FEM (top: 1 layer, bottom: 3 layers).

3.9.3.3 Motor III

For Motor III, the procedure is the same as for the previous two motors. The results for one and three layers, as well as for neglected end rings, are shown in Figure 3.44. Here, the deviation at higher currents is slightly higher than for both two-pole motors. More precise, the slope of the function differs, which is why the deviation gets higher, the higher the voltage is.

To classify the results, the influence of the end ring resistances on the overall resistance is evaluated. Since the motor has four poles, the influence of the ring resistances on the total equivalent rotor resistance is smaller, which means that the deviation is likely to be caused by other effects as well. This can also be proven by the smaller deviation between the simulation with and without end rings considered.

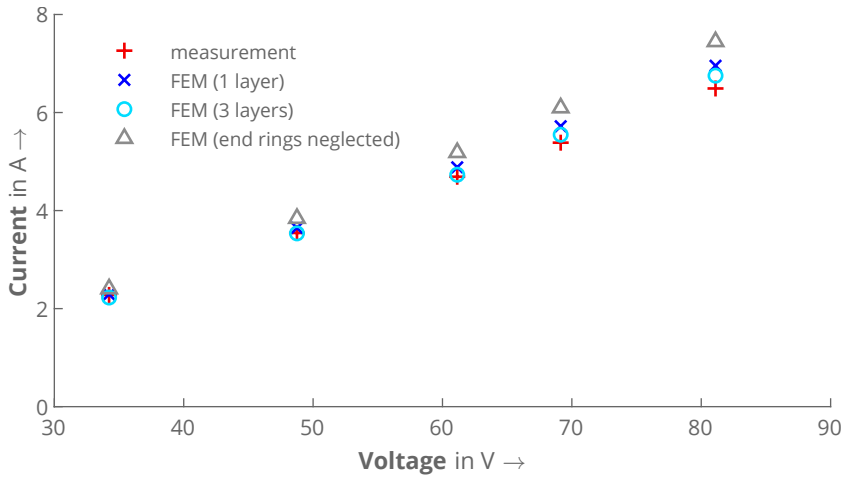

Figure 3.44: RMS current versus voltage from locked rotor measurements for Motor III compared with FEM. The cases of a rotor cage model with one and three layers as well with neglected end rings are shown. Each current value is the average of all three phases.

Comparing the current versus time at 35 V and 80 V in Figures 3.45 and 3.46, respectively, demonstrates that the accuracy of the Finite Element model is still sufficient. This concerns the shape of each individual current as well as the amplitude. Again, each phase current is different.

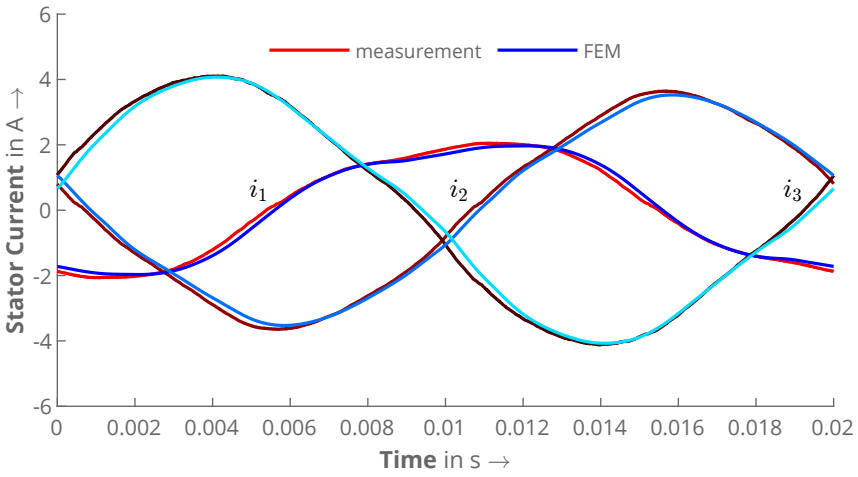

Figure 3.45: Current versus time from locked rotor measurements at $U = 35\,\mathrm{V}$ for Motor III compared with FEM (1 layer). The three currents of the measurement are shown in different shades of red, and those of the FEM in shades of blue.

What also stands out is that especially current i_1 looks different for the higher voltage in Figure 3.46. This can be explained by saturation, which is not high but can still affect the harmonic content of the currents.

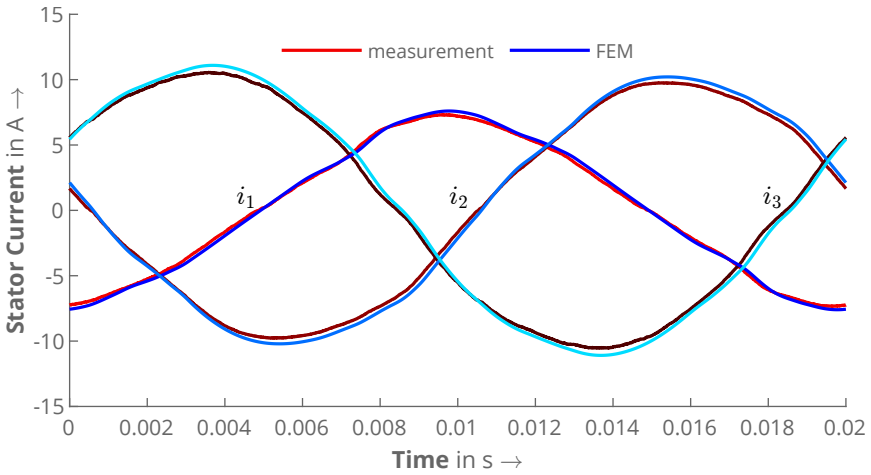

Figure 3.46: Current versus time from locked rotor measurements at $U = 80\,\mathrm{V}$ for Motor III compared with FEM (1 layer). The three currents of the measurement are shown in different shades of red, and those of the FEM in shades of blue.

3.9.4 Start-up measurement

Now that all other measurements have been successfully validated, the start-up measurement can be carried out. Due to the electrical and mechanical system running through a dynamic process that has to be simulated, it is the most complex test. At first, the measurement will therefore be carried out without external load, which means that the motor only has to start up against the friction torque T_{fric}. By adding flywheels of different moments of inertia J_{add}, the total moment of inertia can be gradually increased to test the motor behavior and the validity of the simulation. The setup for this procedure is shown in Figure 3.47.

At one side of the rotor, a coupling for the flywheels is added. This also provides a coupling for a small permanent magnet DC motor that will act as a tachometer, of which the open-circuit voltage is proportional to the rotor speed. For every measurement, the rotor position will be set to the same as during warm up. Although the time at which the voltage is switched on will vary, the parasitic synchronous torque has the same position at the start in both cases.

The entire process is adapted so that it provides as much information as possible about the condition of the machine. An important quantity for the start-up is the winding temperature of both stator and rotor. Because they can change rapidly due to the transient currents during the process, the motor is warmed up so that the change in temperature is kept low. For this purpose, it is again warmed up at reduced voltage with the rotor locked in a predefined position (as done in section 3.9.3). This is recommended because in contrast to Induction Machines, which are usually warmed up at their rated load torque, the Line-Start Synchronous Reluctance Machine has no rotor currents during rated operation.

Once the full motor, including the rotor cage, is warmed up to a sufficiently high temperature, it is fair to assume that the temperature during start-up does not vary significantly. The full measurement procedure is shown in Figure 3.48.

Since the two motors with modern rotor cage, Motor II and Motor III, cannot synchronize a moment of inertia apart from their own, this validation will start with these two motors. The differences in the number of layers can nevertheless be shown using dif-

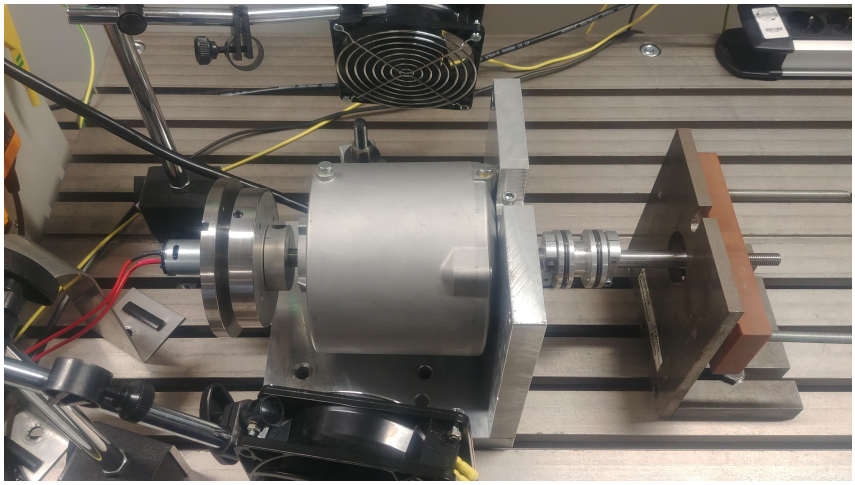

(a) photo (fixed shaft is removed after motor is warmed up)

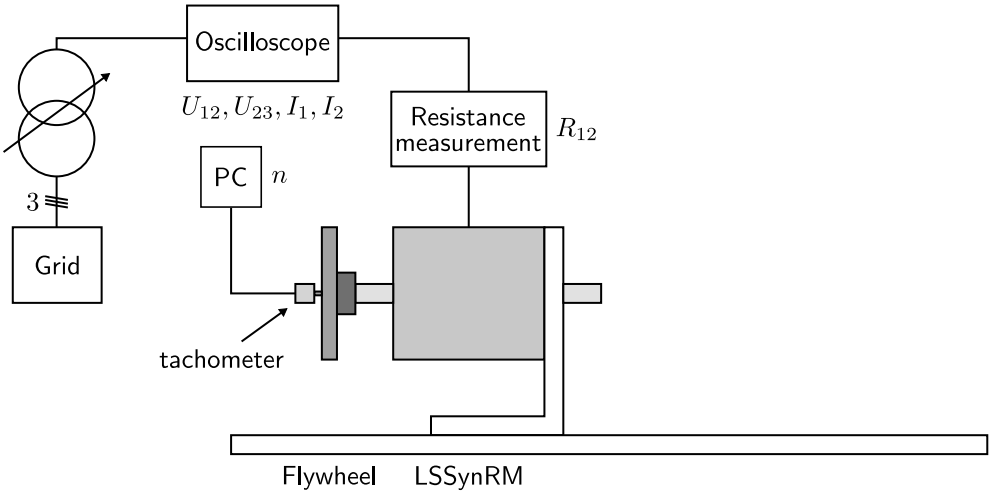

(b) drawing

Figure 3.47: Experimental setup for start-up measurement (without load).

ferent measurements with different moments of inertia. The validation for Motor I is then continued so that it can be demonstrated that the FE model can also bring improvements for the case of a non-standard ring. Comparisons for the case of start-up under load can also be shown for this motor.

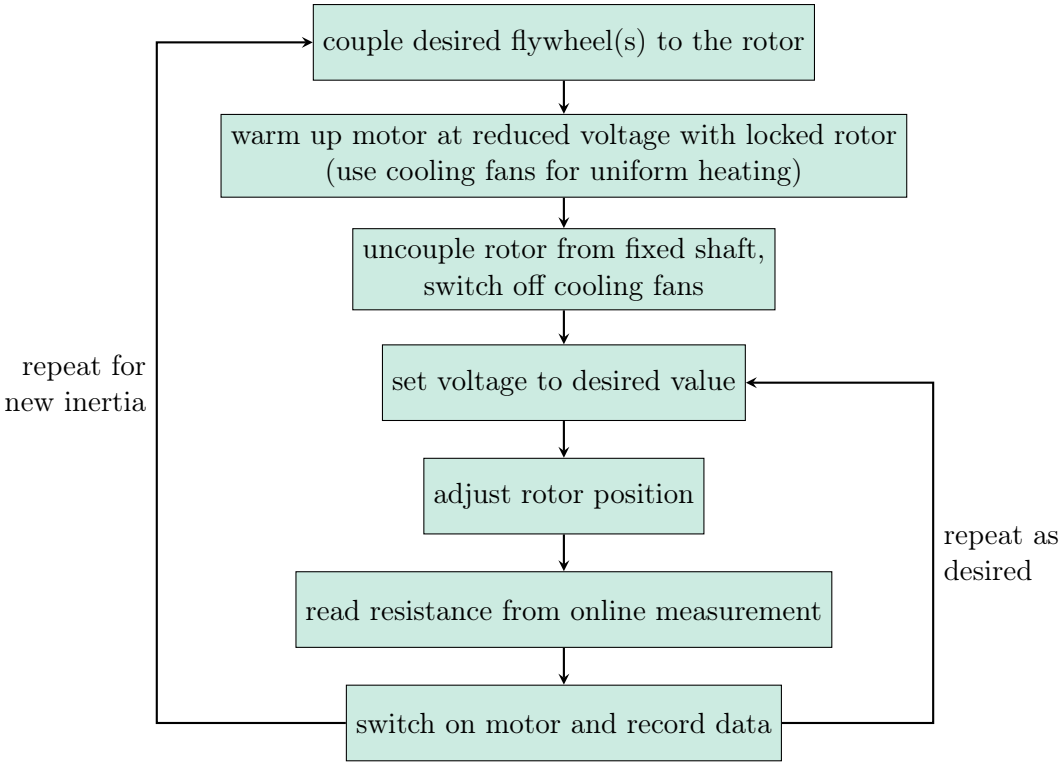

Figure 3.48: Procedure of start-up measurements.

3.9.4.1 Motor II

The first measurement is carried out without additional flywheels at a voltage of 180 V, which is sufficient to pull Motor II into step. In Figure 3.49, the speed is shown for the measurement as well as for the simulation with 1 and 3 layers in the rotor cage. Even though both simulations show that the motor synchronizes, it is noticeable that the simulation with 3 layers is in better agreement with the measurement.

If flywheels are added to increase the inertia, the influence of multiple rotor cage layers becomes even more obvious (Figure 3.50). While the motor is not able to synchronize in the measurement, the simulation with 1 layer shows that it does.

In contrast, the simulation with three layers is in better agreement with the measurement because the motor does not synchronize as well. The resulting quasi-stationary state is almost identical. The speed slightly differs, which can be caused by a remaining difference in the rotor resistance due to the temperature, for example. Hence, the oscillation frequency differs slightly as well, as it depends on the slip frequency of the rotor.

This can be supported by the third measurement, where the total moment of inertia is further increased. Both simulations in Figure 3.51 show that the motor cannot pull into step. Yet, with three layers, the average speed in the quasi-steady state fits much better.

In conclusion, it can be stated that the layer model also provides better results for the start-up and not only for locked rotor conditions. This may seem surprising given the fact that the fundamental rotor frequency near synchronous speed is low and skin effect should not be as important. Several factors could explain this observation. Firstly, the effective resistance of the very deep rotor bars of modern LSSynRM may be affected over the whole speed range. Secondly, the field penetrating the aluminum in the innermost flux barrier, for example, is shielded by all the conductors in the flux barriers above,

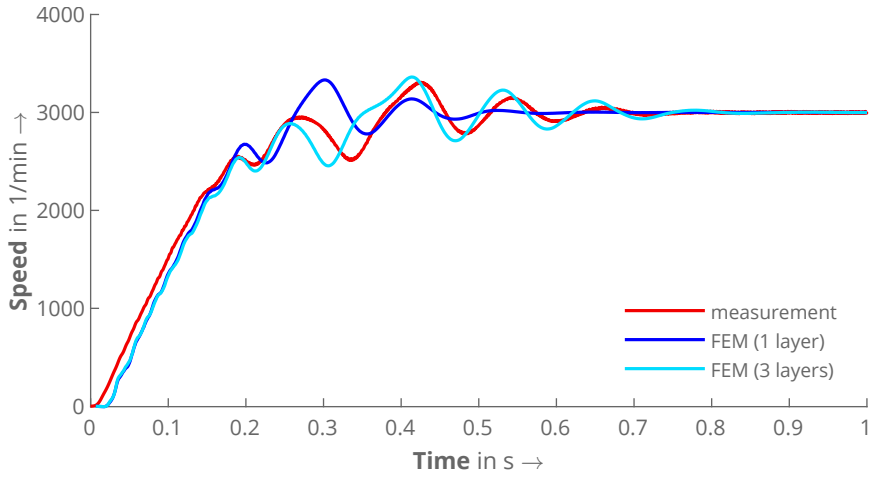

Figure 3.49: Comparison of the speed during dynamic start-up of Motor II at $U = 180\,\mathrm{V}$, $f = 50\,\mathrm{Hz}$, and $T_{\mathrm{load}} = T_{\mathrm{fric}}$ between FEM and measurement. The additional moment of inertia is $J_{\mathrm{add}} = 0$, so that $J_{\mathrm{tot}} = J_{\mathrm{mot}}$.

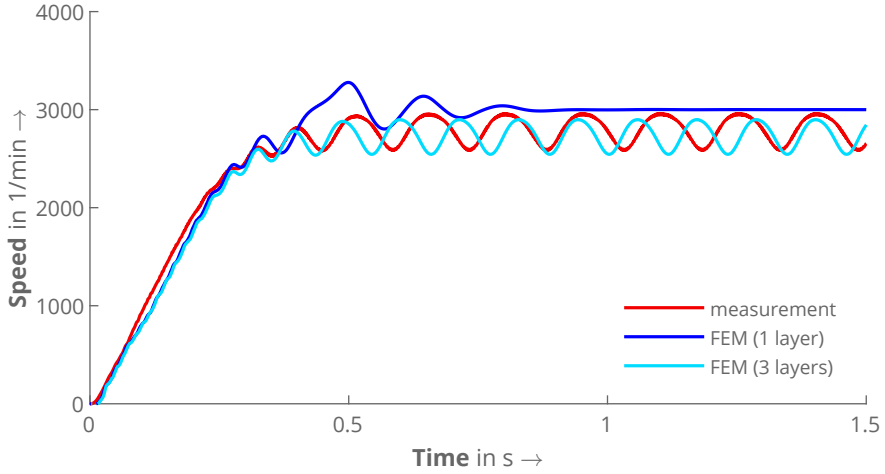

Figure 3.50: Comparison of the speed during dynamic start-up of Motor II at $U = 180\,\mathrm{V}$, $f = 50\,\mathrm{Hz}$, and $T_{\mathrm{load}} = T_{\mathrm{fric}}$ between FEM and measurement. The additional moment of inertia is $J_{\mathrm{add}} = 9.1{\cdot}10^{-4}\,\mathrm{kg{\cdot}m^2}$, so that $J_{\mathrm{tot}} = 2.0{\cdot}J_{\mathrm{mot}}$.

therefore enhancing the skin effect. Lastly, the fundamental and harmonic rotor currents influence the start-up behavior. While the fundamental torque is accelerating the motor, different harmonic torque components can also produce braking torque, depending on their field's direction of rotation. Because harmonic currents do not "see" the total ring cross-sectional area, but flow near the air gap, the effective ring resistance is higher, which can be represented by multiple rotor cage layers. This once again proves that for an accurate representation of the machine behavior, the end ring resistances are important and the rotor cage should be separated into multiple layers to achieve valid results.

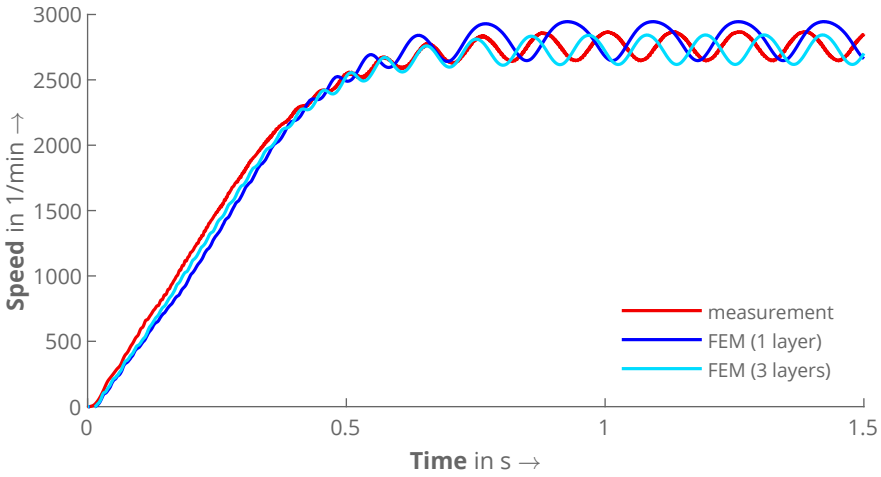

Figure 3.51: Comparison of the speed during dynamic start-up of Motor II at $U = 180\,\mathrm{V}$, $f = 50\,\mathrm{Hz}$, and $T_{\mathrm{load}} = T_{\mathrm{fric}}$ between FEM and measurement. The additional moment of inertia is $J_{\mathrm{add}} = 24.2{\cdot}10^{-4}\,\mathrm{kg{\cdot}m^2}$, so that $J_{\mathrm{tot}} = 3.3{\cdot}J_{\mathrm{mot}}$.

3.9.4.2 Motor III

Turning now to the validation of Motor III. Again, different flywheels have been added to vary the inertia. The measurement has been carried out for different voltages. As only one of the tests was able to show a successful start-up, this will be examined first.

Figure 3.52 shows the speed versus time plot at a voltage of 140 V with no additional flywheel ($J_{\mathrm{add}} = 0$). During the acceleration phase, both simulations with 1 and 3 layers fit good to the measurement and show the same behavior. Then, during synchronization, both simulations show different damping. While the oscillations for 1 layer are damped faster than the measurement, 3 layers show less damping. This leads to two conclusions: On the one hand, it can again be proven that the skin effect is still relevant for the synchronization process because both models show different damping behavior. On the other hand, the correct effective rotor resistance lies between the simulation of 1 and 3 layers, meaning that the damping is overestimated for 1 layer (rotor resistance too high or inductance too low) and underestimated for 3 layers (rotor resistance too low or inductance too high). Nevertheless, there is satisfactory agreement between simulation and measurement, as both acceleration and synchronization are correctly predicted.

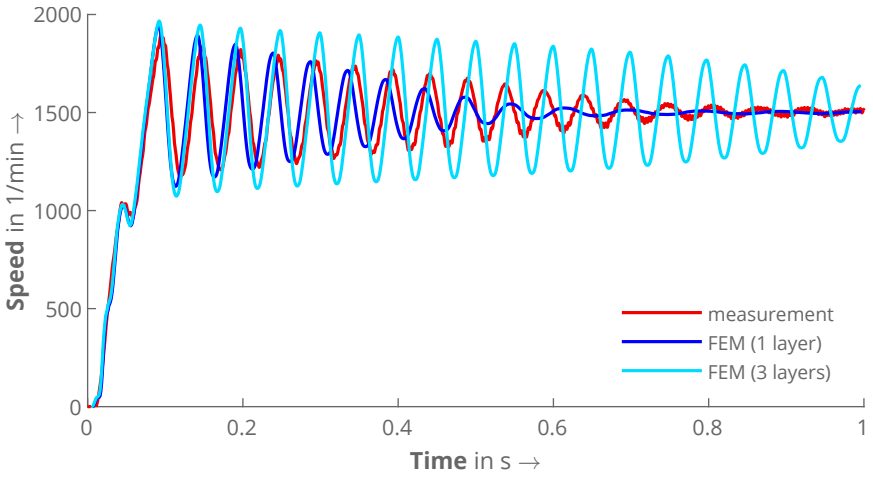

Figure 3.52: Comparison of the speed during dynamic start-up of Motor III at $U = 140\text{V}$, $f = 50\,\text{Hz}$, and $T_{\text{load}} = T_{\text{fric}}$ between FEM and measurement. The additional moment of inertia is $J_{\text{add}} = 0$, so that $J_{\text{tot}} = J_{\text{mot}}$.

As already observed for Motor II, adding flywheels causes Motor III to lose its ability to synchronize. However, for both measurements (Figures 3.53 and 3.54), the simulation results again fit good. The acceleration, as well as the resulting speed, are accurately modelled. Furthermore, the results for 3 rotor cage layers also agree better for the average speed and amplitude of the oscillations.

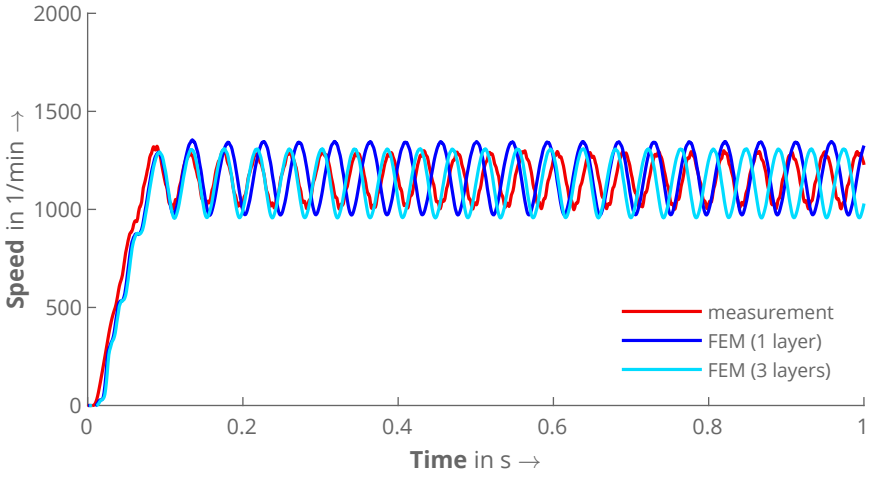

Figure 3.53: Comparison of the speed during dynamic start-up of Motor III at $U = 140\text{V}$, $f = 50\,\text{Hz}$, and $T_{\text{load}} = T_{\text{fric}}$ between FEM and measurement. The additional moment of inertia is $J_{\text{add}} = 9.1{\cdot}10^{-4}\,\text{kg}{\cdot}\text{m}^2$, so that $J_{\text{tot}} = 2.0{\cdot}J_{\text{mot}}$.

The difference in the phase angle of the oscillations in measurement and simulation can be explained by the fact that it is a time-dependent process. Even the smallest deviations can cause the two results to shift against each other. In addition, the slip frequencies are rarely the same.

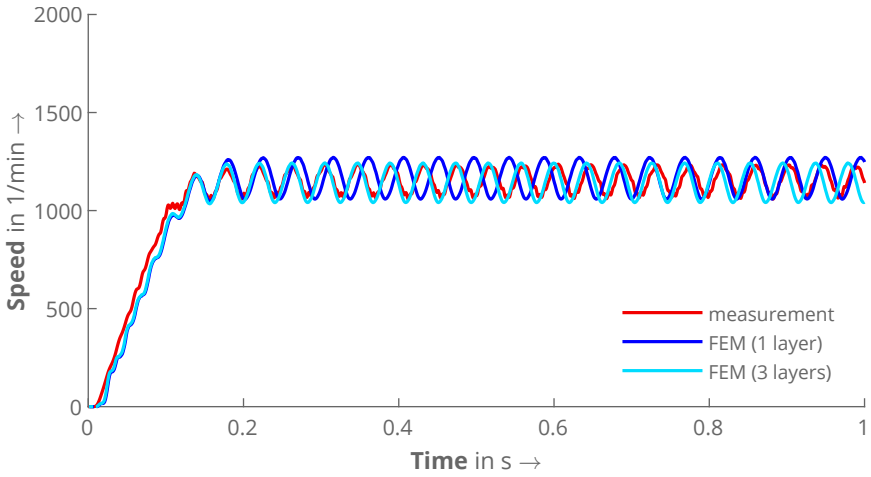

Figure 3.54: Comparison of the speed during dynamic start-up of Motor III at $U = 140\,\mathrm{V}$, $f = 50\,\mathrm{Hz}$, and $T_{\mathrm{load}} = T_{\mathrm{fric}}$ between FEM and measurement. The additional moment of inertia is $J_{\mathrm{add}} = 24.2{\cdot}10^{-4}\,\mathrm{kg{\cdot}m^2}$, so that $J_{\mathrm{tot}} = 3.3{\cdot}J_{\mathrm{mot}}$.

It can be stated therefore that the presented Finite Element model can be considered validated for the simulation of the dynamic start-up process as well. Since Motor III as well as Motor II do not synchronize for any inertia but their own, however, Motor I will be compared to FEM as well to demonstrate the procedure for load conditions.

3.9.4.3 Motor I

At first, the comparison is carried out for the case of no additional flywheel. Figure 3.55 shows that the behavior of the speed versus time corresponds well with the measurement. What is striking, is that also for this motor the model with 3 rotor cage layers shows different results than with 1 layer despite the standard rotor bar geometry. This can be explained by the non-standard ring, which has a huge cross-sectional area and therefore a large width w_{R}. Since this is much deeper than the rotor bars itself, it appears to be proven that currents flowing near the air gap will not use the whole ring area, which has been stated in Section 3.5.4 according to [81]. Hence, the torque at low speed is higher due to the increased rotor resistance.

What stands out as well is the difference in damping behavior compared to Motor II and Motor III. There is almost no overshoot, and the steady state is reached shortly after the motor accelerated to synchronous speed. The reason for this is the end ring, on the one hand, as it significantly reduces the rotor resistance compared to both other motors and therefore provides much better damping. On the other hand, the rotor cage is symmetrical, which also improves the asynchronous performance.

Looking at Figure 3.56, which compares the current for this case, a good agreement is visible as well. This applies to both the transient starting current and the steady state. The only difference can be observed between 0.2 s and 0.4 s, where the current from FEM is slightly higher. This is due to the different slip during measurement and simulation. However, the overall agreement is satisfactory.

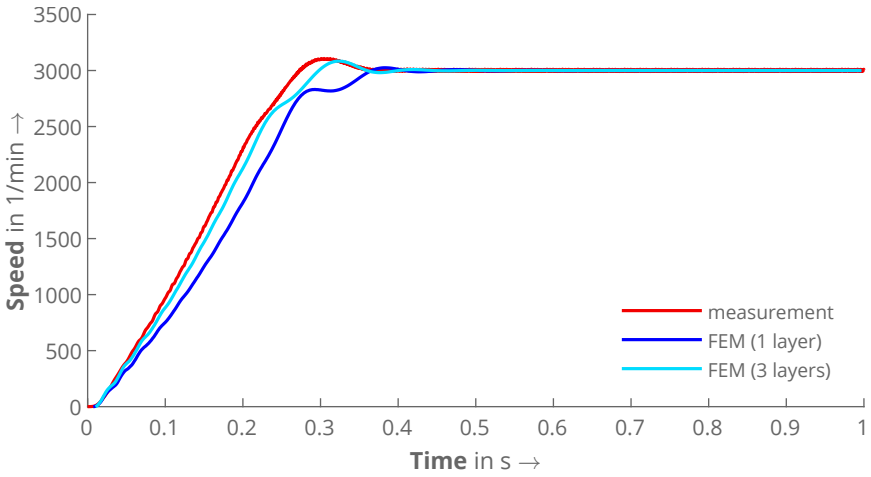

Figure 3.55: Comparison of the speed during dynamic start-up of Motor I at $U = 140\,\mathrm{V}$, $f = 50\,\mathrm{Hz}$, and $T_{\mathrm{load}} = T_{\mathrm{fric}}$ between FEM and measurement. The additional moment of inertia is $J_{\mathrm{add}} = 0$, so that $J_{\mathrm{tot}} = J_{\mathrm{mot}}$.

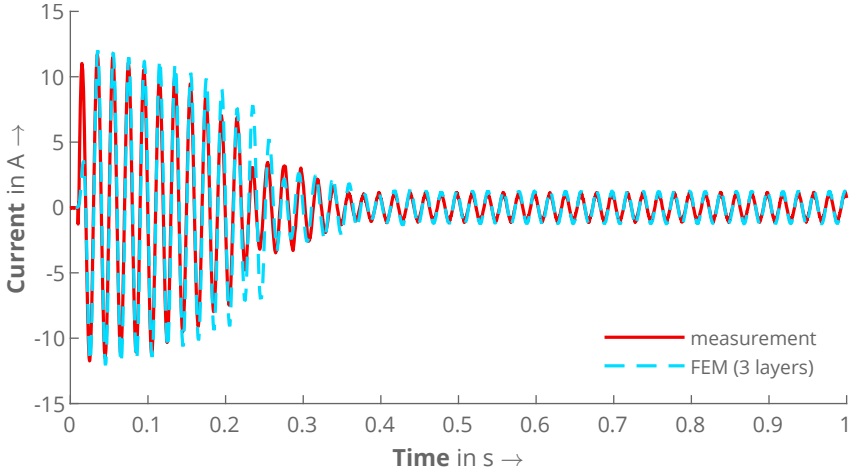

Figure 3.56: Comparison of the stator current during dynamic start-up of Motor I at $U = 140\,\mathrm{V}$, $f = 50\,\mathrm{Hz}$, and $T_{\mathrm{load}} = T_{\mathrm{fric}}$ between FEM and measurement. The additional moment of inertia is $J_{\mathrm{add}} = 0$, so that $J_{\mathrm{tot}} = J_{\mathrm{mot}}$ (corresponds to Figure 3.55).

To prove the good agreement, the comparison for a measurement with an additional flywheel is presented in Figure 3.57. Due to the lower rotor resistance compared to the other motors, the synchronization is successful despite the increased moment of inertia. Here, both simulations show slightly less acceleration, which results in a lower slope. However, as soon as the synchronization phase is reached, the behavior is the same as during the measurement.

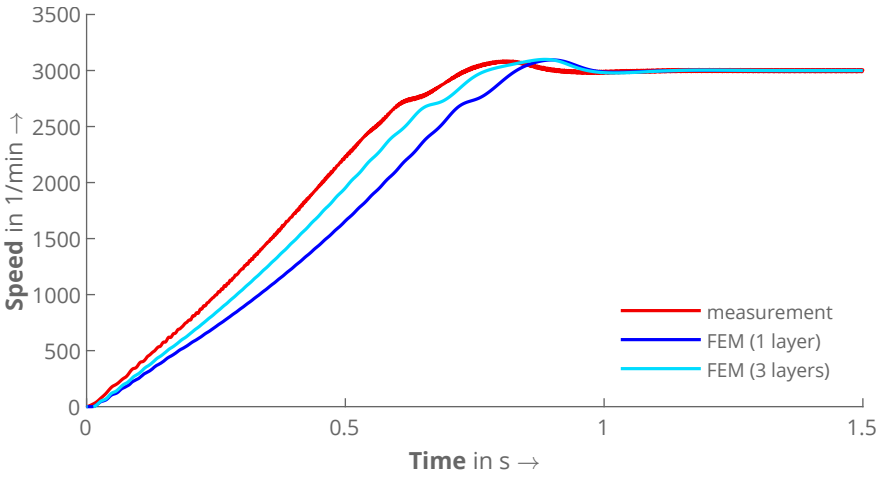

Figure 3.57: Comparison of the speed during dynamic start-up of Motor I at $U = 140\,\mathrm{V}$, $f = 50\,\mathrm{Hz}$, and $T_{\mathrm{load}} = T_{\mathrm{fric}}$ between FEM and measurement. The additional moment of inertia is $J_{\mathrm{add}} = 24.2{\cdot}10^{-4}\,\mathrm{kg{\cdot}m^2}$, so that $J_{\mathrm{tot}} = 3.4{\cdot}J_{\mathrm{mot}}$.

Finally, the finite element model is to be compared for the case of a start-up under load conditions. This means that an additional load must be added to the test setup in Figure 3.47.

The most suitable method for LSSynRM from a measurement and application perspective is to use a DC motor as a load. If the field winding is excited with a direct current and the armature is connected to a resistor, the motor acts as an eddy current brake with a linear torque-speed characteristic ($T_{\mathrm{DC}} = f(n)$). The measured characteristic curve for the chosen field current of the DC motor used is illustrated in Figure 3.58 (the same motor has been used in [55]). The linear approximation of the measured values can thus be used in the FE model to define the torque in the simulation.

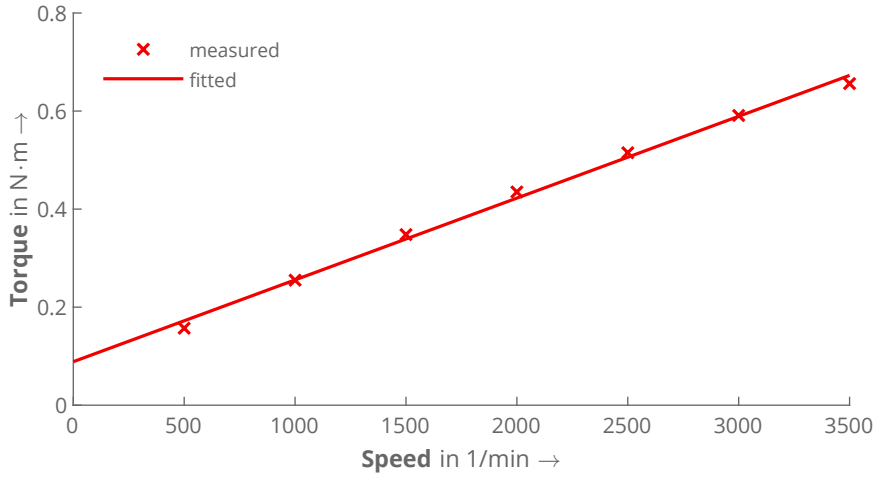

Figure 3.58: Torque versus speed characteristic $T_{\mathrm{DC}}(n)$ of the used DC load motor at a field current of $I_{\mathrm{Fd}} = 200\,\mathrm{mA}$.

If Motor I is coupled to the DC load motor, the test setup changes according to Figure 3.59. The start-up test can be performed for different combinations of load torque and moment of inertia. The former can be varied by changing the field current of the DC motor, the latter by adding additional flywheels. Two of the tests carried out are discussed below.

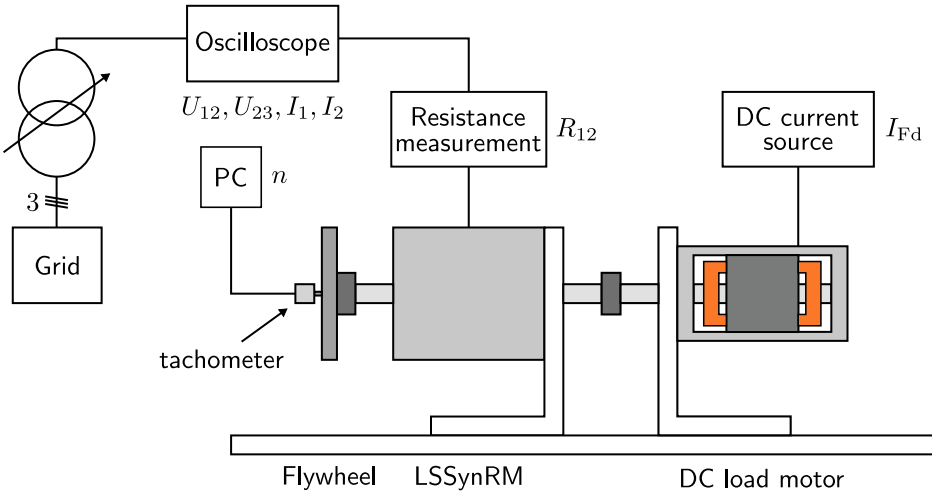

Figure 3.59: Experimental setup for start-up measurement (with load). The armature winding of the load motor is connected to a resistor. Its moment of inertia is $J_{DC} = 5.3{\cdot}10^{-4}\,\mathrm{kg{\cdot}m^2}$.

In the first test, the voltage was 100 V, at which the motor was unable to synchronize. Except for the load motor, no additional moment of inertia was added. The measured and simulated speed curve is shown in Figure 3.60. It is apparent from this figure that both FE simulations accurately predict the final slip of the motor that does not synchronize. However, the model with three rotor cage layers is far more accurate concerning the acceleration during start-up.

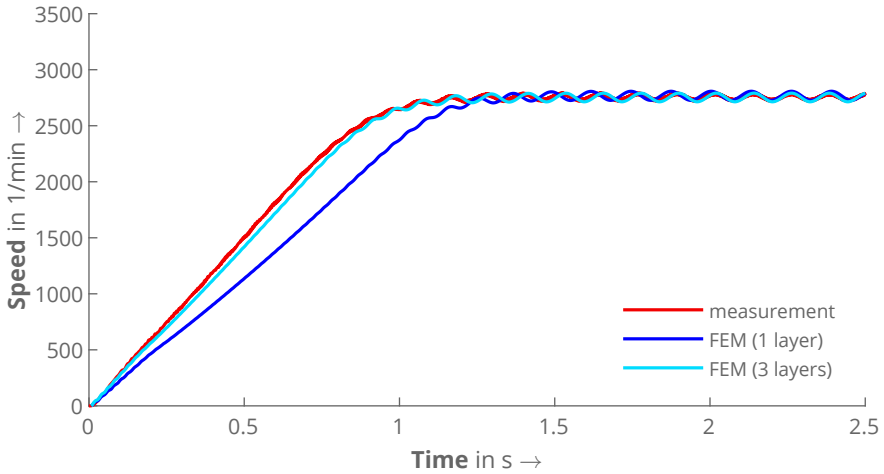

Figure 3.60: Comparison of the speed during dynamic start-up of Motor I at $U = 100\,\mathrm{V}$, $f = 50\,\mathrm{Hz}$, and $T_{load} = T_{DC} + T_{fric}$ between FEM and measurement. The additional moment of inertia is $J_{add} = J_{DC}$, so that $J_{tot} = 1.7{\cdot}J_{mot}$.

This is also obvious when looking at the results of the measurement with an increased voltage of 140 V in Figure 3.61. Both simulations indicate that the motor can synchronize. The three-layer model predicts almost the same shape as the measurement. Only the synchronization phase differs slightly, which is probably due to the initial voltage angle during the measurement.

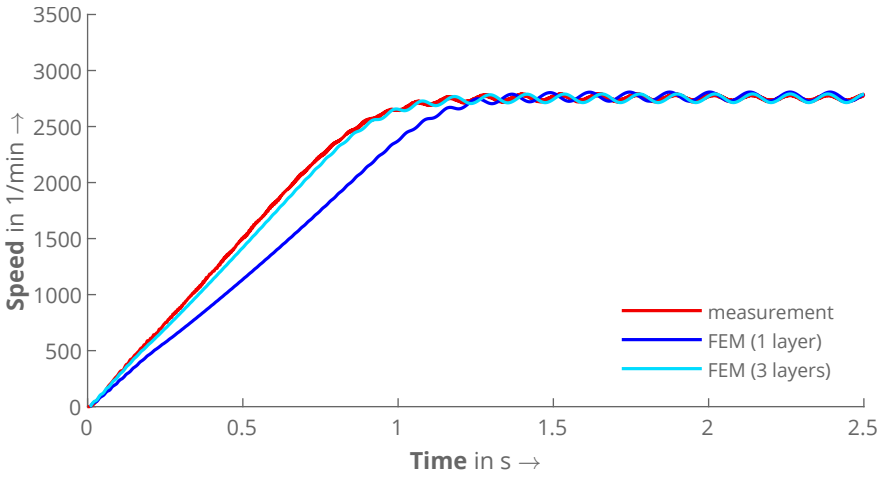

Figure 3.61: Comparison of the speed during dynamic start-up of Motor I at $U = 140\,\mathrm{V}$, $f = 50\,\mathrm{Hz}$, and $T_{\mathrm{load}} = T_{\mathrm{DC}} + T_{\mathrm{fric}}$ between FEM and measurement. The additional moment of inertia is $J_{\mathrm{add}} = J_{\mathrm{DC}}$, so that $J_{\mathrm{tot}} = 1.7{\cdot}J_{\mathrm{mot}}$.

In conclusion, the proposed Finite Element model was able to predict the start-ups of all three motors with good accuracy. As the final tests with Motor I showed, it is also possible to accurately simulate the start-up with load. This can also be expected for Line-Start Synchronous Reluctance Machines with modern rotor cage geometries (such as Motor II and Motor III).

3.10 Conclusion

This chapter presented a two-dimensional Finite Element model for Line-Start Synchronous Reluctance Machines, which accurately takes the end ring into account. The purpose was to develop a precise model which is able to accurately simulate the start-up behavior from zero to synchronous speed. Various adjustments were made to speed up the slow simulation method as much as possible without affecting the accuracy.

The modelling of the electromagnetic circuit in the 2D domain and the consideration of stator and rotor end windings were discussed. For the non-standard rotor cage geometries of modern LSSynRM, a 3D FEM-assisted method to feed the standard Induction Machine equivalent circuit was proposed.

By carrying out an experimental validation, it was proven that the Finite Element model can accurately predict the machine behavior for different modes of operation without the necessity of measurements to estimate machine parameters. The results also indicated that the skin effect in the rotor cage has a large influence on the start-up process, not only for high slips, and has to be taken into account for the end rings as well. One of the strengths of this model is that it covers any type of LSSynRM rotor cage, no matter the complexity. Hence, it is now possible to rely on this FE reference model in the design phase and minimize the need for measurements when investigating applications of a particular LSSynRM or validating other models.

Because the computing time for a start-up simulation with FEM is quite high, however, the chapter that follows moves on to reduce the overall computing time by introducing a less complex numerical parameter model which only focuses on important global effects. The computing times of both models are compared at the end of the next chapter.

Chapter 4

Finite Element-Based Parameter Model

4.1 Introduction

The previous chapter showed that the Finite Element Method can provide good accuracy to act as a reference. However, the requirements defined in Chapter 2 concerning a fast simulation model to investigate numerous start-ups are still not met. The FEM is not suitable for carrying out hundreds of time-step simulations with a reasonable computing time. Hence, this chapter introduces a numerical parameter model. By taking advantage of the precision of 2D magnetostatic FE simulations for the calculation of parameters and reducing the model to analytical equations, the results are generated much faster.

The presented model is based on the one introduced by Güdelhöfer in [54] and [55], which from now on is referred to as "existing model". First, this chapter describes the adaption of the underlying system of equations to obtain a more comprehensive and a more accurate model that meets the requirements of modern Line-Start Synchronous Reluctance Machines. The phase domain model will be slightly adapted so that the flux linkage instead of the current is the state variable. This simplifies the solution and improves the comprehension of the model.

Secondly, the consideration of the two most important effects, skin effect and saturation, is improved. While the skin effect needs an entirely new approach to account for modern LSSynRMs with conductors in flux barriers, the saturation will still be considered for by the saturation factor method. However, it is demonstrated that a dq-saturation factor model with an individual factor for each axis is superior to the existing one-factor model.

Lastly, the model is validated with FEM regarding the investigated effects, before the comparison to measurements is carried out. The chapter will close with a comparison of the computing times and a conclusion.

4.2 Electromagnetic machine model

An electric machine can be described as a system of multiple electrically and magnetically coupled coils. Each coil of the system is represented by its voltage equation

$$u = Ri + \frac{\mathrm{d}}{\mathrm{d}t}\psi, \tag{4.1}$$

where u is the voltage at the coil's terminals, R the electric resistance of the winding, i is the current and ψ the total flux linkage of the coil. The derivation of the equation is explained for the simplified case of a single coil in Appendix B to clarify the relations of the physical quantities and the definition of specific terms.

In the following, the derivation of the system of equations for a Line-Start Synchronous Reluctance Machine with a three-phase stator winding and a rotor cage is presented. Nevertheless, the model works for any type of LSSynRM as well as for Induction Machines.

4.2.1 Stator voltage equations

In LSSynRMs with $m = 3$ stator phases there are 3 equations in the form from Eq. (4.1) which can therefore be expressed in matrix form as

$$\vec{u}_\mathrm{s} = \mathbf{R}_\mathrm{s}\vec{i}_\mathrm{s} + \frac{\mathrm{d}}{\mathrm{d}t}\vec{\psi}_\mathrm{s}, \tag{4.2}$$

where the index s denotes stator quantities. The stator voltage and current vectors

$$\vec{u}_\mathrm{s} = \begin{pmatrix} u_1 \\ u_2 \\ u_3 \end{pmatrix}, \qquad \vec{i}_\mathrm{s} = \begin{pmatrix} i_1 \\ i_2 \\ i_3 \end{pmatrix} \tag{4.3}$$

contain all phase voltages and currents. For line-start machines that are connected directly to the grid, the voltage vector is known, whereas the current vector is unknown. The resistance matrix is a diagonal matrix, containing the phase resistances:

$$\mathbf{R}_\mathrm{s} = \begin{pmatrix} R_\mathrm{ph,1} & 0 & 0 \\ 0 & R_\mathrm{ph,2} & 0 \\ 0 & 0 & R_\mathrm{ph,3} \end{pmatrix}. \tag{4.4}$$

The flux linkage of the k-th phase in the flux linkage vector $\vec{\psi}_\mathrm{s}$ is the sum of flux linkages produced by all m stator phases and $2N_\mathrm{FB}$ rotor coils:

$$\psi_\mathrm{k} = \sum_{k'=1}^{m} \psi_{\mathrm{k,k'}} + \sum_{i'=1}^{2N_\mathrm{FB}} \psi_{\mathrm{k,i'}}, \tag{4.5}$$

where N_FB is the total number of flux barriers in the rotor, each of which is divided into two rotor bars (see Figure 3.12).

At this point, it may already be noted that the model is derived for the abc system (phase-domain model). The advantages are explained in detail in [90]. The existing model was also able to demonstrate that the approach is superior for the goal of achieving the most accurate model possible.

4.2.2 Rotor voltage equations

For the rotor, denoted by index r, the general system of equations looks the same:

$$\vec{u}_\mathrm{r} = \mathbf{R}_\mathrm{r}\vec{i}_\mathrm{r} + \frac{\mathrm{d}}{\mathrm{d}t}\vec{\psi}_\mathrm{r} \tag{4.6}$$

In the case of a rotor cage, as dealt with in this work, however, the first difference is that there are no external voltages. Hence, all elements of the rotor voltage vector are zero:

$$\vec{u}_\mathrm{r} = \vec{0}, \tag{4.7}$$

which yields

$$\vec{0} = \mathbf{R}_\mathrm{r}\vec{i}_\mathrm{r} + \frac{\mathrm{d}}{\mathrm{d}t}\vec{\psi}_\mathrm{r} \tag{4.8}$$

As for the stator, the rotor flux linkages contain the self-flux linkage and all mutual flux linkages:

$$\psi_\mathrm{i} = \sum_{k'=1}^{m} \psi_{\mathrm{i,k'}} + \sum_{i'=1}^{2N_\mathrm{FB}} \psi_{\mathrm{i,i'}}. \tag{4.9}$$

Moreover, the resistance matrix $\mathbf{R}_\mathrm{r}$ is structured differently than for the stator. In the rotor equipped with a cage, each coil consists of two adjacent bars connected by the respective end ring segments on both sides. In addition, neighboring coils i and $i+1$ share the same rotor bar. Therefore, rotor cages are usually described using network analysis [77], [91]. This is illustrated in Figure 4.1, which shows the equivalent circuit typically used for machines equipped with a rotor cage.

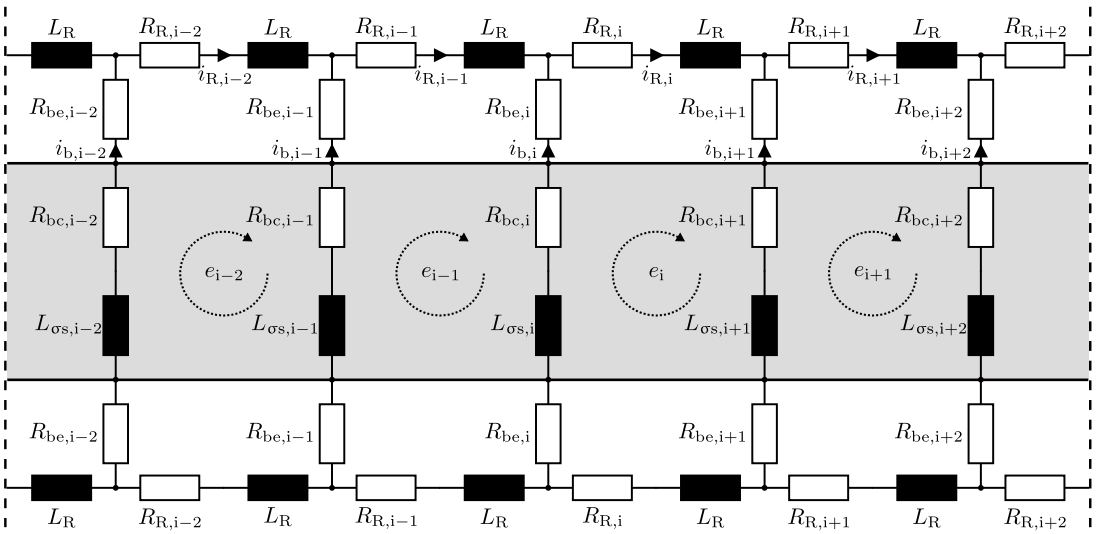

Figure 4.1: Rotor equivalent circuit adopted from the rotor circuit of the Finite Element model in Figure 3.10. The rotor core (gray) is now modelled as a system of coupled coils, each defined by an EMF and discrete bar resistances and inductances. The ring equivalent circuit is the same.

Following the rules of mesh analysis, the diagonal elements $R_\mathrm{i,i}$ of the rotor resistance matrix are now the sum of all resistances of the respective loop, which yields

$$R_\mathrm{i,i} = 2R_\mathrm{R,i} + R_\mathrm{b,i} + R_\mathrm{b,i+1} \tag{4.10}$$

for the i-th loop for example. It is to mention that the rotor bar resistance $R_{\mathrm{b,i}}$ represents the sum of the rotor bar embedded in the iron core $R_{\mathrm{bc,i}}$ as well as both bar end resistances $R_{\mathrm{be,i}}$ (3.14):

$$R_{\mathrm{b,i}} = R_{\mathrm{bc,i}} + 2R_{\mathrm{be,i}}. \tag{4.11}$$

The end ring resistance $R_{\mathrm{R,i}}$ also follows from the improved ring model (Section 3.5.2).

The non-diagonal elements of the matrix contain the negative value of resistances connecting two loops, which in this case is the respective connecting bar resistance:

$$R_{\mathrm{i,i+1}} = R_{\mathrm{i+1,i}} = -R_{\mathrm{b,i+1}}. \tag{4.12}$$

Together with the EMF e_{i}, this leads to the following voltage equation for the i-th rotor loop:

$$0 = 2R_{\mathrm{R,i}}i_{\mathrm{R,i}} + R_{\mathrm{b,i}}\left(i_{\mathrm{R,i}} - i_{\mathrm{R,i-1}}\right) + R_{\mathrm{b,i+1}}\left(i_{\mathrm{R,i+1}} - i_{\mathrm{R,i}}\right) + \frac{\mathrm{d}}{\mathrm{d}t}\sum_{k'=1}^{m}\psi_{\mathrm{i,k'}} + \frac{\mathrm{d}}{\mathrm{d}t}\sum_{i'=1}^{2N_{\mathrm{FB}}}\psi_{\mathrm{i,i'}}. \tag{4.13}$$

As shown in [54], [55], it is also possible to account for inter bar currents and skewing by defining multiple layers in axial direction. Both effects will not be discussed in this thesis because the discussed motors are not skewed. The derivation of the underlying equations therefore is finished.

4.2.3 Full system of voltage equations for linear materials without skin effect

Combining the stator and rotor sets of equations yields

$$\begin{pmatrix}\vec{u}_{\mathrm{s}}\\ \vec{0}\end{pmatrix} = \begin{pmatrix}\mathbf{R}_{\mathrm{s}} & \mathbf{0}\\ \mathbf{0} & \mathbf{R}_{\mathrm{r}}\end{pmatrix}\begin{pmatrix}\vec{i}_{\mathrm{s}}\\ \vec{i}_{\mathrm{r}}\end{pmatrix} + \frac{\mathrm{d}}{\mathrm{d}t}\begin{pmatrix}\vec{\psi}_{\mathrm{s}}\\ \vec{\psi}_{\mathrm{r}}\end{pmatrix}. \tag{4.14}$$

It is obvious that both the current vectors and the flux linkage vectors are unknowns. It must therefore be decided which variable is to be retained as the state variable, and a function must be found to replace the other variable.

In the first step, linear material properties are assumed, that is, saturation is neglected. The current I is therefore related to the flux linkage Ψ by the constant inductance L with

$$\Psi = LI. \tag{4.15}$$

Since for the model multiple coils are coupled, however, the flux linkage of the k-th coil consists of the self-flux linkage excited by the current i_{k} and the mutual flux linkages produced by all other coils of the stator and rotor depending on their respective currents:

$$\psi_{\mathrm{k}} = \sum_{k'=1}^{m} L_{\mathrm{s,s,k,k'}}i_{\mathrm{k'}} + \sum_{i'=1}^{2N_{\mathrm{FB}}} L_{\mathrm{s,r,k,i'}}i_{\mathrm{i'}}. \tag{4.16}$$

Here, $L_{\mathrm{s,s,k,k'}}$ is an element of the stator inductance matrix $\mathbf{L}_{\mathrm{s,s}}$. It corresponds to the k-th stator phase and is excited by the k'-th stator phase. $L_{\mathrm{s,r,k,i'}}$, on the other hand, is the mutual inductance from the i'-th rotor coil. It is an element of the matrix $\mathbf{L}_{\mathrm{s,r}}$. Hence, $i_{\mathrm{k'}}$

and $i_{\mathrm{i}'}$ are the currents of the k'-th stator and i'-th rotor coil, respectively. Similarly, the rotor flux linkages are defined as

$$\psi_{\mathrm{i}} = \sum_{k'=1}^{m} L_{\mathrm{r,s,i,k'}} i_{\mathrm{k'}} + \sum_{i'=1}^{2N_{\mathrm{FB}}} L_{\mathrm{r,r,i,i'}} i_{\mathrm{i'}}. \tag{4.17}$$

Consequently, the full inductance matrix now describes the relationship between the current vector and the flux linkage vector:

$$\vec{\psi} = \mathbf{L}\vec{i} = \begin{pmatrix} \vec{\psi}_{\mathrm{s}} \\ \vec{\psi}_{\mathrm{r}} \end{pmatrix} = \begin{pmatrix} \mathbf{L}_{\mathrm{s,s}} & \mathbf{L}_{\mathrm{s,r}} \\ \mathbf{L}_{\mathrm{r,s}} & \mathbf{L}_{\mathrm{r,r}} \end{pmatrix} \begin{pmatrix} \vec{i}_{\mathrm{s}} \\ \vec{i}_{\mathrm{r}} \end{pmatrix}. \tag{4.18}$$

Writing the flux linkage equation for every single coil leads to a system of $m + 2N_{\mathrm{FB}}$ equations.

Equation (4.18) acts as the current-flux linkage function, which means for every set of stator and rotor currents, the respective flux linkages can be obtained. Furthermore, it is to mention that in a Line-Start Synchronous Reluctance Machine, the inductance matrix $\mathbf{L}$ is a function of the rotor angle ϑ_{r} due to the rotor's anisotropy. This topic will be further explained in a later section.

In the simplified, linear case, the function can then be inverted, therefore yielding a current function for a set of given flux linkages:

$$\begin{pmatrix} \vec{i}_{\mathrm{s}} \\ \vec{i}_{\mathrm{r}} \end{pmatrix} = \begin{pmatrix} \mathbf{L}_{\mathrm{s,s}} & \mathbf{L}_{\mathrm{s,r}} \\ \mathbf{L}_{\mathrm{r,s}} & \mathbf{L}_{\mathrm{r,r}} \end{pmatrix}^{-1} \begin{pmatrix} \vec{\psi}_{\mathrm{s}} \\ \vec{\psi}_{\mathrm{r}} \end{pmatrix}. \tag{4.19}$$

This means that it is possible to freely decide which variable to use as a state variable. In the past, both approaches have been successfully applied. In the existing model, for example, the current was used as a state variable.

However, due to the differentiation of the flux linkage, this yields two terms for the product of $\mathbf{L}\vec{i}$. Especially the differentiation of the inductance matrix will lead to an unnecessary computational effort, which is also error-prone. Furthermore, as discussed in detail in [90], [92], the differentiation of non-linear inductances requires the separation into apparent and differential inductances. Even the approach of saturation factors to account for saturation, which has already been used in the existing model, results in an additional term. Therefore, more matrix operations are needed in any case. For a fast model, however, the least computational effort possible is desired.

In conclusion, as has already been demonstrated in multiple publications of the author [A2]–[A4], the flux linkage is the much better alternative to be used as a state variable. Hence, the current in Equation (4.14) is replaced by Equation (4.19), which yields:

$$\begin{pmatrix} \vec{u}_{\mathrm{s}} \\ \vec{0} \end{pmatrix} = \begin{pmatrix} \mathbf{R}_{\mathrm{s}} & \mathbf{0} \\ \mathbf{0} & \mathbf{R}_{\mathrm{r}} \end{pmatrix} \begin{pmatrix} \mathbf{L}_{\mathrm{s,s}} & \mathbf{L}_{\mathrm{s,r}} \\ \mathbf{L}_{\mathrm{r,s}} & \mathbf{L}_{\mathrm{r,r}} \end{pmatrix}^{-1} \begin{pmatrix} \vec{\psi}_{\mathrm{s}} \\ \vec{\psi}_{\mathrm{r}} \end{pmatrix} + \frac{\mathrm{d}}{\mathrm{d}t} \begin{pmatrix} \vec{\psi}_{\mathrm{s}} \\ \vec{\psi}_{\mathrm{r}} \end{pmatrix}. \tag{4.20}$$

Thus far, it was shown how to derive the basic system of equations. As discussed in Chapter 3, skin effect and saturation are key effects that must be considered for correct results. In contrast to the application of the Finite Element Method, the development of a faster model requires a much more profound understanding of both effects. This is the only way to find methods that reduce the required computing time through simplifications while maintaining sufficient accuracy. Therefore, the next two sections explain both effects in more detail before proposing a method to take each into account in the model.

4.2.4 Consideration of the skin effect

The first effect to focus on is the skin effect. When an alternating electromagnetic field enters an electrically conductive material, an electromotive force is induced, which causes eddy currents to flow. These eddy currents produce losses that are covered by the originating field. This results in a damping effect, as the field becomes weaker the further it penetrates into the conductor. Hence, more current will flow near the surface of the conductor than on the inside. If the frequency is increased, the eddy current losses also increase, which means that the damping effect is higher and the current is concentrated on an even smaller area near the conductor surface.

In electric machines the skin effect generally applies to all parts that are electrically conductive, that is, copper and aluminum windings as well as the iron cores of stator and rotor. The latter, however, are typically made of thin laminations that are electrically insulated from one another. This avoids eddy currents to flow as much as possible and reduces the overall losses of the machine.

Regarding the stator winding, it is to mention that series-produced Induction Machines for industrial applications are typically equipped with a distributed multi-turn winding of copper or aluminum wires. Hence, the cross-sectional area of the individual conductors in combination with the low frequency (in this case 50 Hz) shows no distinct skin effect.

When it comes to the rotor cage, in which the conductors are relatively large and surrounded by iron, however, the skin effect is of particular importance. When the rotor is at standstill ($s = 1$) and the voltage is switched on, the magnetic field of the stator rotates relative to the rotor. Consequently, voltages of the frequency

$$f_\mathrm{r} = s f_\mathrm{s} \tag{4.21}$$

are induced in the rotor cage, where f_s and f_r are the stator and rotor frequency, respectively.

As mentioned earlier, especially the bars of modern LSSynRM rotor cages are very deep, which hence causes a pronounced skin effect. The field penetrating from the air gap mostly drives currents near the conductor surface, as illustrated in Figure 4.2 for Motor II and Motor III.

It is obvious that the current density distribution is not uniform anymore. Therefore, the effective resistances of the rotor bars increase compared to the case of evenly distributed direct currents. From basic Induction Machine theory, it is known that a higher rotor resistance will lead to higher starting torque, which depending on the machine can change the start-up behavior.

When accelerating to synchronous speed, the frequency decreases, so the skin effect becomes less effective. Near synchronous speed, the rotor frequency f_r is very low, which is why the fundamental field can enter deeper into the rotor bars. Nonetheless, as proven in Chapter 3, the skin effect also affects the behavior near synchronous speed for non-standard rotor cages. Moreover, the air gap field also contains harmonic components, for which the skin effect is still active as well.

Thus, due to this behavior over the full speed range, it would not be sufficient to use a fixed resistance for the rotor bar. Especially at low speeds, where the skin effect is most pronounced, the rotor currents and therefore the asynchronous torque would be modelled incorrectly. This is why an approach has to be found which considers for the skin effect in the rotor bars as accurate as possible.

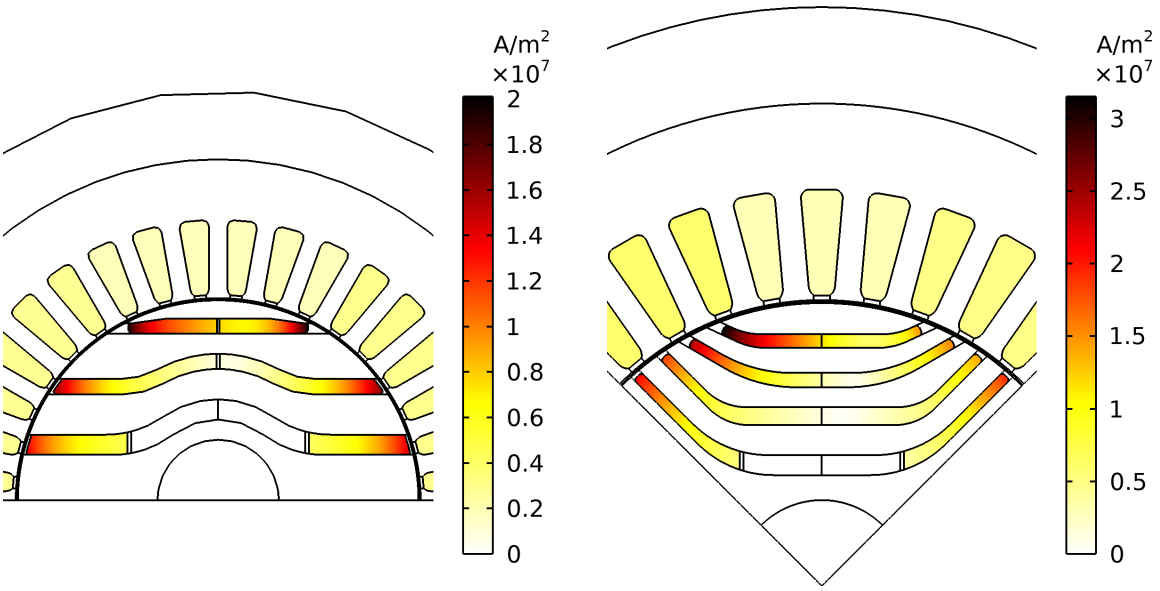

(a) Motor II (b) Motor III

Figure 4.2: Magnitude of the current density for Motor II and Motor III at standstill from time-harmonic 2D FEM.

Traditionally, the consideration of the skin effect in line-start machine models has been dominated by simplified approaches. In particular, the use of skin effect factors, which adjust the rotor bar resistance and inductance depending on the rotor fundamental frequency, is very common [61]. This approach has been successfully applied for LSSynRM with standard Induction Machine cages in the existing model as well.

Yet, in contrast to standard Induction Machine rotor cage geometries, the non-standard geometries discussed in this thesis make it impossible to apply the same method. Instead of being placed in identical slots surrounded by iron with a slot opening at the air gap, the rotor bars are now more complex.

On the one hand, there are several differently shaped rotor bars, as they are placed in the different flux barriers. On the other hand, the flux barriers and thus the conductors placed in them are continuously connected from one side of the pole to the other. This means that the field can penetrate the same conductor from two sides. This can be seen particularly well in Figure 4.2b in the outer three flux barriers of Motor III.

Another limitation is that the factors provide an effective resistance adapted to the fundamental frequency. In Chapter 3, however, it was found that harmonics play a major role in the start-up process as well. Thus, skin effect factors are ruled out as a suitable method.

Another approach that has been proven useful is the multi-layer method [75], [83], [84], which has already been used in the Finite Element model (Section 3.5.4). By dividing each rotor bar into multiple layers and defining self- and mutual inductances for each layer, the influence of the skin effect on the current distribution in the conductors can be approximated. This can be illustrated briefly by taking the example of the current density distribution previously shown in Figure 4.2. It can be observed that the current density changes rapidly in the conductive region near the air gap, whereas it can be considered homogenous for wider areas deeper in the rotor bars. More precise, it is known from electromagnetic field theory that the variation of the current density with increasing distance to the conductor surface can be described with an exponential function [85].

Since all of this has to be considered, it is recommended to choose a logarithmic approach to determine the height of the individual rotor bar layers to account for skin effect in the proposed model. This means that there should be more, smaller layers near the air gap, as this is where the current density changes most, and where also the high-frequency components of the air gap field induce EMFs. Consequently, there are less, bigger layers in the middle of the flux barrier, where the current density is more homogenous. This can be illustrated using again the example of a Finite Element simulation.

Figure 4.3 compares the current density distribution from a 2D time-harmonic FE simulation with the approximated current density distribution when the cage is divided into multiple layers. It corresponds to the simulation from Figure 4.2b, and the same color scale was used. From the first image (Figure 4.3a) it becomes clear that the result for N_L=1 is far from the real current density distribution. Assuming a mean value for the whole rotor bar does not reflect the fact that the currents will mostly flow near the air gap. While the simulation with N_L=2 gives an idea about this fact, it still seems oversimplified.

For the model with N_L=3 layers already, a good agreement can be observed (Figure 4.3c). When further improving the number of layers, as indicated by N_L=4 in Figure 4.3d, the distribution gets closer to the real one. In theory, the skin effect is correctly modelled for an infinite number of layers.

In practice, it is only relevant to represent the Joule losses P_cage as accurately as possible. They generate torque in asynchronous operation and are therefore an important criterion. As indicated in Figure 4.3, the evaluated losses are already close to the result from the real current density distribution with N_L=2 layers. However, this result could not be achieved in every test with other motors, which is why N_L=3 is generally recommended. Depending on the geometry and frequency, however, N_L=2 may also be sufficient.

Moreover, it is to mention that the layers are considered electrically insulated from one another. In the model, this follows from the current density in the 2D model exclusively flowing in axial direction. Hence, the result are N_L separate rotor cages [84]. In this thesis, every rotor bar is divided into the same number of layers.

Moving on now to the implementation of the layer method in the presented model, of which the system of equations is given in Equation (4.14). The following adjustments are made: The number of rotor voltage equations $2N_\mathrm{FB}$ multiplies by the number of rotor cage layers N_L. This can be understood in such a way that the equivalent circuit diagram from Figure 4.1 is now introduced for each cage layer. Hence, the flux linkages of each loop not only contain its self-flux linkage, the mutual flux linkage of the stator and the mutual flux linkages of the other loops of the respective layer, but also those of each loop of each other layer.

This obviously comes with the disadvantage of an increased computing time for the parameters, as well as the solution of the system of equations in each time step. However, regarding the benefits of the method when it comes to considering also harmonic frequencies on the one hand, and the necessity of considering the skin effect in the end-rings of the cage (see Section 3.5.4) on the other hand, the tradeoff is reasonable. In previous work [A2], the validity and the benefits of the method could already be proven. The parameter calculation for the inductances of each rotor loop of each layer and the validation will be part of later sections.

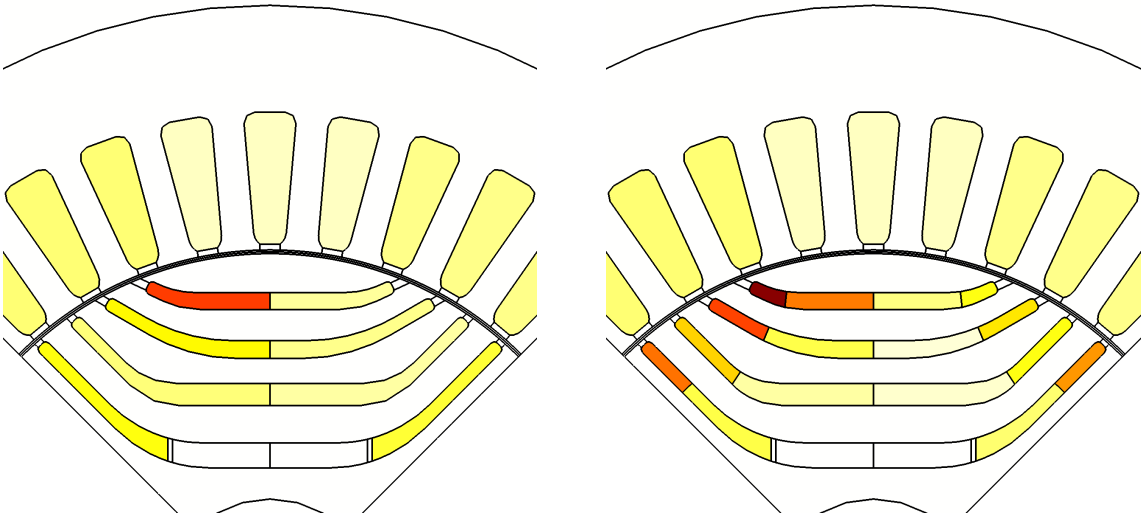

(a) N_L=1, P_cage = 227 W

(b) N_L=2, P_cage = 263 W

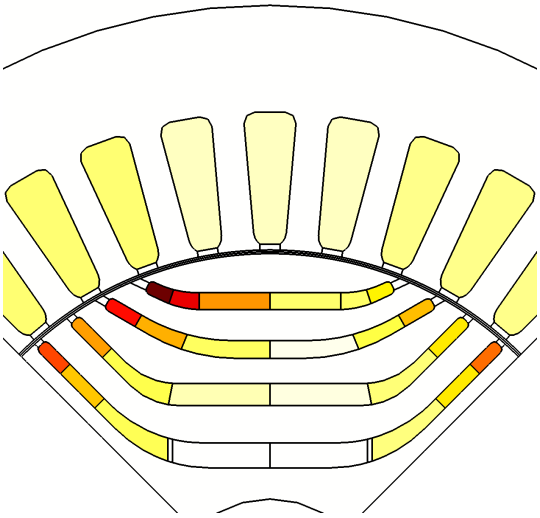

(c) N_L=3, P_cage = 267 W

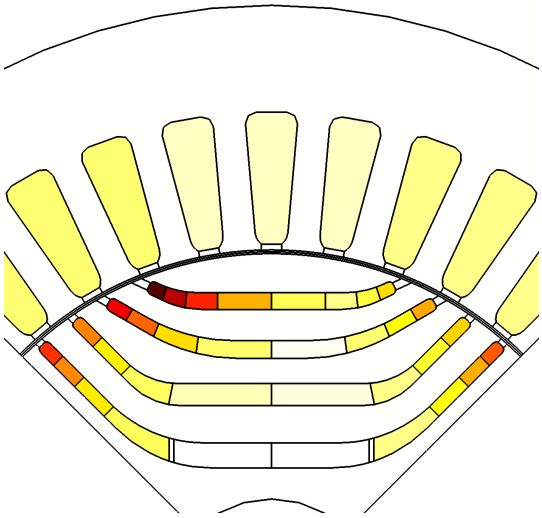

(d) N_L=4, P_cage = 269 W

Figure 4.3: Magnitude of the current density for Motor III at standstill from time-harmonic 2D FEM (corresponds to Figure 4.2b). The rotor cage is modelled with different numbers of rotor cage layers N_L of homogeneously distributed current densities to approximate the real current density distribution. The scaling of the color map is the same as in the original figure. The resulting rotor cage losses P_cage are given. The value evaluated from the original time-harmonic FE simulation is 270 W.

4.2.5 Consideration of saturation

As indicated previously, a function needs to be defined that describes the relation between the flux linkage and the current. In contrast to the simplified approach of a constant inductance L in Section 4.2.3, which implies a linear relationship between both quantities, it must now be clarified, that it is, of course, non-linear in reality. This is caused by the iron core of the stator and rotor saturating at a certain point, which means that the flux linkage of a coil no longer increases proportionally to the impressed current. Hence, what follows is a brief overview of the most important saturation effects in Line-Start Synchronous Reluctance Machines, before a simplified approach to take them into account is introduced.

4.2.5.1 Main flux saturation

Starting with the main flux saturation, first fully isotropic machines are assumed as a simplified example. Furthermore, the rotor is currentless and only the fundamental of the stator current system is considered. If the material in a 2D magnetostatic Finite Element model is now implemented with a real $B(H)$-curve given by the manufacturer (see Figure 3.6), the magnetic permeability μ is a function of the flux density B in each element. Hence, the result is a saturated flux linkage-current function as shown in Figure 4.4 (solid line). If the permeability is set to an infinitely high value instead, a linear function is obtained (dashed line) whose slope is determined only by the air gap in the magnetic circuit.

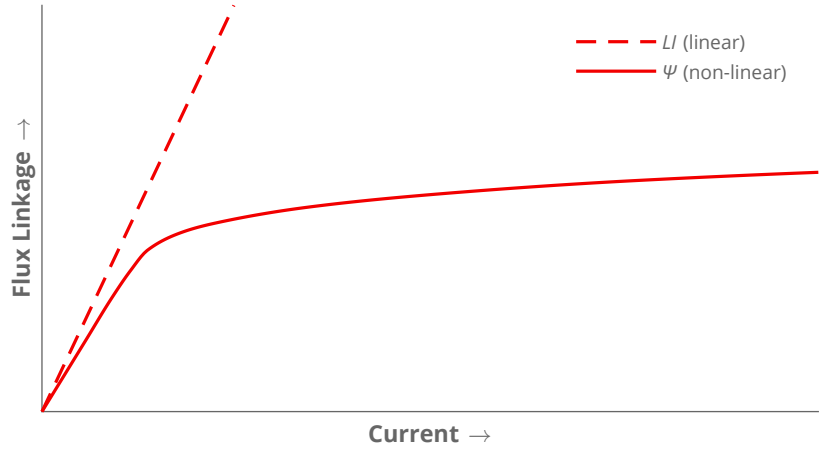

Figure 4.4: Non-linear relation of stator flux linkage and current in an isotropic electric machine compared to the linear current-flux linkage function.

Moreover, the particular feature of reluctance machines is the anisotropic magnetic circuit. This means that the flux linkage function depends on the current and also on the rotor angle [35]. Since the anisotropy of the rotor is caused by the geometry, this is already true for the linear case. Therefore, the inductance matrix $\mathbf{L}$ depends on the rotor angle as well. Figure 4.5a presents the resulting flux linkage for the linear case. For this purpose, a current space vector was impressed in the stator winding of Motor II and the magnitude of the resulting stator flux linkage space vector was evaluated.

It can be seen from the plot that the slope of the linear function is the highest for a current angle of $0°_{\text{el}}$ and $180°_{\text{el}}$. In both cases, the stator current space vector is aligned with the d-axis of the rotor, which has the highest permeance as it consists only of iron

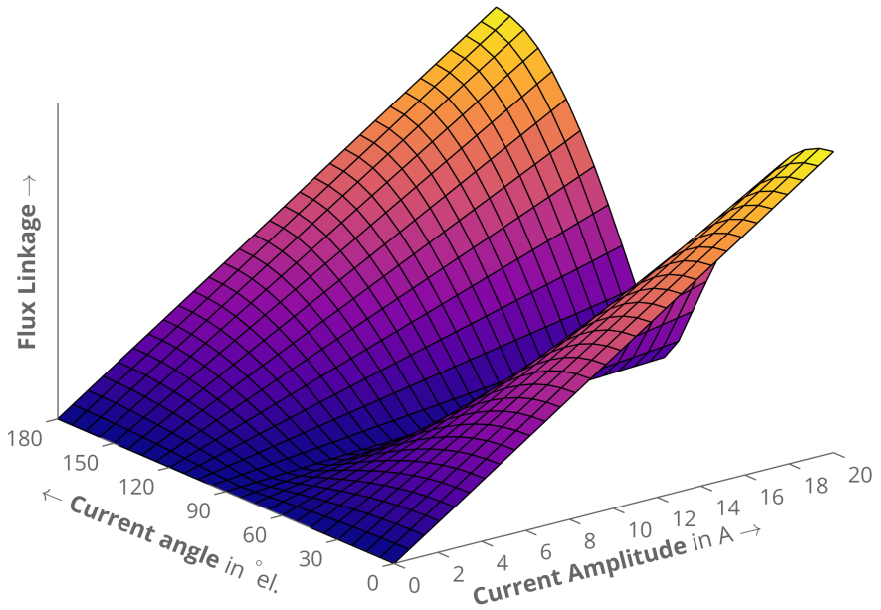

(a) linear

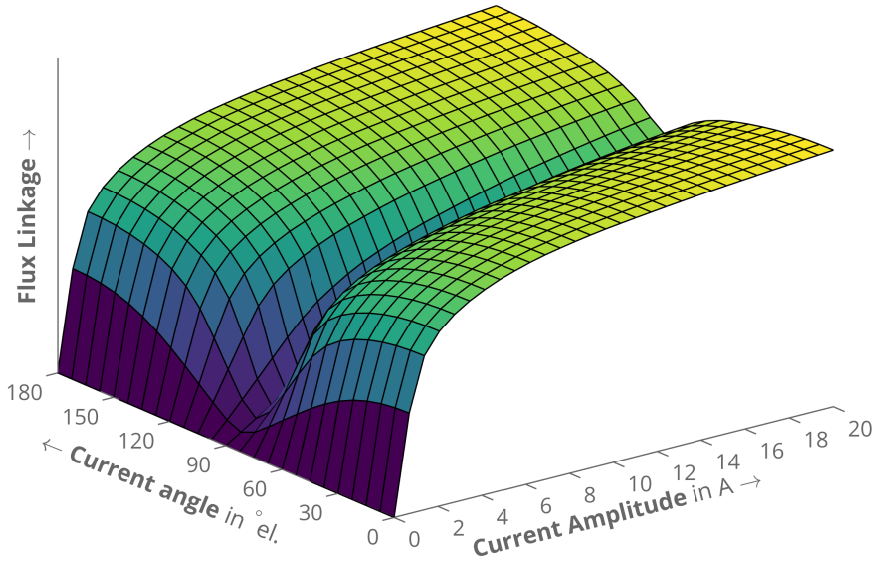

(b) non-linear

Figure 4.5: Magnitude of the resulting stator flux linkage space vector when a current space vector is impressed into the stator winding of Motor II in 2D magnetostatic FEM. The current amplitude is the magnitude of the stator current space vector and the current angle is defined as the angle between the space vector and the rotor's d-axis. Results are shown for the linear (a) and the non-linear (b) case. Different color scales were used to highlight the differently scaled z-axes of both plots.

flux paths apart from the air gap. When the current space vector is rotated towards the rotor's q-axis at 90°el, however, the share of air in the magnetic circuit increases as the flux has to cross the flux barriers. In consequence, the slope of the flux linkage function decreases.

Looking at the non-linear case illustrated in Figure 4.5b reveals that this effect is still dominant. In addition to the linear case, the flux linkage is non-linear as the iron core saturates. For stator current space vectors at angles of 0°el and 180°el, the curve has the same shape as already shown in Figure 4.4. This is due to the fact the flux is principally the highest here (see linear case), which is why the iron saturates the most in this case. For current angles around 90°el, the flux linkage itself is lower and accordingly the influence of the saturation. This is particularly evident in the less curved shape with increasing current, which again comes from the higher amount of air in the magnetic circuit. The remaining saturation mainly occurs in the stator teeth and yoke, and the rotor iron bridges. What follows as well is that it is important to consider the saturation states at current angles between both extreme cases because the shape of the curve slowly transforms from a highly saturated to a less saturated one.

Another important aspect of the saturation in anisotropic machines is that in addition to the different states of saturation for different current angles, the flux paths of the axes themselves also saturate differently [35]. This can best be demonstrated by decomposing the flux linkage vector from the non-linear simulation into a d- and q-component with Park's transform [93]. The results for the transformed values from Figure 4.5b are compared in Figure 4.6.

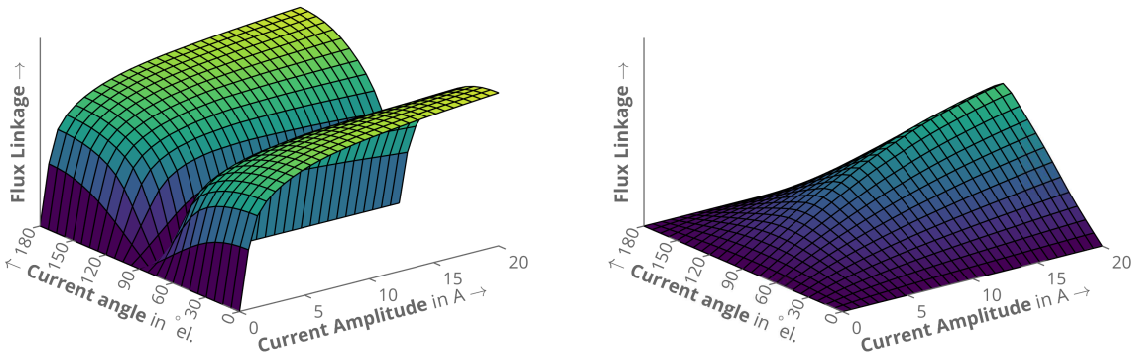

(a) d-component of flux linkage space vector **(b)** q-component of flux linkage space vector

Figure 4.6: D- and q-component of the stator flux linkage space vector for different current space vectors impressed into the stator winding of Motor II in non-linear 2D magnetostatic FEM (corresponds to Figure 4.5b). The current amplitude is the magnitude of the stator current space vector, and the current angle is defined as the angle between the space vector and the rotor's d-axis. Both plots use the same scaling of the z-axis and therefore also the same colors.

It is apparent from the flux linkage maps, that most of the saturation occurs in the d-axis. The d-component in Figure 4.6a shows the typical non-linear shape for almost all current angles except 90°el, where it is approximately zero. The q-component (Figure 4.6b), on the other hand, hardly shows any saturation for most current angles, except near 90°el. There, however, the saturation starts at much higher currents than for the d-component of the flux linkage.

Another effect that is already included in this figure is the so-called cross-saturation. It describes the dependence of the respective flux linkage component of both current components. More precise, this means that the d-component of the flux linkage always depends on both, the d- and q-component of the current. This applies for the q-component of the flux linkage as well.

Furthermore, what is striking in Figure 4.6a is that the slope of the d-component gets negative for high current amplitudes and angles close to 90°el. Therefore, a highly saturated d-axis causes more and more flux to flow through the q-axis. In terms of the flux linkage space vector, this means that although its total magnitude continues to increase in accordance with the non-linear function as the current amplitude increases, the vector itself rotates towards the q-axis.

This behavior is illustrated in Figure 4.7, which displays the angle of the flux linkage space vector in relation to the current amplitude for different current angles (both for the linear and the non-linear case). The figure is quite revealing in several ways. First, it shows the aforementioned phenomenon that the flux linkage space vector rotates towards the d-axis for low currents and then begins to rotate towards the q-axis for higher saturation (Figure 4.7b). This does not occur in the linear case because the iron flux paths do not saturate and μ is constant (Figure 4.7a).

Second, it reveals that the flux linkage space vector is by no means aligned with the current space vector. This is a particular feature of anisotropic machines as well, which is why it is present in the non-linear as well as in the linear case. Hence, for small currents, the angle of the flux linkage space vector is nearly the same. It only differs due to the different permeability defined in the linear case and the one resulting from the $B(H)$-curve for small currents. When the current increases, it only rotates towards the q-axis in the non-linear case due to saturation.

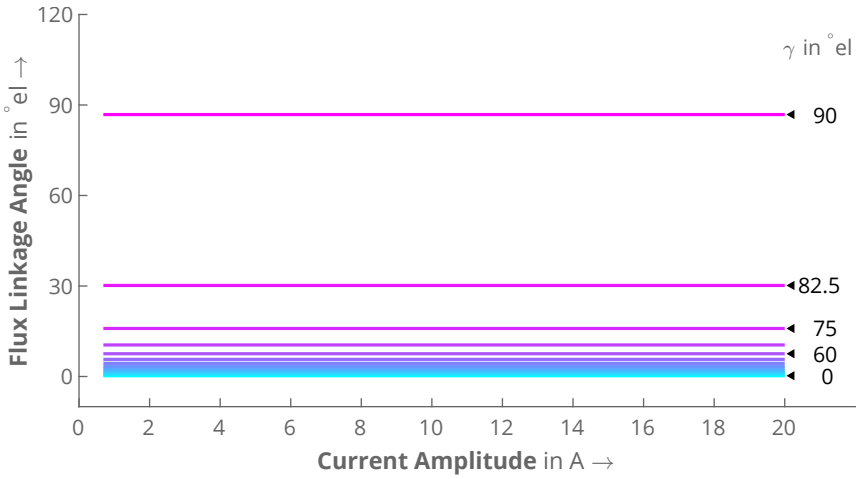

(a) linear

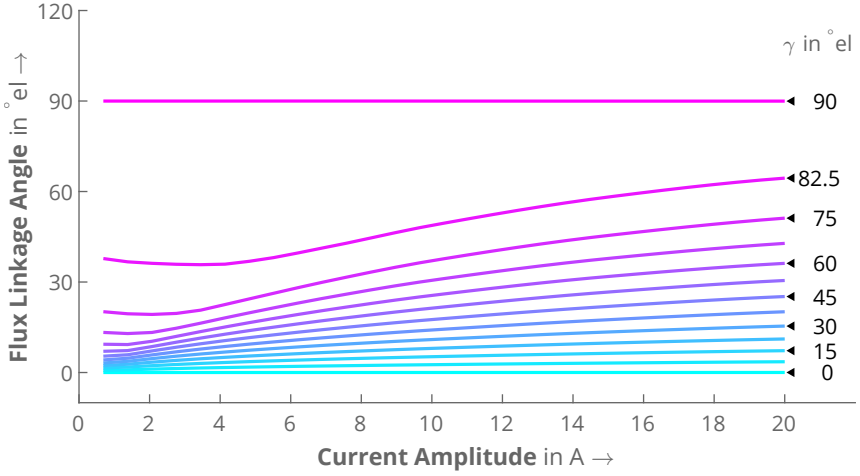

(b) non-linear

Figure 4.7: Angle of the flux linkage space vector versus the amplitude of the current space vector for different current angles in the linear and non-linear case. It was evaluated from the d- and q-component of the flux linkage (non-linear case corresponds to Figure 4.6). Each plot is colored according to the corresponding current angle, whereby the value is given for selected plots on the right. The shown plots refer to current angles from 0 to 90°el in 7.5°el steps.

4.2.5.2 Saturation of iron bridges

Thus far, the important aspects of the main flux saturation caused by the stator currents have been introduced. Before proceeding to describe the influence of the rotor currents, it is necessary to focus on a further effect that occurs in modern Line-Start Synchronous Reluctance Machines and has not been covered in previous work of Güdelhöfer, which is the saturation of iron bridges in the rotor. Figure 4.8 illustrates this phenomenon using the example of Motor III.

If a stator current space vector is impressed at an angle of 0°el, the flux linkage space vector is aligned with the rotor's d-axis (cf. Figure 4.5b). Therefore, the magnetic flux in the rotor flows through the iron paths between the flux barriers and not through the iron bridges (or "iron ribs") in the flux barriers, as they are perpendicular to the iron paths of higher permeance of the d-axis.

However, the tangential iron bridges on the outer diameter of the rotor are an ex-

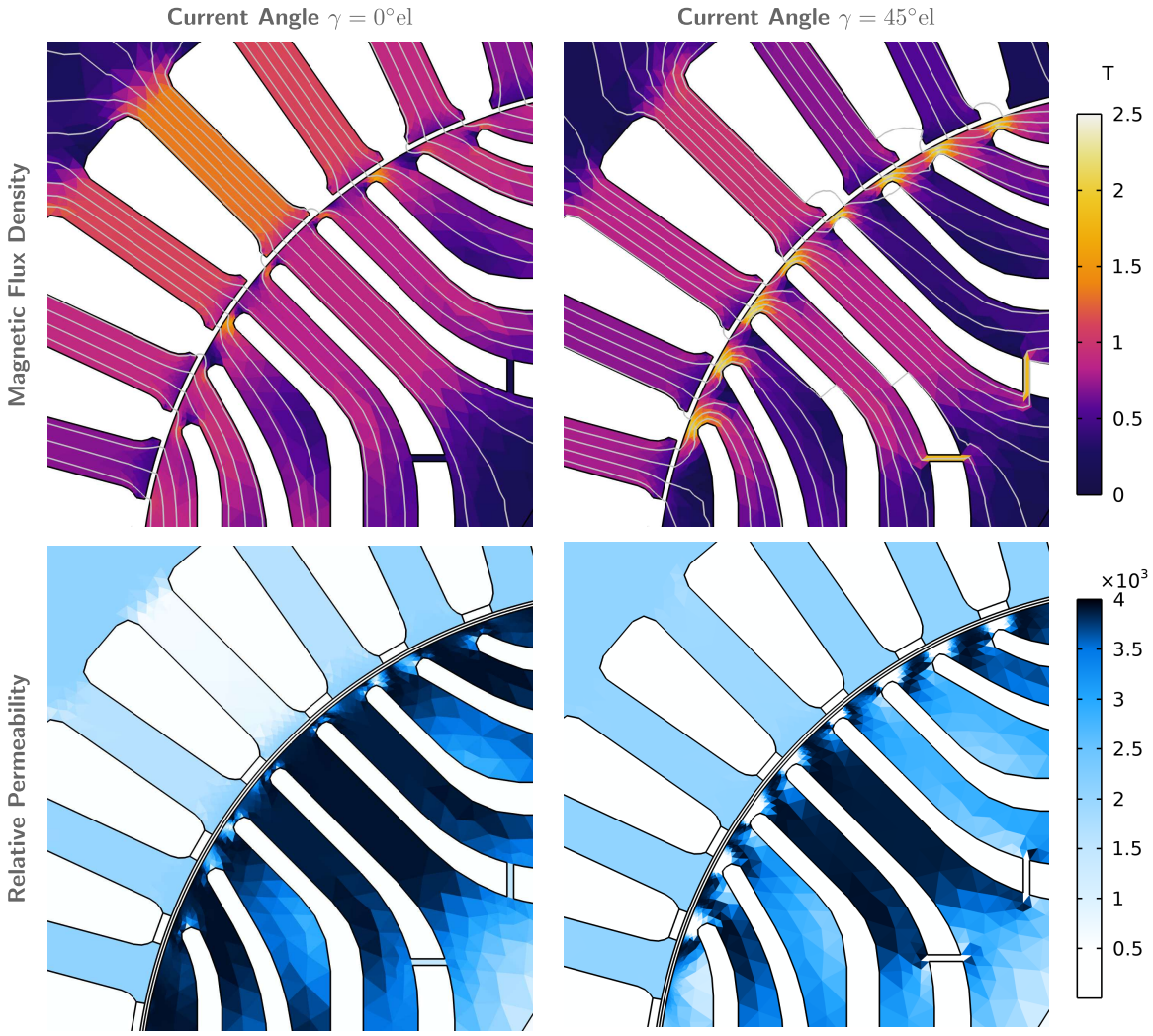

Figure 4.8: Illustration of the saturation of iron bridges using the example of a stator current space vector at two different angles for Motor III from 2D non-linear magnetostatic FEM. The top figures show the magnetic flux density (only in the iron domains), whereby flux lines highlight the orientation of the magnetic field. The bottom figures show the corresponding relative permeability. The difference between the permeability of the stator and rotor is due to the use of different steel grades (cf. Figures 3.2 and 3.3).

ception, as they better collect the air gap flux on the smooth rotor surface and therefore saturate slightly. Hence, their permeability for a flux linkage space vector aligned with the d-axis (Figure 4.8 bottom left) is already slightly decreased compared to the wider iron paths between the flux barriers. The effect on the air gap magnetic field, however, is usually small for low to medium currents.

If the stator current space vector is now rotated to an angle of 45°$_{\text{el}}$, the flux linkage space vector has both a d- and q-component. Hence, the q-component searches for the most conductive flux paths, which are the small iron bridges. The flux density in these areas strongly increases (Figure 4.8 top right), which is why the relative permeability of the bridges is now significantly reduced (Figure 4.8 bottom right). This has a major influence on the air gap field, in which field dips occur above the saturated bridges that are similar to the slotting effect of Induction Machines with slotted rotors, which is illustrated in Figure 4.9. It is observable, that the fundamental of the air gap field decreases due to the rotated current space vector. In addition to the field dips caused by the stator slotting,

which are already visible for $0°_{el}$, there are now also field dips due to the saturated bridges. This could be expressed with a higher carter factor, for example. Of course, the harmonics increase as well and can vary depending on the saturation state.

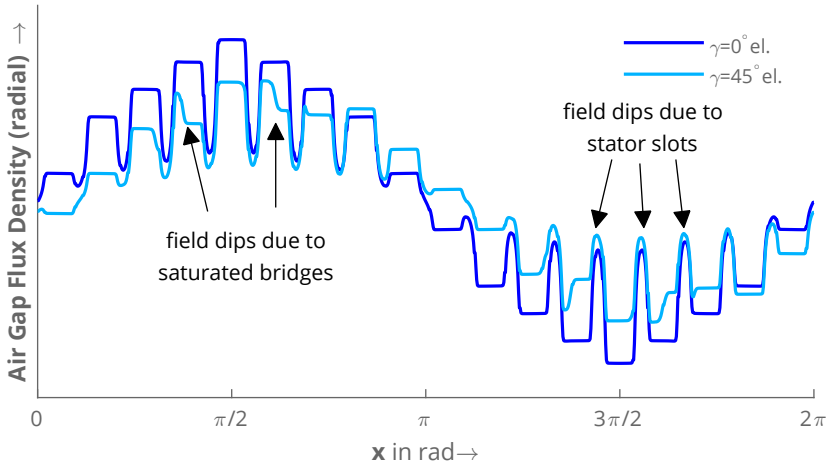

Figure 4.9: Radial component of the air gap flux density for one pole-pair of Motor III, corresponding to the simulations in Figure 4.8.

4.2.5.3 Influence of the rotor currents

Moving on now to discuss the influence of rotor currents on the saturation of a Line-Start Synchronous Reluctance Machine. Since all the effects mentioned so far already occur when the rotor cage is currentless, they can be assigned to the synchronous operation of the machine. However, during the start-up in asynchronous operation, currents flow in the rotor cage that also influence the saturation behavior. As the asynchronous operation of an LSSynRM is similar to that of an IM, the saturation effects known from Induction Machine theory can be applied here.

The rotor current increases with increasing slip. Since the resulting rotor field is induced by the stator field, it counteracts its cause and thus dampens the generating stator field. The fundamental wave therefore becomes smaller at high slip (if the rotor is not skewed), which is why it does not cause the iron to saturate as much. It is therefore essential to take the effect of the rotor field into account. Otherwise, if only the stator currents were considered, the saturation in asynchronous operation would be overestimated.

In addition, the effect of the damped stator field in causes the flux to flow closer to the air gap because it cannot enter the rotor as much. This can be described as a shielding effect of the rotor cage, which becomes greater as the slip frequency increases. Since in the most extreme case at standstill ($s = 1$) the flux only flows along the leakage paths (that is, the stator tooth tips and rotor iron bridges), this effect is called leakage path saturation [35], [75]. As already mentioned for the existing model, neglecting this effect can lead to deviations in the start-up behavior predicted by the model. This will be investigated in the validation.

4.2.5.4 Finding a fast and sufficiently accurate method

Now that the main saturation effects that occur in a Line-Start Synchronous Reluctance Machine have been explained, a suitable method for consideration in the model can be derived. While in early calculation models saturation has been neglected to simplify the model, the previous introduction has clarified that it would lead to wrong results.

The question is, however, how much in detail it should be modelled because it will increase the computing time, which is a key factor for this model. As innumerable studies in the field of electrical machine modeling (including the existing model and previous work of the author) have proven, it is often sufficient to consider only the most important effects of iron saturation on the machine behavior. Thus, it is worked out in the following, how to consider for saturation accurate enough but as simple as possible.

In general, different methods can be applied to find the non-linear flux linkage-current function. Typically, these are analytical methods, numerical methods and measurements. Due to the high availability of computing power and the advantage of being able to simulate a machine without prior measurements, numerical methods are particularly suitable. However, not every method fulfills the requirement of a short computing time if a certain accuracy is to be achieved.

This is the case with standard lookup tables, for example, which are one of the most popular methods nowadays. For synchronous machines, usually lookup tables are calculated with magnetostatic FEM and then interpolated for each time step in the model to provide the current for a given flux linkage or vice versa. In practice, the flux linkages therefore have to be calculated for many sets of different input currents using magnetostatic FEM. In the case of synchronous machines, this is usually not a major effort, as there are only m stator currents and, in the case of electrically excited machines, no more than one additional rotor excitation current [90], [92].

Regarding the saturation phenomena presented, this corresponds to saturation in synchronous operation, in which a stator current space vector varies in magnitude and angle and thus changes the saturation state of the machine. The optional excitation current is an additional parameter that also changes the main saturation. The function to be described therefore has a stator space vector and a value for the excitation in the rotor as input and output variables:

$$\left(\vec{\Psi}_\mathrm{s}, \Psi_\mathrm{exc}\right) = \vec{f}\left(\vec{i}_\mathrm{s}, i_\mathrm{exc}\right). \tag{4.22}$$

In Line-Start Synchronous Reluctance Machines, however, there are m stator and additional $2N_\mathrm{FB}$ rotor currents, which influence the saturation state during asynchronous and synchronous operation. The chosen method of considering the skin effect through several rotor cage layers even multiplies the number of rotor currents by a factor of N_L:

$$\left(\vec{\Psi}_\mathrm{s}, \Psi_\mathrm{r,1}, \Psi_\mathrm{r,2}, \ldots, \Psi_{\mathrm{r,2N_{FB}N_L}}\right) = \vec{f}\left(\vec{i}_\mathrm{s}, i_\mathrm{r,1}, i_\mathrm{r,2}, \ldots, i_{\mathrm{r,2N_{FB}N_L}}\right). \tag{4.23}$$

It is obvious that this leads to an enormous number of variations for the $m + 2N_\mathrm{FB}N_\mathrm{L}$ currents, which would cause a considerable computational effort that is impractical.

In contrast to the stator current system, which is fully symmetrical, the rotor current system now lies in arbitrary arranged flux barriers. Replacing it with a space vector (based on a dq0 system, for example) would lead to a loss of accuracy and an increase in complexity in the parameter calculation. Moreover, even the case of only one rotor current as in [90], [92] can lead to computing times that are impractical. Therefore, it follows that a suitable method for taking saturation into account must be further simplified.

4.2.5.5 Saturation factor method

In the case of Induction Machines [94] as well as for LSSynRM in the existing model [54], [55], a global saturation factor has already been applied successfully. The basic principle can be best explained for the simplified case of one single current and flux linkage, as previously shown in Figure 4.4.

The constant inductance L of the linear flux linkage function is now multiplied by a current-dependent saturation factor Λ_{sat}. This adjusts the proportionality for a given current so that the relationship

$$\Psi = f(I) = \Lambda_{\mathrm{sat}} L I \tag{4.24}$$

with

$$0 < \Lambda_{\mathrm{sat}} \leq 1$$

is correct for that particular current. The same is possible for finding the current to the given flux linkage:

$$I = f(\Psi) = k_{\mathrm{sat}} \frac{\Psi}{L}, \tag{4.25}$$

where k_{sat} is now the inverse of Λ_{sat} and therefore $k_{\mathrm{sat}} \geq 1$.

Figure 4.10 further demonstrates this principle. For the first current value at point **a**, the saturation factor Λ_{sat} is at its maximum because the current-flux linkage function is still in the unsaturated, linear range. As the slope is constant in this range, Λ_{sat} is constant as well.

When the current is further increased, as for the points **b** and **c**, the iron saturates and the slope has to be adapted by the saturation factor. This can be best observed when looking at the slopes of the functions indicated with gray dotted lines. The higher the saturation, the lower the factor Λ_{sat} and therefore the lower the slope of the adapted linear function for the respective current.

Since it originates from analytical models, this principle is often explained by saying that the saturation factor Λ_{sat} reduces the air gap permeance of the machine, or that the geometric air gap width is virtually increased by k_{sat}. Both cases lead to the same result of a lower slope, but are merely illustrative.

In practice, the saturation factors are best obtained by measurements or the non-linear Finite Element Method by determining the non-linear function $\Psi(I)$ for multiple sample currents and dividing it by the linear reference LI:

$$\Lambda_{\mathrm{sat}} = \frac{\Psi(I)}{LI}. \tag{4.26}$$

Then it can be interpolated from a lookup table for any given current in the model (Figure 4.10b). This is particularly useful if more than one current is to be modeled, but their influence on the saturation is assumed to be the same because the same factor can be multiplied by the entire system of equations. Hence, it follows:

$$\vec{\psi} = \Lambda_{\mathrm{sat}} \mathbf{L} \vec{i} \tag{4.27}$$

for the system of multiple coupled stator and rotor coils.

Yet, as already mentioned, many of the assumptions and simplifications do not apply to LSSynRM. First, it was pointed out above that the saturation also depends on the angle of the stator current space vector and differs for both axes. Second, the effect of the rotor currents has to be considered. Both aspects will be explained in the following.

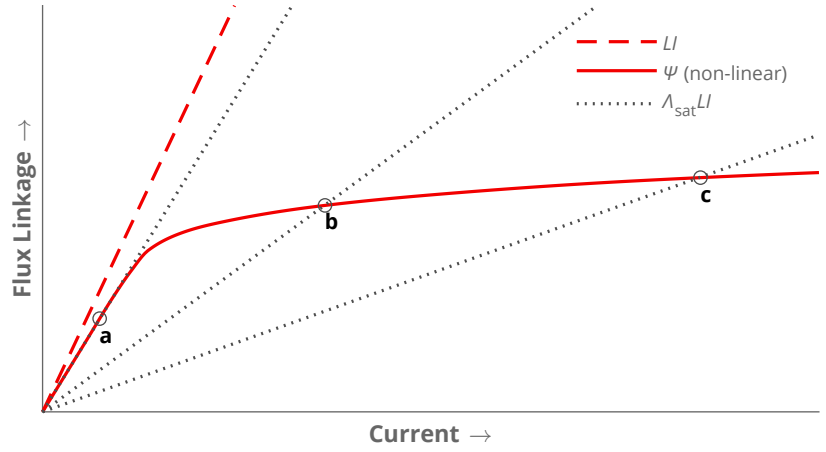

(a) Adaption of the function LI to fit to the non-linear flux linkage Ψ.

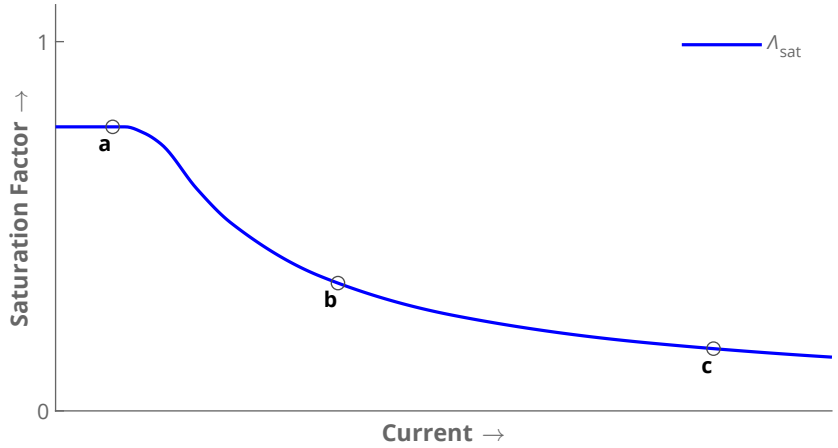

(b) Corresponding saturation factor Λ_{sat}.

Figure 4.10: Illustration of the principle of adapting the linear flux linkage function LI with a current-dependent saturation factor Λ_{sat} to fit the non-linear flux linkage Ψ for every current value. For three selected points (**a**,**b**,**c**) on the non-linear flux linkage function, the corresponding saturation factors are highlighted.

4.2.5.6 Stator saturation factors

Due to the dependence of the saturation on the current angle, the saturation factor function depends on two input variables $\Lambda_{\mathrm{sat}}(I, \gamma)$. This has already been successfully implemented in the existing model. As mentioned above, however, the saturation states of the d- and q-axis differ from each other (cf. Figure 4.6), which must also be represented by the saturation model. Therefore, a dq-saturation factor model is introduced, which follows the principle presented in [47] and will improve the accuracy of the existing model. It has already been published in [A3] and [A4] and will be explained more detailed in the following.

Using the d- and q-component of the non-linear stator flux linkage space vectors as presented in Figure 4.6, the information on the saturation behavior of both axes is already known. Hence, in addition to these functions evaluated for non-linear material properties

$$\Psi_{\mathrm{s,d}}\left(I, \gamma\right)_{\mu=f(B)} \qquad \text{and} \qquad \Psi_{\mathrm{s,q}}\left(I, \gamma\right)_{\mu=f(B)}\,,$$

the linear functions

$$\Psi_{\mathrm{s,d}}\left(I, \gamma\right)_{\mu=\mathrm{const.}} \qquad \text{and} \qquad \Psi_{\mathrm{s,q}}\left(I, \gamma\right)_{\mu=\mathrm{const.}}\,,$$

have to be evaluated as well. Just as for the saturated case, the d- and q-components of the flux linkage vector are determined as a function of I and γ for the linear case (Figure 4.11).

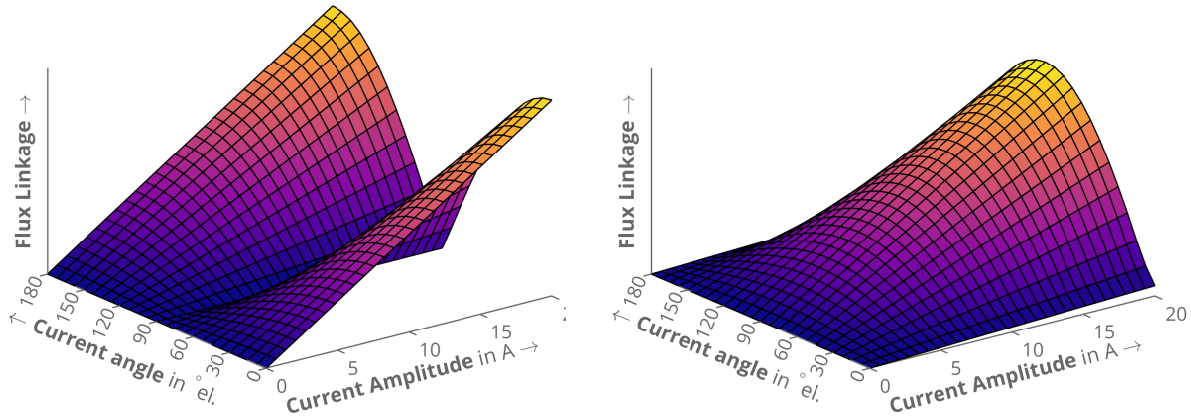

(a) d-component of flux linkage space vector **(b)** q-component of flux linkage space vector

Figure 4.11: D- and q-component of the stator flux linkage space vector $\Psi_{\mathrm{s,d}}(I,\gamma)_{\mu=\mathrm{const.}}$ and $\Psi_{\mathrm{s,q}}(I,\gamma)_{\mu=\mathrm{const.}}$ for different current space vectors impressed into the stator winding of Motor II (corresponds to Figure 4.5a). The current amplitude is the magnitude of the stator current space vector, and the current angle is defined as the angle between the space vector and the rotor's d-axis. Both plots use different z-axis scalings.

The two calculations can then be used to determine the saturation factors of the two axes for each pair of stator current amplitude and angle:

$$\Lambda_{\mathrm{sat,d}}(I,\gamma) = \frac{\Psi_{\mathrm{s,d}}(I,\gamma)_{\mu=f(B)}}{\Psi_{\mathrm{s,d}}(I,\gamma)_{\mu=\mathrm{const.}}} \qquad \text{and} \qquad \Lambda_{\mathrm{sat,q}}(I,\gamma) = \frac{\Psi_{\mathrm{s,q}}(I,\gamma)_{\mu=f(B)}}{\Psi_{\mathrm{s,q}}(I,\gamma)_{\mu=\mathrm{const.}}}, \tag{4.28}$$

where $\Psi_{\mathrm{s,d}}(I,\gamma)_{\mu=\mathrm{const.}}$ and $\Psi_{\mathrm{s,q}}(I,\gamma)_{\mu=\mathrm{const.}}$ are evaluated from the results of the linear function $\mathbf{L}\vec{I}$.

Figure 4.12 shows the resulting saturation factor functions for both axes for the sample points shown in the example in Figures 4.6 and 4.11.

If both plots are compared, it is obvious once more that both axes saturate differently, which could already be assumed looking at the flux linkage plots. Therefore, it is also possible to reproduce the rotation of the flux linkage vector towards the q-axis at high saturation in the model. This could not be achieved with a single saturation factor.

Looking at Figure 4.12a, which shows the saturation factor of the d-axis, it is apparent that the saturation is quite similar for current angles $0 \leq \gamma \leq 60°_{\mathrm{el}}$. This matches the observation made for the non-linear flux linkage component of this axis (Figure 4.6a), which also looks similar for these current angles. First, the saturation factor drops fast for increasing current amplitudes, whereas the slope converges to a small negative value for higher currents, once the iron domains are fully saturated.

The difference in absolute value for these current angles, which increases for increasing current values, is caused by the change of the linear flux linkage function, which varies more in this area (see Figure 4.11a). For current angles $\gamma > 60°_{\mathrm{el}}$, the saturation factor is significantly higher because the iron paths of the d-axis do not saturate as much, when the flux linkage space vector is (almost) aligned with the q-axis and becomes shorter due to the less permeable flux paths.

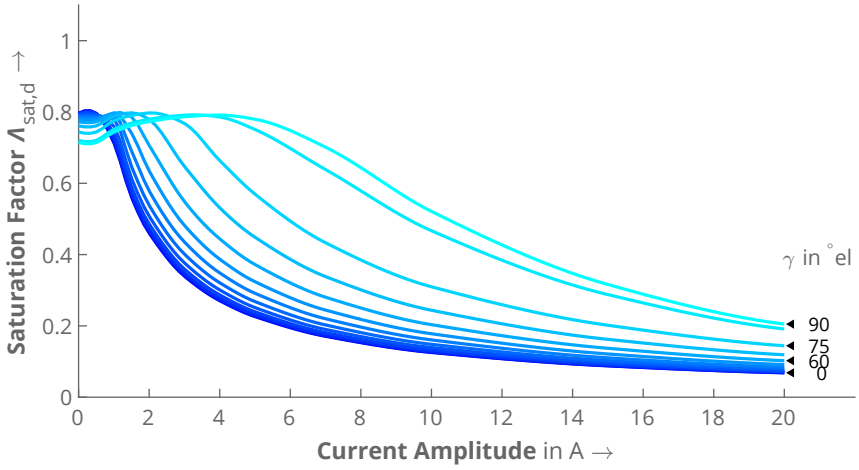

(a) d-axis saturation factor

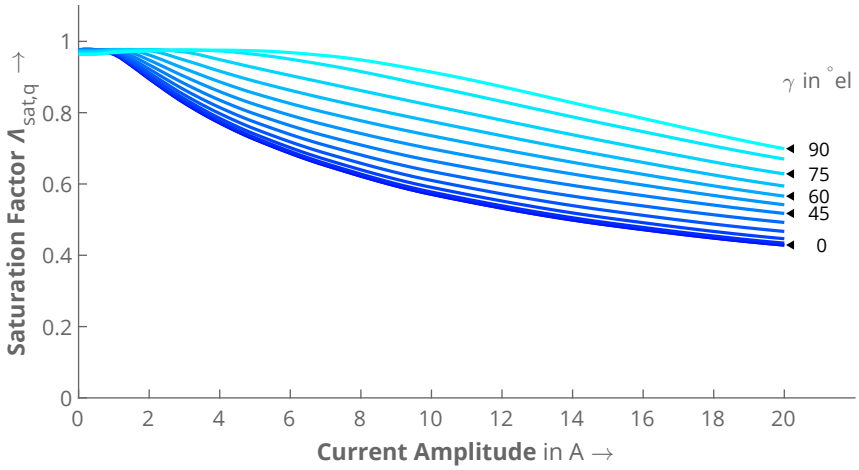

(b) q-axis saturation factor

Figure 4.12: Saturation factor functions for the d- and q-axis evaluated as the relation between non-linear and linear current-flux linkage components shown in Figures 4.6 and 4.11, respectively. Both functions have been evaluated with 2D magnetostatic FEM for different current angles, which are indicated with different colors.

Moreover, what stands out in the figure is that neither of the functions start at a saturation factor of 1 for a current of 0 A. This is caused by the chosen value of relative permeability in the linear flux linkage calculation, which was set to $\mu_\mathrm{r} = 10^7$. This makes the iron domains ideally conductive compared to the air domains, where $\mu_\mathrm{r} = 1$. Because the $B(H)$-curve used for the non-linear calculation has a lower maximum value of permeability (approximately $\mu_r \approx 4000$ depending on the electric steel grade) the slope of the linear function is different. However, this does not have any effect on the model, which is why the permeability can be set to arbitrary values. The saturation factor always yields the correct non-linear flux linkage.

In contrast to the d-axis, the saturation factor of the q-axis (Figure 4.12b) shows much less saturation for all current angle values. The q-axis mainly consists of large air domains in relation to the iron domains, which is why its behavior is "more linear", meaning the curves are much flatter than those of the d-axis saturation factor. Furthermore, the absolute values are obviously higher when comparing them for the same currents as for the d-axis.

The observation that the saturation factor is lower than 1 for small currents can be

made here as well. However, the value is higher than for the d-axis because the share of iron domains, of which the relative permeability is set to $\mu_\mathrm{r} = 10^7$, is smaller. Hence, the influence of the higher permeability is not as high, which causes the results of the linear flux linkage calculation to be closer to the non-linear one.

It should also be mentioned that the saturation of iron bridges (as presented in Figure 4.8) is already included in this model if the non-linear reference is calculated accordingly. However, the saturation factor method can only take into account the influence on the fundamental wave, that is, the adjustment of the magnetizing current to a higher value required to saturate the iron bridges. Hence, saturation effects on the third and fifth harmonic of the current due to the saturation of stator teeth and yoke [95], for example, cannot be represented by this method.

In contrast, the saturation-dependent Carter factor, which results from a virtual opening of the rotor bridges, is taken into account. The harmonics caused by the saturated bridges, however, also cannot be considered. Further aspects on this topic will be discussed in the section for parameter calculation.

4.2.5.7 Application to the model

Both saturation factors for the stator must now be included in the model. Hence, Equation (4.27) changes to

$$\vec{\psi} = \mathbf{\Lambda}_\mathrm{sat,s}\mathbf{L}_\mathrm{s,s}\vec{i}_\mathrm{s} \tag{4.29}$$

for the stator equations, where $\mathbf{\Lambda}_\mathrm{sat,s}$ is the stator saturation factor matrix, including both saturation factors. As a result, from this point onwards, the flux linkage vector in the model always refers to the resulting variable from the non-linear function. It should also be noted that the flux linkage and the current vectors are now labeled with lowercase letters, as these are the time-varying variables of the model and no longer constant variables for derivation purposes. Consequently, this also results in the fact that the instantaneous value of both vectors will be used as input for the saturation reference in each time step in the model.

Since the model in this chapter is derived as a phase-domain model, the saturation factors $\Lambda_\mathrm{sat,d}$ and $\Lambda_\mathrm{sat,q}$ cannot be inserted directly into the matrix. Instead, the matrix must be transformed from the dq0 system into the abc system. For this purpose, the complete matrix for the stator in the dq0 system

$$\mathbf{\Lambda}_\mathrm{sat,s,dq0} = \mathrm{diag}\left(\Lambda_\mathrm{sat,d}, \Lambda_\mathrm{sat,q}, \Lambda_\mathrm{sat,0}\right) = \begin{pmatrix} \Lambda_\mathrm{sat,d} & 0 & 0 \\ 0 & \Lambda_\mathrm{sat,q} & 0 \\ 0 & 0 & \Lambda_\mathrm{sat,0} \end{pmatrix}$$

is defined at first. The additional factor for the zero system $\Lambda_\mathrm{sat,0}$ is set to the mean value of the values for d- and q-axes. Applying Park's transformation to the current-flux linkage function in the dq0 coordinate system

$$\vec{\psi}_\mathrm{s,dq0} = \mathbf{\Lambda}_\mathrm{sat,s,dq0}\left(\mathbf{L}_\mathrm{s,s}\vec{i}_\mathrm{s}\right)_\mathrm{dq0}, \tag{4.30}$$

yields

$$\vec{\psi}_\mathrm{s} = \mathbf{K}_\mathrm{P}^{-1}\mathbf{\Lambda}_\mathrm{sat,s,dq0}\mathbf{K}_\mathrm{P}\mathbf{L}_\mathrm{s,s}\vec{i}_\mathrm{s}, \tag{4.31}$$

where $\mathbf{K}_\mathrm{P}$ is the transformation matrix. Then

$$\mathbf{\Lambda}_\mathrm{sat,s} := \mathbf{\Lambda}_\mathrm{sat,s,abc} = \mathbf{K}_\mathrm{P}^{-1}\mathbf{\Lambda}_\mathrm{sat,s,dq0}\mathbf{K}_\mathrm{P}, \tag{4.32}$$

yields

$$\mathbf{\Lambda}_{\mathrm{sat,s}} = \begin{pmatrix} \Lambda_{\mathrm{s},11} & \Lambda_{\mathrm{s},12} & \Lambda_{\mathrm{s},13} \\ \Lambda_{\mathrm{s},21} & \Lambda_{\mathrm{s},22} & \Lambda_{\mathrm{s},23} \\ \Lambda_{\mathrm{s},31} & \Lambda_{\mathrm{s},32} & \Lambda_{\mathrm{s},33} \end{pmatrix}, \tag{4.33}$$

which is not a diagonal matrix anymore but a fully occupied one.

4.2.5.8 Rotor saturation factor

In the existing model, the single saturation factor has been multiplied by the whole set of equations, and hence the rotor equations. Since the saturation factor matrix $\mathbf{\Lambda}_{\mathrm{sat,s}}$ now only manipulates the stator flux linkages, a rotor saturation factor matrix $\mathbf{\Lambda}_{\mathrm{sat,r}}$ has to be defined as well.

It is assumed that the saturation state of the flux paths of the rotor coils is also mainly caused by the influence of the saturation by the stator currents. Thus, the saturation factors of the stator also serve as the basis for the saturation factors of the rotor. They can be transformed to rotor saturation factors that depend on the angular position of the rotor loop relative to the d-axis. Hence, the i-th rotor loop that is positioned at the angle θ_{i} receives its saturation factor from:

$$\Lambda_{\mathrm{r,i}} = \sqrt{\left(\Lambda_{\mathrm{sat,d}} \cos\theta_{\mathrm{i}}\right)^2 + \left(\Lambda_{\mathrm{sat,q}} \sin\theta_{\mathrm{i}}\right)^2}. \tag{4.34}$$

The angle is evaluated from the centroid of both rotor bar ends of a loop, as indicated in Figure 4.13. Loop 1 in this figure is on the d-axis, for example. Hence, when Equation (4.34) is evaluated, $\Lambda_{\mathrm{r,1}} = \Lambda_{\mathrm{sat,d}}$. In contrast, loop 4 is on the q-axis, and its saturation factor equals $\Lambda_{\mathrm{sat,q}}$. Every other loop in between those two therefore receives a saturation factor between both values.

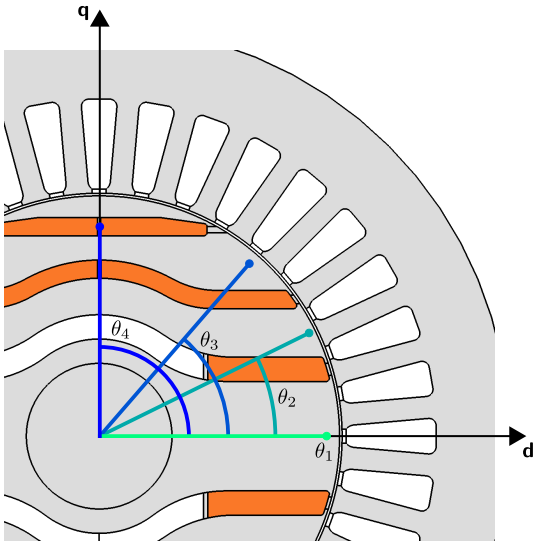

Figure 4.13: Definition of the angle θ_{i} for the first four rotor loops. It defines the relative angle between the rotor's d-axis and the i-th loop.

Concerning the layer model to account for skin effect, it is to mention that the angle is the same for each layer. This makes the most sense in terms of simple implementation, but also regarding the saturation state of the machine.

The rotor saturation factor matrix is then constructed as a diagonal matrix with the corresponding values as follows:

$$\mathbf{\Lambda}_{\mathrm{sat,r}} = \mathrm{diag}\left(\Lambda_{\mathrm{r},1}, \Lambda_{\mathrm{r},2}, \ldots, \Lambda_{\mathrm{r},2\mathrm{N_{FB}N_L}}\right). \tag{4.35}$$

The complete current-flux linkage function for the model hence becomes

$$\begin{pmatrix} \vec{\psi}_{\mathrm{s}} \\ \vec{\psi}_{\mathrm{r}} \end{pmatrix} = \begin{pmatrix} \mathbf{\Lambda}_{\mathrm{sat,s}} & \mathbf{0} \\ \mathbf{0} & \mathbf{\Lambda}_{\mathrm{sat,r}} \end{pmatrix} \begin{pmatrix} \mathbf{L}_{\mathrm{s,s}} & \mathbf{L}_{\mathrm{s,r}} \\ \mathbf{L}_{\mathrm{r,s}} & \mathbf{L}_{\mathrm{r,r}} \end{pmatrix} \begin{pmatrix} \vec{i}_{\mathrm{s}} \\ \vec{i}_{\mathrm{r}} \end{pmatrix}. \tag{4.36}$$

4.2.5.9 Consideration of the influence of the rotor currents with the saturation factor matrix

Moving on now to the influence of the rotor currents, for which a convenient solution has already been presented in the existing model [54], [55]. The key factor in retaining a fast model is that the rotor currents were not considered when calculating the saturation factors. Otherwise, the calculation of saturation factor lookup tables would still require an unreasonable number of sample points for different sets of input currents.

Instead, a method is introduced that generates the same saturation state of the machine in the model for a virtual machine with stator currents only. A virtual stator current vector is thus obtained that generates the same stator flux linkages as the entire vector of stator and rotor currents in the model. The procedure is clarified in the following.

An arbitrary input current vector is defined

$$\vec{i}_{\mathrm{in}} = \begin{pmatrix} \vec{i}_{\mathrm{s}} \\ \vec{i}_{\mathrm{r}} \end{pmatrix},$$

which, when inserted into the non-linear current-flux linkage function (4.36) defined by the model, creates a specific output flux linkage vector:

$$\vec{\psi}_{\mathrm{out}} = \begin{pmatrix} \vec{\psi}_{\mathrm{s}} \\ \vec{\psi}_{\mathrm{r}} \end{pmatrix} = \vec{f}\left(\vec{i}_{\mathrm{s}}, \vec{i}_{\mathrm{r}}\right). \tag{4.37}$$

In this vector, the information on how the stator magnetic field is damped by the rotor magnetic field is already included.

Then, the method assumes that the stator flux linkage vector $\vec{\psi}_{\mathrm{s}}$ is only produced by a virtual stator current vector $\vec{I}_{\mathrm{s}}^{*}$, which is unknown. By reducing the current-flux linkage function in (4.36) to the stator equations and hence only using the stator saturation factor matrix $\mathbf{\Lambda}_{\mathrm{sat,s}}$ and the self-inductance matrix $\mathbf{L}_{\mathrm{s,s}}$, it can be solved for $\vec{I}_{\mathrm{s}}^{*}$:

$$\vec{I}_{\mathrm{s}}^{*} = \left(\mathbf{\Lambda}_{\mathrm{sat,s}}\mathbf{L}_{\mathrm{s,s}}\right)^{-1}\vec{\psi}_{\mathrm{s}}. \tag{4.38}$$

In this case, $\vec{\psi}_{\mathrm{s}}$ has a lowercase letter because it refers to the instantaneous value obtained from the model. In contrast, $\vec{I}_{\mathrm{s}}^{*}$ refers to the virtual machine, which always has a static saturation state that is independent of time.

Transferred to the motor model, this results in a stator current vector that produces the same stator flux linkages $\vec{\psi}_{\mathrm{s}}$ as the real current vector $(\vec{i}_{\mathrm{s}}, \vec{i}_{\mathrm{r}})^{\mathrm{T}}$, consisting of stator and rotor currents. Hence, $\vec{I}_{\mathrm{s}}^{*}$ can now be transformed to a space vector and its magnitude I_{s}^{*} and angle γ^{*} are used as inputs for the saturation factor lookup tables.

This method massively reduces the preliminary calculation time because the saturation factors depend uniquely on the magnitude and angle of the virtual stator current space vector and not on the rotor currents. However, the limitation of this approach

is that the saturation state usually is more complex during asynchronous operation because the air gap field is influenced by both stator and rotor field. This cannot be fully represented by the method of a virtual stator field.

Furthermore, especially during asynchronous operation, it is to assume that the rotor iron bridges are mainly saturated due to leakage flux of the rotor coils. In different saturation states during start-up, the leakage inductances of each defined coil are therefore not constant, as the bridges are saturated by both the stator and rotor fields.

In general, the model is limited by the fact that the air gap magnetic field is unknown. This means that only the fundamental, but no harmonic content, can be manipulated. Harmonics resulting from the slotting effects will therefore always be the same as in the linear case. Any local saturation effect cannot be fully represented.

However, the consideration of the resulting fundamental field is assumed to be sufficiently accurate. With the existing model, it has already been demonstrated that the combination of a single saturation factor and the virtual stator current method provides good results. The gain in computing time compensated for the loss in accuracy. Furthermore, it can be assumed that the improved consideration of saturation using a dq-saturation factor model as presented above can increase the accuracy even further. This will be demonstrated and discussed in the final validation in this chapter.

4.2.5.10 Remarks on the computing time

Overall, it is obvious that the separation into two single saturation factors already provides much more insight on the machine's saturation behavior. In addition, it is to be mentioned at this point that the evaluation of two saturation factors instead of one single factor does not require more preliminary calculations. In the existing model, the method for evaluating the single saturation factor has been the same, but the information on the angle of the resulting flux linkage space vector has not been used. Instead, the saturation factor has been evaluated only from the amplitude of the linear and non-linear flux linkage space vectors. Therefore, only the evaluation procedure of the saturation factors has to be adapted by splitting both vectors into their d- and q-components, as demonstrated above.

Looking at the preliminary calculation in terms of the overall computing time, the additional time required is small compared to the computationally intensive calculation of non-linear flux linkage samples for numerous stator current space vectors. The amount of additional storage is no challenge for modern computers as well. However, for the model itself, a second saturation factor requires a second interpolation step, which doubles the amount of interpolation time. Nevertheless, this increase is relatively small and still reasonable regarding the gain in accuracy from the improvement. The whole process of saturation factor evaluation and interpolation in the model will be clarified later in this chapter.

To conclude this section, the key aspects of saturation, namely the main flux saturation of LSSynRM and the influence of the rotor currents, have been discussed. It was briefly explained, how the saturation will be considered in the model. In the next section, the final system of equations of the model will be derived, which takes into account the discussed saturation phenomena and the skin effect. When the model is finally complete, the section on parameter calculation explains exactly how the methods described are to be implemented in practice. A further section then explains the solution of the system of equations, considering all the previously discussed extensions.

4.2.6 Final system of equations (electromagnetic)

At first, the stator equations are adapted. Now, the sum of the mutual flux linkages from the rotor to the stator contains $2N_{\mathrm{FB}}N_{\mathrm{L}}$ single flux linkages:

$$u_{\mathrm{k}} = R_{\mathrm{ph,k}} i_{\mathrm{k}} + \frac{\mathrm{d}}{\mathrm{d}t}\psi_{\mathrm{k}} = R_{\mathrm{ph,k}} i_{\mathrm{k}} + \frac{\mathrm{d}}{\mathrm{d}t}\left(\sum_{k'=1}^{m} \psi_{\mathrm{k,k'}} + \sum_{i'=1}^{2N_{\mathrm{FB}}N_{\mathrm{L}}} \psi_{\mathrm{k,i'}}\right). \tag{4.39}$$

This also applies to the rotor equations:

$$0 = 2R_{\mathrm{R,i}} i_{\mathrm{R,i}} + R_{\mathrm{b,i}}\left(i_{\mathrm{R,i}} - i_{\mathrm{R,i-1}}\right) + R_{\mathrm{b,i+1}}\left(i_{\mathrm{R,i+1}} - i_{\mathrm{R,i}}\right) + \frac{\mathrm{d}}{\mathrm{d}t}\sum_{k'=1}^{m} \psi_{\mathrm{i,k'}} + \frac{\mathrm{d}}{\mathrm{d}t}\sum_{i'=1}^{2N_{\mathrm{FB}}N_{\mathrm{L}}} \psi_{\mathrm{i,i'}}. \tag{4.40}$$

The matrix form of the full system of equations following from Equation (4.20)

$$\begin{pmatrix} \vec{u}_{\mathrm{s}} \\ \vec{0} \end{pmatrix} = \begin{pmatrix} \mathbf{R}_{\mathrm{s}} & \mathbf{0} \\ \mathbf{0} & \mathbf{R}_{\mathrm{r}} \end{pmatrix} \begin{pmatrix} \vec{i}_{\mathrm{s}} \\ \vec{i}_{\mathrm{r}} \end{pmatrix} + \frac{\mathrm{d}}{\mathrm{d}t} \begin{pmatrix} \vec{\psi}_{\mathrm{s}} \\ \vec{\psi}_{\mathrm{r}} \end{pmatrix} \tag{4.41}$$

must then be completed by inserting the new current-flux linkage function (4.36) including the saturation factor matrix, which is transformed to:

$$\begin{pmatrix} \vec{i}_{\mathrm{s}} \\ \vec{i}_{\mathrm{r}} \end{pmatrix} = \begin{pmatrix} \mathbf{\Lambda}_{\mathrm{sat,s}} & \mathbf{0} \\ \mathbf{0} & \mathbf{\Lambda}_{\mathrm{sat,r}} \end{pmatrix}^{-1} \begin{pmatrix} \mathbf{L}_{\mathrm{s,s}} & \mathbf{L}_{\mathrm{s,r}} \\ \mathbf{L}_{\mathrm{r,s}} & \mathbf{L}_{\mathrm{r,r}} \end{pmatrix}^{-1} \begin{pmatrix} \vec{\psi}_{\mathrm{s}} \\ \vec{\psi}_{\mathrm{r}} \end{pmatrix}. \tag{4.42}$$

If $\mathbf{k}_{\mathrm{sat}}$ is defined as the inverse of the saturation factor matrix $\mathbf{\Lambda}_{\mathrm{sat}}$, Equation (4.41) results in:

$$\begin{pmatrix} \vec{u}_{\mathrm{s}} \\ \vec{0} \end{pmatrix} = \begin{pmatrix} \mathbf{R}_{\mathrm{s}} & \mathbf{0} \\ \mathbf{0} & \mathbf{R}_{\mathrm{r}} \end{pmatrix} \begin{pmatrix} \mathbf{k}_{\mathrm{sat,s}} & \mathbf{0} \\ \mathbf{0} & \mathbf{k}_{\mathrm{sat,r}} \end{pmatrix} \begin{pmatrix} \mathbf{L}_{\mathrm{s,s}} & \mathbf{L}_{\mathrm{s,r}} \\ \mathbf{L}_{\mathrm{r,s}} & \mathbf{L}_{\mathrm{r,r}} \end{pmatrix}^{-1} \begin{pmatrix} \vec{\psi}_{\mathrm{s}} \\ \vec{\psi}_{\mathrm{r}} \end{pmatrix} + \frac{\mathrm{d}}{\mathrm{d}t} \begin{pmatrix} \vec{\psi}_{\mathrm{s}} \\ \vec{\psi}_{\mathrm{r}} \end{pmatrix}. \tag{4.43}$$

This is transformed to

$$\frac{\mathrm{d}}{\mathrm{d}t} \begin{pmatrix} \vec{\psi}_{\mathrm{s}} \\ \vec{\psi}_{\mathrm{r}} \end{pmatrix} = \begin{pmatrix} \vec{u}_{\mathrm{s}} \\ \vec{0} \end{pmatrix} - \begin{pmatrix} \mathbf{R}_{\mathrm{s}} & \mathbf{0} \\ \mathbf{0} & \mathbf{R}_{\mathrm{r}} \end{pmatrix} \begin{pmatrix} \mathbf{k}_{\mathrm{sat,s}} & \mathbf{0} \\ \mathbf{0} & \mathbf{k}_{\mathrm{sat,r}} \end{pmatrix} \begin{pmatrix} \mathbf{L}_{\mathrm{s,s}} & \mathbf{L}_{\mathrm{s,r}} \\ \mathbf{L}_{\mathrm{r,s}} & \mathbf{L}_{\mathrm{r,r}} \end{pmatrix}^{-1} \begin{pmatrix} \vec{\psi}_{\mathrm{s}} \\ \vec{\psi}_{\mathrm{r}} \end{pmatrix}, \tag{4.44}$$

which is the final system of equations to be solved.

As can be seen in this equation, the flux linkage vector $\vec{\psi} = (\vec{\psi}_{\mathrm{s}}, \vec{\psi}_{\mathrm{r}})^{\mathrm{T}}$ from the non-linear current-flux linkage function is now the state variable. This is a clear advantage over the approach previously published in [A3] in terms of computing time and simplicity of the model. Instead of a complicated derivation with an additional virtual linear flux linkage, the model now only contains real physical quantities except for the saturation factor. The time derivative of the saturation factor, which could worsen the convergence of the model and was already present in the existing model, is avoided. This considerably improves the numerical stability of the model.

4.2.7 Parameter calculation

4.2.7.1 Inductance matrix

The inductance matrix is a crucial part of the calculation procedure. It provides the basis for the current-flux linkage function that is adapted by the saturation factors to fit the non-linear relation of both quantities. Even though the saturation factors can only manipulate the fundamental wave, the inductance matrix can still represent space-harmonics induced by the geometry. In this way, the real behavior can be reproduced as closely as possible. Hence, special focus in this section lies on the accurate representation of slotting effects and the rotor's anisotropy.

Moreover, it is to note that, in general, the inductances can be defined as desired. This means that every stator phase can be broken down into groups of coils, single coils or even parts of it. The same is valid for rotor loops. However, for the case of a Line-Start Synchronous Reluctance Machine in 2D with linear materials, it is sufficient to define the inductances as already introduced in the linear model (Section 4.2.3). To clarify the definition and calculation of inductances for non-standard rotor cages, the procedure is described in detail in this section using Motor II as an example.

At first, the indexing of matrix elements should be defined. For a three-phase stator winding, the stator self-inductance matrix is constructed as follows:

$$\mathbf{L}_{\mathrm{s,s}} = \begin{pmatrix} L_{\mathrm{s,s,1,1}} & L_{\mathrm{s,s,1,2}} & L_{\mathrm{s,s,1,3}} \\ L_{\mathrm{s,s,2,1}} & L_{\mathrm{s,s,2,2}} & L_{\mathrm{s,s,2,3}} \\ L_{\mathrm{s,s,3,1}} & L_{\mathrm{s,s,3,2}} & L_{\mathrm{s,s,3,3}} \end{pmatrix}, \tag{4.45}$$

where $L_{\mathrm{s,s,1,1}}$ is the self-inductance of the first phase, and $L_{\mathrm{s,s,1,2}}$ and $L_{\mathrm{s,s,1,3}}$ are the mutual inductances from the second and third to the first phase, respectively. This matrix equals the standard self-inductance matrix of a three-phase stator winding.

To complete the stator equations, the mutual inductances from rotor to stator have to be defined as well. Each element $L_{\mathrm{s,r,k,i',l'}}$ refers to the respective phase k and the loop i' in the layer l':

$$\mathbf{L}_{\mathrm{s,r}} = \begin{pmatrix} L_{\mathrm{s,r,1,1,1}} & \cdots & L_{\mathrm{s,r,1,2N_{FB},1}} & \cdots & L_{\mathrm{s,r,1,1,N_L}} & \cdots & L_{\mathrm{s,r,1,2N_{FB},N_L}} \\ & & & \vdots & & & \end{pmatrix}. \tag{4.46}$$

Therefore, $L_{\mathrm{s,r,1,1,1}}$ describes the mutual inductance of the first rotor loop in the first rotor cage layer to the first stator phase. Each row has $2N_{\mathrm{FB}}N_{\mathrm{L}}$ elements.

The indexing of the rotor inductance matrices follows the same rules. It is worth mentioning that the inductance matrix $\mathbf{L}_{\mathrm{r,r}}$ is expanded according to the number of layers N_{L}. The full inductance matrix $\mathbf{L}$ and its indexing is given in Figure 4.14.

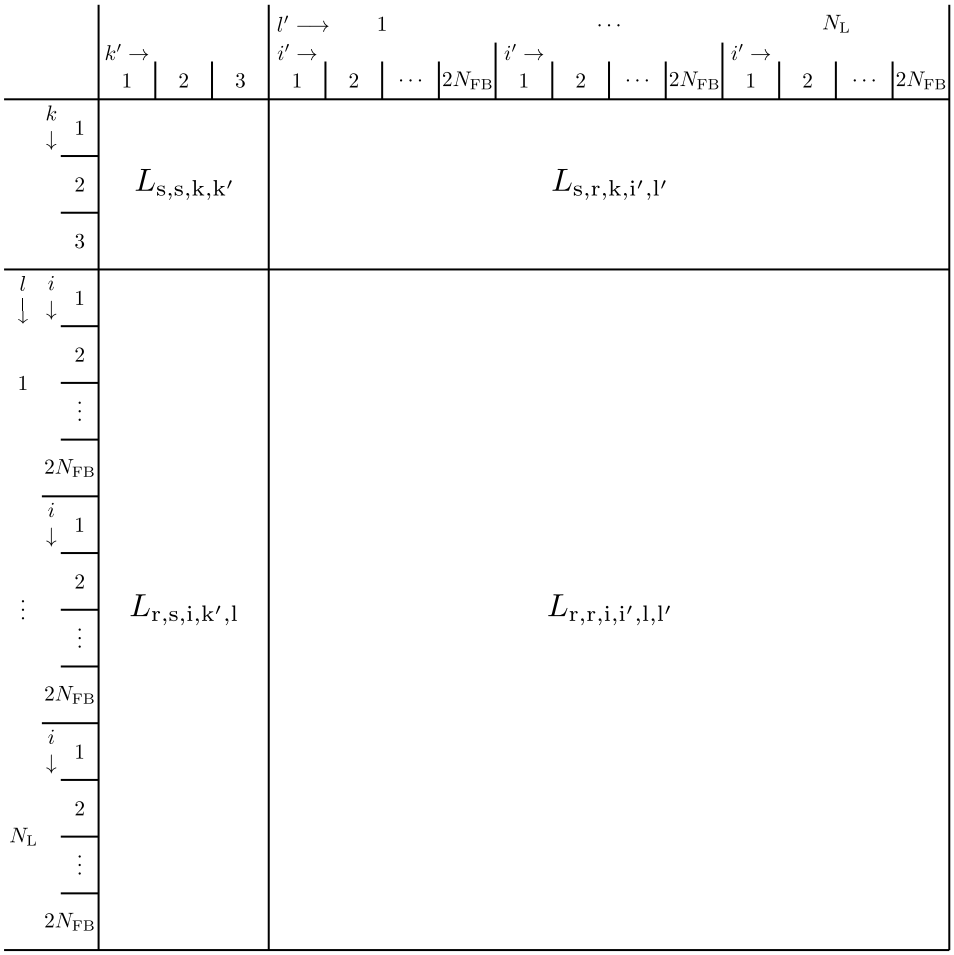

Figure 4.14: Inductance matrix of a three-phase Line-Start Synchronous Reluctance Machine with $2N_{\mathrm{FB}}$ rotor loops in each of the N_{L} rotor cage layers.

Since the 2D Finite Element Method is applied, the resulting inductances only represent the part of the coil embedded in the iron core. Before explaining the calculation procedure, it is therefore necessary to break down the self-inductances and mutual inductances into their components.

The self-inductance of a stator phase consists of the air gap inductance $L_{\mathrm{s},\delta}$, the slot leakage inductance $L_{\mathrm{s},\sigma\mathrm{s}}$, and the end winding leakage inductance $L_{\mathrm{s},\sigma\mathrm{e}}$, which yields

$$L_{\mathrm{s,s,k,k}} = L_{\mathrm{s},\delta,\mathrm{k}} + L_{\mathrm{s},\sigma\mathrm{s},\mathrm{k}} + L_{\mathrm{s},\sigma\mathrm{e},\mathrm{k}} \tag{4.47}$$

for the k-th stator phase. This also applies to the self-inductance of the i-th rotor loop in the l-th layer:

$$L_{\mathrm{r,r,i,i,l,l}} = L_{\mathrm{r},\delta,\mathrm{i,l}} + L_{\mathrm{r},\sigma\mathrm{s},\mathrm{i,l}} + L_{\mathrm{r},\sigma\mathrm{R},\mathrm{i,l}}, \tag{4.48}$$

where $L_{\mathrm{r},\sigma\mathrm{R},\mathrm{i,l}}$ is the ring leakage inductance.

Due to the calculation of the inductances with 2D FEM, the air gap inductances and the slot leakage inductances are already included in the resulting inductances $L_{\mathrm{s,FEM,k}}$ and $L_{\mathrm{r,FEM,i,l}}$. This means, the end winding leakage inductances have to be calculated separately. Because the objective is a versatile model, both end winding leakage inductances are estimated based on empirical leakage factors [73]. These have already proven to be accurate enough in the previously presented FE model.

Now, the 2D magnetostatic Finite Element model can be discussed. First, it is to note that a constant permeability for iron domains is defined, which is set to a (numerically) infinite value ($\mu_r = 10^7$ is sufficient in this case). However, as the iron bridges in the rotor do not saturate in this case, they create a magnetic short circuit for the rotor flux. This would cause the stator inductances to not represent the anisotropy correctly.

Hence, they have to be "opened", which means their permeability is set to $\mu_r = 1$ (Figure 4.15). This has already been proposed in [54], [55], where one motor design had iron bridges placed underneath the rotor cage. Yet, bridges are now also placed at the air gap, which means that an opening causes a slotting effect that is not actually present in the unsaturated case.

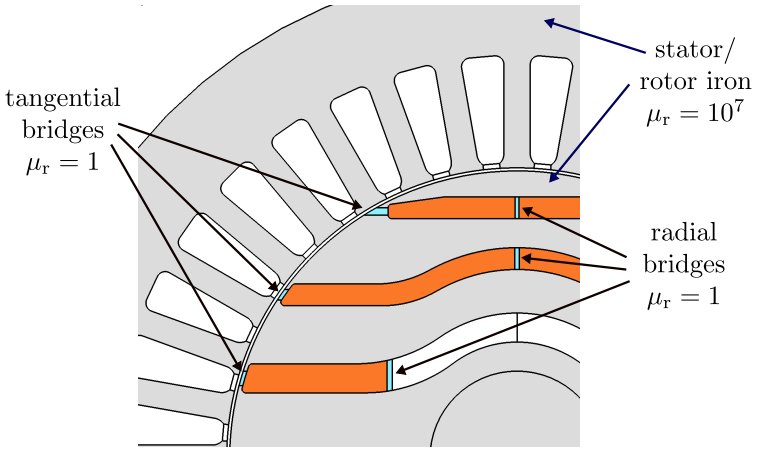

Figure 4.15: Open rotor iron bridges (highlighted in light blue) in Motor II to avoid magnetic short-circuits in the inductance calculation with constant permeability.

Nevertheless, it can be expected that the results will not deviate too much. The slotting effect will also occur in the non-linear case, where the saturated iron bridges will have a small relative permeability. The harmonics that also occur in the air gap field and cause a reaction of the stator and rotor currents therefore also occur in reality. Only the amplitude of the individual frequency components will differ depending on the saturation state. However, if the slot width is well-chosen, it comes relatively close to reality for many operating points. This topic will be further explained in the validation section.

Each element of the inductance matrix is then calculated by impressing a current in the respective stator phase or rotor loop and evaluating the flux linkages off all coils of the system. The total inductance matrix is calculated as a function of the rotor angle ϑ_r for a sufficient number of discrete sampling points (one step per $1°_{\text{mech}}$, for example). This allows for consideration of space harmonics caused by the stator slots and saturated rotor bridges. Because in this thesis the rotor cage geometry differs from standard cages, the definition of rotor loops and the inductance calculation is illustrated for three different cases and N_L=1 as an example in Figure 4.16.

As can be seen, the calculation for the self- and mutual inductances of the stator phases is straightforward (Figure 4.16 left). For the example of the second rotor loop (middle), the top figure shows the current densities in both contiguous bars. This results in a magnetic flux distribution mostly in between both flux barriers, as shown in the bottom figure. This behavior can also be observed for almost all other loops. Only those consisting of the bars in the outermost flux barriers show fundamentally different field lines (right). As indicated by the figure on the bottom right, the flux is now forced to

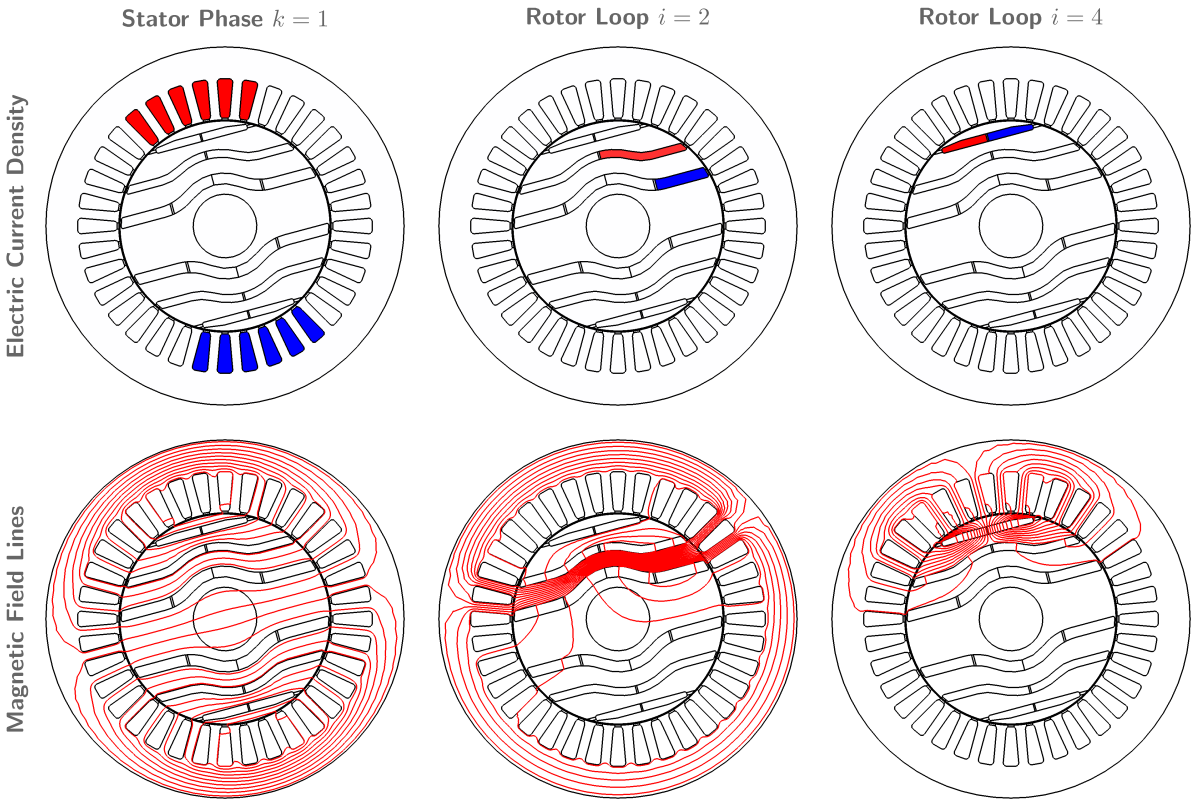

Figure 4.16: Illustration of the inductance calculation of Motor II for the first stator phase and two different rotor loops at a rotor angle of $\vartheta_\mathrm{r} = 0°_\mathrm{mech}$ with N_L=1 layer. A current of 1 A is impressed in the respective stator phase or rotor loop (top row), which results in a magnetic field as indicated by the magnetic field line plots (bottom row). The self-inductance of the respective phase or loop and all mutual inductances are then obtained by evaluating the flux linkages.

flow vertically through the flux barrier due to the impressed currents on both sides. This is a particular feature of the modern rotor cage design.

Comparing the resulting inductance functions, the need for a sufficient number of discrete steps for the rotor angle becomes obvious. Figure 4.17 displays selected elements of the inductance matrix of Motor II versus the rotor angle. The angle was varied in $1°_\mathrm{mech}$ steps. Note that the indices l and l' have been removed for the sake of simplification because the rotor cage is only modelled with 1 layer.

Looking at the stator self-inductance $L_{\mathrm{s,s,1,1}}$ in Figure 4.17a, the typical shape for a reluctance machine is observed. At $\vartheta_\mathrm{r} = 0°_\mathrm{mech}$, the flux is aligned with the d-axis of the rotor, so the inductance is at its maximum. If the rotor angle is increased, the inductance decreases until it finally reaches its minimum at $90°_\mathrm{mech}$. At this angle, the flux vector is exactly aligned with the q-axis. From $0°_\mathrm{mech}$ to $360°_\mathrm{mech}$, the two-pole motor therefore has two maxima and two minima.

From the data in the same plot, it is also apparent that the inductance varies due to the slotting effect of the rotor. It is influenced by the relative position of the rotor to the stator slots. Taking these minor changes into account is crucial for the consideration of space harmonics.

This can also be seen in the mutual inductances from the rotor to the stator, two selected examples of which are shown in Figure 4.17b. Especially for $L_{\mathrm{s,r,1,2}}$ (light blue)

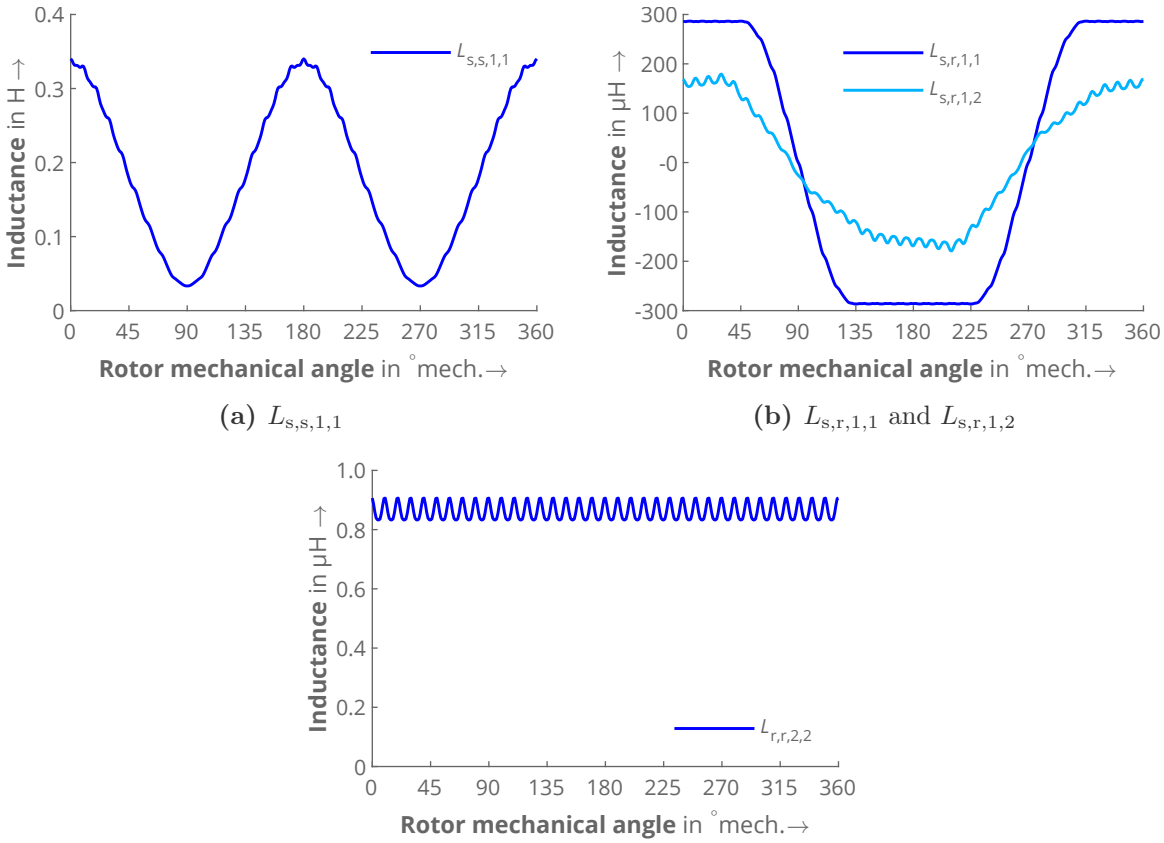

(a) $L_{\mathrm{s,s,1,1}}$ **(b)** $L_{\mathrm{s,r,1,1}}$ and $L_{\mathrm{s,r,1,2}}$

(c) $L_{\mathrm{r,r,2,2}}$

Figure 4.17: Selected elements of the inductance matrix of Motor II for N_{L}=1 as a function of the rotor angle ϑ_{r} calculated with linear 2D magnetostatic FEM. The function is evaluated for steps of 1°mech and then interpolated with monotone spline-interpolation.

the slotting effect is obvious. But also the plot of $L_{\mathrm{s,r,1,1}}$ (dark blue) reveals a slight influence of the slotting.

The effect caused by the stator slots are best highlighted with the self-inductance of the second rotor loop, shown in Figure 4.17c. The function is periodic for 10°, which equals the stator slot pitch. This is hence a good measure for the maximum step size, since the inductance for one slot pitch should be modelled with enough discrete steps.

Regarding the time needed to obtain the full matrix for a discrete number of sample points, it is best to use symmetries to minimize the computing time. The total number of single FE evaluations is $(m + 2N_{\mathrm{FB}}N_{\mathrm{L}})$ multiplied by the number of discrete steps for the rotor angle. In the case of Motor II with 3 stator phases and 12 rotor loops in N_{L}=1 rotor cage layer, there would be already

$$(3 + 12 \cdot N_{\mathrm{L}}) \cdot 360 = 15 \cdot 360 = 5400$$

evaluations. The need to have at least N_{L}=2 layers for considering the skin effect further increases this number.

4.2.7.2 Saturation factors

The calculation method for the saturation factors introduced in section 4.2.5 will be explained in more detail in this section. Furthermore, the method to account for iron bridges in the rotor will be discussed.

The general procedure for calculating the saturation factors has already been explained: A reference is required for the linear and for the non-linear flux linkage function. Both are a function of the magnitude I and angle γ of the stator current space vector. For the linear reference, it makes sense to use the previously calculated inductance matrix to obtain the sample points:

$$\Psi_{\mathrm{s,d}}(I,\gamma)_{\mu=\mathrm{const.}} = \mathbf{L}\vec{I}. \tag{4.49}$$

This is far more efficient than calculating each point with the 2D magnetostatic FEM, even if it is only a linear model.

The non-linear reference $\Psi_{\mathrm{s,d}}(I,\gamma)_{\mu=\mathrm{f(B)}}$ is then calculated with non-linear FEM. A parameter study is defined to vary the magnitude and the angle of the current space vector.

In both cases, the resulting flux linkages of the three stator phases are then transformed to a flux linkage space vector, to obtain its d- and q-component by applying Park's transform. Finally, Equation (4.28) is applied, which yields the saturation factors of both axes.

Furthermore, it should be noted that the result also depends on the relative position of the stator and rotor. This is due to the slotting effects that cause a changing flux linkage space vector for different rotor positions, which was already discussed for the inductance calculation. Figure 4.18 shows examples of the resulting functions for three different current angles and their sample points. This figure clearly proves that the sample points for different rotor positions deviate from the mean value, especially in the non-linear range of the function and at higher current angles.

The following recommendation can be derived from this finding: Depending on the desired accuracy, several sample points for the rotor angle per I,γ pair must be calculated. For the sake of visualization, 25 points were calculated in this case. However, a number of 5 points or more should be sufficient without losing too much accuracy.

A closer look at the two graphs reveals another fact: The flux linkage of the d-axis is zero at an angle of 90°$_{\mathrm{el}}$, since there is only flux in the q-axis (Figure 4.18a). Conversely, this also applies to the flux linkage of the q-axis for a pure d-axis flux at 0°$_{\mathrm{el}}$ (Figure 4.18b). As this is also the case in the linear reference, the saturation factors cannot be calculated for these respective angles.

For this reason, the following solution is proposed: The saturation factors for the respective angles are interpolated from those of the nearest calculated angles. This means that the saturation factors of the d-axis in this case are determined from those for 80° and 100°. Likewise, the functions for -10° and 10° are used for the q-axis. Due to the symmetry, both neighboring functions are the same in each case, which is why the corresponding values can simply be adopted.

As the flux flows mainly along the other axis at these points, the estimated saturation factor only has a minor influence on the result. This is to be expected for intermediate values as well (that is, between 0 and 10°$_{\mathrm{el}}$ for the q-axis factor or between 80 and 90°$_{\mathrm{el}}$ for the d-axis factor). Although the flux of the orthogonal axis increases here, it is too small to have a significant influence on the result. Moreover, it is to be expected that the interpolated value will be close to the real value anyway.

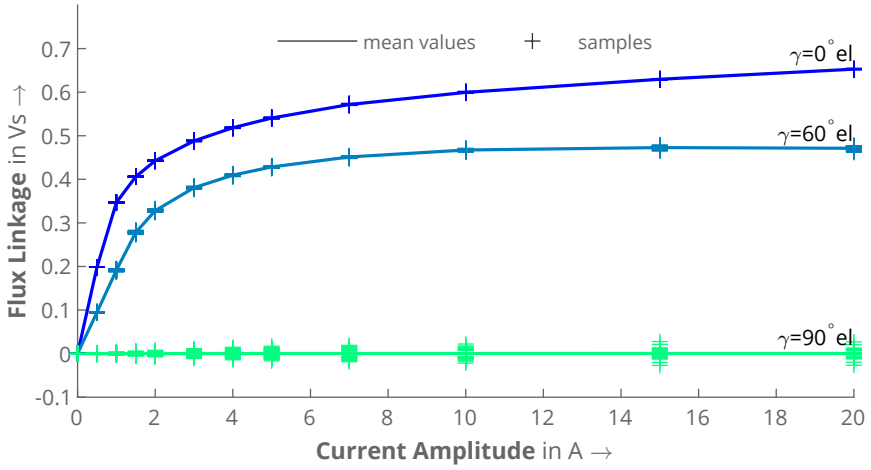

(a) d-component of flux linkage

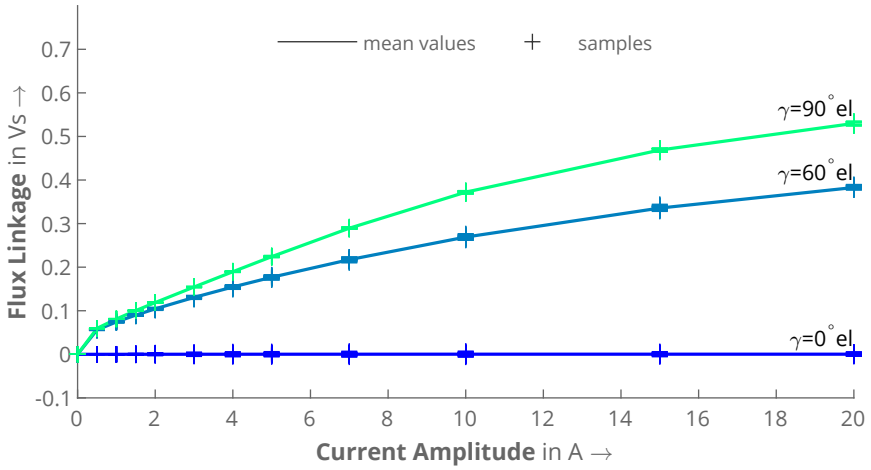

(b) q-component of flux linkage

Figure 4.18: Evaluation of the flux linkage components of d- and q-axis for different stator current space vectors which are rotated over time. The sample points are marked with '+' and the function evaluated from their mean values is drawn with a solid line.

Similarly, the saturation factors for a current of 0 A (regardless of the current angle) are also taken from the smallest calculated current value. The assumption about the minimum deviation of the real value applies here as well.

A recommendation can also be made about interpolation in the model: Since in the final system of equations from (4.44) the inverse of the saturation factors are needed, they can already be used for interpolation. As shown in Figure 4.19, the functions of both factors

$$k_{\mathrm{sat,d}} = \frac{1}{\Lambda_{\mathrm{sat,d}}} \qquad \text{and} \qquad k_{\mathrm{sat,q}} = \frac{1}{\Lambda_{\mathrm{sat,q}}}$$

are significantly smoother and can therefore be properly interpolated even with fewer interpolation points.

Moreover, it is worth mentioning that the magnitude of the current vector can be converted to an MMF to take different windings into account. This makes it possible for the design process to adapt the winding without having to recalculate the saturation reference.

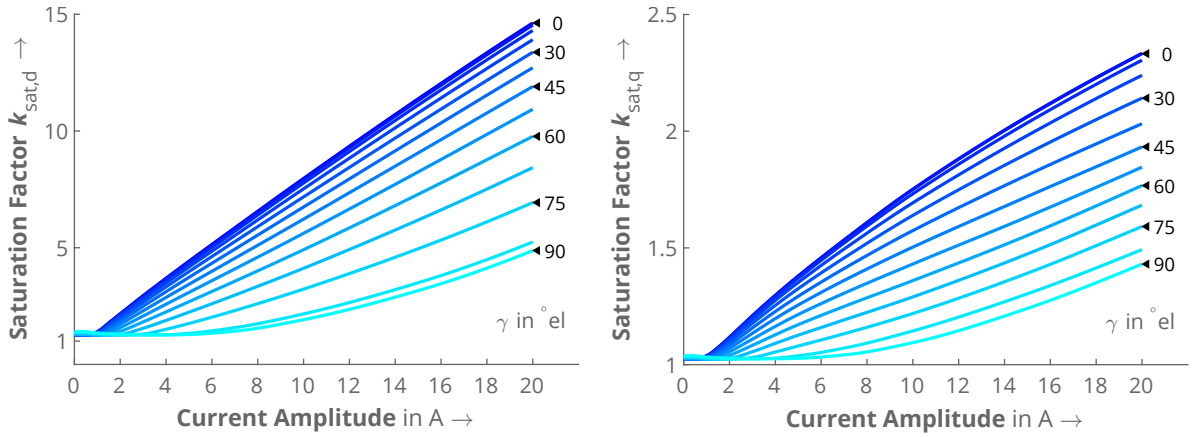

(a) d-axis saturation factor

(b) q-axis saturation factor

Figure 4.19: Saturation factor functions $k_{\mathrm{sat,d}}$ and $k_{\mathrm{sat,q}}$ for the d- and q-axis evaluated as the relation between linear and non-linear current-flux linkage components (corresponding to Figure 4.12). Note that the y-axes do not have the same scaling.

Turning now to the consideration of iron bridges in the rotor, a further improvement compared to the existing model can be introduced. As explained in the previous section on the inductance calculation, the iron bridges should only be opened in the linear reference. If the non-linear reference is calculated according to the real machine geometry, the saturation factor compensates for the following two effects: First, the rotor slots due to open tangential bridges in the linear reference and their effect of increasing the carter factor. Secondly, the increased magnetizing current, as the iron bridges also have to be magnetized.

In contrast, the saturation factors cannot influence the harmonic content that is caused by different saturation states of the iron bridges. This also depends on both the magnitude and angle of the stator current space vector, as well as on the rotor currents, which creates leakage flux flowing through the thin iron parts of the q-axis. Because the saturation factors only manipulate the fundamental of the flux linkage, the reaction of the stator due to the rotor slots will only be related to the chosen slot width in the linear reference and the respective leakage flux.

Therefore, a slight error will always remain, which cannot be avoided with this method. However, it is minimized as much as possible, if the real machine geometry is used as non-linear reference.

Lastly, it is to mention that the proposed method in [54], [55] is flawed when it comes to the saturation of leakage inductances. While it is reasonable to exclude the end winding leakage inductances from the saturation factor adaption, it is not clear why this is applied for the slot leakage inductances as well. The end winding leakage inductances, on the one hand, are not included in the 2D FE model and it can be assumed that they do not change due to saturation because the end windings are mostly surrounded by air (or materials in which $\mu_{\mathrm{r}} \approx 1$). The slot leakage inductances, on the other hand, are indeed included in the 2D reference, which means the result of the non-linear current-flux linkage function implicitly includes the saturation of leakage paths for no load operation.

As correctly mentioned by Güdelhöfer [54], [55], however, this does not apply for operating points where $s > 0$. In these cases, the leakage path saturation massively depends on the damping of the stator magnetic field due to the rotor magnetic field. In

this model, however, this damping effect and the resulting saturation is approximated with the method of a virtual stator magnetizing current vector. Hence, it will be worked out in the validation section, to which extent the model is still valid. In general, it would be possible to account for these effects with leakage saturation factors as presented in [96], [97].

4.3 Mechanical machine model

To model the mechanical subsystem, the equation of motion, which is the same as for the Finite Element model in (3.27) is added to the full system of equations:

$$\frac{\mathrm{d}\omega_\mathrm{r}}{\mathrm{d}t} = \frac{T_\mathrm{el} - T_\mathrm{load}}{J_\mathrm{tot}}. \tag{4.50}$$

Again, the mechanical angular velocity is evaluated from the time-derivative of the rotor angle ϑ_r:

$$\omega_\mathrm{r} = \frac{\mathrm{d}\vartheta_\mathrm{r}}{\mathrm{d}t}. \tag{4.51}$$

However, the calculation of the electromagnetic torque T_el is different from FEM because the air gap field is unknown.

In this model, the method of virtual work is applied. This approach has been derived for a numerical parameter model containing currents and flux linkages in [54], [55] based on [98]:

$$T_\mathrm{el} = \frac{1}{2}\left(\vec{i}^\mathrm{T}\frac{\mathrm{d}\vec{\psi}}{\mathrm{d}\vartheta_\mathrm{r}} - \vec{\psi}^\mathrm{T}\frac{\mathrm{d}\vec{i}}{\mathrm{d}\vartheta_\mathrm{r}}\right). \tag{4.52}$$

4.4 Solution

As a final step before validating the model, this section explains the solution procedure that was used for this thesis to provide a fast and reliable simulation. The model is implemented in MATLAB® [99].

At first, the initial conditions at $t = 0$ need to be defined for every state variable. These are:

$$\vec{\psi}(0) = \vec{\psi}_0 = \vec{0}, \qquad \text{and} \qquad \omega_{\mathrm{r},0} = 0, \tag{4.53}$$

whereas the rotor angle $\vartheta_{\mathrm{r},0}$ can be set to a desired value. Moreover, it makes sense to define the initial values of the saturation factors. As stated above, the values can differ due to the different magnetic permeability in the reference calculations. Hence, a small current at an arbitrary current angle can be used to interpolate reasonable initial values.

To solve the initial value problem, MATLAB® offers a wide variety of ODE solvers. However, in this model the saturation state defined by the non-linear current-flux linkage function (4.36) needs to be iterated. This is because the saturation factors used in the equation depend on its results. The fact that the standard solvers do not use values of previous time steps despite the state variables, makes this iteration process too time-consuming. To obtain a comprehensive model that uses knowledge of previous time steps and that fulfills the requirements, it is therefore recommended not to use the standard solvers.

Instead, the solution can be as simple as presented in the existing model: The predictor-corrector-method [100] provides a reliable algorithm that is suited to this kind of model. In this case, the fourth-order Adams-Bashforth method is used for the predictor, and the fifth-order Adams-Moulton method for the corrector. The disadvantage that the step size is usually fixed is compensated for by the knowledge of values of previous time steps, which avoids time-consuming iteration steps for the saturation factors. In addition, if the predict-evaluate-correct-evaluate (PECE) strategy is applied, the model will be numerically stable. This is explained again in detail below to clarify the function of the model and the relationships between the individual variables.

Figure 4.20 illustrates the implemented solution procedure. First, the inductance matrix has to be interpolated from the lookup table for the current rotor angle. This is then used to iterate the current-flux linkage function (4.42) in a subprocess, which will be explained below. After finding the appropriate current for the given flux linkage, the full system of equations (4.44) can be evaluated for the time derivative of the flux linkage. Since the current vector is already known, $\mathbf{R}\vec{i}$ can be directly evaluated.

Only after the electromagnetic system of equations has been solved is the torque evaluated and finally the mechanical system of equations from (4.50) solved. This is a reasonable simplification because it can be assumed that the electromagnetic time constants are significantly smaller than the mechanical ones. Finally, all the values found can be saved, and the next time step can be solved.

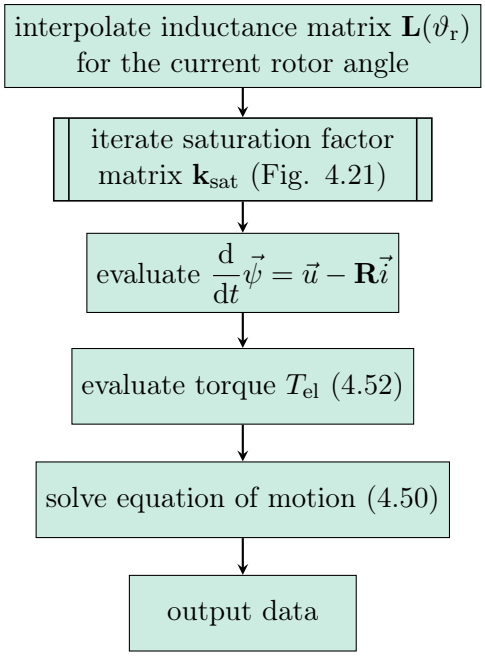

Figure 4.20: Solution process of the proposed model for one evaluation in one time-step.

Moving on now to the iteration process of the current-flux linkage function, which is illustrated in Figure 4.21. As discussed in Section 4.2.7, the end-winding leakage flux of stator and rotor are not influenced by saturation. Before the first iteration, the end winding leakage inductance matrix $\mathbf{L}_{\sigma\mathrm{e}}$ therefore must be subtracted from the inductance matrix $\mathbf{L}$. This leaves only the inductance matrix, which was calculated using FEM:

$$\mathbf{L}_\mathrm{FEM} = \mathbf{L}_\delta + \mathbf{L}_{\sigma\mathrm{s}} = \mathbf{L} - \mathbf{L}_{\sigma\mathrm{e}} \tag{4.54}$$

Then, the loop for iterating the current flux linkage function is entered, where ν is the current iteration step. First, the saturation factor matrix $\mathbf{k}_\mathrm{sat}$ is calculated for the current factors $k_\mathrm{sat,d}^{(\nu)}$ and $k_\mathrm{sat,q}^{(\nu)}$. This means that the dq0-matrix of the stator is transformed to an abc-matrix according to (4.32) with the current rotor angle ϑ_r. Furthermore, the rotor saturation factor matrix is constructed, whereby each diagonal element is evaluated according to (4.34).

Then, only the stator matrix $\mathbf{k}_\mathrm{sat,s}$ is being used to calculate the virtual stator current vector $\vec{I}_\mathrm{s}^*$ (4.38).

Next, the vector is transformed to a space vector to obtain its magnitude and angle, which can be used to interpolate the corresponding saturation factors $k_\mathrm{sat,d}(I_\mathrm{s}^*, \gamma^*)$ and $k_\mathrm{sat,q}(I_\mathrm{s}^*, \gamma^*)$. Because they are stored in a 2D lookup table, a simplified 2×1D interpolation is recommended: First, the saturation factor is interpolated as a function of the current for the current angle γ^*. Second, its value is interpolated for the input current I_s^*. For this purpose, as well as for any other interpolation in this model, the Piecewise Cubic Hermite Interpolating Polynomial (PCHIP) was used [101], [102]. It is monotone and has no overshoot between the sample points.

In the following, the saturation factors are compared to the ones used in the current iteration step:

$$\epsilon > |k_\mathrm{sat,d}(I_\mathrm{s}^*, \gamma^*) - k_\mathrm{sat,d}^{(\nu)}| \quad \wedge \quad \epsilon > |k_\mathrm{sat,q}(I_\mathrm{s}^*, \gamma^*) - k_\mathrm{sat,q}^{(\nu)}|. \tag{4.55}$$

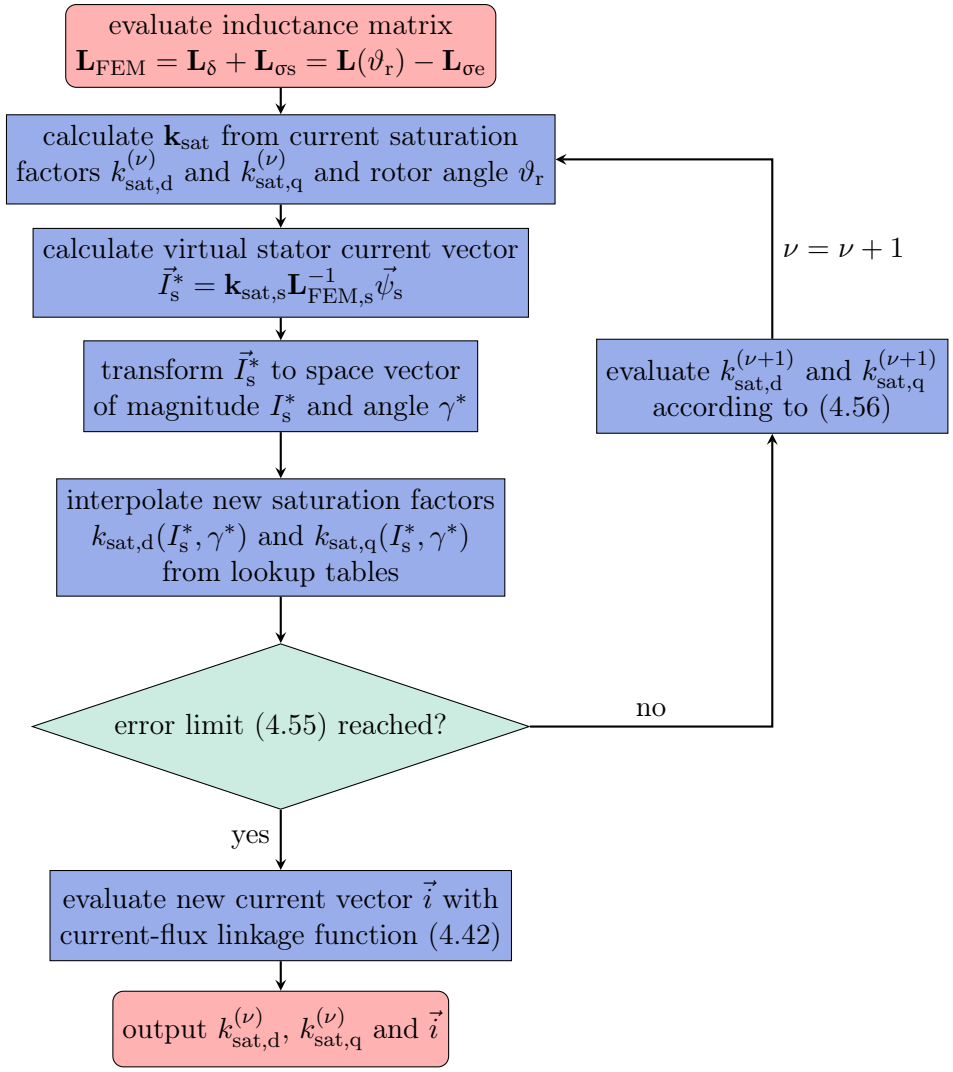

Figure 4.21: Subprocess for the iteration of the non-linear current-flux linkage function.

If they exceed the error limit ϵ, the saturation factors are adjusted using the relaxation method:

$$k_{\mathrm{sat,d}}^{(\nu+1)} = k_{\mathrm{sat,d}}^{(\nu)} + \alpha \left(k_{\mathrm{sat,d}}(I_{\mathrm{s}}^{*}, \gamma^{*}) - k_{\mathrm{sat,d}}^{(\nu)} \right), \tag{4.56}$$

where α is the relaxation factor. Experience has shown that it can be set to 1, which ensures rapid convergence. However, if convergence problems arise, it should be reduced. As soon as the new values are found, the iteration counter ν is incremented and the process starts again with the evaluation of $\mathbf{k}_{\mathrm{sat}}$.

If the evaluation in (4.55) yields that the error limit is reached, however, the saturation factors $k_{\mathrm{sat,d}}^{(\nu)}$ and $k_{\mathrm{sat,q}}^{(\nu)}$ are saved. Finally, the new current vector can be calculated from the current-flux linkage function and all three quantities can be saved. The process then goes on as illustrated in the previous diagram in Figure 4.20.

Regarding the step-size of the solver, the same recommendations as for the FE model in Section 3.8 have proven useful. Hence, for an accurate simulation, 500 steps per cycle are recommended. Yet, 300 steps are also possible, even though the higher harmonics will not be modelled as accurate.

4.5 Validation with FEM

The aim of this section is to validate the model that has been introduced in this chapter. As in Section 3.9 for the FE model, the validation will be carried out step by step. This means that the goal is to focus initially on selected effects rather than comparing the final model with the results. This way, it is possible to distinguish between the influence of each effect on the accuracy of the model.

For this purpose, the Finite Element Method is used as a reference. It allows activating and deactivating various effects as required. Moreover, it provides a much better insight into the machine quantities than measurements. As it has already been validated for the motors to be studied, a reliable validation process without the immediate need for measurements is guaranteed. Only after the entire model matches sufficiently to FEM, the results of the model must be compared with measurements to determine the remaining deviations from reality. Hence, this section starts with the validation of the skin effect, then moving on to the validation of saturation, and finally both combined.

Numerous validation steps were carried out for this work. In this section, the most important ones are discussed to clarify the procedure and to examine the accuracy and validity of the model. Further possibilities that go beyond those presented are mentioned at the relevant point.

4.5.1 Validation of the skin effect model

To validate the skin effect, it is best to use a linear model, that is, saturation is not considered. Therefore, the material properties of the Finite Element model are defined as linear, whereby the permeability is set to $\mu_\mathrm{r} = 10^7$ as has been done for the parameter calculation of the model. Again, the bridges in the rotor have to be opened to avoid magnetic short-circuits. In the model, the saturation factors are set to 1.

To check whether the implementation itself is correct, the validation should be started with the stator equations only, that is, the rotor cage is inactive. If the model provides accurate results for different speeds (including $n = 0$ and $n = n_0$), the rotor equations are activated. Now the skin effect influences the results.

However, before testing the complete rotor cage model, the end ring elements (resistances and inductances) should be set to zero. Moreover, the FE model should be implemented so that it models the skin effect correctly in the first step. This way, the accuracy of the layer method can be tested for the real current density distribution in the rotor bars. Only if these results are satisfactory, the full cage model should be tested. This also requires FEM to incorporate the layer method for the accurate modeling of the end rings.

In addition, the comparison should initially focus on a locked rotor ($n = 0$), as this is where the skin effect is most pronounced. As with the locked rotor measurements in Section 3.9.3, both the FEM and the model are simulated until the transients have disappeared. The model can be tested with different numbers of rotor cage layers N_L. To evaluate the validity and accuracy of the method, stator currents and rotor cage losses P_cage are compared for one electrical period in the steady state. Other quantities, such as flux linkages, EMFs and rotor currents can be compared as well. As the rotor losses at standstill are proportional to the torque, it is not compared separately. For a better illustration, only the current of the first stator phase is compared.

4.5.1.1 Motor II

The validation starts with Motor II. Even though the comparison for a different number of layers has already been presented in Chapter 3, the Finite Element Method also offers the possibility of comparing losses and other variables over time.

Figure 4.22 therefore shows the comparison between FEM and the model for N_L=1 and N_L=3 layers. As mentioned, the end-ring parameters are set to zero. The results for 1 rotor cage layer (Figure 4.22a) indicate that the stator current already fits good. However, the rotor cage losses are underestimated by the model. Furthermore, a phase shift between FEM and the model is observable, which also comes from the incorrect rotor resistance due to skin effect.

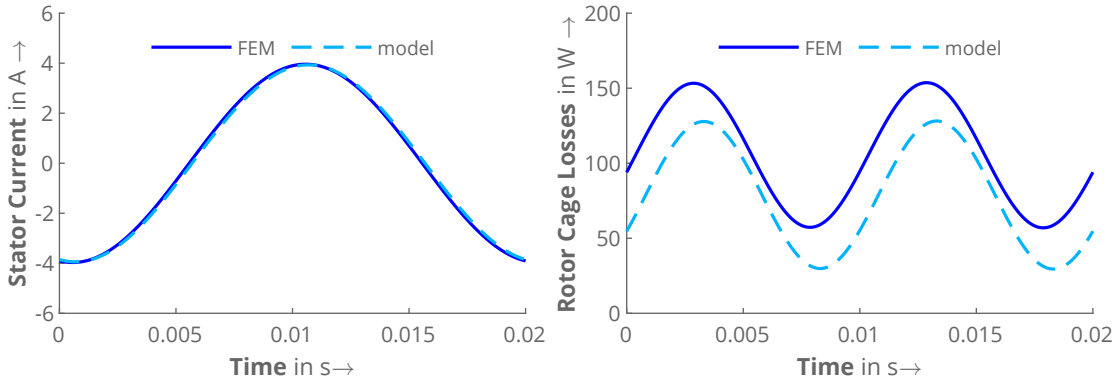

(a) FEM: physical (without layers), model: 1 layer

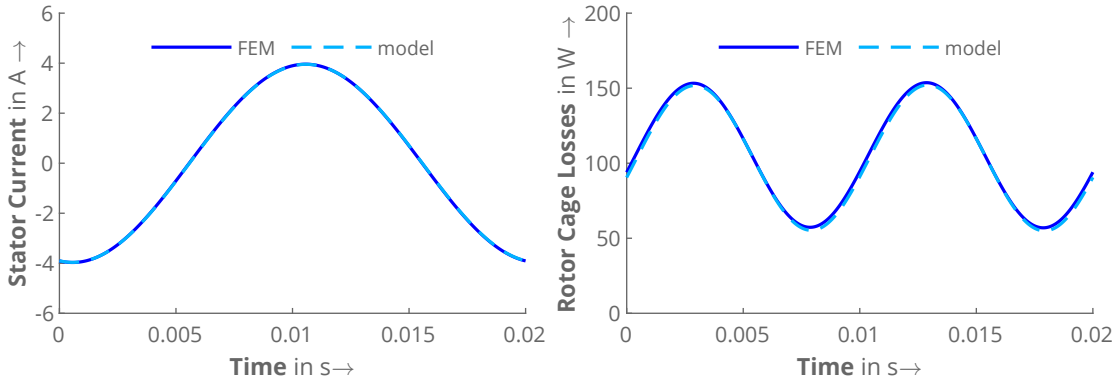

(b) FEM: physical (without layers), model: 3 layers

Figure 4.22: Stator current and rotor cage losses over time in comparison between FEM (physical model without layers) and the model with 1 and 3 rotor cage layers for Motor II at $U = 100\,\mathrm{V}$, $f = 50\,\mathrm{Hz}$, and $n = 0$. Saturation is neglected, end-ring parameters are set to zero.

If the number of layers is increased to N_L=3 as shown in Figure 4.22b, the stator current fits exactly the results of FEM. The rotor cage losses also show a good agreement. The deviation of the mean value over one electrical period decreased from -25.2% with 1 layer to -1.7% with 3 layers. The phase shift between both results is now minimal. From this, it can be concluded that 3 layers are sufficient in this case, as a further increasing the number of layers would only lead to an increase in computing time without significantly improving accuracy. This also confirms the result of the investigation using time-harmonic FEM in Figure 4.3.

The same validation can be carried out for different values of the stator frequency and the conductivity of the rotor bar. As the frequency or conductivity increases, the

influence of the skin effect increases so that the limitations of the model can be tested. Similarly, a reduction in both values results in a less pronounced skin effect. However, as the comparison for 50 Hz meets the expectations for the desired parameters, no further comparison needs to be shown at this point.

In the next step, the full rotor cage model will be tested, which means that the end-ring parameters are now set to their values according to the presented ring model. This also means that the FEM reference is now equally simulated with 3 layers in the rotor cage. The skin effect in the rotor bars (and the ring) is therefore only with the same layer method in both cases. The results are shown in Figure 4.23.

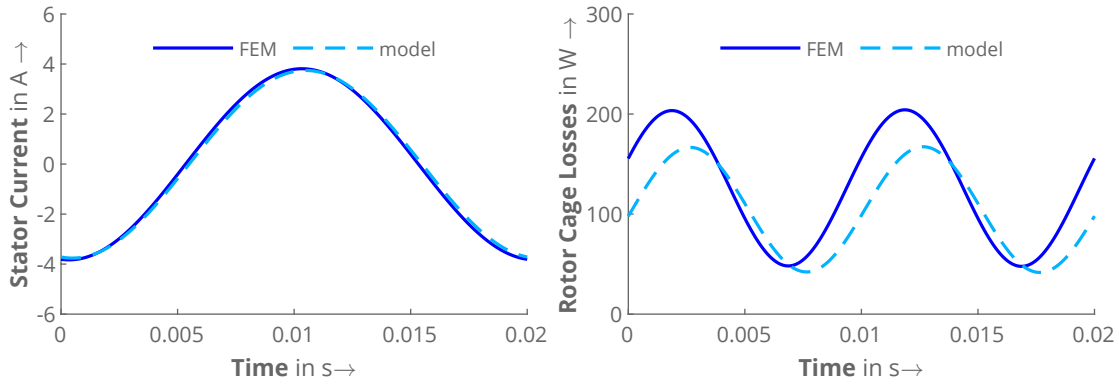

(a) FEM: 3 layers, model: 1 layer

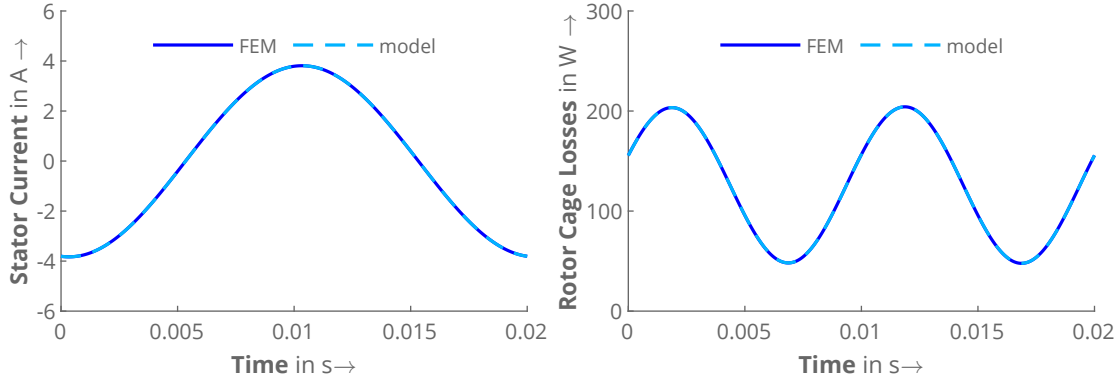

(b) FEM: 3 layers, model: 3 layers

Figure 4.23: Stator current and rotor cage losses over time in comparison between FEM (3 layers) and the model with 1 and 3 rotor cage layers for Motor II at $U = 100\text{V}$, $f = 50\text{Hz}$, and $n = 0$. Saturation is neglected, end-ring parameters are set to their respective values from the presented end-ring model.

Here, both results show the same overall behavior as in the previous comparison. However, it is noticeable that the rotor cage losses in the model with 3 layers now fit even better than in the previous comparison. This is because both rotor cages are modelled in the same way with the layer method.

As the results for standstill were satisfactory, the model can be tested for a speed greater than 0 in the next step. In principle, the skin effect is less pronounced with decreasing slip frequency, until finally the fundamental wave has 0 Hz at synchronous speed. However, currents of higher frequencies still flow in the rotor cage at this point, which also produce losses.

Figure 4.24 shows the comparison of stator current and rotor cage losses, again for 1 and 3 rotor cage layers. What stands about the figures are two things: On the one hand, the stator current has significantly higher harmonics, as the stator and rotor slots move relative to each other. This is modelled accurately by the model, as the current fits exactly the reference. On the other hand, the harmonic rotor cage losses are modelled more accurate with N_{L}=3 layers as well.

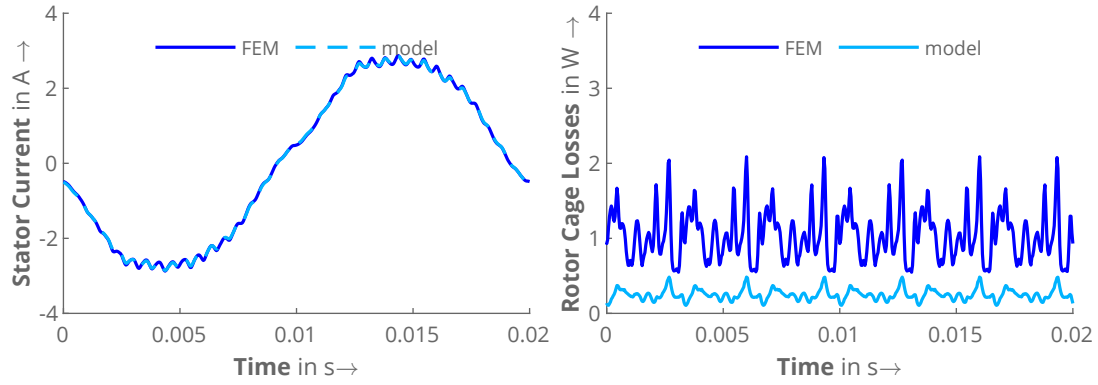

(a) FEM: 3 layers, model: 1 layer

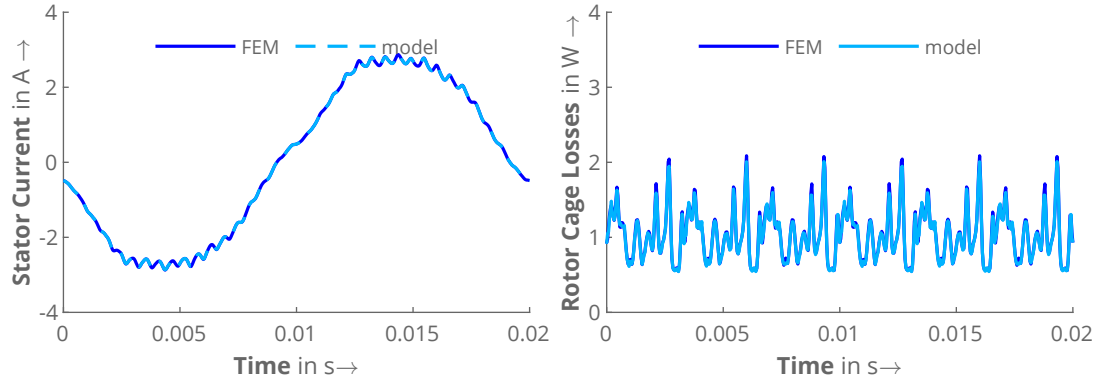

(b) FEM: 3 layers, model: 3 layers

Figure 4.24: Stator current and rotor cage losses over time in comparison between FEM (3 layers) and the model with 1 and 3 rotor cage layers for Motor II at $U = 100\,\mathrm{V}$, $f = 50\,\mathrm{Hz}$, and $n = 3000\,1/\mathrm{min}$. Saturation is neglected, end-ring parameters are set to their respective values from the presented end-ring model.

Looking at the rotor cage losses for 1 layer in Figure 4.24a, it is obvious that the losses are underestimated when the rotor resistance does not consider for skin effect. This is because the rotor currents of harmonic frequencies have a much smaller skin depth [85], which means the effective resistance is higher for harmonic currents. In the model with 3 rotor cage layers, the current that is assumed to be flowing only in the outermost rotor cage layer already sees this higher resistance, which is why the results fit much better (Figure 4.24b).

4.5.1.2 Motor III

Moving on now to the validation of Motor III. Figure 4.25 displays the results for the comparison of the linear calculation with a locked rotor for 3 layers in both models. As expected, the current and the rotor losses match the FEM reference exactly.

The results are also satisfactory at synchronous speed. The stator current, including the higher harmonics, is reproduced precisely. The rotor cage losses show only a minimal

deviation from the high-frequency curve that can be seen in FEM.

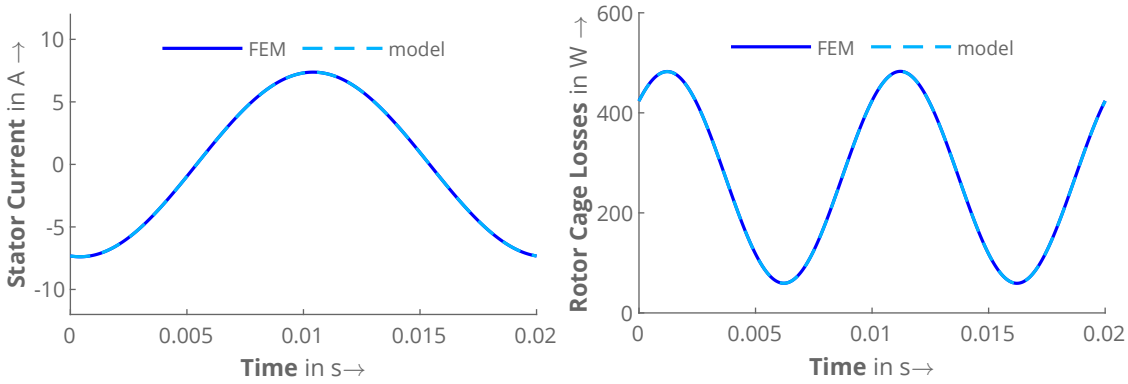

Figure 4.25: Stator current and rotor cage losses over time in comparison between FEM (3 layers) and the model with 3 rotor cage layers for Motor III at $U = 100\,\mathrm{V}$, $f = 50\,\mathrm{Hz}$, and $n = 0\,1/\mathrm{min}$. Saturation is neglected, end-ring parameters are set to their respective values from the presented end-ring model.

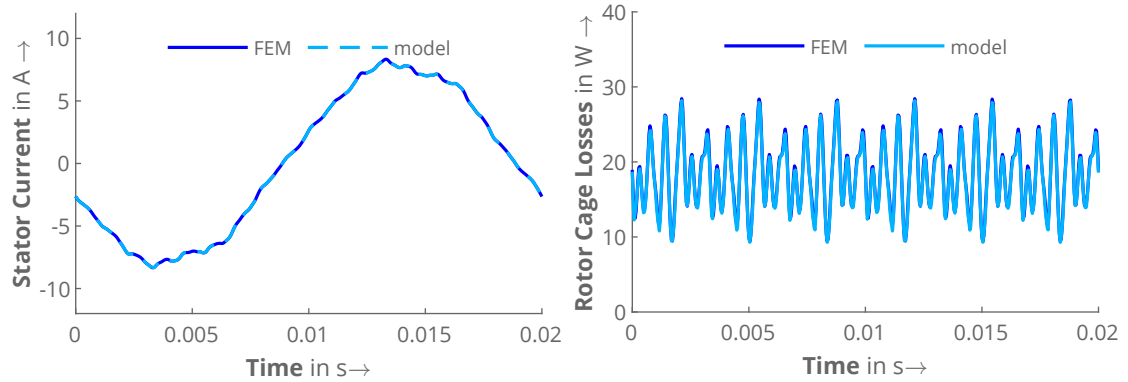

Figure 4.26: Stator current and rotor cage losses over time in comparison between FEM (3 layers) and the model with 3 rotor cage layers for Motor III at $U = 100\,\mathrm{V}$, $f = 50\,\mathrm{Hz}$, and $n = 1500\,1/\mathrm{min}$. Saturation is neglected, end-ring parameters are set to their respective values from the presented end-ring model.

All results combined, it can be concluded that the layer method is valid and accurate enough to consider for skin effect in the parameter model. Both motors with non-standard cage geometries, Motor II and Motor III, were investigated in the linear case to prove that the skin effect itself can be considered for arbitrary rotor bars. Hence, the validation is now continued for the method to consider for saturation before combining both methods and finally comparing the model to measurements.

4.5.2 Validation of the saturation model

To validate the saturation model, it is best to compare the motor at synchronous operation, as this is where it saturates the most. Furthermore, the simplified case of a motor without a rotor cage is compared, which offers the advantage that the rotor is entirely currentless. This means that the validity of the dq-saturation factor method can be tested first, before the method to account for rotor currents is validated. This again is an advantage of the Finite Element Method over measurements.

Moreover, the difference between the previously used global saturation factor method and the new dq-saturation factor method introduced in section 4.2.5 is to be made clear. To this end, the results for each model are compared to visualize the improvements.

4.5.2.1 Motor II

Starting with Motor II, three different voltages are compared for two different current angles each. In the first step, the rotor bridges are open. This means that the inductance matrix, the saturation factors, and the FE simulation for comparison are all calculated with the same geometry that has open bridges. This does not reflect reality, but allows an assessment of the accuracy and limitations of the saturation factor method before further simplifications are introduced.

Figure 4.27 shows the first comparison for a voltage of 120 V, which results in a medium saturation. Furthermore, the initial angle of the rotor was set to a value that results in a small current angle, which is $\gamma \approx 10°_{\mathrm{el}}$ in this case. This means that the flux will mainly pass through the rotors d-axis. Hence, the highest saturation is expected for this current angle compared to higher ones (cf. Figure 4.18).

Looking at the stator currents (left figures), it is revealed that the fundamental as well as the harmonics of the current are modelled accurately in both cases. Hence, the saturation in this case does not affect the results too much. The fact that the difference between the existing and the improved model is hardly visible can be explained as follows: Since the current angle is small and the saturation not too high, the saturation state of the q-axis does not influence the results as much. In the plots on the right, it is observable that the saturation factor k_{sat} of the existing model is equal to the factor of the d-axis $k_{\mathrm{sat,d}}$ of the improved model. The q-axis factor in this case is close to 1.

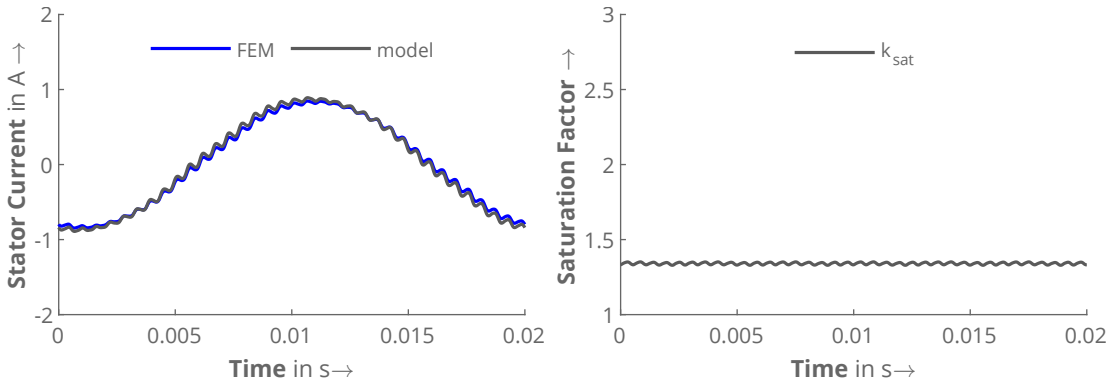

(a) existing model with k_{sat}

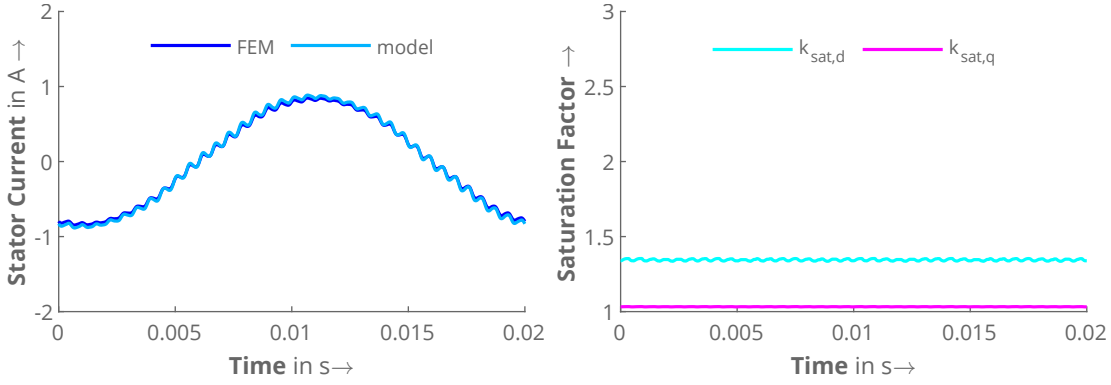

(b) improved model with $k_{\mathrm{sat,d}}$ and $k_{\mathrm{sat,q}}$

Figure 4.27: Comparison of stator currents versus time with FEM (left) and corresponding saturation factors (right) for Motor II at $U = 120\,\mathrm{V}$, $f = 50\,\mathrm{Hz}$, and $n = 3000\,1/\mathrm{min}$ with a resulting current angle of $\gamma \approx 10°_{\mathrm{el}}$: **(a)** existing model with one saturation factor, **(b)** improved model with dq-saturation factors. The rotor cage is inactive, the rotor bridges are open.

The difference becomes more obvious once the voltage is increased. This is shown in Figure 4.28. Now the stator current from the existing model (Figure 4.28a left) has a slight phase shift and its amplitude is too high. Even though for this saturation state the improved model shows a slight deviation as well, the current still fits better.

Yet, the fact that the harmonics are overestimated cannot be avoided with this method. While the FE model can accurately model the local saturation effects that cause the harmonics to change, the saturation factor can only manipulate the fundamental of the current. However, the agreement is still satisfactory, given that the saturation is already high, and the simplified model is still close to FEM.

What also stands out is that the saturation factor now oscillates at a high frequency and with a significantly higher amplitude than before. This occurs because the harmonics of the stator current are significantly higher than before. The magnitude of the real stator current space vector hence varies over a period due to the high-frequency components. As the saturation factor is always calculated from the instantaneous value of the magnitude of the virtual stator current space vector, it shows the same oscillation.

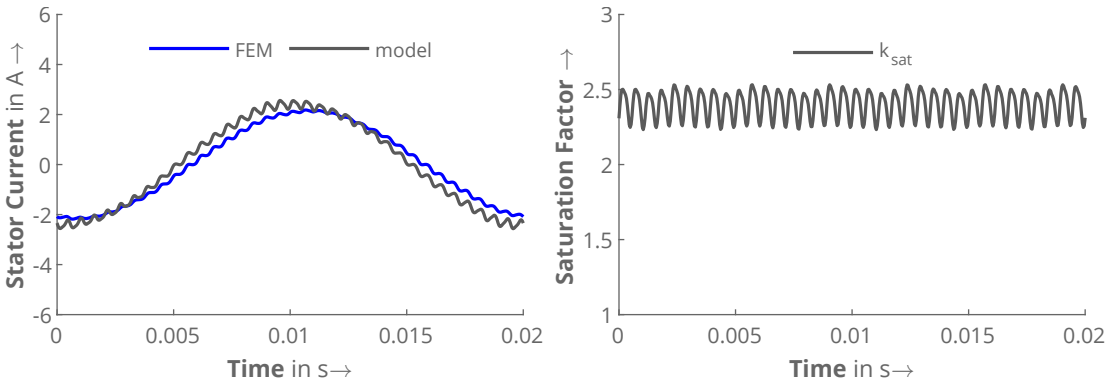

(a) existing model with k_{sat}

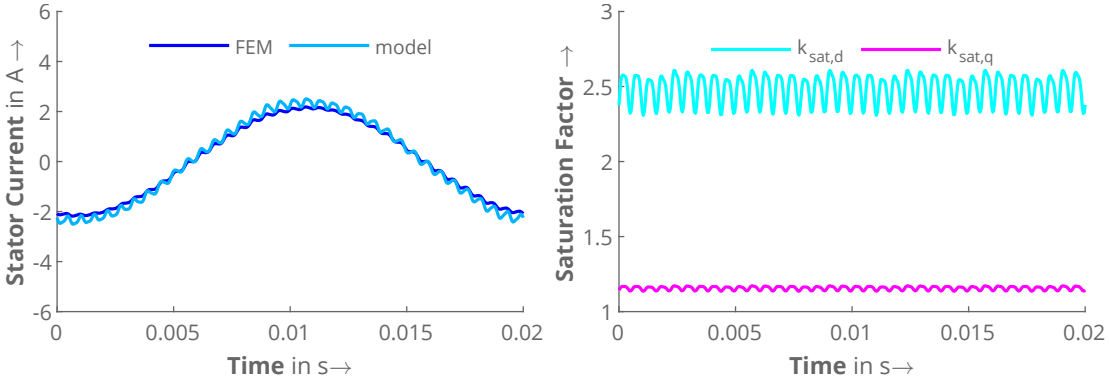

(b) improved model with $k_{\mathrm{sat,d}}$ and $k_{\mathrm{sat,q}}$

Figure 4.28: Comparison of stator currents versus time with FEM (left) and corresponding saturation factors (right) for Motor II at $U = 180\,\mathrm{V}$, $f = 50\,\mathrm{Hz}$, and $n = 3000\,1/\mathrm{min}$ with a resulting current angle of $\gamma \approx 15°_{\mathrm{el}}$: **(a)** existing model with one saturation factor, **(b)** improved model with dq-saturation factors. The rotor cage is inactive, the rotor bridges are open.

In the next step, the initial rotor angle of the simulation is changed, so that the simulation results in an operating point with a current angle that provides a high torque. Due to saturation, the current angle for maximum torque is usually between $50°_{\mathrm{el}}$ and $60°_{\mathrm{el}}$, as has been shown in the synchronous torque measurement in Section 3.9.1.

Figure 4.29 shows the comparison at a voltage of 120 V and a current angle of $58°_{\mathrm{el}}$. The difference between the existing and the improved model is now already visible for this moderate saturation state. The current is overestimated with the one-factor model. Because the flux now flows through both the d- and q-axis, the saturation state of the q-axis is more relevant than before and hence deviates.

In contrast to the existing model, the saturation factors of the improved model (Figure 4.29b right) prove that their saturation states are, in fact, different. The saturation factor of the q-axis is still close to 1. Therefore, the current at the given input voltage is lower than in the case of an equally saturated q-axis, as predicted by the existing model.

The fact that the saturation is lower due to the higher current angle also leads to a better prediction by the improved model. The harmonics now match good, as they are less influenced by the saturation than in the previous case.

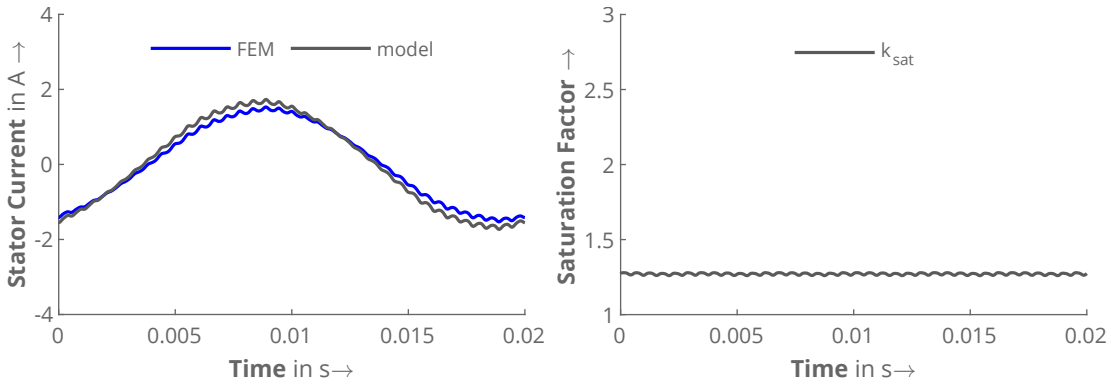

(a) existing model with k_{sat}

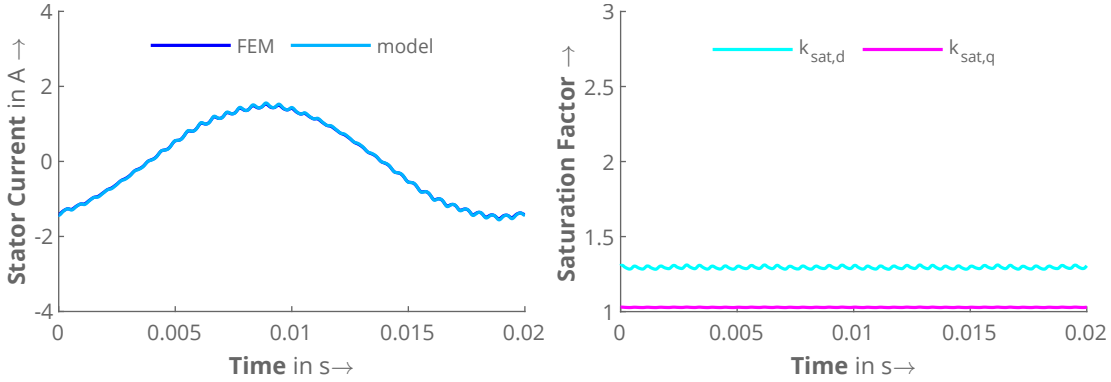

(b) improved model with $k_{\mathrm{sat,d}}$ and $k_{\mathrm{sat,q}}$

Figure 4.29: Comparison of stator currents versus time with FEM (left) and corresponding saturation factors (right) for Motor II at $U = 120\,\mathrm{V}$, $f = 50\,\mathrm{Hz}$, and $n = 3000\,1/\mathrm{min}$ with a resulting current angle of $\gamma \approx 58°_{\mathrm{el}}$: **(a)** existing model with one saturation factor, **(b)** improved model with dq-saturation factors. The rotor cage is inactive, the rotor bridges are open.

Finally, the voltage is again increased to 180 V for this case. The plots in Figure 4.30 clearly indicate that the one-factor model loses its validity. The current with the existing model is too high and shows a phase shift as well. In contrast, the improved model still matches well with the same unavoidable deviation in current harmonics.

Moreover, the dq-saturation factors of the improved model in Figure 4.30b (right) show, what already was discussed in Section 4.2.5: For current angles of this magnitude, the d-axis still saturates significantly. However, the flux in the q-axis only increases with a much higher current as soon as the flux vector rotates from the saturated d-axis to the q-axis (cf. Figure 4.7b). Consequently, it saturates much later and the corresponding saturation factor in this comparison is still significantly smaller. Thus, an overall smaller current is required for the impressed flux linkage with the given voltage.

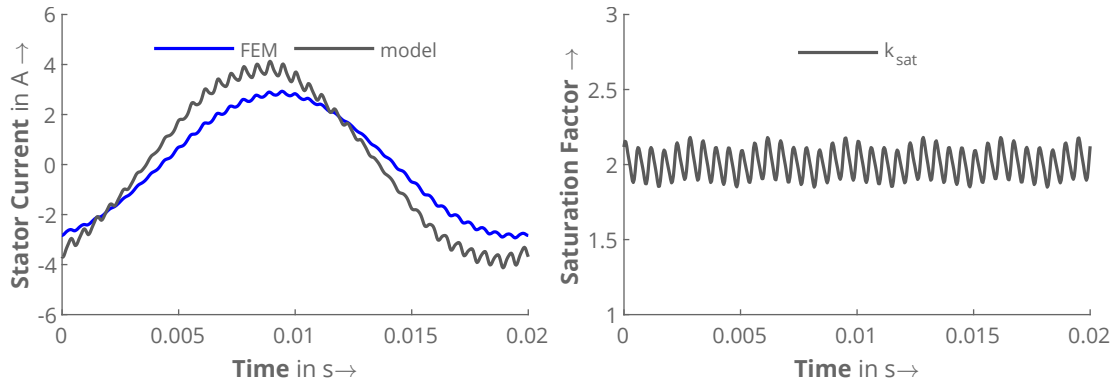

(a) existing model with k_{sat}

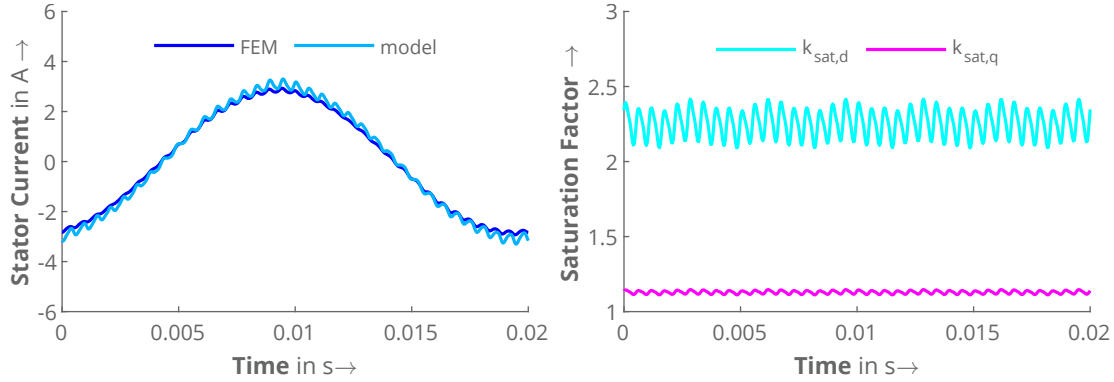

(b) improved model with $k_{\mathrm{sat,d}}$ and $k_{\mathrm{sat,q}}$

Figure 4.30: Comparison of stator currents versus time with FEM (left) and corresponding saturation factors (right) for Motor II at $U = 180\,\mathrm{V}$, $f = 50\,\mathrm{Hz}$, and $n = 3000\,1/\mathrm{min}$ with a resulting current angle of $\gamma \approx 50°_{\mathrm{el}}$: **(a)** existing model with one saturation factor, **(b)** improved model with dq-saturation factors. The rotor cage is inactive, the rotor bridges are open.

In the next step, the simulation with closed iron bridges in the rotor as in the real motor is carried out. The model is adapted as follows: In the non-linear 2D FEM reference for calculating the saturation factors, the bridges are defined as iron. This means that the permeability is iterated from the stored material curve in several iteration steps. Since the linear reference must still have open bridges, the saturation factor will change accordingly. The effects on the results are examined and explained below.

At first, Motor II is compared to FEM for a low voltage and hence low saturation at a current angle of $\gamma \approx 2°_{\mathrm{el}}$. Figure 4.31 shows the stator current of the first phase and the corresponding saturation factors for the d- and q-axis.

Two things stand out when looking at the plots: First, the current from FEM is smooth without visible harmonics. This is because the rotor has a smooth surface that does not cause slotting effects when the bridges are not saturated, as in this case. As the linear reference of the model still contains the open bridges, the harmonics are still visible there. Second, the saturation factor of the q-axis is less than 1. This will now be explained in more detail.

As already mentioned, the open bridges in the linear reference lie in the flux paths of the q-axis. This means that a higher current is needed for a predefined q-axis flux than in the case of closed bridges because the magnetic circuit contains more air. In contrast, the bridges are closed in the non-linear reference. Especially at low flux, they are still

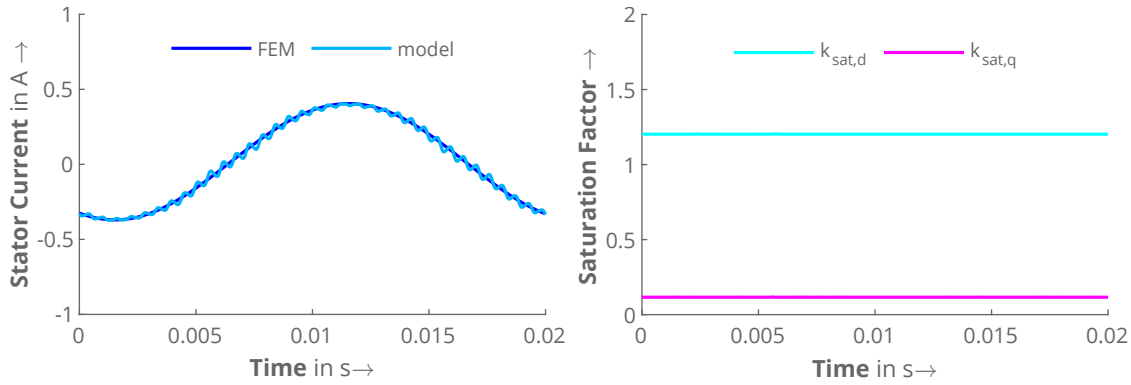

Figure 4.31: Comparison of stator currents versus time with FEM (left) and corresponding saturation factors (right) for Motor II at $U = 60\,\mathrm{V}$, $f = 50\,\mathrm{Hz}$, and $n = 3000\,1/\mathrm{min}$ with a resulting current angle of $\gamma \approx 2°_{\mathrm{el}}$. The rotor cage is inactive, the rotor bridges are closed.

unsaturated and have a high permeability. The current required for the same predefined q-axis flux is therefore lower. As the saturation factor represents the ratio between the current in a non-linear calculation and in a linear calculation, it becomes less than 1 in this case.

To further illustrate this effect, the saturation factors of the d- and q-axis for open bridges are shown in Figure 4.32 for different current angles. While the d-axis factor shows the usual behavior, it is clear to see that the q-axis factor always starts with values less than 1, regardless of the current angle.

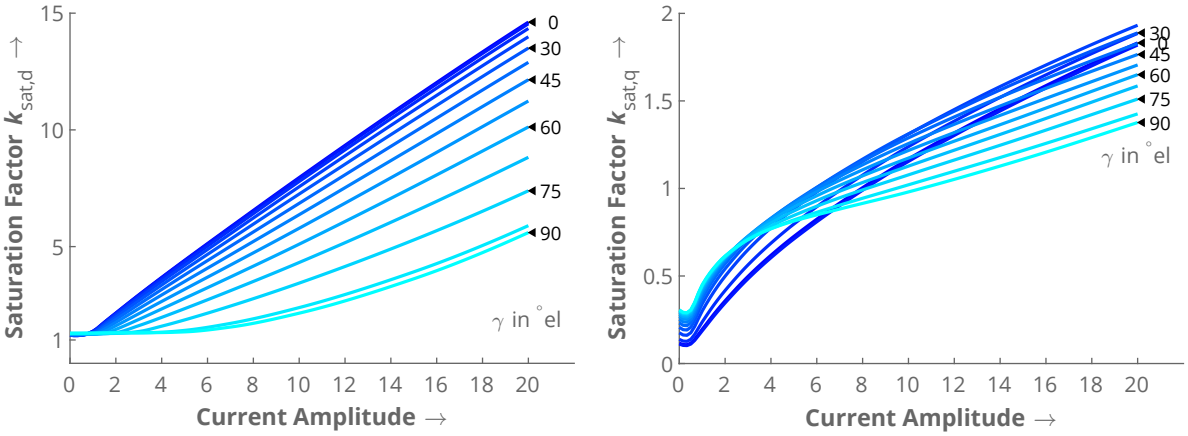

(a) d-axis saturation factor

(b) q-axis saturation factor

Figure 4.32: Saturation factor functions $k_{\mathrm{sat,d}}$ and $k_{\mathrm{sat,q}}$ for the d- and q-axis evaluated as the relation between linear and non-linear current-flux linkage components. The rotor bridges are closed in the non-linear reference. Note that the y-axes do not have the same scaling.

As the current increases, the saturation factor also increases and, depending on the current angle, is only equal to 1 from a value of approximately 6 to 10 A. This means that for these values, the input current for a given flux linkage of the q-axis corresponds to the linear calculation with open and non-linear calculation with closed bridges. In the latter case, the corresponding domains are saturated so that the magnetic circuit of the q-axis corresponds to the linear case. If the current is increased further, the saturation

factor eventually becomes greater than 1, as the outer bridges are more "open" than in the linear reference due to the increased saturation.

Another striking observation is that the saturation factor of the q-axis increases more quickly for higher current angles (lighter blue tones) than for smaller current angles (darker blue tones). As larger portions of the magnetic flux flow over the q-axis, the saturation and the above described effect occur much sooner. Nevertheless, at currents between 4 and 8 A the plot order reverses: For higher current angles the slope gets much smaller, whereas it hardly changes for current angles $< 45°_{\text{el}}$. This is again due to the different magnetic circuits of d- and q-axis. The flux paths (including the bridges) saturate faster with a flux vector that is oriented more closely to the d-axis. The q-axis does not allow as much flux at the same current, which is why it saturates more slowly.

If the voltage is increased for the same simulation as in the previous figure, all of the above described effects are amplified. Figure 4.33 provides a comparison of the stator current with FEM and the corresponding saturation factors for 120 V and a resulting current angle of $\gamma \approx 2°_{\text{el}}$.

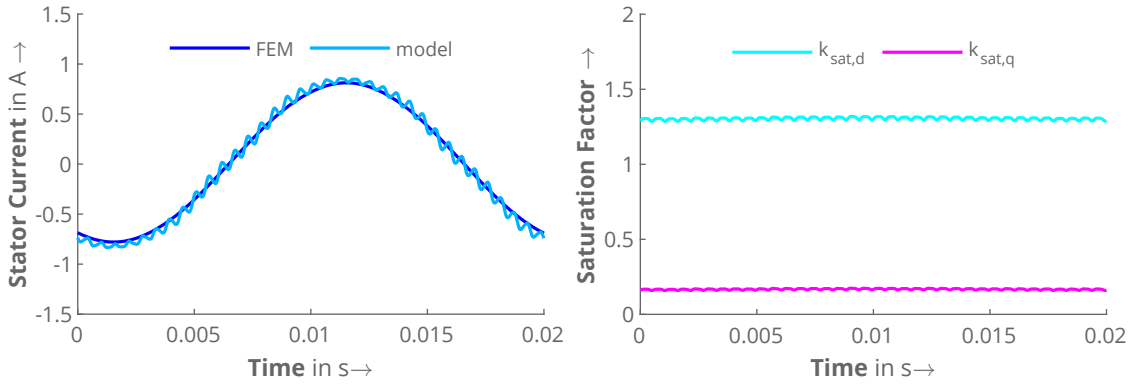

Figure 4.33: Comparison of stator currents versus time with FEM (left) and corresponding saturation factors (right) for Motor II at $U = 120$ V, $f = 50$ Hz, and $n = 3000$ 1/min with a resulting current angle of $\gamma \approx 2°_{\text{el}}$. The rotor cage is inactive, the rotor bridges are closed.

The agreement is also satisfactory in this case, as the visible difference is mainly due to the higher harmonics in the model. These are also responsible for the variation of the saturation factors over time. Apart from a slight difference in the fundamental, this is also true for the comparison at 180 V shown in Figure 4.34.

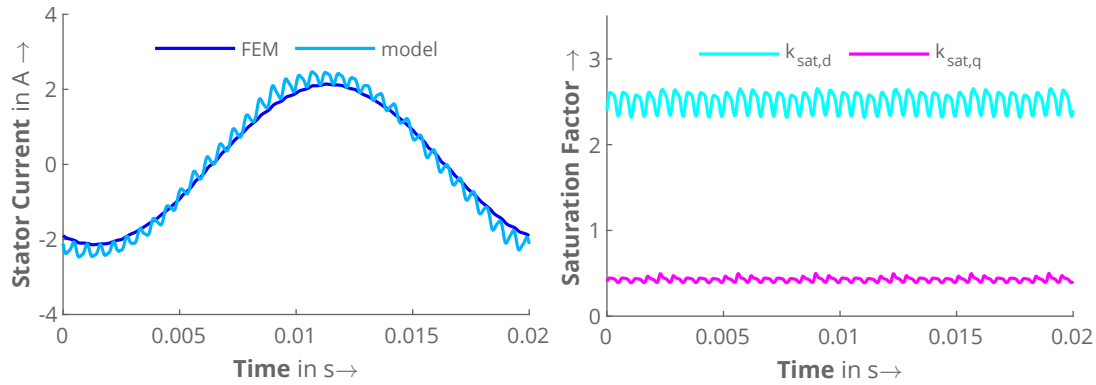

Figure 4.34: Comparison of stator currents versus time with FEM (left) and corresponding saturation factors (right) for Motor II at $U = 180\,\mathrm{V}$, $f = 50\,\mathrm{Hz}$, and $n = 3000\,1/\mathrm{min}$ with a resulting current angle of $\gamma \approx 7°_{\mathrm{el}}$. The rotor cage is inactive, the rotor bridges are closed.

A comparison of the same quantities for a voltage of 120 V and a current angle of approximately $55°_{\mathrm{el}}$ reveals further insights. Firstly, the outer bridges are more saturated than in the previous case, as more flux now flows through the q-axis. Therefore, the difference between the current harmonics is smaller. Secondly, the difference in the fundamental remains approximately the same.

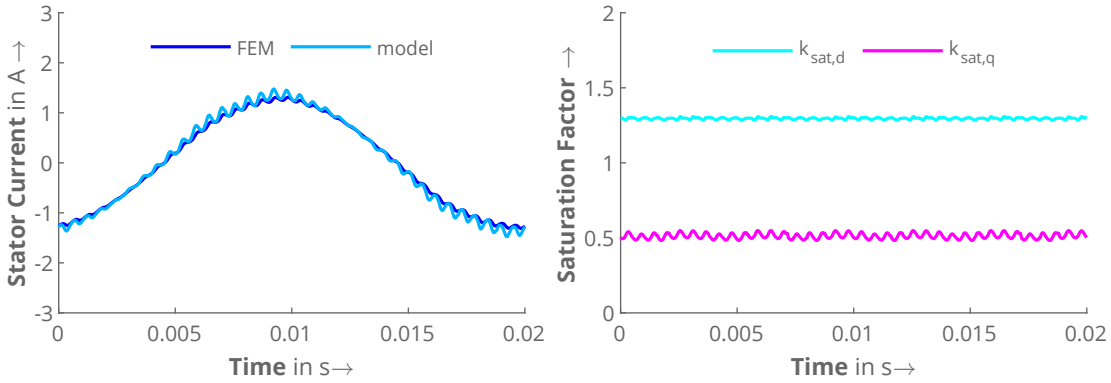

Figure 4.35: Comparison of stator currents versus time with FEM (left) and corresponding saturation factors (right) for Motor II at $U = 120\,\mathrm{V}$, $f = 50\,\mathrm{Hz}$, and $n = 3000\,1/\mathrm{min}$ with a resulting current angle of $\gamma \approx 55°_{\mathrm{el}}$. The rotor cage is inactive, the rotor bridges are closed.

Finally, if the results are compared for an increased voltage of 180 V, which leads to a high saturation, the model still shows a satisfactory agreement (Figure 4.36). This means that the saturation factor method is also suitable for modern Line-Start Synchronous Machines with rotor iron bridges. The only limitation seems to be that the harmonics are overestimated due to the open bridges in the linear reference. This will be further analyzed with Motor III.

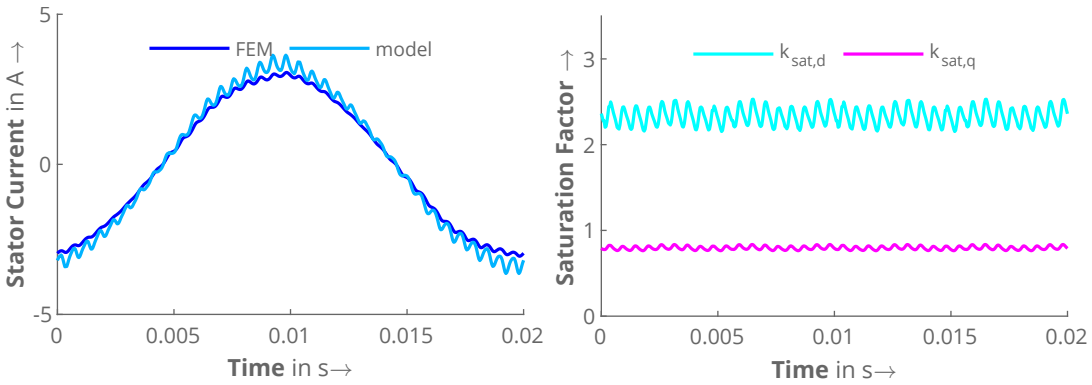

Figure 4.36: Comparison of stator currents versus time with FEM (left) and corresponding saturation factors (right) for Motor II at $U = 180\,\mathrm{V}$, $f = 50\,\mathrm{Hz}$, and $n = 3000\,1/\mathrm{min}$ with a resulting current angle of $\gamma \approx 53°_{\mathrm{el}}$. The rotor cage is inactive, the rotor bridges are closed.

4.5.2.2 Motor III

Following the extensive validation using Motor II, the next step is to validate Motor III. In this case, this starts with comparing the simulation with closed bridges, that is, the real geometry. Figure 4.37 displays the comparison of the stator currents with FEM as well as the saturation factors for 120 V (top) and 160 V (bottom) and a current angle of approximately $1°_{\mathrm{el}}$.

The comparisons reveal that the behavior of this motor is slightly different compared to the previous one. On the one hand, the harmonics predicted by the model are no longer overestimated as much as before. This means that the chosen slot width for opening the outer bridges in the rotor is closer to what can be expected in reality. However, since the model must always open the bridges to a certain degree, the case of unsaturated, closed bridges can never be modeled with 100% accuracy.

On the other hand, it stands out that in contrast to the lower voltage (Figure 4.37a), the current for higher voltage (Figure 4.37b), is overestimated. This result can be explained by the fact that the saturation factor in the model is always interpolated according to the magnitude of the instantaneous (virtual) stator current space vector. This vector is the result of the fundamental and all harmonics. In contrast, the FEM reference used to calculate the saturation factors only contains the fundamental current. The problem is that if the magnitude of the vector in the model is increased or decreased by harmonics (depending on time), the adjustment of the saturation factor assumes a higher or lower fundamental current. As the harmonic currents do not have the same influence on the fundamental saturation, this leads to slightly different results.

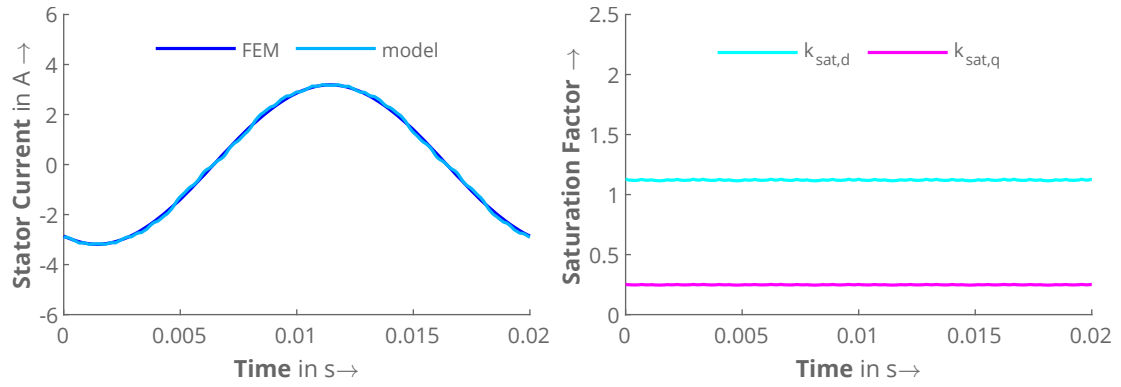

(a) $U = 120$ V

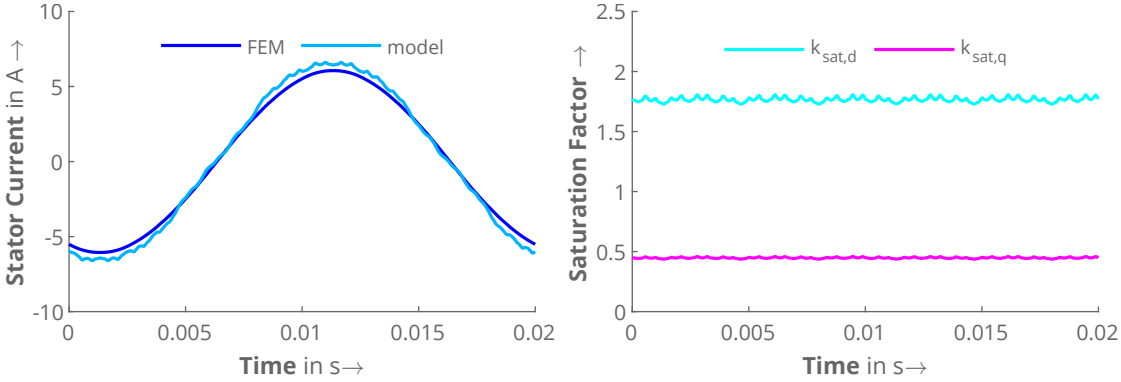

(b) $U = 160$ V

Figure 4.37: Comparison of stator currents versus time with FEM (left) and corresponding saturation factors (right) for Motor III at two different voltages, $f = 50$ Hz, and $n = 1500$ 1/min with a resulting current angle of $\gamma \approx 1°_{\text{el}}$. The rotor cage is inactive, the rotor bridges are closed.

The next comparison is for a resulting current angle of approximately $49°_{\text{el}}$. The results for the same voltages are displayed in Figure 4.38. Overall, the behavior is similar to the previous comparison. The model currents are slightly higher than in the FEM, as they contain more harmonics. Despite the slight deviation, the results are still satisfactory and do not reveal any limitations other than those already explained.

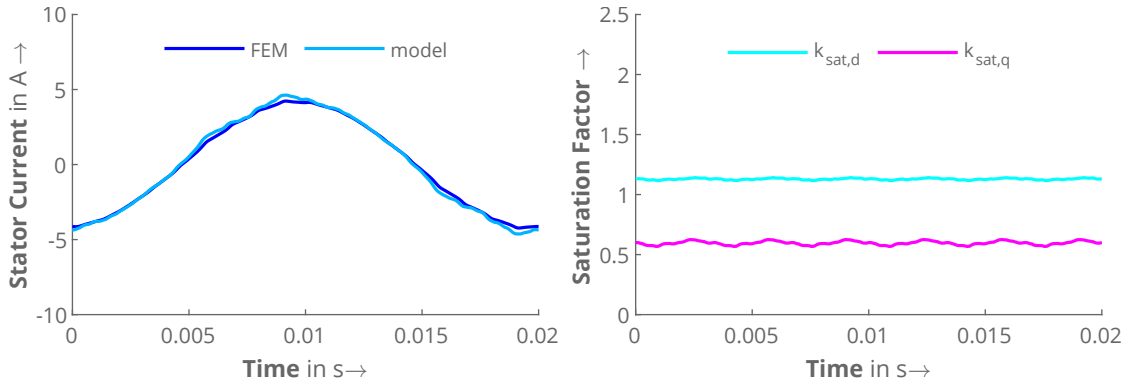

(a) $U = 120\,\mathrm{V}$

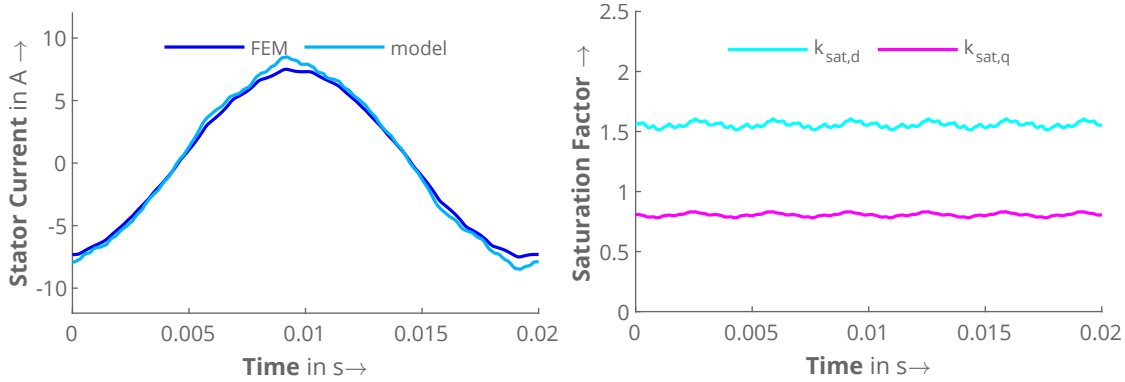

(b) $U = 160\,\mathrm{V}$

Figure 4.38: Comparison of stator currents versus time with FEM (left) and corresponding saturation factors (right) for Motor III at two different voltages, $f = 50$ Hz, and $n = 1500\,1/\mathrm{min}$ with a resulting current angle of $\gamma \approx 49°_{\mathrm{el}}$. The rotor cage is inactive, the rotor bridges are closed.

In summary, it has been shown from this part of the validation that the saturation factor model was improved compared to the previous work of Güdelhöfer [54], [55]. The dq-saturation factor approach both improves the accuracy of the results and the comprehension of the saturation phenomena in Line-Start Synchronous Reluctance Machines. Since the validation at no load conditions without rotor cage has shown good results, the rotor cage could be activated and the results could be compared for synchronous speed as well.

As this would only lead to slight changes in the results, however, this step is skipped. Hence, it makes more sense to move on to a validation of the saturation and the skin effect combined. This is done by evaluating the steady-state torque versus speed curve of the motors. Starting at a speed close to the synchronous speed and gradually reducing it, the influence of the skin effect increases while the saturation decreases. This allows a joint investigation of both effects. In addition, the aim of this work is to simulate the start-up behavior. The steady-state torque versus speed simulation is therefore particularly useful as an intermediate step towards the dynamic start-up calculation. It will be covered in the next section.

4.5.3 Steady-state torque versus speed simulation

The following part of the validation procedure moves on to investigate the steady-state torque versus speed behavior of the machine. To this end, both models are set up as follows: The stator circuit as well as the rotor circuits for N_L=3 layers are activated. The voltage and the rotor speed are set to the desired value. The voltage is switched on and the simulation is carried out at constant speed until all transients have disappeared. The torque and current (and other quantities as required) can then be evaluated for the duration of a slip period

$$t_\mathrm{s} = \frac{1}{s f_\mathrm{s}}.$$

This procedure can be repeated for different speeds so that the steady-state torque-speed characteristic can be approximated.

4.5.3.1 Motor II

Starting with Motor II, the case of linear materials is compared first. In this way, the influence of iron saturation on the accuracy of the results can be eliminated before testing the skin effect and saturation together. Figure 4.39 shows the torque versus speed curve as well as the corresponding stator currents for $U = 100\,\mathrm{V}$. For both quantities, there is no visible difference between FEM and the model.

What is striking in this figure, however, is that the torque is negative for $n = 2900\mathrm{min}$. This is because the rotor's anisotropy also produces an asynchronous torque [33]–[35] as explained in Chapter 2. Since this torque is negative for $s < 0.5$, it reduces the steady-state torque provided by the cage even to a negative value.

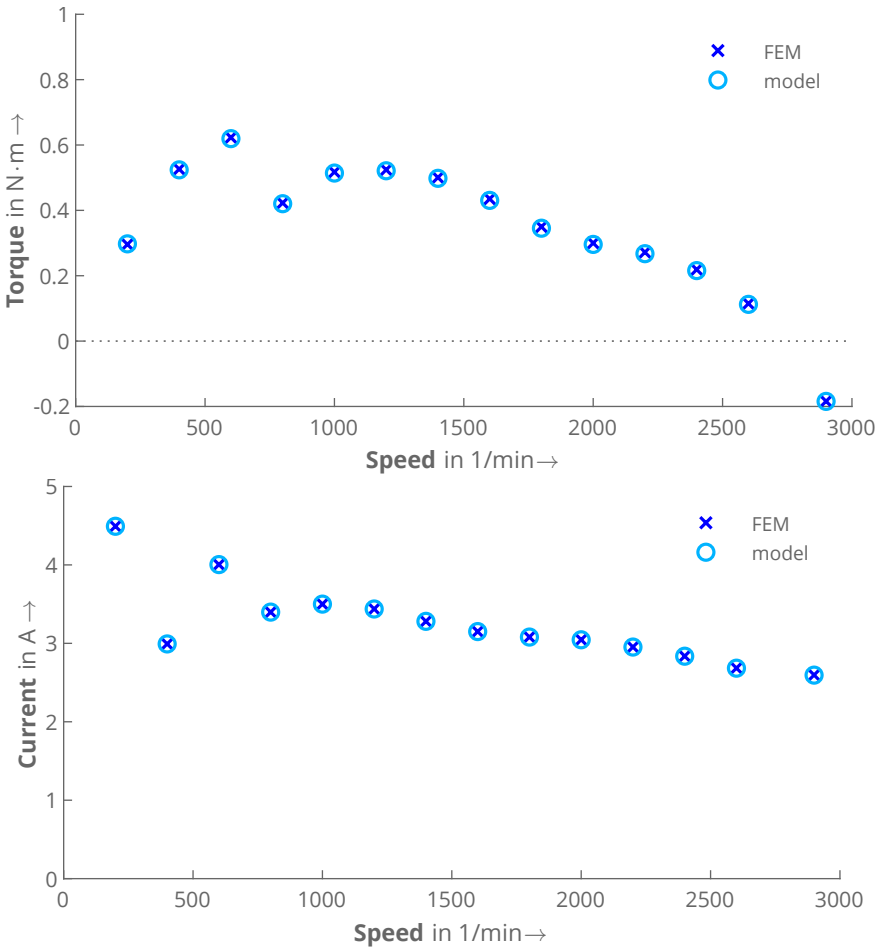

Figure 4.39: Comparison of the steady-state torque (top) and current (bottom) versus speed with FEM for Motor II at $U = 100\,\mathrm{V}$ and $f = 50\,\mathrm{Hz}$. Saturation is neglected, the end-ring parameters are set to their respective values from the presented end-ring model. Both the model and FEM were calculated with 3 rotor cage layers. The iron bridges in the rotor are open.

As an intermediate step to investigate the influence on the results as well as on the torque versus speed behavior, the non-linear simulation with open rotor iron bridges at 100 V is compared (Figure 4.40). In this case, a deviation of the torque and the current can be observed, both of which are higher in FEM than in the model. Yet, this was expected, as the existing model already exhibited the same phenomenon.

As already mentioned in section 4.2.5, this is due to the saturation of the leakage paths, which is not considered in the model. While the results fit good for the highest speed values, the deviation begins where $n < 2500\,\mathrm{min}$. Because the tooth tips of the stator and rotor parts near the air gap saturate, the current and the torque are higher. Since the chosen voltage of 100 V only causes a low saturation of the fundamental wave, neglecting leakage path saturation is probably the main cause for the deviation.

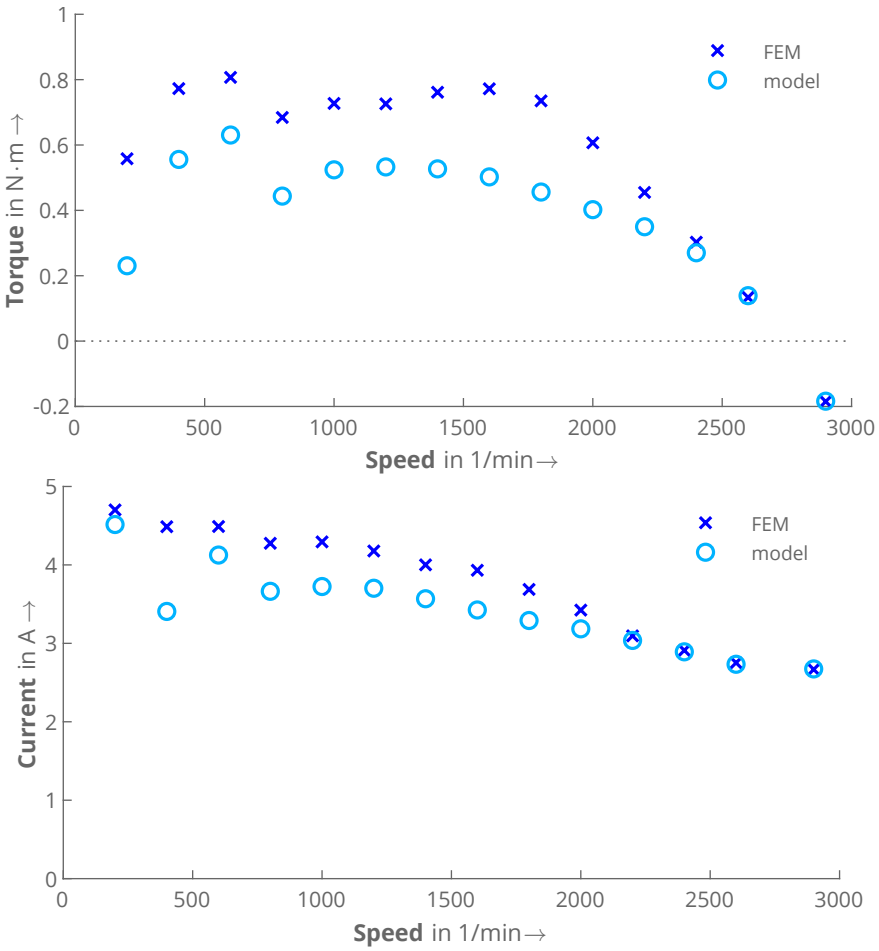

Figure 4.40: Comparison of the steady-state torque (top) and current (bottom) versus speed with non-linear FEM for Motor II at $U = 100\,\mathrm{V}$, $f = 50\,\mathrm{Hz}$. The end-ring parameters are set to their respective values from the presented end-ring model. Both the model and FEM were calculated with 3 rotor cage layers. The iron bridges in the rotor are open.

If the comparison is made for the real motor, in which all rotor iron bridges are closed, the relative deviation overall looks the same (Figure 4.41). Thus, it can be concluded that the main saturation is modelled quite good, but in both cases (100 V and 140 V) there is a higher torque in the low speed area due to the phenomenon of leakage path saturation.

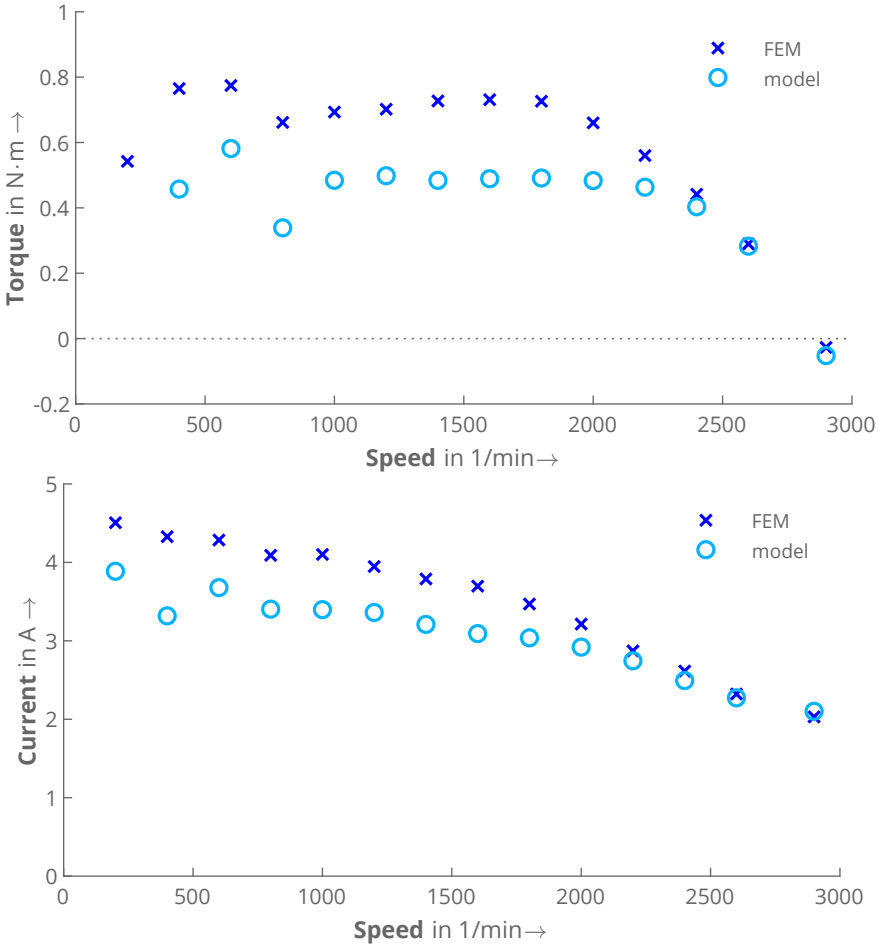

Figure 4.41: Comparison of the steady-state torque (top) and current (bottom) versus speed with non-linear FEM for Motor II at $U = 100\text{V}$, $f = 50\text{Hz}$. The end-ring parameters are set to their respective values from the presented end-ring model. Both the model and FEM were calculated with 3 rotor cage layers. The iron bridges in the rotor are closed.

4.5.3.2 Motor III

If the linear simulation is compared to FEM for Motor III, the agreement is good as well (Figure 4.42). However, the shape of the curve itself is significantly more deformed than for Motor II. The torque is negative for $n \approx 900\ 1/\text{min}$, whereby the cause is the same as before. In this particular case, there is the additional factor that the anisotropy of the rotor is very high. On top of this, the cage housed in the flux barriers is asymmetrical. Both facts generate air gap harmonics, which reduce the torque accordingly. Since the cage in this design is poor, it cannot filter out these harmonics. Instead, they are fully effective.

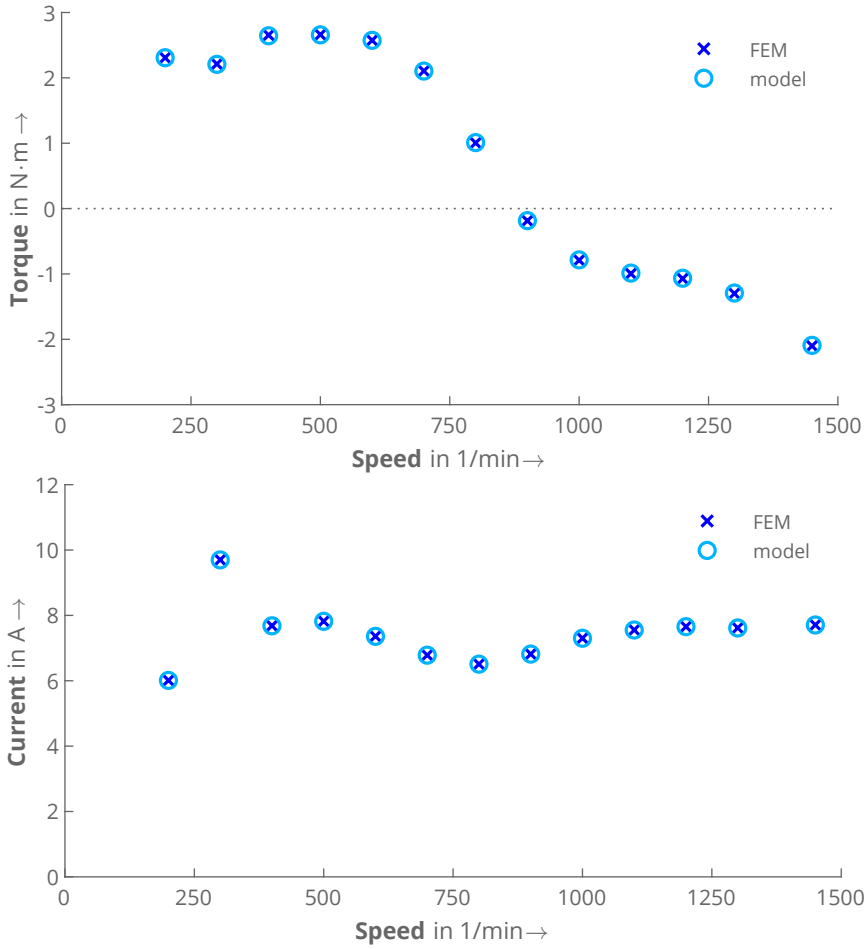

Figure 4.42: Comparison of the steady-state torque (top) and current (bottom) versus speed with FEM for Motor III at $U = 100\ \text{V}$ and $f = 50\ \text{Hz}$. Saturation is neglected, the end-ring parameters are set to their respective values from the presented end-ring model. Both the model and FEM were calculated with 3 rotor cage layers. The iron bridges in the rotor are open.

However, since the model is able to reproduce this effect in the same way as FEM, the result is good in terms of the aim of the work. The fact that the selected motor designs are deliberately not optimized in order to show such effects must be mentioned again at this point.

If the voltage is now kept constant, but the iron saturation is considered in both models, the effect still occurs, as Figure 4.43 proves. The rotor iron bridges are still open in this case. Due to the saturation, however, the point, where the torque becomes negative, slightly shifted to the right. The shape itself also changed a bit. Yet, apart from the known weakness of not including the saturation of leakage paths, both torque and current fit good with FEM.

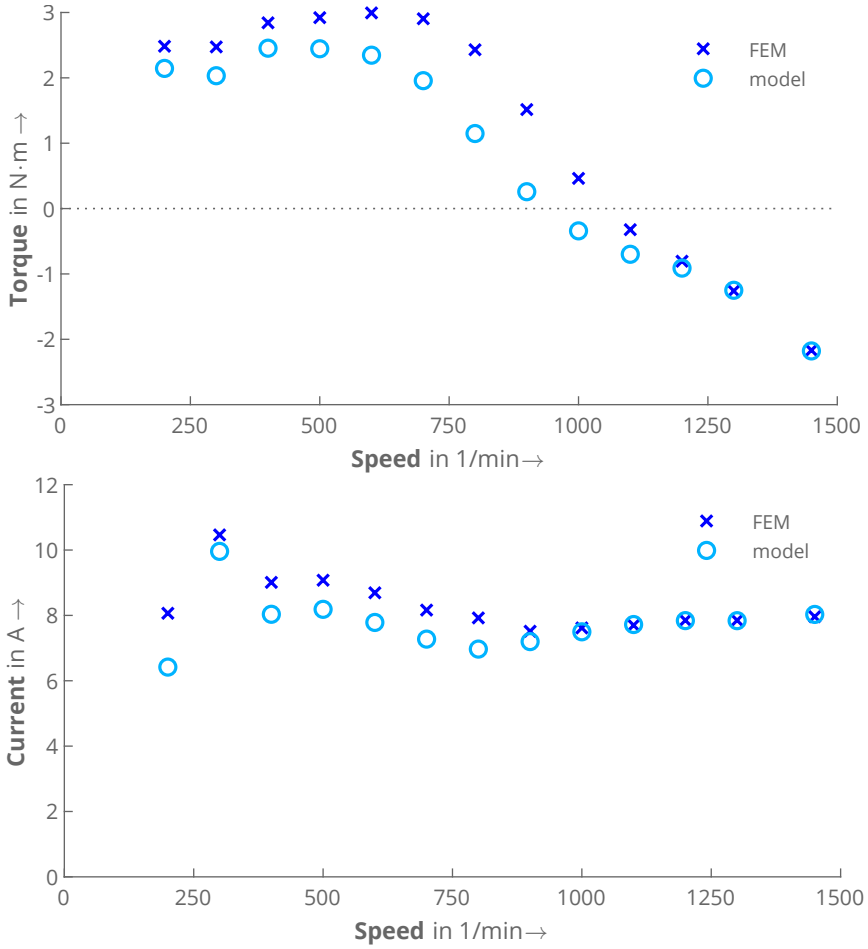

Figure 4.43: Comparison of the steady-state torque (top) and current (bottom) versus speed with non-linear FEM for Motor III at $U = 100\text{V}$, $f = 50\text{Hz}$. The end-ring parameters are set to their respective values from the presented end-ring model. Both the model and FEM were calculated with 3 rotor cage layers. The iron bridges in the rotor are open.

Figure 4.44 shows the comparison for closed iron bridges in the rotor and the same voltage of 100 V. This means that the model now has to account for the iron bridges by adapting the saturation factors accordingly.

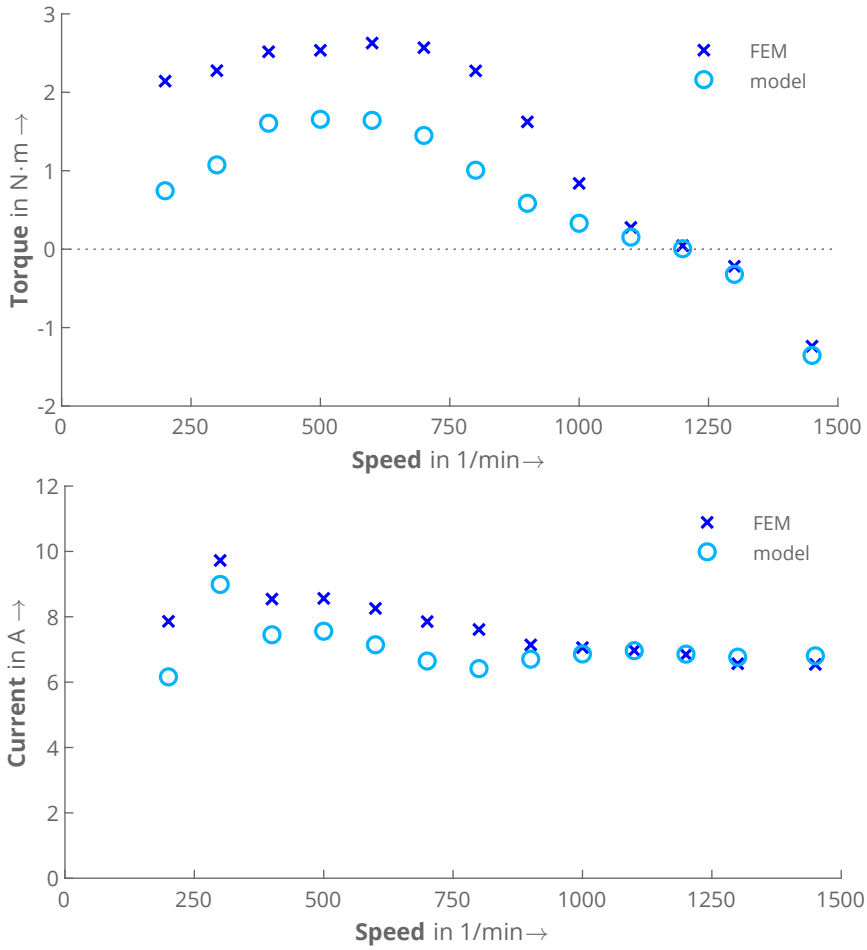

Figure 4.44: Comparison of the steady-state torque (top) and stator current (bottom) versus speed with non-linear FEM for Motor III at $U = 100\,\mathrm{V}$, $f = 50\,\mathrm{Hz}$. The end-ring parameters are set to their respective values from the presented end-ring model. Both the model and FEM were calculated with 3 rotor cage layers. The iron bridges in the rotor are closed.

As before, the accuracy for $n > 1000\,1/\mathrm{min}$ is satisfactory. At lower speeds, the model still underestimates the current and the torque. As now the rotor bridges are closed, the leakage path saturation differs even more from the saturation state in the model, which means that the difference between the asynchronous torque is even higher.

If the voltage is increased to 140V, the saturation increases and the difference becomes apparent again. In Figure 4.45, it is obvious that the torque from FEM is more than twice as high as before, whereas the torque from the model increased only by about 60%. The fact that the current fits well means that the influence of saturation on the mean current is modeled properly, but not the effects on the behavior of the machine.

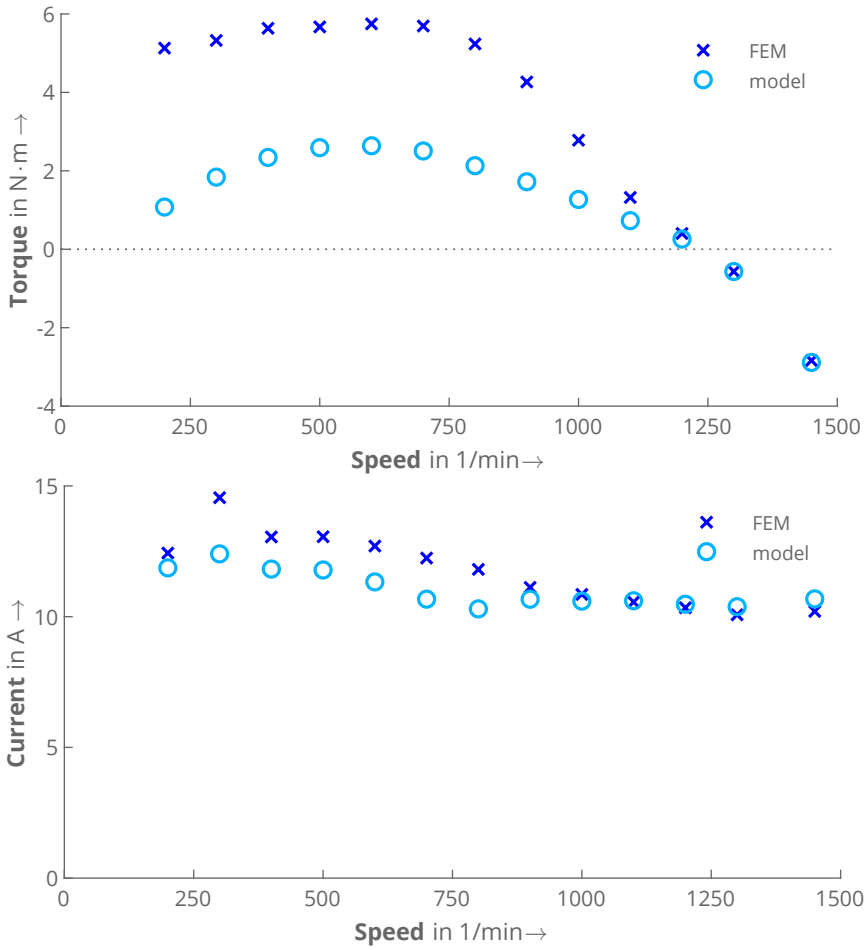

Figure 4.45: Comparison of the steady-state torque (top) and stator current (bottom) versus speed with non-linear FEM for Motor III at $U = 140\,\mathrm{V}$, $f = 50\,\mathrm{Hz}$. The end-ring parameters are set to their respective values from the presented end-ring model. Both the model and FEM were calculated with 3 rotor cage layers. The iron bridges in the rotor are closed.

The assertion that this is only due to the saturation of the leakage paths can be proven using a magnetic field plot that can be generated from the FEM simulation. Figure 4.46 shows the norm of the magnetic flux density in each element, as well as selected magnetic field lines from the simulation with $n = 600\,1/\mathrm{min}$ at the last time step.

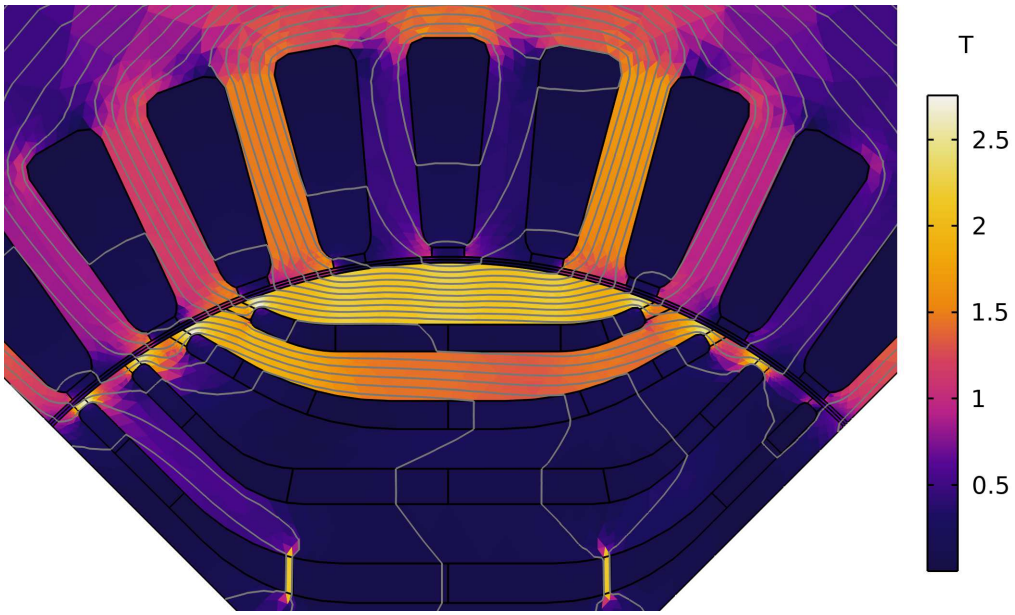

Figure 4.46: Norm of the magnetic field density and magnetic field lines for $t = 1\,\mathrm{s}$ at $n = 600\,1/\mathrm{min}$ corresponding to Figure 4.45.

In this time step, the current angle of the stator current space vector is 164°el, which is close to the d-axis. As explained in section 4.2.5, the flux linkage in this case would flow mainly through the d-axis if the no-load case was considered (see Figure 4.7b).

However, it is obvious from the field lines, that the field does not penetrate the whole rotor core and the paths between the flux barriers. Instead, the stator magnetic field is shielded by the rotor cage and its counter-acting field. Consequently, the flux can only flow through the iron bridges and near the rotor surface. As can be clearly seen when looking at the flux density, these bridges are highly saturated as a result.

Thus, in this extreme case, the saturation reference differs strongly from the actual saturation state, which explains the high deviations. However, from all comparisons, the following conclusion can be drawn: The agreement for speeds near synchronous speed is good. Since this is the most important area when it comes to synchronization behavior, the results in this aspect are expected to be accurate enough.

Considering the leakage path saturation, on the other hand, is a topic that has not been treated for any parameter model suited for Line-Start Synchronous Machines. As proven in [96], [97] for Induction Machines, it would be possible to consider for this effect by additional leakage saturation factors. As this is beyond the scope of this work, however, the validation will continue as before and the differences due to this effect will be discussed.

4.5.4 Start-up simulation

The final step for the validation of the model with FEM is the most important: This section compares the model-predicted dynamic start-up behavior. In this case, the start-up in uncoupled no-load operation is compared. This means that the load torque T_{load} is the friction torque T_{fric} determined in the measurement. The total inertia of the rotating shaft J_{tot} is equal to the motor inertia J_{mot}.

For the simulation, the rotor cage is still divided in N_{L}=3 layers. The only change to the previous validation step is that the speed is no longer fixed. Instead, it is determined using the equation of motion, whereby the voltage is switched on at standstill.

4.5.4.1 Motor II

Starting with the comparison of the linear case for Motor II, Figure 4.47 shows a good agreement between the model and FEM. The speed versus time curve (top figure) proves that the slope in the beginning is modelled well. This also includes slight oscillations of the speed, which can be modelled because the torque harmonics are accurately modelled in the linear case.

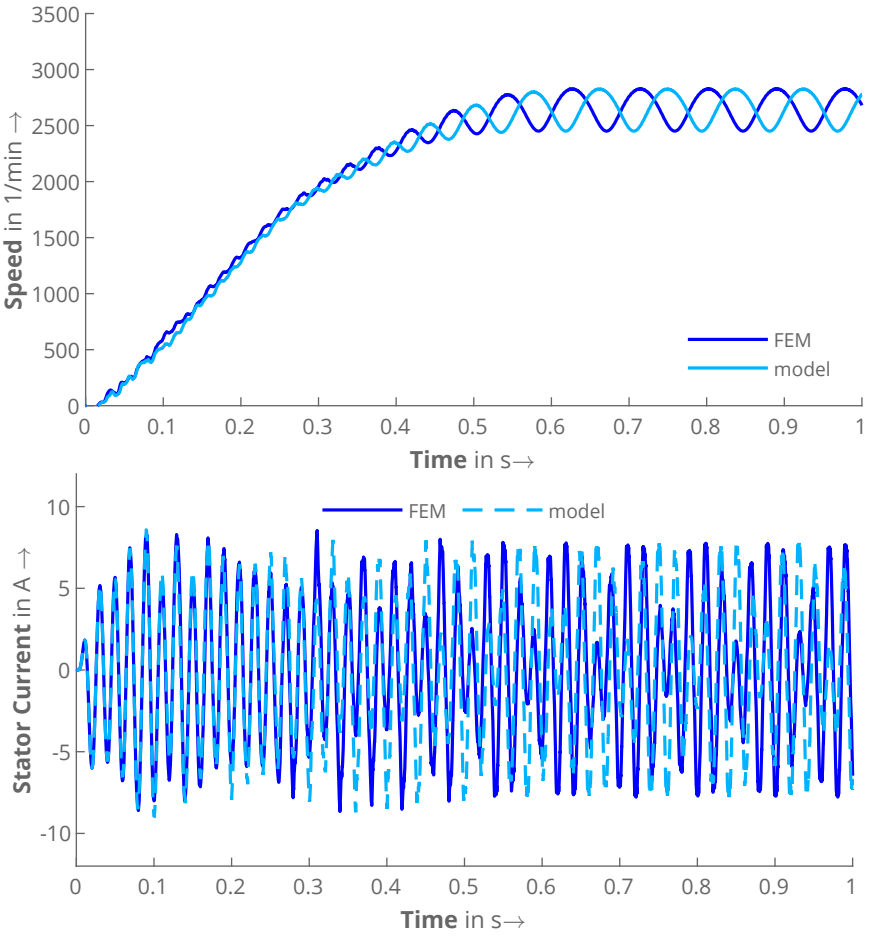

Figure 4.47: Comparison of the speed (top) and stator current (bottom) versus time with FEM for Motor II at $U = 140\,\mathrm{V}$, $f = 50\,\mathrm{Hz}$, $T_{\mathrm{load}} = T_{\mathrm{fric}}$ and $J_{\mathrm{tot}} = J_{\mathrm{mot}}$. Saturation is neglected, the end-ring parameters are set to their respective values from the presented end-ring model. Both the model and FEM were calculated with 3 rotor cage layers. The iron bridges in the rotor are open.

The motor does not reach synchronous speed in this case. It remains at a typical quasi-stationary state where it oscillates around a mean speed lower than the synchronous speed of $n_0 = 3000\ 1/\text{min}$. Here, the model can accurately predict the resulting mean speed, and the oscillation is the same as in FEM concerning amplitude and frequency.

The only slight difference between the model and FEM is that the oscillations are slightly shifted against each other in time. On closer inspection, the first difference between both models occurs at around 0.1 s. As the speed is an integral variable in this calculation, the difference persists over the entire simulation time. However, this is not a disadvantage in terms of the accuracy of the model. It is clear to see that the behavior in the entire speed range corresponds exactly to the FEM, and the method is therefore valid.

The same conclusion can also be drawn for the current, which is shown in the bottom plot in Figure 4.47. Here, the curve starts exactly as in the FEM, but the curves are offset from the same point. However, it can also be seen here that the amplitude always matches the FEM curve.

The next comparison is carried out for the same voltage, but considering the saturation of the iron. The rotor bridges are still open (Figure 4.48). Here, two things are striking when looking at the speed versus time curve. On the one hand, the model ends in the same state as the FEM, where the amplitude and frequency of the oscillation are again the same. This is a good result concerning the prediction of the synchronization behavior.

On the other hand, it is obvious that the acceleration in the starting phase is smaller in the model than in FEM. This was expected because, as explained in the previous section, the leakage path saturation increases the torque at low speeds in FEM. Since the model ends in the same state, however, this has no major influence on the result concerning the failed synchronization. Regarding the current, a good match can also be seen (apart from the phase shift).

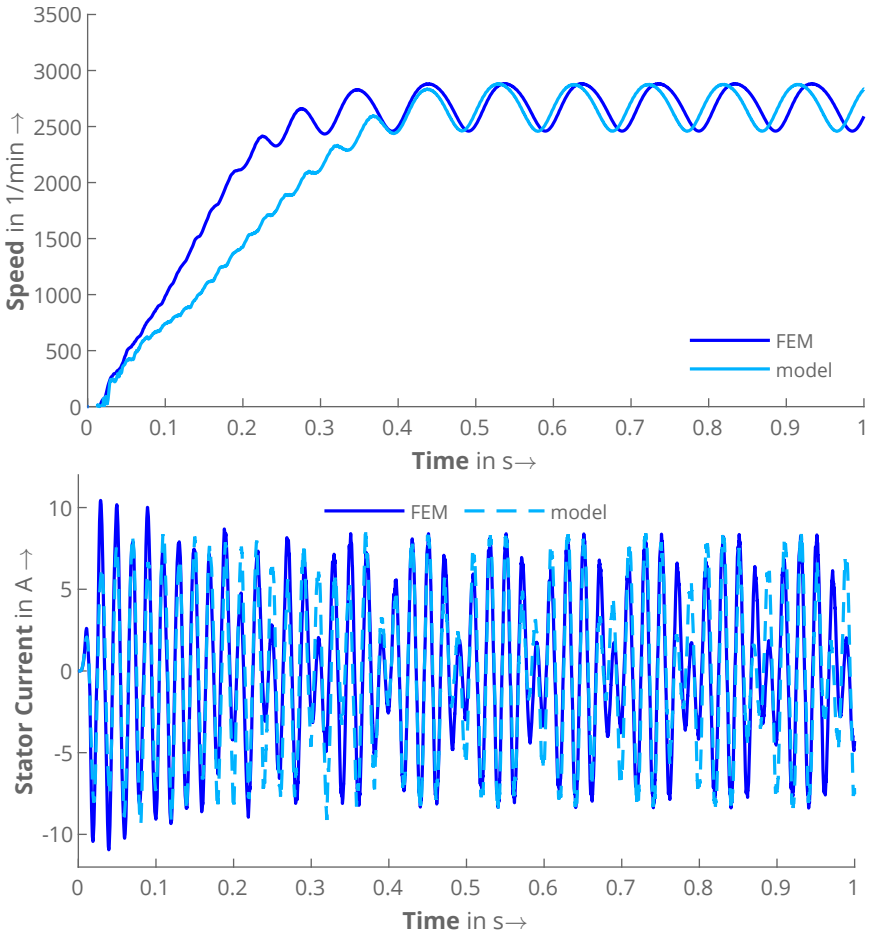

Figure 4.48: Comparison of the speed (top) and stator current (bottom) versus time with non-linear FEM for Motor II at $U = 140\,\mathrm{V}$, $f = 50\,\mathrm{Hz}$, $T_{\mathrm{load}} = T_{\mathrm{fric}}$ and $J_{\mathrm{tot}} = J_{\mathrm{mot}}$. The end-ring parameters are set to their respective values from the presented end-ring model. Both the model and FEM were calculated with 3 rotor cage layers. The iron bridges in the rotor are open.

Next, the start-up for the real geometry is compared, which means the bridges are set to iron. As Figure 4.49 proves, the model is still valid for this case. Both simulations show that the motor would reach synchronous speed in this case. Apart from the difference in slope, both curves look almost the same.

The fact that the motor with closed bridges starts up successfully can be explained by the lower Carter factor. Because the motor with closed bridges has a smaller effective air gap than the motor with open bridges, a higher torque can be produced at the same voltage.

Yet, what has to be noted is that the damping behavior slightly differs for the model. While FEM is almost at constant speed after 1 s, the speed in the model still oscillates. Consequently, the current is also still higher because the motor did not reach steady state. However, as the result concerning the synchronization is the same and the shape of the curve in wide areas is modelled accurately, the model still fulfills the requirements.

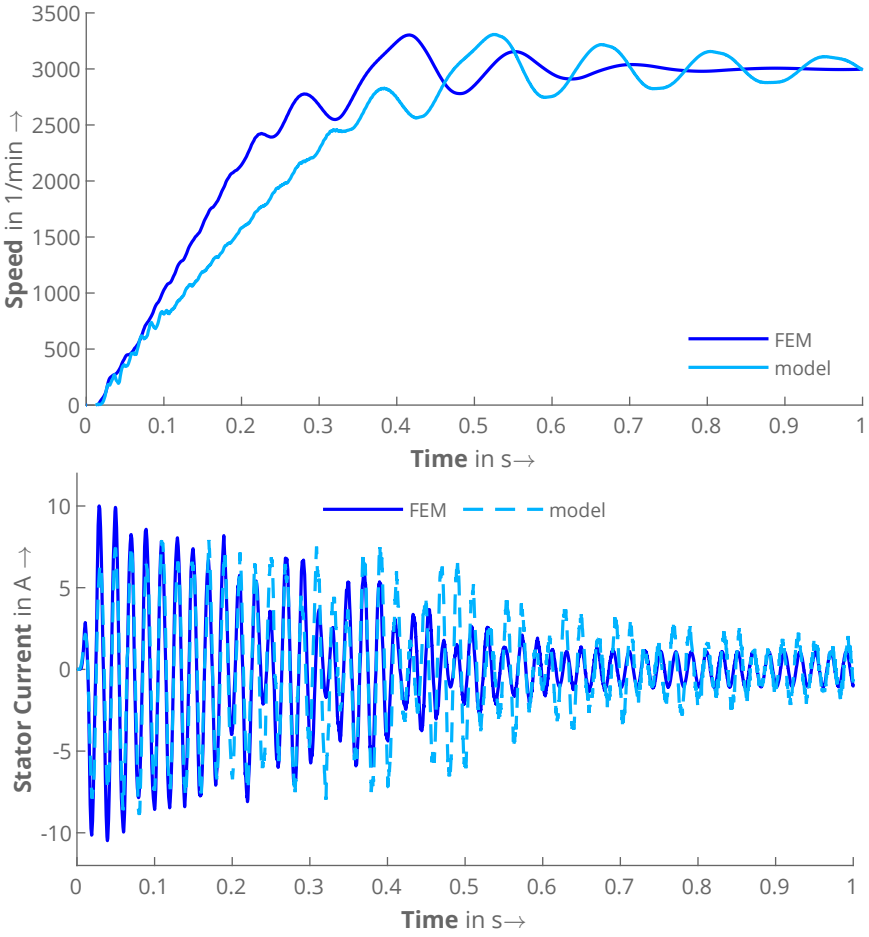

Figure 4.49: Comparison of the speed (top) and stator current (bottom) versus time with non-linear FEM for Motor II at $U = 140\,\mathrm{V}$, $f = 50\,\mathrm{Hz}$, $T_{\mathrm{load}} = T_{\mathrm{fric}}$ and $J_{\mathrm{tot}} = J_{\mathrm{mot}}$. The end-ring parameters are set to their respective values from the presented end-ring model. Both the model and FEM were calculated with 3 rotor cage layers. The iron bridges in the rotor are closed.

In the last step, the voltage is now increased to 180 V, which results in a highly saturated state. Figure 4.50 shows the torque and speed versus time curves for this case.

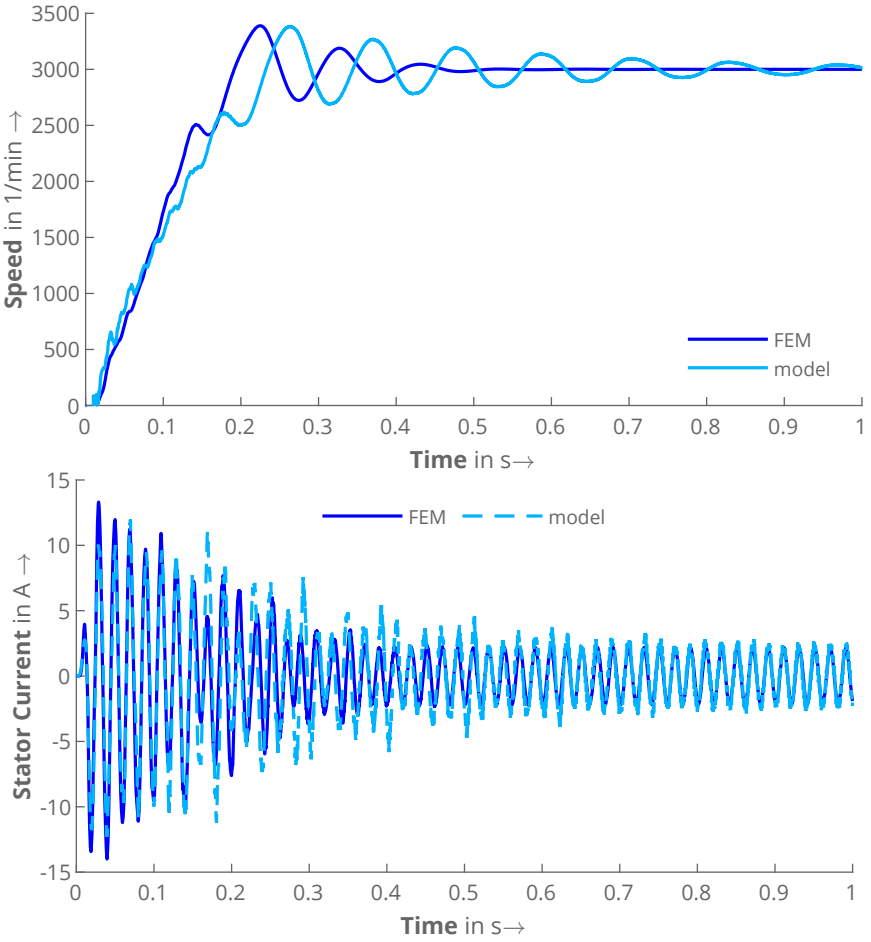

Figure 4.50: Comparison of the speed (top) and stator current (bottom) versus time with non-linear FEM for Motor II at $U = 180\,\mathrm{V}$, $f = 50\,\mathrm{Hz}$, $T_{\mathrm{load}} = T_{\mathrm{fric}}$ and $J_{\mathrm{tot}} = J_{\mathrm{mot}}$. The end-ring parameters are set to their respective values from the presented end-ring model. Both the model and FEM were calculated with 3 rotor cage layers. The iron bridges in the rotor are closed.

In general, the same conclusion can be drawn here as in the previous calculation: the overall match is good. The slope of the speed curve is now significantly steeper, and the model shows a small difference. However, the general course is again well-matched, and the synchronization behavior is also very similar. As far as the current is concerned, there is again a good match except for the difference in damping.

4.5.4.2 Motor III

Hence, the next step is the validation of Motor III. At first, the test is again carried out for the linear case (Figure 4.51). Here, the matching between the model and FEM is excellent because both torque and curve are the same without any visible difference.

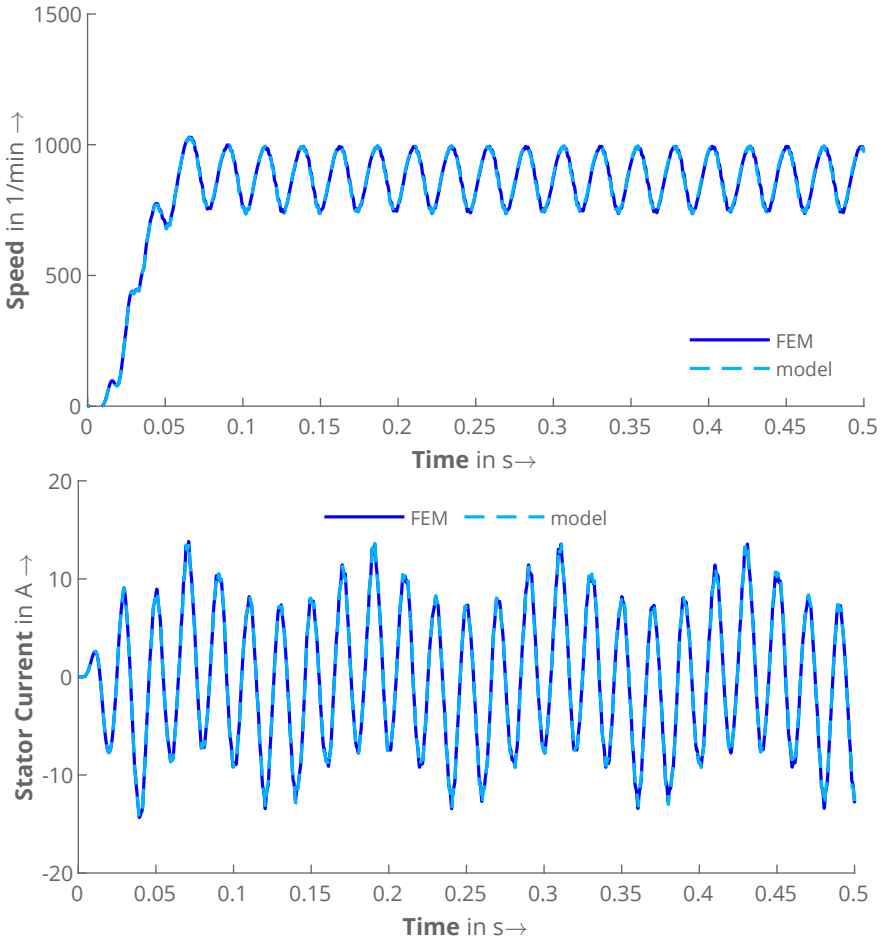

Figure 4.51: Comparison of the speed (top) and stator current (bottom) versus time with FEM for Motor III at $U = 100$ V, $f = 50$ Hz, $T_{\mathrm{load}} = T_{\mathrm{fric}}$ and $J_{\mathrm{tot}} = J_{\mathrm{mot}}$. Saturation is neglected, the end-ring parameters are set to their respective values from the presented end-ring model. Both the model and FEM were calculated with 3 rotor cage layers. The iron bridges in the rotor are open.

The speed versus time plot also shows, what was expected from the torque versus speed evaluation in Figure 4.42. As the asynchronous torque becomes negative near $n = 1000$ 1/min, the resulting speed in the dynamic start-up is also below this value. Consequently, the current oscillates as well.

The intermediate step, in which the motor is compared taking saturation and open bridges into account, is skipped in this case. Therefore, the simulation of the real motor (saturation taken into account, bridges in the rotor set to iron) is shown directly in Figure 4.52 for a voltage of 100 V.

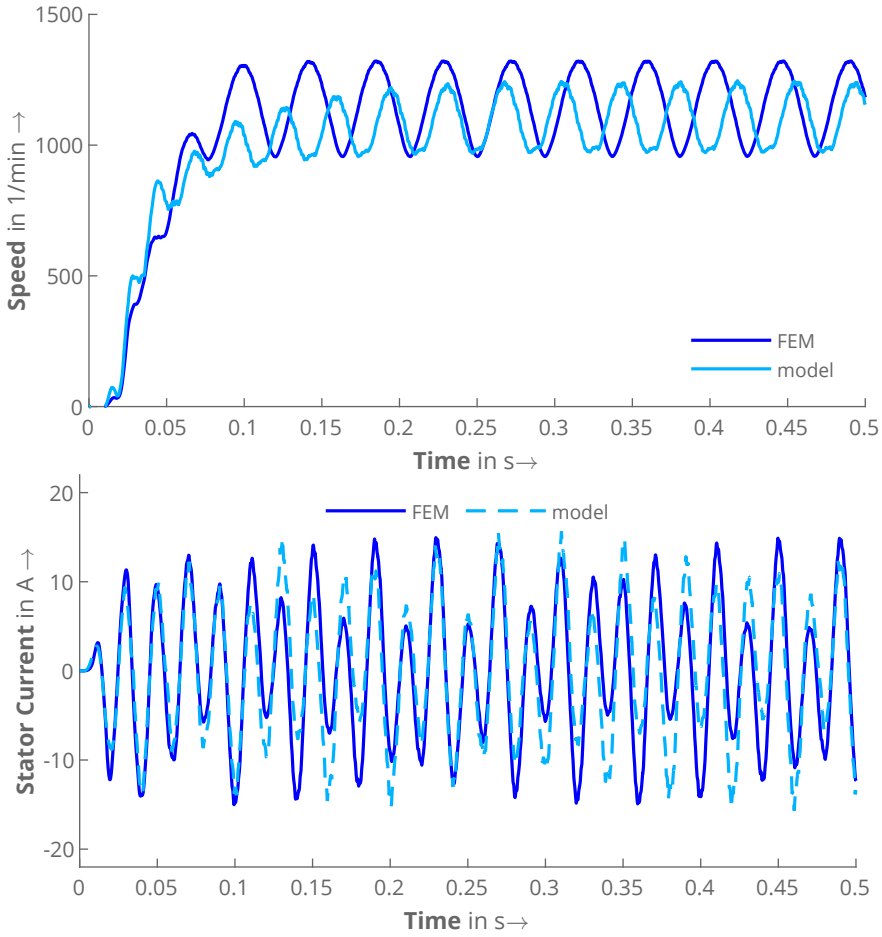

Figure 4.52: Comparison of the speed (top) and stator current (bottom) versus time with non-linear FEM for Motor III at $U = 100\,\mathrm{V}$, $f = 50\,\mathrm{Hz}$, $T_{\mathrm{load}} = T_{\mathrm{fric}}$ and $J_{\mathrm{tot}} = J_{\mathrm{mot}}$. The end-ring parameters are set to their respective values from the presented end-ring model. Both the model and FEM were calculated with 3 rotor cage layers. The iron bridges in the rotor are closed.

Here, the overall behavior is still good. The slope of the speed curve during the starting period is good. However, the resulting speed and hence the oscillation amplitude and frequency slightly differ. As the difference is not too great and the speed of the model is only slightly lower, this result is still satisfactory.

Moving on now to the last comparison, which is for the real motor at 140 V, as shown in Figure 4.53. Since both models now predict successful synchronization, the result can generally be described as good. However, there are again differences in the damping, which is underestimated by the model. Apart from this, there is good agreement, particularly regarding the simplified consideration of important effects such as saturation and skin effect. This indicates that the large differences that were previously found in the corresponding torque-speed curve (Figure 4.45) generally do not affect the result in the dynamic start-up as much as expected.

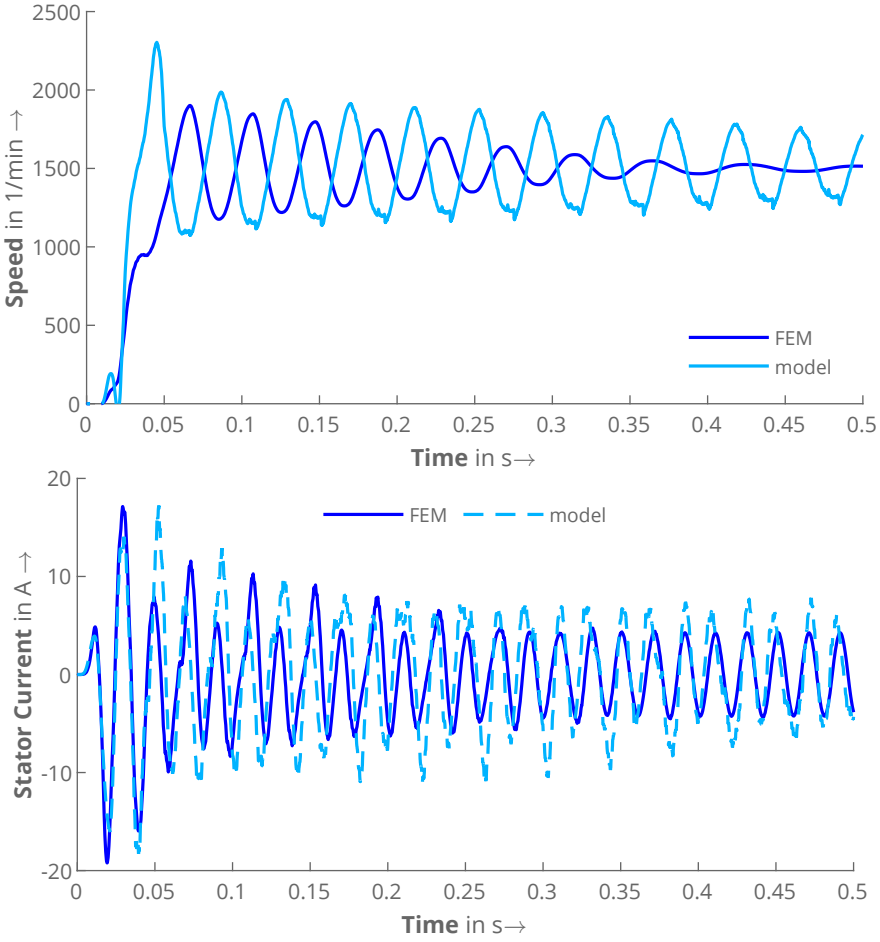

Figure 4.53: Comparison of the speed (top) and stator current (bottom) versus time with non-linear FEM for Motor III at $U = 140\,\mathrm{V}$, $f = 50\,\mathrm{Hz}$, $T_{\mathrm{load}} = T_{\mathrm{fric}}$ and $J_{\mathrm{tot}} = J_{\mathrm{mot}}$. The end-ring parameters are set to their respective values from the presented end-ring model. Both the model and FEM were calculated with 3 rotor cage layers. The iron bridges in the rotor are closed.

4.6 Validation with measurements

Since the comparisons with FEM in different operating modes have shown good results, the model is finally compared with measurements. In this case, the start-up measurements of Motor II and Motor III from Section 3.9.4 are compared. As the aim of the model is to provide a faster alternative to the FEM, the results of the FEM are also shown.

4.6.0.1 Motor II

The first comparison is for Motor II in the no-load start-up without external moment of inertia at a voltage of 180 V. The speed versus time plot for the measurement, the FEM, and the model is shown in Figure 4.54.

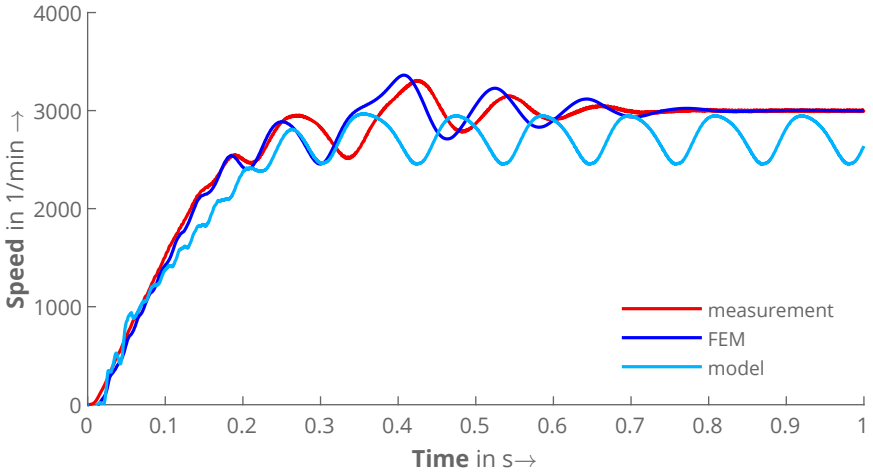

Figure 4.54: Comparison of the speed during dynamic start-up of Motor II at $U = 180\,\mathrm{V}$, $f = 50\,\mathrm{Hz}$, and $T_{\mathrm{load}} = T_{\mathrm{fric}}$ between model, FEM and measurement. The additional moment of inertia is $J_{\mathrm{add}} = 0$, so that $J_{\mathrm{tot}} = J_{\mathrm{mot}}$.

Comparing the two results, it can be seen that the model predicts an unsuccessful synchronization, whereas both measurement and FEM show a successful synchronization for this case. However, it can also be seen that the resulting speed in the model is only slightly lower than the synchronous speed. It can therefore be assumed that a critical case can be observed here, in which a small change in voltage can already result in a successful start-up.

Further analysis in fact indicates that the motor can synchronize if the voltage is increased by only 1.7%. The result for this case is given in Figure 4.55. Both the FEM and the measurement have remained unchanged.

Therefore, the model is only slightly off the FEM prediction. As the model is more pessimistic than the FEM and the measurement in this case, the result does not pose a problem for practical application and the validity of the model. If the critical load torque versus inertia characteristic curve (cf. Figure 2.5) is calculated for optimized motors, the characteristic curve of the model in this case would be slightly below the characteristic curve predicted by the FEM. In practice, only inertia-torque combinations that have a certain tolerance in relation to the limit curve are suitable for the application anyway.

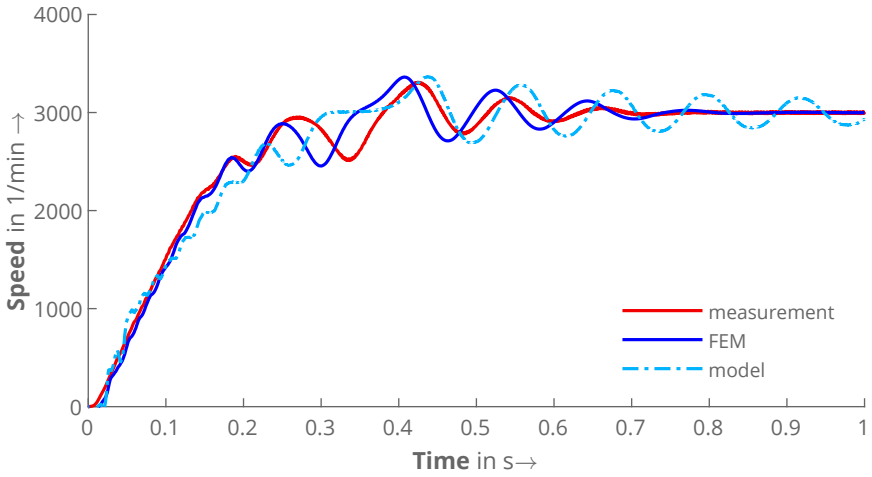

Figure 4.55: Comparison of the speed during dynamic start-up of Motor II at $U = 180\,\mathrm{V}$, $f = 50\,\mathrm{Hz}$, and $T_{\mathrm{load}} = T_{\mathrm{fric}}$ between model, FEM and measurement. The additional moment of inertia is $J_{\mathrm{add}} = 0$, so that $J_{\mathrm{tot}} = J_{\mathrm{mot}}$. The voltage was increased by 1.7% in the model (corresponds to Figure 4.54).

Next, the moment of inertia is increased to the maximum value from the measurement. The comparison of speed and current versus time with FEM and the measurement are shown in Figure 4.56 and Figure 4.57, respectively.

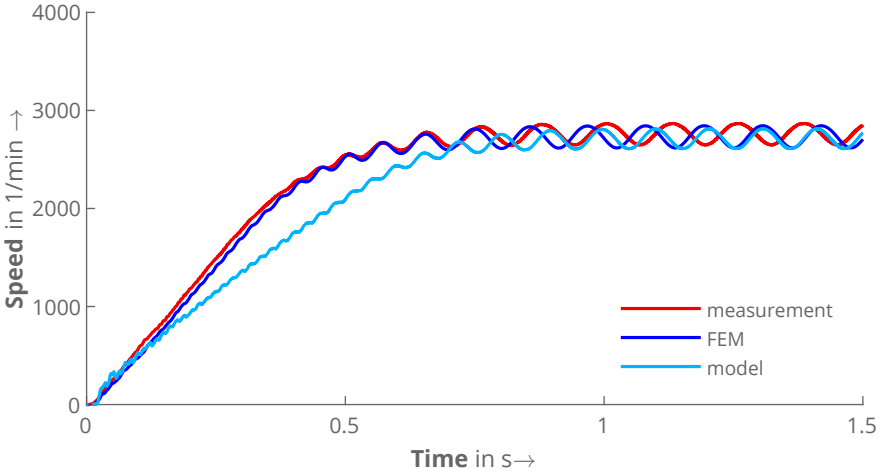

Figure 4.56: Comparison of the speed during dynamic start-up of Motor II at $U = 180\,\mathrm{V}$, $f = 50\,\mathrm{Hz}$, and $T_{\mathrm{load}} = T_{\mathrm{fric}}$ between model, FEM and measurement. The additional moment of inertia is $J_{\mathrm{add}} = 24.2{\cdot}10^{-4}\,\mathrm{kg{\cdot}m^2}$, so that $J_{\mathrm{tot}} = 3.3{\cdot}J_{\mathrm{mot}}$.

Several findings can be derived from the speed comparison: Firstly, the lower acceleration due to the underestimated torque during acceleration can also be identified here. Secondly, the quasi-steady state predicted by the model agrees well with the FEM and the measurement. As in the previous comparison, it can also be seen that the final speed of the model is slightly lower than both others, and therefore the model makes the most pessimistic prediction.

When comparing the current (Figure 4.57), which is shown for approximately one slip period, the slight differences in slip can also be seen. The basic shapes resulting from the speed oscillations are very similar, but the model (highest slip) also shows the highest current. In contrast, the measurement (lowest slip) shows the smallest current. The phase shift between all three curves is only due to the unavoidable phase shift of the speed.

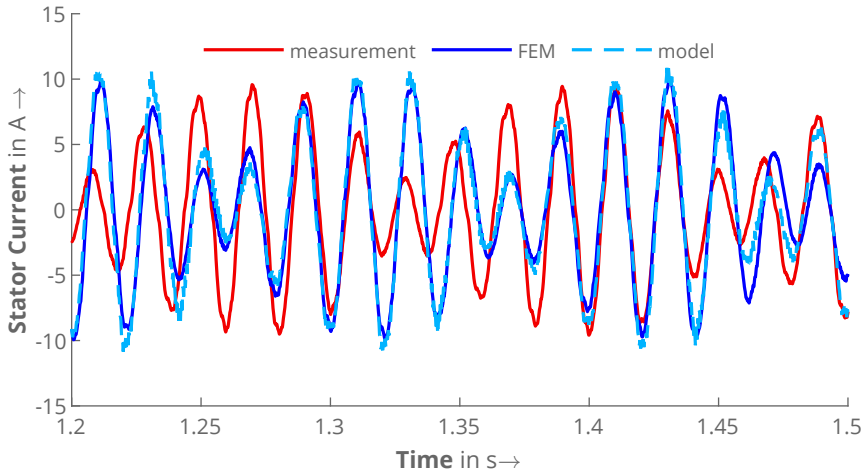

Figure 4.57: Comparison of the stator current during dynamic start-up of Motor II at $U = 180\,\mathrm{V}$, $f = 50\,\mathrm{Hz}$, and $T_{\mathrm{load}} = T_{\mathrm{fric}}$ between model, FEM and measurement (corresponds to Figure 4.56). The additional moment of inertia is $J_{\mathrm{add}} = 24.2{\cdot}10^{-4}\,\mathrm{kg{\cdot}m^2}$, so that $J_{\mathrm{tot}} = 3.3{\cdot}J_{\mathrm{mot}}$.

The last comparison for Motor II is shown in Figures 4.58 and 4.59. Here, the moment of inertia has been reduced to 1.98 times the motor's moment of inertia.

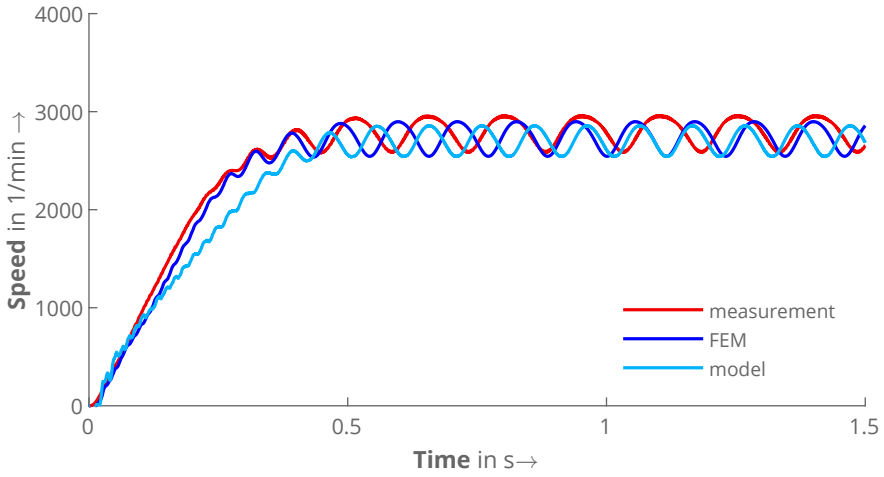

Figure 4.58: Comparison of the speed during dynamic start-up of Motor II at $U = 180\,\mathrm{V}$, $f = 50\,\mathrm{Hz}$, and $T_{\mathrm{load}} = T_{\mathrm{fric}}$ between model, FEM and measurement. The additional moment of inertia is $J_{\mathrm{add}} = 9.1{\cdot}10^{-4}\,\mathrm{kg{\cdot}m^2}$, so that $J_{\mathrm{tot}} = 2.0{\cdot}J_{\mathrm{mot}}$.

The final speed has increased compared to the previous case, but is still below synchronous speed. The resulting speed oscillations predicted by the model in this case are in good agreement with FEM and the measurement. Again, the model shows the highest slip.

Regarding the current (Figure 4.59), the agreement in shape and amplitude is good as well. Only the phase shift due to the different phase angle of the speed oscillations is apparent.

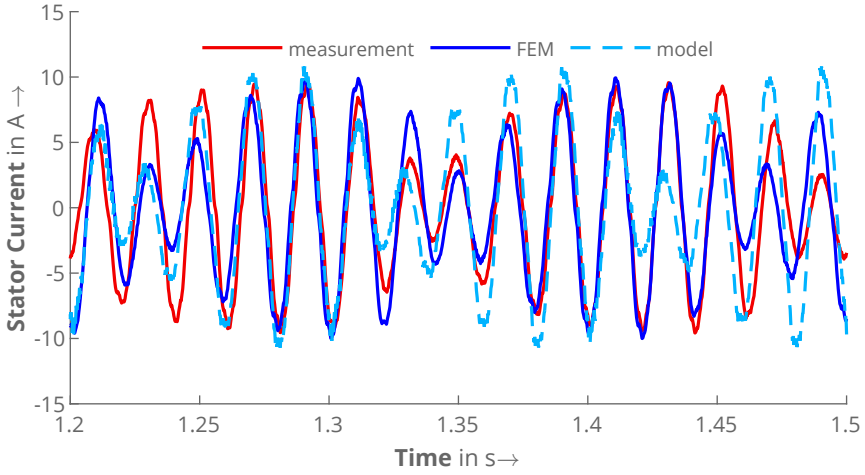

Figure 4.59: Comparison of the stator current during dynamic start-up of Motor II at $U = 180\,\mathrm{V}$, $f = 50\,\mathrm{Hz}$, and $T_{\mathrm{load}} = T_{\mathrm{fric}}$ between model, FEM and measurement (corresponds to Figure 4.58). The additional moment of inertia is $J_{\mathrm{add}} = 9.1{\cdot}10^{-4}\,\mathrm{kg{\cdot}m^2}$, so that $J_{\mathrm{tot}} = 2.0{\cdot}J_{\mathrm{mot}}$.

4.6.0.2 Motor III

In the last step, the results for the start-up of Motor III are compared. Figure 4.60 shows the case of a start-up without additional moment of inertia at no-load. As in the FEM, the model correctly predicts the synchronization, whereas in this case, the damping is even worse.

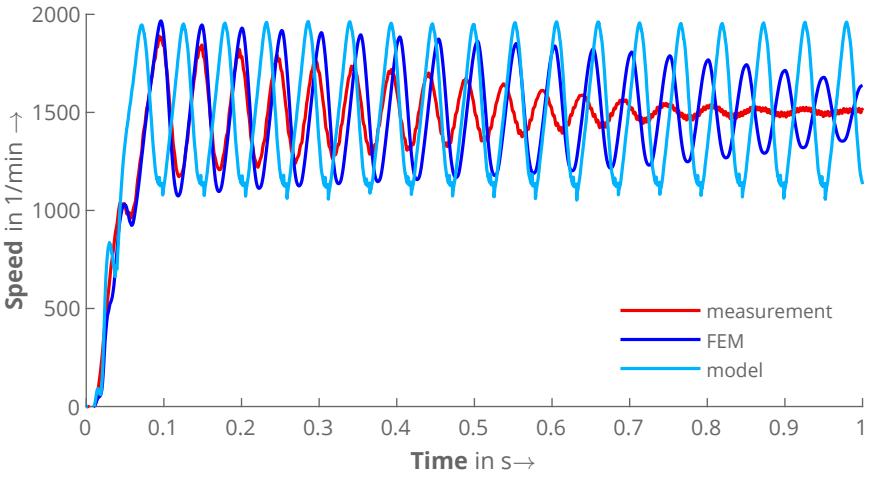

Figure 4.60: Comparison of the speed during dynamic start-up of Motor III at $U = 140\mathrm{V}$, $f = 50\,\mathrm{Hz}$, and $T_{\mathrm{load}} = T_{\mathrm{fric}}$ between model, FEM and measurement. The additional moment of inertia is $J_{\mathrm{add}} = 0$, so that $J_{\mathrm{tot}} = J_{\mathrm{mot}}$.

However, since both calculation models show deviations from the measurement in this aspect, it can be said that the error must be sought between measurement and simulation

in general and not between the model and the FEM. This is therefore not a limitation regarding the validation of the model.

If the total moment of inertia is increased to twice the motor's inertia, the motor cannot synchronize anymore. Figure 4.61 proves that the model is almost as accurate as FEM. Both simulations show a slight deviation of the final speed in the quasi-steady state, but the agreement is satisfactory. The model in this case overestimates the torque during start-up.

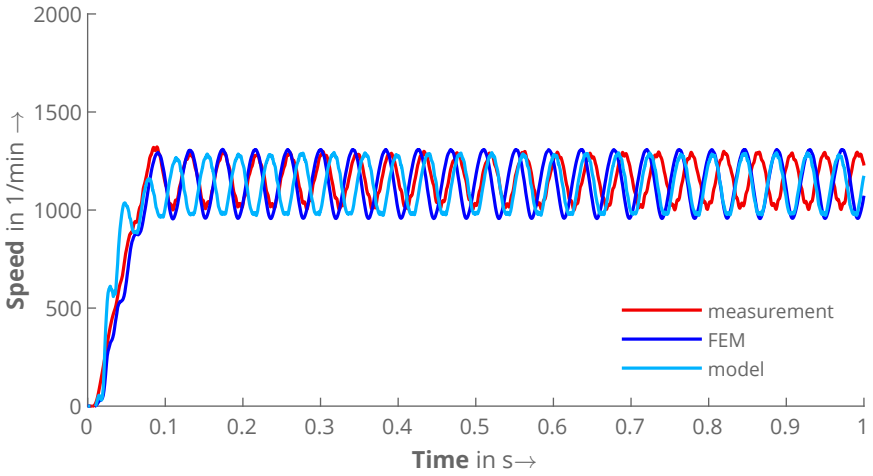

Figure 4.61: Comparison of the speed during dynamic start-up of Motor III at $U = 140\text{V}$, $f = 50$ Hz, and $T_{\text{load}} = T_{\text{fric}}$ between model, FEM and measurement. The additional moment of inertia is $J_{\text{add}} = 9.1{\cdot}10^{-4}$ kg·m^2, so that $J_{\text{tot}} = 2.0{\cdot}J_{\text{mot}}$.

Finally, the comparison with the highest moment of inertia, which equals 3.32 times the motor's inertia, is shown in Figure 4.62. Here, the oscillations of the speed are lower in both the measurement and the simulations. The model is again in close agreement with FEM.

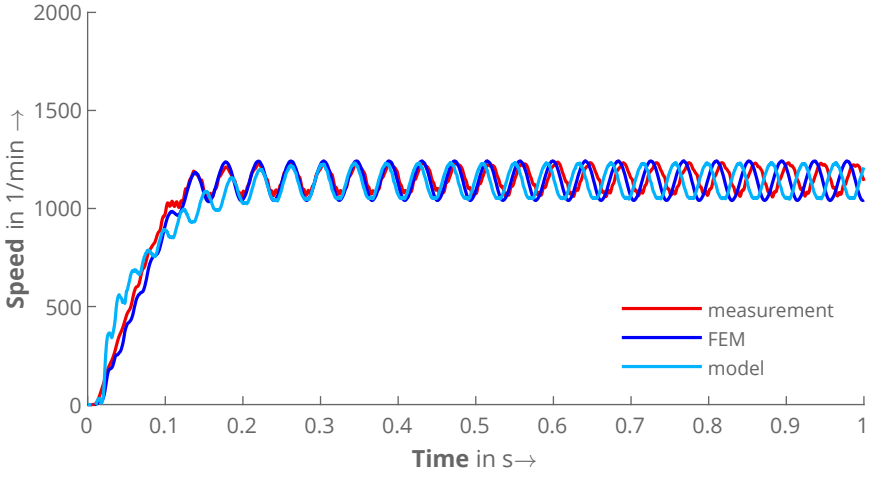

Figure 4.62: Comparison of the speed during dynamic start-up of Motor III at $U = 140\text{V}$, $f = 50$ Hz, and $T_{\text{load}} = T_{\text{fric}}$ between model, FEM and measurement. The additional moment of inertia is $J_{\text{add}} = 24.2{\cdot}10^{-4}$ kg·m^2, so that $J_{\text{tot}} = 3.3{\cdot}J_{\text{mot}}$.

Regarding the comparison of both motors with measurement results, it can be concluded that the model has satisfactory accuracy. The deviations compared to the Finite Element Method are small enough to enable a reliable prediction to be made about the

synchronization behavior of both motors using the model. As these are not optimized and, as discussed throughout the thesis, exhibit many parasitic effects, the validation is all the more important as the model was able to reproduce each of these effects well. It can be assumed that motors that are optimized in their start-up and operating behavior and exhibit fewer parasitic effects can therefore also be simulated reliably. In order to clearly highlight the greatest advantage of the model, the following section compares the computing times of both methods.

4.7 Comparison of the computing time

Now that the accuracy of the model has been verified using FEM and measurements, the computing times of both simulation models are to be compared. The following Table 4.1 compares the computing times for Motor II with the model and the FEM for the three start-up simulations shown in the previous section[1]. The first column lists the additional moment of inertia J_{add} in each case, and the second column the simulation time t_{sim}. For the model, both the computing time needed for the preliminary parameter calculations (inductances, resistances, saturation factors) and the computing time for the start-up simulation are given. To highlight the influence of the multi-layer method in the FE model, the times are shown for both 3 layers and 1 layer.

J_{add} in kg·cm^2	t_{sim}	**Model** (prelim.)	**Model** (3 layers)	**FEM** (3 layers)	**FEM** (1 layer)
0	1.0 s	2:06 h	51 s	8:59 h	3:55 h
9.1	1.5 s	-	81 s	13:20 h	5:56 h
24.2	1.5 s	-	79 s	13:17 h	5:44 h
total		2:06 h	211 s	35:36 h	15:35 h

Table 4.1: Comparison of computing times for Motor II for the simulations with the model and FEM from Section 4.6. The preliminary calculations for the model are required only once. The computing times for the FE model with 1 layer is given as a reference

It can be seen from the data that the model is considerably faster than the FEM. Even though the parameter calculation takes about 2 hours, the model is tremendously fast after that process. As each simulation with varying moment of inertia can be carried out with the same parameters, the preliminary calculations only have to be done once. Thereafter, each individual simulation of a dynamic start only takes around 1 to 1.5 minutes (depending on the simulation time). Even if the voltage (as shown in Figure 4.55), the load torque, the parameters of the stator and rotor windings and many other parameters are changed, no new parameter calculation is necessary.

In contrast, the Finite Element model has to be solved for each single set of parameters. Hence, the time for all three start-ups sums to 35.5 hours, whereby one single simulation can last more than 13 hours as shown in the last two of the three cases. The need to divide the rotor cage into multiple layers in the FE model leads to a more than doubling of the computing time compared to the standard model with one layer.

[1] All simulations were carried out on the same system equipped with an Intel® Core™ i9-10900K and 64 GB RAM.

The comparison of the results for Motor III in Table 4.2 also shows clear differences between the two models. The parameter calculation takes less than 2 hours and the solution of the model for each start-up less than one and a half minutes for 1 s of simulation time. In contrast, FEM takes more than 27 hours in total.

J_{add} in kg·cm^2	t_{sim}	**Model** (prelim.)	**Model** (3 layers)	**FEM** (3 layers)	**FEM** (1 layer)
0	1.0 s	1:55 h	82 s	9:02 h	2:40 h
9.1	1.0 s	-	78 s	9:12 h	2:35 h
24.2	1.0 s	-	77 s	8:59 h	2:35 h
total		1:55 h	237 s	27:12 h	7:50 h

Table 4.2: Comparison of computing times for Motor III for the simulations with the model and FEM from Section 4.6. The preliminary calculations for the model are required only once. The computing times for the FE model with 1 layer is given as a reference

Both comparisons show the clear strength of the model: Even if the parameter calculation is included, the model is already many times faster than a single solution of the FE model. The longer the simulation time and the greater the number of start-ups to be calculated, the greater the advantage in terms of computing time. For the application of the model in practice, this means that the determination of the load torque for which the motor synchronizes at a given moment of inertia (which requires multiple simulations) can be completed with the model in a shorter time than the FEM requires for a single simulation.

4.8 Conclusion

This chapter presented a fast numerical parameter model that can accurately predict the dynamic start-up behavior of Line-Start Synchronous Reluctance Machines with rotor designs that include non-standard rotor cages in the flux barriers. Based on the model introduced by Güdelhöfer in [54], [55], alternative and improved methods for considering the skin effect and saturation as the most important effects were used to improve the accuracy of the model.

The skin effect can no longer be considered for non-standard cages by simple factors that manipulate the resistance and inductance according to the rotor fundamental frequency. The previous method was hence replaced by the multi-layer method, which divides the rotor cage into multiple cages. This showed good agreement with the FEM for three layers already. Both the fundamental frequency and the harmonics matched well over the entire speed range.

The approach of considering saturation with a global saturation factor was retained. However, it was extended to a dq-saturation factor model that can better represent the influence of the anisotropy on the saturation. Additionally, the model was extended to consider iron bridges in the rotor.

Both the validation with FEM and measurements have demonstrated that the model can accurately predict the dynamic start-up behavior of LSSynRM with non-standard rotor cage designs. The comparison of the computing times emphasized the need for such a model, as it is significantly faster than the 2D FEM.

Chapter 5

Conclusion

This study set out to improve existing Finite Element and numerical parameter models for the simulation of the dynamic start-up of Line-Start Synchronous Reluctance Machines with non-standard rotor cages, which are housed in the flux barriers.

The Finite Element model was essentially extended by considering the non-standard rotor cage and its end rings. Previous studies could not provide an adequate method to calculate the resistances of the different ring segments, which are coupled to the 2D FE model via an external rotor circuit. This thesis hence presented a 3D FE-assisted approach to calculate the parameters for any type of ring geometry.

By calculating the resistance with electrostatic FEM, any desired conductor geometry can be specified. This resistance is then divided into a virtual bar end and a ring resistance so that it can be used with the standard rotor cage model for induction machines. The comparison with a standard Induction Machine cage showed that the method delivers good results.

Moreover, the skin effect in the end ring of the non-standard rotor cages was investigated. The findings clearly indicate that it is not only important during the starting phase with high rotor frequencies, but also during the synchronization phase. Because the rotor bars are particularly deep, and the ring has a corresponding radial height, the skin effect of the bars is transferred to the ring. The experimental validation revealed that this influences the synchronization behavior, as the effective rotor resistance is increased for the fundamental and the harmonics due to this effect. The finding from this is that in such cage geometries, taking this effect into account can decide whether the motor synchronizes or not.

Furthermore, an existing numerical parameter model for Line-Start Synchronous Reluctance Machines introduced in [54], [55] was improved mainly in terms of skin effect and saturation.

For the skin effect, which was previously considered using factors that manipulate the resistance and inductance as a function of the rotor fundamental frequency, the well-known multi-layer method was used. This not only covers an accurate representation of the skin effect of the fundamental frequency, but can also take harmonic losses into account to a certain extent. The multi-layer ring model that was already introduced for the Finite Element model to account for non-standard rotor cages was applied as well.

The saturation model used in the existing model, on the other hand, has neglected the different saturation behavior of both axes in an anisotropic machine. Since the existing

saturation factor approach was already a suitable method in terms of the desired drastic reduction in computing time compared to FEM, only the accuracy of the method needed to be improved. By introducing two different factors for the saturation of the d- and q-axis, it was possible to better represent the different saturation states and improve the model without a significant increase in computing time.

In Line-Start Synchronous Reluctance Machines adapted from classic Synchronous Reluctance Machines, there are also significantly more iron bridges in the rotor that provide mechanical stability. However, it was shown in this work that they have a major influence on the magnetic circuit and hence on the operating behavior of the machine.

On the one hand, closed tangential bridges on the outer diameter of the rotor cause the air gap to be smooth on one side, which results in a lower Carter factor and a reduced magnetizing current. The harmonics in the air gap field are also reduced. On the other hand, in contrast to air, the iron bridges cause the q-axis to have a higher permeance and therefore change the $L_\mathrm{d}/L_\mathrm{q}$ ratio depending on the saturation.

However, the model only had to be changed slightly for this purpose. While the inductances of the model for constant material properties still have to be calculated with open bridges, the real geometry can be used for the calculation of the saturation factors. With the dq-saturation factor model, the fundamental flux linkages of the two axes are then always manipulated so that they correspond to the real model.

Finally, the underlying system of equations was also changed compared to the existing model. By defining the flux linkage as a state variable, the derivation was greatly simplified and the understanding of the model was improved.

The validation was initially carried out with the FEM, which is to be replaced by the presented model in different stages of the design process. The results proved that the skin effect can be modeled accurately regardless of the geometry of the rotor cage. In addition, clear improvements in the accuracy of the consideration of saturation were observable when using dq-saturation factors.

However, regarding the saturation model, some limitations need to be acknowledged as well. Firstly, the saturation factor method can only manipulate the fundamental current related to a specific flux linkage. Hence, the change in harmonic effects of any kind due to saturation cannot be considered with this model. However, it was observed that the results were nevertheless very close to the results of the FEM and often differed only in the harmonic content.

Secondly, the validation of both effects combined based on the comparison of the steady-state torque-speed characteristic indicated that not considering the saturation of the leakage paths in the model can lead to deviations in the start-up phase. In Line-Start Synchronous Reluctance Machines with tangential bridges at the air gap, this effect is even more pronounced. The starting current and the starting torque therefore cannot be accurately predicted with the model.

On the one hand, however, these are tasks for the FEM and measurements anyway. On the other hand, most applications of LSSynRM (pumps, fans, spindles) only require a small starting torque, which is why the influence of the error can be considered small. Moreover, the comparison of the dynamic start-up proved that the area in which the motor is in the synchronization phase can still be simulated well by the model. This could also be proven in the comparison with start-up measurements, in which the model led to the same predictions of successful and unsuccessful start-ups in most cases.

In conclusion, it can be said that the model was significantly improved and can now be used for modern Line-Start Synchronous Reluctance Machine geometries as well. As

the comparison of the computing time proved, it is considerably faster than the FEM, with the time-saving increasing significantly the longer the simulation time and with each additional simulation of the same motor. The results of the model were consistently satisfactory and its applicability and accuracy were further improved compared to Güdelhöfer's model, which is why it can make a significant contribution to practice.

Finally, the most important contributions of this work will be briefly listed once again:

- The transient 2D Finite Element model was expanded by a rotor circuit with ring and bar end resistances calculated with 3D electrostatic FEM, which is suited for non-standard rotor cages.
- The investigation of the skin effect in the rotor cage with the multi-layer method revealed that the skin effect in the rotor bars of die-cast rotor cages transfers to the end rings and hence has to be considered to accurately predict the rotor resistance and the start-up behavior.
- An existing numerical parameter model was extended to non-standard rotor cages by applying the multi-layer method to accurately account for skin effect during start-up and steady-state operation.
- The saturation factor approach used previously was improved in that the saturation states of the d- and q-axis are now each represented by a separate factor.
- The consideration of the iron bridges, which were previously neglected, could also be implemented with this approach. It was demonstrated that it massively influences the operating behavior for modern LSSynRM.
- For both FEM and the numerical parameter model, three rotor cage layers seem to be a good compromise between accuracy and computing time.

References

[1] The European Commission, *Electric motors and variable speed drives*, 2021. [Online]. Available: https://commission.europa.eu/energy-climate-change-environment/standards-tools-and-labels/products-labelling-rules-and-requirements/energy-label-and-ecodesign/energy-efficient-products/electric-motors-and-variable-speed-drives_en (visited on 10/23/2023) (cit. on p. 1).

[2] The European Commission, *COMMISSION REGULATION (EU) 2021/341*, The European Commission, Ed., 2021. [Online]. Available: http://data.europa.eu/eli/reg/2021/341/oj (visited on 10/23/2023) (cit. on p. 1).

[3] K. Oberretl, "13 Regeln für minimale Zusatzverluste in Induktionsmotoren," *Bulletin Oerlikon*, no. 389/390, pp. 2–12, 1969 (cit. on p. 1).

[4] M. Villani, G. Fabri, A. Credo, L. Di Leonardo, and F. Parasiliti Collazzo, "Line-Start Synchronous Reluctance Motor: A Reduced Manufacturing Cost Avenue to Achieve IE4 Efficiency Class," *IEEE Access*, vol. 10, pp. 100 094–100 103, 2022. DOI: 10.1109/ACCESS.2022.3208154 (cit. on pp. 1, 2).

[5] CIGRE Working Group A1.47, "Technological Feasibility Studies for Super and Ultra Premium Efficient Motors," *CIGRE Technical Brochures*, vol. 729, 2018. [Online]. Available: https://e-cigre.org/publication/729-technological-feasibility-studies-for-super-and-ultra-premium-efficient-motors (cit. on pp. 2, 4).

[6] A. H. Isfahani and S. Vaez-Zadeh, "Line start permanent magnet synchronous motors: Challenges and opportunities," *Energy*, vol. 34, no. 11, pp. 1755–1763, 2009, ISSN: 03605442. DOI: 10.1016/j.energy.2009.04.022 (cit. on p. 2).

[7] D. Gielen and M. Lyons, *Critical materials for the energy transition: Rare earth elements*. Abu Dhabi: International Renewable Energy Agency, 2022, ISBN: 978-92-9260-437-0 (cit. on p. 2).

[8] Digital Science, *Dimensions [Software]*, 2018. [Online]. Available: https://app.dimensions.ai (visited on 10/24/2023) (cit. on p. 3).

[9] J. K. Kostko, "Polyphase reaction synchronous motors," *Journal of the American Institute of Electrical Engineers*, vol. 42, no. 11, pp. 1162–1168, 1923, ISSN: 0360-6449. DOI: 10.1109/JoAIEE.1923.6591529 (cit. on p. 3).

[10] M. Doppelbauer, *Eine kleine Historie der elektrischen Motorentechnik - Teil 1: Die Erfindung des Elektromotors 1800-1854*. [Online]. Available: https://www.eti.kit.edu/1376.php (visited on 02/23/2024) (cit. on p. 3).

[11] M. Doppelbauer, *Eine kleine Historie der elektrischen Motorentechnik - Teil 2: Die Erfindung des Elektromotors 1856-1893*. [Online]. Available: https://www.eti.kit.edu/1390.php (visited on 02/23/2024) (cit. on p. 3).

[12] E. Jasse, "Über Synchronmotoren ohne Erregung," *Archiv für Elektrotechnik*, vol. 2, no. 1, pp. 26–48, 1913. DOI: 10.1007/BF01656739 (cit. on p. 3).

[13] J. Kučera, "Die synchrone Drehfeld-Reaktionsmaschine," *Elektrotechnik und Maschinenbau*, vol. 56, no. 14, pp. 173–178, 1938. [Online]. Available: https://anno.onb.ac.at/cgi-content/anno-plus?aid=emb&datum=1938&pos=257&size=45 (cit. on p. 3).

[14] W. Schuisky, "Beitrag zur Theorie und Berechnung des Reaktionsmotors," *Archiv für Elektrotechnik*, vol. 39, no. 9, pp. 571–578, 1950. DOI: 10.1007/BF01429756 (cit. on p. 3).

[15] S. A. Hassan, A. M. Osheiba, and A. L. Mohamadein, "Performance of Different Types of Reluctance Motors - Experimental Comparative Study," *Electric Machines & Power Systems*, vol. 5, no. 3, pp. 225–236, 1980, ISSN: 0731-356X. DOI: 10.1080/07313568008955405 (cit. on p. 3).

[16] P. F. Bauer and V. Honsinger, "Synchronous Induction Motor Having a Segmented Rotor and Squirrel Cage Winding," pat. 2 733 362, 1956 (cit. on p. 4).

[17] N. O. Risch, "Segmented Rotor Core Lamination for Use in a Synchronous Induction Motor," pat. 2 769 108, 1956 (cit. on p. 4).

[18] H.-D. Stölting and A. Beisse, *Elektrische Kleinmaschinen: Eine Einführung* (Teubner-Studienbücher Elektrotechnik). Stuttgart: Teubner, 1987, ISBN: 3-519-06321-2 (cit. on p. 4).

[19] V. Honsinger, "Inherently Stable Reluctance Motors Having Improved Performance," *IEEE Transactions on Power Apparatus and Systems*, vol. PAS-91, no. 4, pp. 1544–1554, 1972, ISSN: 0018-9510. DOI: 10.1109/TPAS.1972.293307 (cit. on pp. 4, 6).

[20] M. A. Rahman, "History of interior permanent magnet motors [History]," *IEEE Industry Applications Magazine*, vol. 19, no. 1, pp. 10–15, 2013, ISSN: 1077-2618. DOI: 10.1109/MIAS.2012.2221996 (cit. on p. 4).

[21] A. Vagati, G. Franceschini, I. Marongiu, and G. P. Troglia, "Design criteria of high performance synchronous reluctance motors," in *Conference Record of the 1992 IEEE Industry Applications Society Annual Meeting*, IEEE, 1992, pp. 66–73, ISBN: 0-7803-0635-X. DOI: 10.1109/IAS.1992.244463 (cit. on p. 4).

[22] A. Vagati, "Synchronous Reluctance Electrical Motor Having a Low Torque Ripple Design," pat. 5 818 140, 1998 (cit. on p. 4).

[23] M. Gamba, G. Pellegrino, A. Vagati, and F. Villata, "Design of a line-start synchronous reluctance motor," in *2013 International Electric Machines & Drives Conference*, IEEE, 52013, pp. 648–655, ISBN: 978-1-4673-4974-1. DOI: 10.1109/IEMDC.2013.6556163 (cit. on pp. 4, 5, 7).

[24] M. Gamba, E. Armando, G. Pellegrino, A. Vagati, B. Janjic, and J. Schaab, "Line-start synchronous reluctance motors: Design guidelines and testing via active inertia emulation," in *2015 IEEE Energy Conversion Congress and Exposition (ECCE)*, IEEE, 92015, pp. 4820–4827, ISBN: 978-1-4673-7151-3. DOI: 10.1109/ECCE.2015.7310340 (cit. on p. 4).

[25] T.-U. Jung, C.-H. Yun, H.-R. Cha, H.-M. Kim, H. Nam, and J.-P. Hong, "The Rotor Conductor Design for Starting Stability of Line-Start Synchronous Reluctance Motor," in *IECON 2006 - 32nd Annual Conference on IEEE Industrial Electronics*, IEEE, 112006, pp. 1107–1112, ISBN: 1-4244-0390-1. DOI: 10.1109/IECON.2006.347605 (cit. on p. 4).

[26] A. Negahdari and H. A. Toliyat, "Studying crawling effect in Line-Start Synchronous Reluctance Motors (LS-SynRM)," in *2016 IEEE 25th International Symposium on Industrial Electronics (ISIE)*, IEEE, 62016, pp. 210–215, ISBN: 978-1-5090-0873-5. DOI: 10.1109/ISIE.2016.7744891 (cit. on p. 4).

[27] Q. Smit, A. Sorgdrager, and R.-J. Wang, "Design and Optimisation of a Line-Start Synchronous Reluctance Motor," in *24th Southern African Universities Power Engineering Conference*, 2016. DOI: 10.13140/RG.2.1.4266.8560 (cit. on pp. 4, 5, 7).

[28] M. Villani, M. Santececca, and F. Parasiliti, "High-Efficiency Line-Start Synchronous Reluctance Motor for Fan and Pump Applications," in *2018 XIII International Conference on Electrical Machines (ICEM)*, IEEE, 92018, pp. 2178–2184, ISBN: 978-1-5386-2477-7. DOI: 10.1109/ICELMACH.2018.8507230 (cit. on pp. 4–7).

[29] C.-T. Liu, P.-C. Shih, Z.-H. Cai, *et al.*, "Rotor Conductor Arrangement Designs of High-Efficiency Direct-on-Line Synchronous Reluctance Motors for Metal Industry Applications," *IEEE Transactions on Industry Applications*, vol. 56, no. 4, pp. 4337–4344, 2020, ISSN: 0093-9994. DOI: 10.1109/TIA.2020.2983903 (cit. on pp. 4, 5, 7).

[30] Y. Hu, B. Chen, Y. Xiao, J. Shi, X. Li, and L. Li, "Rotor Design and Optimization of a Three-Phase Line-Start Synchronous Reluctance Motor," *IEEE Transactions on Industry Applications*, vol. 57, no. 2, pp. 1365–1374, 2021, ISSN: 0093-9994. DOI: 10.1109/TIA.2020.3043224 (cit. on pp. 4, 6, 7).

[31] V. Abramenko, J. Barta, I. Lolova, I. Petrov, and J. Pyrhönen, "Design of a Low-Power Direct-on-Line Synchronous Reluctance Motor Based on the Modified Natural Flux Line Curve Approach," *IEEE Transactions on Industry Applications*, vol. 57, no. 6, pp. 5894–5906, 2021, ISSN: 0093-9994. DOI: 10.1109/TIA.2021.3108947 (cit. on pp. 4, 5, 7).

[32] H. L. Garbarino and E. T. B. Gross, "The goerges phenomenon: Induction motors with unbalanced rotor impedances," *Electrical Engineering*, vol. 70, no. 7, p. 604, 1951, ISSN: 0095-9197. DOI: 10.1109/EE.1951.6436707 (cit. on pp. 5, 14).

[33] J. M. Stephenson and P. J. Lawrenson, "Average asynchronous torque of synchronous machines, with particular reference to reluctance machines," *Proceedings of the Institution of Electrical Engineers*, vol. 116, no. 6, p. 1049, 1969, ISSN: 00203270. DOI: 10.1049/piee.1969.0195 (cit. on pp. 5, 14, 125).

[34] G. Müller and B. Ponick, *Theorie elektrischer Maschinen* (Elektrische Maschinen), 6., völlig neu bearb. Aufl. Weinheim: Wiley-VCH, 2009, vol. 3, ISBN: 9783527405268 (cit. on pp. 5, 14, 125).

[35] A. Binder, *Elektrische Maschinen und Antriebe: Grundlagen, Betriebsverhalten.* Berlin and Heidelberg: Springer, 2012, ISBN: 978-3-540-71849-9. DOI: 10.1007/978-3-540-71850-5 (cit. on pp. 5, 14, 28, 80, 82, 86, 125).

[36] I. Lolova, J. Barta, G. Bramerdorfer, and S. Silber, "Topology optimization of line-start synchronous reluctance machine," in *2020 19th International Conference on Mechatronics - Mechatronika (ME)*, IEEE, 1222020, pp. 1–7, ISBN: 978-1-7281-5602-6. DOI: 10.1109/ME49197.2020.9286643 (cit. on pp. 5–7).

[37] V. Abramenko, I. Petrov, and J. Pyrhonen, "Analysis of damper winding designs for direct-on-line synchronous reluctance motor," in *Proceedings IECON 2017 - 43nd Annual Conference of the IEEE Industrial Electronics Society*, Piscataway, NJ: IEEE, 2017, pp. 1802–1809, ISBN: 978-1-5386-1127-2. DOI: 10.1109/IECON.2017.8216305 (cit. on pp. 5–7).

[38] J. Tampio, T. Kansakangas, S. Suuriniemi, J. Kolehmainen, L. Kettunen, and J. Ikaheimo, "Analysis of Direct-On-Line Synchronous Reluctance Machine Start-Up Using a Magnetic Field Decomposition," *IEEE Transactions on Industry Applications*, vol. 53, no. 3, pp. 1852–1859, 2017, ISSN: 0093-9994. DOI: 10.1109/TIA.2016.2642891 (cit. on pp. 5, 6).

[39] H.-C. Liu and J. Lee, "Optimum Design of an IE4 Line-Start Synchronous Reluctance Motor Considering Manufacturing Process Loss Effect," *IEEE Transactions on Industrial Electronics*, vol. 65, no. 4, pp. 3104–3114, 2018, ISSN: 0278-0046. DOI: 10.1109/TIE.2017.2758738 (cit. on pp. 5–7).

[40] Y. Hu, B. Chen, Y. Xiao, J. Shi, L. Li, and X. Li, "Rotor Design and Optimization of the Three-phase Line-start Synchronous Reluctance Motor," in *2019 22nd International Conference on Electrical Machines and Systems (ICEMS)*, Piscataway, NJ: IEEE, 2019, pp. 1–6, ISBN: 978-1-7281-3398-0. DOI: 10.1109/ICEMS.2019.8922128 (cit. on pp. 5–7, 14).

[41] V. Abramenko, I. Petrov, and J. Pyrhonen, "Design of Low-Power Direct-on-Line Synchronous Reluctance Motors Based on Modified Natural-FluxLine-Curve Approach," in *2020 International Conference on Electrical Machines (ICEM)*, IEEE, 8232020, pp. 2272–2279, ISBN: 978-1-7281-9945-0. DOI: 10.1109/ICEM49940.2020.9270893 (cit. on pp. 5, 6).

[42] J. Barta, L. Knebl, O. Vitek, G. Bramerdorfer, and S. Silber, "Optimization of Line-Start Synchronous Reluctance Machine Amended From an Induction Machine," in *2020 International Conference on Electrical Machines (ICEM)*, IEEE, 8232020, pp. 272–277, ISBN: 978-1-7281-9945-0. DOI: 10.1109/ICEM49940.2020.9270722 (cit. on pp. 5, 6).

[43] Y. Hu, B. Chen, Y. Xiao, J. Shi, and L. Li, "Study on the Influence of Design and Optimization of Rotor Bars on Parameters of a Line-Start Synchronous Reluctance Motor," *IEEE Transactions on Industry Applications*, vol. 56, no. 2, pp. 1368–1376, 2020, ISSN: 0093-9994. DOI: 10.1109/TIA.2019.2962431 (cit. on pp. 5–7).

[44] H. Kim, Y. Park, S.-T. Oh, *et al.*, "A Study on the Rotor Design of Line Start Synchronous Reluctance Motor for IE4 Efficiency and Improving Power Factor," *Energies*, vol. 13, no. 21, p. 5774, 2020. DOI: 10.3390/en13215774 (cit. on pp. 5, 6).

[45] L. Knebl, J. Barta, G. Bramerdorfer, O. Vitek, and C. Ondrusek, "Multi-Objective Optimization of a Line-Start Synchronous Machine Using a Self-Organizing Algorithm," *IEEE Transactions on Magnetics*, vol. 57, no. 6, pp. 1–4, 2021, ISSN: 00189464. DOI: 10.1109/TMAG.2021.3056403 (cit. on pp. 5, 6).

[46] S. R. Mousavi-Aghdam and A. Azimi, "Design and analysis of a new improved rotor structure in line-start synchronous reluctance motors," *Archiv für Elektrotechnik*, 2023. DOI: 10.1007/s00202-023-02058-0 (cit. on p. 5).

[47] S.-A. Tahan and I. Kamwa, "A two-factor saturation model for synchronous machines with multiple rotor circuits," *IEEE Transactions on Energy Conversion*, vol. 10, no. 4, pp. 609–616, 1995, ISSN: 08858969. DOI: 10.1109/60.475830 (cit. on pp. 5, 89).

[48] S. T. Boroujeni, N. Bianchi, and L. Alberti, "Fast Estimation of Line-Start Reluctance Machine Parameters by Finite Element Analysis," *IEEE Transactions on Energy Conversion*, vol. 26, no. 1, pp. 1–8, 2011, ISSN: 08858969. DOI: 10.1109/TEC.2010.2061851 (cit. on pp. 5, 7).

[49] S. Enache, A. Campeanu, I. Vlad, M.-A. Enache, and M. Dobriceanu, "Modeling of line-starting of reluctance synchronous motors considering magnetic saturation, with experimental validation," in *2014 International Conference on Optimization of Electrical and Electronic Equipment (OPTIM)*, IEEE, 52014, pp. 324–329, ISBN: 978-1-4799-5183-3. DOI: 10.1109/OPTIM.2014.6850886 (cit. on pp. 5–7).

[50] D. Mingardi and N. Bianchi, "FE-aided analytical method to predict the capabilities of line-start synchronous motors," in *2014 IEEE Energy Conversion Congress and Exposition (ECCE)*, IEEE, 92014, pp. 5123–5130, ISBN: 978-1-4799-5776-7. DOI: 10.1109/ECCE.2014.6954104 (cit. on pp. 5, 7).

[51] A. Kersten, Y. Liu, D. Pehrman, and T. Thiringer, "Rotor Design of Line-Start Synchronous Reluctance Machine With Round Bars," *IEEE Transactions on Industry Applications*, vol. 55, no. 4, pp. 3685–3696, 2019, ISSN: 0093-9994. DOI: 10.1109/TIA.2019.2914010 (cit. on pp. 5–7).

[52] C.-T. Liu, Y.-X. Li, S.-C. Yen, *et al.*, "Structural Optimizations of High-efficiency Direct-On-Line Synchronous Reluctance Motors for Metal Industry Applications," *IEEE Transactions on Industry Applications*, vol. 57, no. 3, pp. 3004–3011, 2021, ISSN: 0093-9994. DOI: 10.1109/TIA.2021.3064550 (cit. on pp. 5, 6).

[53] U.-J. Seo, D.-J. Kim, P.-W. Han, and Y.-D. Chun, "FE-Aided Synchronization Analysis of Line-Start Synchronous Reluctance Motors," *Applied Sciences*, vol. 11, no. 24, p. 11 673, 2021. DOI: 10.3390/app112411673 (cit. on p. 5).

[54] J. Güdelhöfer, R. Gottkehaskamp, and A. Möckel, "Transient Model of Direct on Line Induction and Synchronous Reluctance Motors with Inter-bar Currents," in *2018 XIII International Conference on Electrical Machines (ICEM)*, IEEE, 92018, pp. 440–446, ISBN: 978-1-5386-2477-7. DOI: 10.1109/ICELMACH.2018.8507162 (cit. on pp. 6–8, 42, 71, 74, 88, 94, 99, 104, 105, 124, 148, 149).

[55] J. Güdelhöfer, "Analytisches transientes Berechnungsmodell für selbstanlaufende Synchronreluktanzmaschinen," Dissertation, Karlsruher Institut für Technologie (KIT), 2019 (cit. on pp. 6–8, 43, 44, 67, 71, 74, 88, 94, 99, 104, 105, 124, 148, 149).

[56] J. F. H. Douglas, "Pull-in criterion for reluctance motors," *Transactions of the American Institute of Electrical Engineers, Part II: Applications and Industry*, vol. 79, no. 3, pp. 139–142, 1960, ISSN: 0097-2185. DOI: 10.1109/TAI.1960.6371657 (cit. on pp. 6, 13).

[57] A. Negahdari, V. M. Sundaram, and H. A. Toliyat, "An analytical approach for determining harmonic cusps and torque dips in line start synchronous reluctance motors," in *2016 IEEE Energy Conversion Congress and Exposition (ECCE)*, IEEE, 92016, pp. 1–6, ISBN: 978-1-5090-0737-0. DOI: 10.1109/ECCE.2016.7854838 (cit. on p. 6).

[58] V. Abramenko, I. Petrov, J. Pyrhonen, and L. Aarniovuori, "Design Aspects of Direct-on-Line Synchronous Reluctance Motors," in *2018 XIII International Conference on Electrical Machines (ICEM)*, IEEE, 92018, pp. 138–145, ISBN: 978-1-5386-2477-7. DOI: 10.1109/ICELMACH.2018.8506710 (cit. on p. 6).

[59] S. Baka, S. Sashidhar, and B. G. Fernandes, "Design of an Energy Efficient Line-Start Two-Pole Ferrite Assisted Synchronous Reluctance Motor for Water Pumps," *IEEE Transactions on Energy Conversion*, vol. 36, no. 2, pp. 961–970, 2021, ISSN: 08858969. DOI: 10.1109/TEC.2020.3029110 (cit. on pp. 6, 8).

[60] J. R. Hendershot and T. J. E. Miller, *Design of brushless permanent-magnet machines*. Venice, Florida: Motor Design Books, 2010, ISBN: 9780984068708 (cit. on pp. 12, 13).

[61] W. Nürnberg, *Die Asynchronmaschine: Ihre Theorie und Berechnung unter besonderer Berücksichtigung der Keilstab- und Doppelkäfigläufer*, 2. ed. Berlin, Heidelberg: Springer Berlin Heidelberg, 1952, ISBN: 978-3-642-64969-1. DOI: 10.1007/978-3-642-64968-4 (cit. on pp. 12, 35, 77).

[62] R. Gottkehaskamp, "Elektrische Maschinen," Lecture Notes, University of Applied Sciences Düsseldorf, Düsseldorf, 2017 (cit. on p. 12).

[63] K. Oberretl, "Parasitäre synchrone Dreh- und Pendelmomente in Asynchronmotoren, Einfluß von Ausgleichsvorgängen und Eisensättigung: Teil I: Stationärer Zustand," *Archiv für Elektrotechnik*, vol. 77, no. 3, pp. 179–190, 1994. DOI: 10.1007/BF01573893 (cit. on p. 14).

[64] K. Oberretl, "Parasitäre synchrone Dreh- und Pendelmomente in Asynchronmotoren, Einfluß von Ausgleichsvorgängen und Eisensättigung: Teil II: Schneller Hochlauf, feldabhängige Permeabilität," *Archiv für Elektrotechnik*, vol. 77, no. 4, pp. 277–288, 1994. DOI: 10.1007/BF01577389 (cit. on p. 14).

[65] COMSOL AB, *COMSOL Multiphysics® [Software]*, Stockholm, Sweden. [Online]. Available: www.comsol.com (cit. on p. 19).

[66] K. Oberretl, "Die genauere Berechnung des Magnetisierungsstromes von dreiphasigen Asynchronmaschinen," *Bulletin Oerlikon*, no. 335, pp. 66–84, 1959 (cit. on pp. 25, 44).

[67] A. Schoppa, J. Schneider, and J.-O. Roth, "Influence of the cutting process on the magnetic properties of non-oriented electrical steels," *Journal of Magnetism and Magnetic Materials*, vol. 215-216, pp. 100–102, 2000, ISSN: 03048853. DOI: 10.1016/S0304-8853(00)00077-9 (cit. on pp. 25, 44).

[68] A. P. Schoppa, "Einfluss der Be- und Verarbeitung auf die magnetischen Eigenschaften von schlussgeglühtem, nichtkornorientiertem Elektroband," Dissertation, Technische Hochschule, Aachen, 2001 (cit. on pp. 25, 44).

[69] J. P. A. Bastos and N. Sadowski, *Electromagnetic modeling by finite element methods* (Electrical engineering and electronics). New York and Basel: Dekker, 2003, vol. 117, ISBN: 0-8247-4269-9 (cit. on p. 26).

[70] R. Gottkehaskamp, *Nichtlineare Berechnung von Asynchronmaschinen mit massiveisernem Rotor und zusätzlichem Käfig im transienten Zustand mittels Finiter Differenzen und Zeitschrittrechnung: Dortmund, Univ., Diss* (Fortschritt-Berichte VDI Reihe 21, Elektrotechnik). Düsseldorf: VDI-Verl., 1993, vol. 131, ISBN: 3181431214 (cit. on pp. 27, 29, 31).

[71] A. Krings and J. Soulard, "Overview and Comparison of Iron Loss Models for Electrical Machines," *Journal of Electrical Engineering*, no. 10, pp. 162–169, 2010 (cit. on p. 27).

[72] D. Kowal, P. Sergeant, L. Dupre, and L. Vandenbossche, "Comparison of Iron Loss Models for Electrical Machines With Different Frequency Domain and Time Domain Methods for Excess Loss Prediction," *IEEE Transactions on Magnetics*, vol. 51, no. 1, pp. 1–10, 2015, ISSN: 00189464. DOI: 10.1109/TMAG.2014.2338836 (cit. on p. 27).

[73] R. Richter, *Elektrische Maschinen, 4. Die Induktionsmaschinen* (Elektrische Maschinen), 2., verb. Aufl. Berlin: Springer, 1954 (cit. on pp. 28, 29, 35, 98).

[74] A. Arkkio, *Analysis of induction motors based on the numerical solution of the magnetic field and circuit equations: Otaniemi, Helsinki Univ. of Technology, Diss., 1987* (Acta polytechnica Scandinavica Electrical engineering series El / Scandinavian Council for Applied Research). Helsinki: Finnish Acad. of Technic. Sciences, 1987, vol. 59, ISBN: 9516662501 (cit. on pp. 29, 40).

[75] I. Boldea and S. A. Nasar, *The induction machines design handbook* (The electric power engineering series), 2nd ed. Boca Raton, Fla.: CRC Press/Taylor & Francis, 2010, ISBN: 9781315222592. DOI: 10.1201/9781315222592 (cit. on pp. 29, 38, 77, 86).

[76] R. de Weerdt, K. Hameyer, and R. Belmans, "End ring inductance of a squirrel-cage induction motor using 2D and 3D finite element methods," in *Conference record of the 1995 IEEE Industry Applications Conference - Thirtieth IAS Annual Meeting*, Piscataway, NJ: IEEE Service Center, 1995, pp. 515–522, ISBN: 0-7803-3008-0. DOI: 10.1109/IAS.1995.530343 (cit. on p. 29).

[77] J. Güdelhöfer, R. Gottkehaskamp, and A. Hartmann, "Numerical Calculation of the Dynamic Behavior of Asynchronous Motors with COMSOL Multiphysics," in *2012 COMSOL Conference in Milan*, COMSOL, 2012 (cit. on pp. 31, 39, 73).

[78] P. H. Trickey, "Induction Motor Resistance Ring Width," *Transactions of the American Institute of Electrical Engineers*, vol. 55, no. 2, pp. 144–150, 1936, ISSN: 0096-3860. DOI: 10.1109/T-AIEE.1936.5057231 (cit. on pp. 31, 33).

[79] P. Lombard and F. Zidat, "Determining end ring resistance and inductance of squirrel cage for induction motor with 2D and 3D computations," in *Proceedings, 2016 XXII International Conference on Electrical Machines (ICEM)*, Piscataway, NJ: IEEE, 2016, pp. 266–271, ISBN: 978-1-5090-2538-1. DOI: 10.1109/ICELMACH.2016.7732537 (cit. on p. 34).

[80] W. Schuisky, *Induktionsmaschinen*, 1st ed. 1957. Vienna: Springer Vienna and Imprint: Springer, 1957, ISBN: 978-3-7091-7879-9. DOI: 10.1007/978-3-7091-7878-2 (cit. on p. 35).

[81] S. Williamson and R. Schiferl, "An Investigation of the Influence of Deep-Bar Effect on the Resistance of Cage Rotor End-Rings," *IEEE Transactions on Industry Applications*, vol. IA-23, no. 4, pp. 696–704, 1987, ISSN: 0093-9994. DOI: 10.1109/TIA.1987.4504968 (cit. on pp. 37, 65).

[82] C. Frohne, "Elektromagnetische Vorgänge im Kurzschlußringbereich großer Käfigläufermotoren," *Electrical Engineering*, vol. 80, no. 5, pp. 299–307, 1997, ISSN: 0948-7921. DOI: 10.1007/BF01370967 (cit. on p. 37).

[83] G. Müller, K. Vogt, and B. Ponick, *Berechnung elektrischer Maschinen* (Elektrische Maschinen / Germar Müller), 6., völlig neu bearb. Aufl, Nachdr. Weinheim: Wiley-VCH, 2011, vol. Bd. 2, ISBN: 3527405259 (cit. on pp. 38, 77).

[84] V. Ostović, *Dynamics of saturated electric machines*. New York and Heidelberg: Springer, 1989, ISBN: 978-1-4613-8935-4 (cit. on pp. 38, 77, 78).

[85] W. H. Hayt and J. A. Buck, *Engineering Electromagnetics* (McGraw-Hill Series in Electrical and Computer Engineering). McGraw-Hill, 2001, vol. 6 (cit. on pp. 38, 77, 112).

[86] F. Piriou and A. Razek, "A model for coupled magnetic-electric circuits in electric machines with skewed slots," *IEEE Transactions on Magnetics*, vol. 26, no. 2, pp. 1096–1100, 1990, ISSN: 00189464. DOI: 10.1109/20.106510 (cit. on p. 40).

[87] S. Williamson, T. J. Flack, and A. F. Volschenk, "Representation of skew in time-stepped two-dimensional finite-element models of electrical machines," in *Conference record of the 1994 IEEE Industry Applications Conference - Twenty-Ninth IAS Annual Meeting*, Piscataway, NJ: IEEE Service Center, 1994, pp. 143–148, ISBN: 0-7803-1993-1. DOI: 10.1109/IAS.1994.345486 (cit. on p. 40).

[88] S. L. Ho and W. N. Fu, "A comprehensive approach to the solution of direct-coupled multislice model of skewed rotor induction motors using time-stepping eddy-current finite element method," *IEEE Transactions on Magnetics*, vol. 33, no. 3, pp. 2265–2273, 1997, ISSN: 00189464. DOI: 10.1109/20.573842 (cit. on p. 40).

[89] J. Güdelhöfer, D. Strbac, and R. Gottkehaskamp, "Optimization of synchronous reluctance rotors as replacements for squirrel cages of small induction motors up to an IEC frame of 90," in *IKMT 2015*, Piscataway, NJ: IEEE, 2015, pp. 182–187 (cit. on p. 42).

[90] L. Queval and H. Ohsaki, "Nonlinear abc-Model for Electrical Machines Using N-D Lookup Tables," *IEEE Transactions on Energy Conversion*, vol. 30, no. 1, pp. 316–322, 2015, ISSN: 08858969. DOI: 10.1109/TEC.2014.2358854 (cit. on pp. 72, 75, 87).

[91] A. R. Munoz and T. A. Lipo, "Complex vector model of the squirrel-cage induction machine including instantaneous rotor bar currents," *IEEE Transactions on Industry Applications*, vol. 35, no. 6, pp. 1332–1340, 1999, ISSN: 0093-9994. DOI: 10.1109/28.806047 (cit. on p. 73).

[92] L. Queval and H. Ohsaki, "abc-Modeling of Permanent Magnet Machines using N-D Lookup Tables: a Finite Element Validation," in *Symposium de Génie Électrique 2014*, 2014. [Online]. Available: https://hal.science/hal-01065214 (cit. on pp. 75, 87).

[93] R. H. Park, "Two-reaction theory of synchronous machines generalized method of analysis-part I," *Transactions of the American Institute of Electrical Engineers*, vol. 48, no. 3, pp. 716–727, 1929, ISSN: 0096-3860. DOI: 10.1109/T-AIEE.1929.5055275 (cit. on p. 82).

[94] D. Štrbac, "Berechnungsverfahren für Asynchronmaschinen kleiner Leistung," Dissertation, Technische Universität Ilmenau, 2015 (cit. on p. 88).

[95] J. C. Moreira and T. A. Lipo, "Modeling of saturated AC machines including air gap flux harmonic components," *IEEE Transactions on Industry Applications*, vol. 28, no. 2, pp. 343–349, 1992, ISSN: 0093-9994. DOI: 10.1109/28.126740 (cit. on p. 92).

[96] C. Alteheld and R. Gottkehaskamp, "Consideration of Leakage Path Saturation in an Analytical Calculation Model of an Induction Machine," in *ICEMS 2018*, C.-E. Kim, Ed., Piscataway, NJ: IEEE, 2018, pp. 628–633, ISBN: 978-89-86510-20-1. DOI: 10.23919/ICEMS.2018.8549003 (cit. on pp. 105, 133).

[97] C. Alteheld, "Berechnung, Entwurf und Optimierung von Asynchronmaschinen unter besonderer Berücksichtigung von Sättigungseffekten und Wicklungen in kombinierter Stern-Dreieckschaltung," Dissertation, TU Dortmund University, Dortmund, 2020 (cit. on pp. 105, 133).

[98] K. Oberretl, "To the Calculation of Forces from the Magnetic Energy by Virtual Displacement," *Acta Technica CSAV*, no. 2, pp. 184–196, 1976 (cit. on p. 105).

[99] The MathWorks Inc., *MATLAB 9.13.0 (R2022b)*, 2022. [Online]. Available: https://www.mathworks.com (cit. on p. 106).

[100] R. L. Burden, J. D. Faires, and A. M. Burden, *Numerical analysis*, Tenth edition. Boston, MA: Cengage Learning, 2016, ISBN: 9781305253667 (cit. on p. 106).

[101] F. N. Fritsch and R. E. Carlson, "Monotone Piecewise Cubic Interpolation," *SIAM Journal on Numerical Analysis*, vol. 17, no. 2, pp. 238–246, 1980, ISSN: 0036-1429. DOI: 10.1137/0717021 (cit. on p. 107).

[102] D. Kahaner, C. B. Moler, and S. Nash, *Numerical methods and software* (Prentice-Hall series in computational mathematics). Englewood Cliffs, NJ: Prentice-Hall, 1989, ISBN: 013626672X (cit. on p. 107).

Author's Publications

[A1] J. Rituper and R. Gottkehaskamp, "Initial Design and Measurement of Line-Start Synchronous Reluctance Machines for Industrial Applications up to 1 kW," in *Electromechanical Drive Systems 2021; ETG Symposium*, 2021, pp. 1–6 (cit. on p. 4).

[A2] J. Rituper, J. Güdelhöfer, and R. Gottkehaskamp, "Consideration of the Skin Effect in a Transient Model of Line-Start Synchronous Reluctance Machines," in *2020 International Conference on Electrical Machines (ICEM)*, IEEE, 8232020, pp. 97–103, ISBN: 978-1-7281-9945-0. DOI: 10.1109/ICEM49940.2020.9270644 (cit. on pp. 9, 38, 75, 78).

[A3] J. Rituper and R. Gottkehaskamp, "Consideration of the Saturation in a Transient Model of Line-Start Synchronous Reluctance Machines," in *2022 International Conference on Electrical Machines (ICEM)*, Piscataway, NJ: IEEE, 2022, pp. 62–68, ISBN: 978-1-6654-1432-6. DOI: 10.1109/ICEM51905.2022.9910731 (cit. on pp. 9, 75, 89, 96).

[A4] J. Rituper and R. Gottkehaskamp, "Lumped Parameter Model for Transient Simulation of Line-Start Synchronous Reluctance Machines," in *Symposium de Génie Electrique (SGE 2023)*, 2023 (cit. on pp. 9, 75, 89).

[A5] J. Rituper and R. Gottkehaskamp, "End Ring Resistance Calculation for Line-Start Synchronous Reluctance Machines with Non-Standard Rotor Cage Geometries," in *Electromechanical Drive Systems 2023; ETG Symposium*, 2023 (cit. on pp. 29, 53).

[A6] J. Rituper, C. Alteheld, J. Güdelhöfer, and R. Gottkehaskamp, "Analytical Method to Consider the Slot Opening Effects in Nonlinear Magnetic Equivalent Circuits of Induction Machines," in *2018 XIII International Conference on Electrical Machines (ICEM)*, IEEE, 92018, pp. 86–90, ISBN: 978-1-5386-2477-7. DOI: 10.1109/ICELMACH.2018.8507209.

Supervised Student Work

[S1] M. Erdmann, "Berechnung der Eisenverluste von Synchron-Reluktanzmaschinen unter Berücksichtigung harmonischer magnetischer Flussdichten," Student Project (M.Sc.) University of Applied Sciences Düsseldorf, Düsseldorf, 2022 (cit. on p. 27).

[S2] M. Malyska, "Berechnung der Kurzschlussringwiderstände von Line-Start Synchron-Reluktanzmaschinen," Student Project (M. Sc.) University of Applied Sciences Düsseldorf, Düsseldorf, 2022 (cit. on p. 31).

[S3] D. Dispyrakis, "Berechnung des Hochlaufverhaltens eines selbstanlaufenden Synchron-Reluktanzmotors unter genauer Berücksichtigung des Stromverdrängungseffektes," Bachelor's Thesis, University of Applied Sciences Düsseldorf, Düsseldorf, 2019.

[S4] D. Al Janabi, "Berechnung des stationären Betriebsverhaltens geregelter fremderregter Synchronmaschinen mit der Grundwellentheorie," Bachelor's Thesis, University of Applied Sciences Düsseldorf, Düsseldorf, 2020.

[S5] L. Wüller, "Ermittlung des Energieverbrauchs einer geregelten Synchronmaschine bei vorgegebenen Lastzyklen auf Basis eines erweiterten Grundwellenmodells," Bachelor's Thesis, University of Applied Sciences Düsseldorf, Düsseldorf, 2020.

[S6] J. Joseph, "Zeiteffiziente Berechnung des Anlauf- und Betriebsverhaltens einer Line-Start Synchron-Reluktanzmaschine mit der Finite Elemente Methode," Bachelor's Thesis, University of Applied Sciences Düsseldorf, Düsseldorf, 2023.

Appendix A

Geometries of the Tested Motors

A.1 Stator geometry

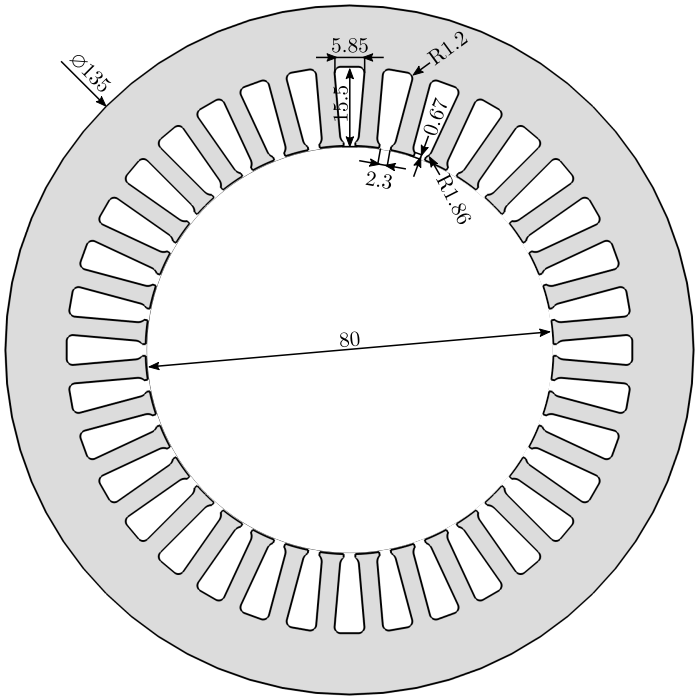

Figure A.1: Stator geometry

A.2 Rotor geometries

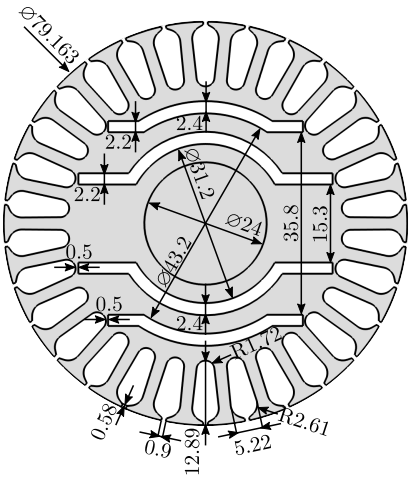

(a) Motor I ($J_{\mathrm{mot}} = 0.00110\,\mathrm{kg{\cdot}m^2}$)

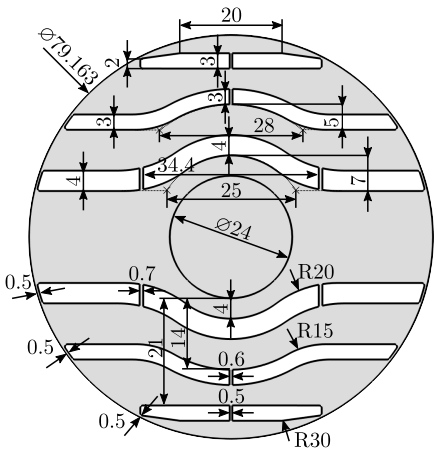

(b) Motor II ($J_{\mathrm{mot}} = 0.00118\,\mathrm{kg{\cdot}m^2}$)

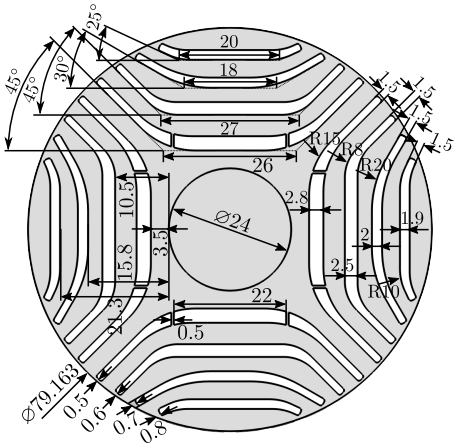

(c) Motor III ($J_{\mathrm{mot}} = 0.00115\,\mathrm{kg{\cdot}m^2}$)

Figure A.2: Rotor geometries

Appendix B

Lumped Parameter Model of a Single Coil

To develop a complex lumped parameter model of an electrical machine with multiple electrically and magnetically coupled coils, the simple case of one single coil in a magnetic field is described at first. This clarifies the procedure itself, and also the distinction between voltage and Electromotive Force (often called 'induced voltage').

B.1 Derivation of the equation

In the first step, a closed, solid ring made of a conductive material is considered (see Figure B.1). The shown cross-section of the ring lies in the xy-plane.

If a magnetic field penetrates the area spanned by the ring, the magnetic flux linkage is defined as

$$\psi = \iint \vec{B}\,\mathrm{d}\vec{A}. \tag{B.1}$$

A time-varying magnetic field $\vec{B}$ in negative z-direction (i.e., into the paper) causes a flux linkage ψ in the coil which changes over time so we can write Faraday's induction law

$$e = -\frac{\mathrm{d}}{\mathrm{d}t}\psi \tag{B.2}$$

which yields an electromotive force (EMF) e around the ring. It is to mention that the negative sign is just a matter of definition. In this case, a decreasing flux linkage leads to a positive EMF, which causes a right-hand assigned current i to flow in the ring.

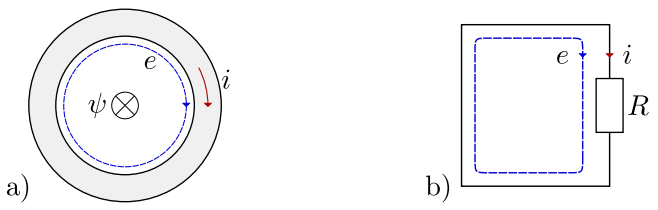

Figure B.1: Ring made of conductive material acting as a coil: a) Cross-section, b) equivalent circuit. The electromotive force e caused by the variation of ψ over time drives a current i.

From Maxwell's second equation, it is known that

$$-\frac{\mathrm{d}}{\mathrm{d}t}\psi = \oint \vec{E}\mathrm{d}\vec{s}, \tag{B.3}$$

where the right-hand side can be described as the sum of all voltages around the ring. Introducing the resistance R as the first lumped parameter, defined as the resistance of the circumferential current path through the ring, one can write

$$e = \oint \vec{E}\mathrm{d}\vec{s} = Ri. \tag{B.4}$$

It is obvious that there is no locally assignable voltage drop in the ring because the starting and endpoint of the resistance R are the same wherever this point is chosen. Practically, this means that there is no potential difference between any two points, so no voltage can be measured. Nonetheless, current is flowing through the ring due to induction. Hence, the EMF e which causes the current to flow should not be considered a voltage. More precisely, it is the sum of all voltages on the defined path.

Equation B.3 now yields:

$$-\frac{\mathrm{d}}{\mathrm{d}t}\psi = Ri \tag{B.5}$$

which transforms to

$$0 = Ri + \frac{\mathrm{d}}{\mathrm{d}t}\psi \tag{B.6}$$

as the general lumped parameter voltage equation of the ring. The equivalent circuit of this geometry is hence a single resistance which is short-circuited (see Figure B.1b).

Now, when one section of the ring is cut off, therefore creating an opening, current can no longer flow (Figure B.2). Therefore, the equivalent circuit is opened as well and a voltage u across the open terminals can be measured (Figure B.2b).

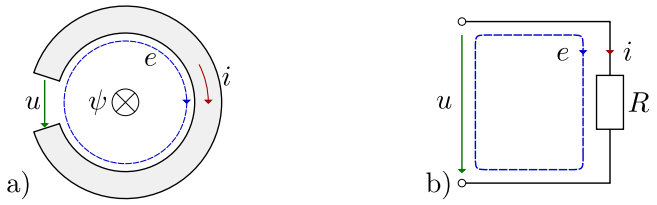

Figure B.2: Ring from Figure B.1 with one section removed: a) Cross-section, b) equivalent circuit. Now a voltage u can be measured at the open ends of the ring. The current i equals zero.

With e as the sum of all voltages follows:

$$e = -u \tag{B.7}$$

because $i = 0$. This means that the EMF can be measured at both terminals as voltage u (often referred to as induced voltage u_{ind}).

If an external voltage source is added to the ends of the cutoff (Figure B.3), current can flow again. The equation for this arrangement is

$$e = -u + Ri, \tag{B.8}$$

where e can be replaced with Equation B.2 again. In addition, u now denotes an impressed voltage, unlike in the previous case. Transformed to

$$u = Ri + \frac{\mathrm{d}}{\mathrm{d}t}\psi, \tag{B.9}$$

yields the well-known general voltage equation of a coil.

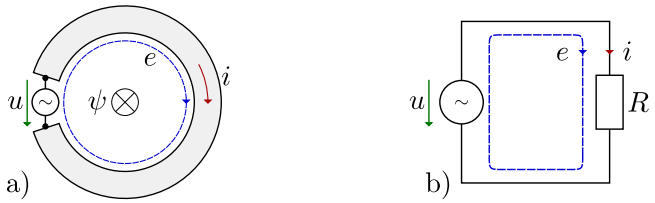

Figure B.3: Ring from Figure B.2 with an external voltage source added: a) Cross-section, b) equivalent circuit.